Experimental Analysis and Computational Modelling of Adsorption Separation of Methane and Carbon Dioxide by Carbon Materials

by

Amirhosein Jahanshahi

Thesis submitted to the University of Ottawa
in partial fulfillment of the requirements for the degree of
Master of Applied Science in Chemical Engineering

Department of Chemical and Biological Engineering
Faculty of Engineering
University of Ottawa

ABSTRACT

It is very important today to address the impacts of climate change as its effects can be observed every day. Nowadays many scientists believe that earth's climate is changing as a result of human-caused greenhouse gas emissions such as carbon dioxide and methane.

Global energy demand is also rapidly evolving. A sustainable approach that balances economic growth with social and environmental responsibility should be considered as an effective and long-term strategy. Carbon dioxide is the foremost greenhouse gas of anthropogenic origin, responsible for the majority of the earth's warming effects. It is estimated that around 60% of the global warming impact can be traced back to the release of carbon dioxide into the atmosphere. Lowering methane emissions offers a range of notable advantages in terms of energy, safety, economy, and the environment. Firstly, since methane is a potent greenhouse gas (25 times more powerful than CO_2 over a 100-year period), reducing methane emissions will contribute significantly to mitigating climate change in the short term. Additionally, methane is the primary component of natural gas and biogas, which means collecting and utilizing methane can be a valuable source of clean energy that fosters local economic growth and minimizes local environmental pollution. Generating energy through methane recovery eliminates the need for traditional energy resources, thus lessening end-user and power plant CO_2 and air pollutant emissions. Physical adsorption separation processes have proven to be an effective technique for simultaneous carbon dioxide capture and methane enrichment applications.

The objective of this study is to conduct a thorough assessment of the adsorption separation of methane and carbon dioxide gases employing a commercially available carbon molecular sieve, CMS(C), and an activated carbon, AC(B). The accomplishment of the objective involved conducting an in-depth characterization of the adsorbents. Part of the characterization included measurements of the internal surface area and pore size distributions, as well as the measurements of the equilibrium adsorption isotherms using gravimetric techniques. These isotherms enabled detailed kinetic analyses, such as evaluating diffusivity and mass transfer coefficients at various temperatures and pressure steps. The prediction of binary isotherms were based on theoretical models, which can describe the gas mixture adsorption equilibria using pure component equilibrium data. Breakthrough curves were generated to describe the dynamic response of an adsorption column under different pressures, temperatures, and flow rates. A mechanistic model was developed utilizing gPROMS simulation software for adsorption breakthrough process and it was validated by comparing its results to the experimental breakthrough curves. Parametric studies were conducted to

determine the optimal operating conditions for gas adsorption separation of CO_2 and CH_4 gases.

By examining the data obtained from breakthrough curves, pure and predicted binary adsorption equilibria, we calculated adsorption capacities, selectivity, sorbent selection parameter (S parameter), and the adsorbent performance indicator (API). These calculations were carried out to evaluate the initial potential for gas adsorption separation of the carbon molecular sieve (CMS(C)) and the activated carbon (AC(B)) under a range of operating conditions. Increasing pressure, decreasing temperature, and reduced feed flow improved breakthrough time and adsorption capacity for both gases on these adsorbents. CMS(C) showed superior selectivity, while AC(B) had a higher API value at specific conditions. The API was considered a more practical parameter for evaluating the initial gas separation potential. CMS(C) proved to be the better choice for methane purification, achieving the longest purification time under optimal conditions. Additionally, the study explored the kinetic behavior of methane and carbon dioxide with these adsorbent materials, revealing faster carbon dioxide uptake rates and the potential advantages of activated carbon in reducing adsorption/desorption cycle times in separation processes. At a pressure of 1 atm, a temperature of 294 K, and a flow rate of 400 ml min^{-1}, CMS(C) had the highest values of selectivity and the S parameter, while AC(B) had the highest API value at 9 atm of pressure, a temperature of 294 K, and a flow rate of 400 ml min^{-1}. The API was considered a more practical parameter for evaluating the initial gas separation potential. CMS(C) proved to be the better choice for methane purification, achieving the longest purification time of 420 seconds at a pressure of 9 atm, a temperature of 294 K, and a flow rate of 400 ml min^{-1}. Additionally, the study explored the kinetic behavior of methane and carbon dioxide with these adsorbent materials, revealing faster carbon dioxide uptake rates and the potential advantages of activated carbon in reducing adsorption/desorption cycle times in separation processes.

The analysis of the study, when compared to existing literature, reveals a coherent and logical progression. Our results align with similar studies, validating key points such as the improvement of methane purification through reduced feed flow rates and increased pressures, enhanced adsorption separation performance at lower temperatures and pressures, the superior adsorption capacity of activated carbon over carbon molecular sieves, and the greater selectivity of carbon molecular sieves over activated carbon and faster diffusion of carbon dioxide compared to methane within the carbon porous materials.

RÉSUMÉ

Il est très important aujourd'hui de prendre en compte les impacts du changement climatique, car ses effets sont observables au quotidien. De nos jours, de nombreux scientifiques estiment que le climat de la Terre évolue en raison des émissions de gaz à effet de serre d'origine humaine, tels que le dioxyde de carbone et le méthane.

La demande mondiale en énergie évolue également rapidement. Une approche durable qui concilie la croissance économique avec la responsabilité sociale et environnementale devrait être considérée comme une stratégie efficace et à long terme. Le dioxyde de carbone est le principal gaz à effet de serre d'origine anthropique, responsable de la majeure partie de l'effet de réchauffement de la Terre. On estime qu'environ 60 % de l'impact du réchauffement global peut être attribué aux émissions de dioxyde de carbone dans l'atmosphère.

La réduction des émissions de méthane offre de nombreux avantages notables en termes d'énergie, de sécurité, d'économie et d'environnement. Tout d'abord, étant donné que le méthane est un puissant gaz à effet de serre (25 fois plus puissant que le CO_2 sur une période de 100 ans), la réduction des émissions de méthane contribuera de manière significative à atténuer le changement climatique à court terme. De plus, le méthane est le composant principal du gaz naturel et du biogaz, ce qui signifie que la collecte et l'utilisation du méthane peuvent constituer une source précieuse d'énergie propre favorisant la croissance économique locale et réduisant la pollution environnementale locale et les odeurs désagréables. La production d'énergie grâce à la récupération du méthane élimine le besoin de ressources énergétiques traditionnelles, réduisant ainsi les émissions de CO_2 des utilisateurs finaux et des centrales électriques, ainsi que les émissions de polluants atmosphériques.

L'objectif de cette étude est de réaliser une évaluation approfondie de la séparation par adsorption des gaz méthane et dioxyde de carbone en utilisant un tamis moléculaire de carbone commercial, CMS(C), et du charbon actif, AC(B).

L'objectif de cette étude est de déterminer le meilleur adsorbant à base de carbone commercialement disponible pour la séparation du méthane et du dioxyde de carbone. La réalisation de l'objectif implique la réalisation d'une caractérisation approfondie des adsorbants. La caractérisation comprend des mesures de la surface interne et de la distribution de la taille des pores. Des mesures d'équilibre ont été réalisées pour générer des isothermes d'adsorption en utilisant des techniques gravimétriques. Ces isothermes ont permis des analyses cinétiques détaillées, telles que l'évaluation de la diffusivité et des coefficients de transfert de masse à différentes températures et pressions.

La prédiction des isothermes binaires s'est basée sur des modèles théoriques, pouvant décrire les équilibres d'adsorption de mélanges gazeux en utilisant des données d'équilibre de composants purs. Des courbes de percée ont été générées pour décrire la réponse dynamique d'une colonne d'adsorption sous différentes pressions, températures et débits. La modélisation de la percée d'adsorption a utilisé le logiciel de simulation gPROMS. Le modèle développé a été validé en le comparant aux courbes de percée expérimentales. Des études paramétriques ont été réalisées pour déterminer les conditions de fonctionnement optimales pour la séparation par adsorption de gaz.

En examinant les données des courbes de percée, les équilibres d'adsorption binaire purs et prédits, nous avons calculé les capacités d'adsorption, la sélectivité, le paramètre de sélection du sorbant (S paramètre) et l'indicateur de performance du sorbant (API). Ces calculs ont été réalisés pour évaluer le potentiel initial de séparation par adsorption de gaz du tamis moléculaire de carbone (CMS(C)) et du charbon actif (AC(B)) dans une gamme de conditions opérationnelles. L'augmentation de la pression, la réduction de la température et la diminution du débit d'alimentation ont amélioré le temps de percée et la capacité d'adsorption pour les deux gaz sur ces adsorbants. À une pression de 1 atm, une température de 294 K et un débit de 400 ml/min, le CMS(C) présentait les valeurs les plus élevées de sélectivité et du paramètre S, tandis que le AC(B) affichait la valeur la plus élevée de l'API à une pression de 9 atm, une température de 294 K et un débit de 400 ml/min. L'API a été considéré comme un paramètre plus pratique pour évaluer le potentiel initial de séparation des gaz. Le CMS(C) s'est révélé être le choix optimal pour la purification du méthane, atteignant le temps de purification le plus long de 420 secondes à une pression de 9 atm, une température de 294 K et un débit de 400 ml/min. De plus, l'étude a exploré le comportement cinétique du méthane et du dioxyde de carbone avec ces matériaux adsorbants, révélant des taux d'absorption plus rapides du dioxyde de carbone et les avantages potentiels du charbon actif dans la réduction des temps de cycle d'adsorption/désorption dans les processus de séparation.

L'analyse de l'étude, comparée à la littérature existante, révèle une progression cohérente et logique. Nos résultats s'alignent avec des études similaires, validant des points clés tels que l'amélioration de la purification du méthane par la réduction des débits d'alimentation et l'augmentation des pressions, des performances accrues de séparation par adsorption à des températures et pressions plus basses, la capacité d'adsorption supérieure du charbon actif par rapport aux tamis moléculaires de carbone, la plus grande sélectivité des tamis moléculaires de carbone par rapport au charbon actif et une diffusion plus rapide du dioxyde de carbone par rapport au méthane au sein des matériaux poreux de carbone.

STATEMENT OF CONTRIBUTIONS OF COLLABORATORS

I hereby certify that the thesis presented here is solely my own work, and I am the exclusive author responsible for all experiments and analyses conducted, except when explicitly stated otherwise. Throughout the process, I was under the scientific guidance and oversight of Prof. F. Handan Tezel. Whenever appropriate, I have recognized and credited external resources that have provided information and support for my analyses. I am the author of all the chapters included in this thesis. Prof. F. Handan Tezel, my research project supervisor, conducted both scientific and editorial assessments for this research.

The adsorption breakthrough experimental set up was designed by myself and built with the help of technical officers, Franco Ziroldo, Gerard Nina and Patrick Pageau.

Dana Li and Griffin Worboy were responsible for obtaining the equilibrium data for single component adsorption isotherm experiments. This data was utilized for both the adsorption kinetic analysis in Chapter 4, as well adsorption equilibrium analysis and input data for the computational model representing the adsorption separation process in a packed-bed adsorption column in Chapters 2 and 3.

ACKNOWLEDGMENTS

I would like to begin by expressing my profound appreciation to my supervisor, Prof. Handan Tezel, for the invaluable support and guidance provided to me throughout this endeavor. Your unwavering enthusiasm and dedication served as a constant source of motivation, and I feel fortunate to have had the privilege of working under your supervision. I would also like to extend my appreciation to the technical and administrative staff of the Chemical and Biological Engineering Department at the University of Ottawa, namely Patrick Pageau, Gerard Nina, Franco Ziroldo, Francine Pétrin and Frantz Célestin. I wish to express my gratitude to the Natural Sciences and Engineering Research Councils of Canada (NSERC), MITACS Accelerate program, and Xebec Adsorption Company for their generous support in terms of funding, sample provision, and technical assistance. It is through their contributions that this project was made possible. I am also thankful to my friends in Prof. Tezel's research group, Dana, Ji Sub, Lara, Suboohi, and Griffin, with whom I had the privilege of discussing my work and sharing delightful moments. A special thank you to Dr. Qinglin Huang from Siemens Process Systems Engineering Ltd. for his extremely useful assistance throughout the computational model development of this research. I wish to express my heartfelt appreciation to the individuals who are the most important people in my life: my father, Hassan Jahanshahi, my mother, Fatemeh Safinejad, and my younger sisters, Faezeh Jahanshahi and Ateeyeh Jahanshahi. Their endless love and unconditional support have been an invaluable source of strength and motivation for me throughout my life.

DEDICATION

I would like to dedicate this thesis to my father, Hassan Jahanshahi and my mother, Fatemeh Safinejad, for their endless support, unconditional love and selfless devotion.

Table of Contents

List of Figures

List of Tables

CHAPTER 1

GLOBAL INTRODUCTION

1.1. INTRODUCTION

As the demand for energy rises, significant amount of greenhouse gases (GHG) are being discharged into the atmosphere due to the continued use of fossil fuels as a primary energy source[1]. These gases function as heat retainers, leading to a surge in worldwide temperatures. Carbon dioxide (CO_2) and methane (CH_4) are the two primary gases with substantial effects[1,2]. Consequently, reducing emissions from their sources and discovering cleaner energy alternatives are crucial methods to combat climate change. Although many initiatives concentrate on boosting energy efficiency, the present priority is to isolate, store and utilize CO_2 to develop high-value products as a short-term solution[1,3]. Carbon dioxide is the foremost greenhouse gas of anthropogenic origin, responsible for the majority of the Earth's warming effect. It is estimated that around 60% of the global warming impact can be traced back to the release of carbon dioxide into the atmosphere[4]. Lowering methane emissions offers a range of notable advantages in terms of energy, safety, economy, and the environment. Firstly, since methane is a potent greenhouse gas (25 times more powerful than CO_2 over a 100-year period), reducing methane emissions will contribute significantly to mitigating climate change in the short term. Additionally, methane is the primary component of natural gas and biogas, which means collecting and utilizing methane can be a valuable source of clean energy that fosters local economic growth and minimizes local environmental pollution. Generating energy through methane recovery eliminates the need for traditional energy resources, thus lessening end-user and power plant CO_2 and air pollutant emissions[5].

The most common gas separation processes to remove CO_2 from CH_4 in a gaseous mixture are physical and chemical absorption, cryogenic separation, adsorption, and membrane separation. The utilization of adsorption technology in gas separation processes is becoming increasingly popular in various industries. This is primarily due to the method's capacity to deliver better cost-effectiveness and reliability compared to traditional techniques mentioned above. Adsorption separation requires less energy and has lower costs, making it a more attractive option in industries where environmental and quality regulations are stringent. This has led to the widespread implementation of adsorption technology in several industrial applications[6]. Despite the advantages of adsorption technology, there are still obstacles that must be overcome in terms of designing the adsorption process to achieve optimal purity and

maximum recovery of the desired end-products. The success of the design for carbon dioxide capture and methane enrichment applications, is reliant on identifying the most suitable adsorbent that meets specific requirements such as capacity, compatible pore size, high selectivity, easy regenerability, fast kinetics, and cost-effectiveness. However, it is rare to find an adsorbent that can satisfy all of these criteria simultaneously[6].

Adsorption is a surface phenomenon in which the surface of the adsorbent engages with either a gas or a liquid. In the case of separation through adsorption, one component of the fluid stream has a higher affinity towards the adsorbent surface compared to the other components, resulting in the preferential adsorption of that specific component[7].

The adsorbent is the central element of the adsorption process, and its effectiveness is a key factor in determining the efficiency of the separation system. Therefore, the selection of the appropriate adsorbent is critical in achieving selectivity, capacity, recovery, and longevity for the separation of a specific mixture of gas or liquid[8]. To achieve separation, the adsorbents are placed in an adsorption column to segregate the feed gas mixture. Subsequently, the feed gas mixture with known thermophysical characteristics is passed through the packed adsorption column as shown in Figure 1.1[9]. Depending on the adsorbent selectivity and the objective of the adsorption separation process, the target gas will preferentially get adsorbed more while the product gas is collected leaving the adsorption column. The obtained selectivity and other parameters such as the sorbent selection parameter (S parameter) and the adsorbent performance indicator (API) can be used to initially assess the adsorbent gas separation performance.

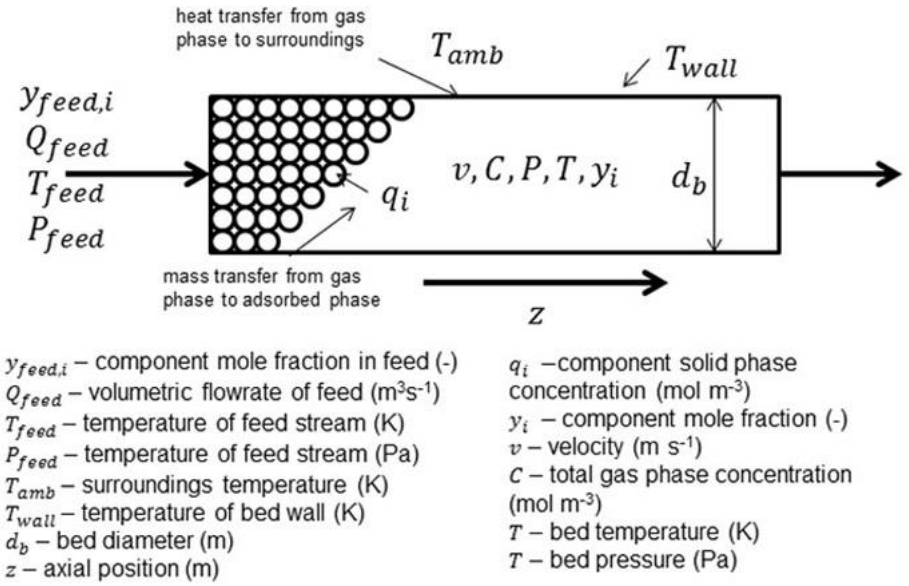

Figure 1.1 Schematic diagram of a packed adsorption column with the inlet stream (feed) and the outlet stream[9]

Different adsorbent materials have been proposed and screened in the literature, for the separation of carbon dioxide from methane including different types of zeolites[10-26], porous carbons[27-36], metal organic frameworks[37-42], amine functionalized silica materials[43,44] and many others. Although zeolites, metal organic frameworks (MOFs), amine functionalized silica materials have proven to be high quality materials for CO_2 capture they also have their own limitations. MOFs are susceptible to collapse and the loss of porosity and order, resulting in the formation of amorphous solid when desorption is carried out at elevated temperatures. Additionally, the composition of flue gas greatly affects the structure of MOFs. The hydrolysis of oxygen-metal coordination bonds in MOFs is facilitated by low moisture levels, which irreversibly damages the frameworks. In addition to other drawbacks, MOFs have the additional disadvantages of high cost synthesis and difficulty in large-scale production[45]. The adsorption capacity of zeolites for carbon dioxide drastically reduces as the temperature rises. Furthermore, zeolites are particularly sensitive to the amount of water in the flue gas, and due to their highly hydrophilic nature, significant flue gas drying is necessary prior to carbon dioxide capture, or very high regeneration temperatures are required (often in excess of 300 °C). This additional drying and high regeneration temperature comes at a cost, which has a considerable impact on zeolites' adsorption applications[4]. In upcoming applications for CO_2 capture, amine functionalized silica materials have shown significant potential. However, a serious challenge that remains is the stability problem during cyclic CO_2 adsorption-desorption runs. This issue is primarily caused by amine leaching and degradation[46].

Porous carbon adsorbents are the most often utilized adsorbents for CO_2 capture and CH_4 enrichment because of their many advantages. For instance, there is no need for pretreatment to eliminate moisture for separation, low heat of adsorption which reduces the energy requirement for regeneration, and abundance and inexpensive raw material. The most commonly used adsorbents among all carbon adsorbents are the carbon molecular sieves (CMSs) and activated carbons (ACs) for gas separation applications.

In this study, we intend to use carbon-based material for the separation of methane and carbon dioxide. Although in the literature it was observed that some of the carbon based materials (e.g. activated carbons) exhibit lower selectivity towards CO_2 compared to zeolites and MOFs but in an industrial scale, in terms of economy, the production of carbon based materials is more affordable, have a high raw material availability, and are less affected by the presence of moisture in the feed gas relative to other solid adsorbents and easier to regenerate (low regeneration energy, low regeneration temperature) compared to zeolites and MOFs.

Therefore, for the time being, carbon-based materials are still the most promising materials for CO_2 capture by adsorption methods.

To enhance the efficiency and effectiveness of adsorption separation processes computational modeling can play a crucial role. It allows to gain a deeper understanding of the adsorption mechanisms at play, helps in the selection of the most suitable materials, by tweaking parameters like temperature, pressure, flow rates, bed configurations etc. It can help optimize the process to maximize efficiency and minimize energy consumption, aids in the scale-up of adsorption processes from the laboratory to industrial scales and can significantly reduce the number of experiments required, making the development and optimization of adsorption systems more cost-effective.

This study aims to perform an extensive evaluation of the adsorption-based separation of methane and carbon dioxide gases using readily accessible materials, including a commercially available carbon molecular sieve known as CMS(C) and an activated carbon known as AC(B). This will be accomplished by conducting an in-depth characterization of the adsorbent, which will include measurements of the internal surface area and pore size distribution, as well as equilibrium measurements generating adsorption isotherms through the use of gravimetric techniques, which will allow for detailed kinetic analyses such as diffusivity at various temperatures and pressure steps. Also, prediction of binary isotherms based on theoretical models will be utilized to describe gas mixture adsorption equilibria using pure component equilibrium data. Experimental breakthrough curves will be obtained describing the dynamic response of an adsorption column at different pressures, temperatures, and flow rates. A mechanistic model will be developed using gPROMS simulation software for adsorption breakthrough model and it will be validated with the experimental breakthrough curves. Parametric studies will be conducted to determine the optimal operating conditions for gas adsorption separation of CO_2 and CH_4 gases.

1.2. THESIS STRUCTURE

The thesis consists of 6 chapters, with the current one as the first.

CHAPTER- 2, 3,

Chapters 2 and 3 present a comprehensive evaluation based on experiments conducted and computational modelling of adsorption separation of methane and carbon dioxide by commercially available carbon molecular sieve and activated carbon, respectively. These

chapters include equilibrium measurements of the above-mentioned adsorbents for pure methane and carbon dioxide gases using the gravimetric method at multiple temperatures over the pressure range of interest, predicted binary isotherms based on adsorption isotherm models using pure component data, pore size distribution and BET surface area measurements, experimental breakthrough curves and simulated breakthrough curves validated with experimental data. The obtained gravimetric data were analyzed in terms of adsorption capacity, selectivity, and sorbent selection parameter. The effect of variations of temperature, pressure and flow rate on the breakthrough curves were also discussed to identify optimal adsorption gas separation operating conditions for a CO_2/CH_4 separation system.

CHAPTER 4- This chapter discusses the kinetics of adsorption of carbon dioxide and methane on commercially available activated carbon and carbon molecular sieve. The different mechanisms of adsorption kinetics are described, and their outcomes are compared to the experimental uptake data. This chapter also highlights the initial gas separation potential (separation CO_2 from CH_4) of these adsorbents through the adsorbent performance indicator, API.

CHAPTER 5- Conclusions

This section provides an overall summary of the preceding chapters, highlights the original contributions of the research, and offers recommendations for future work.

APPENDIX A- Additional equations used in adsorption breakthrough modeling (thermophysical properties of the fluid, diffusivity relations, heat and mass transfer relations and momentum balance)

APPENDIX B- gPROMS codes (Concentration and temperature gradients exist in the axial direction in the column the radial direction in the pellet, the radial direction in of the crystals)

APPENDIX C- gPROMS codes (Concentration and temperature gradients exist in the axial direction in the column)

1.3. ABBREVIATIONS

AC	Activated carbon
API	Adsorbent performance indicator
CMS	Carbon molecular sieve
GHG	Greenhouse gas
MOF	Metallic Organic Framework

1.4. REFRENCES

(1) Al-Akwaa, S. Synthesis and New Characterization Method of Silicalite-1 Membranes for Gas Separation. Diss. Université d'Ottawa/University of Ottawa, 2020.

(2) Pera-Titus, M. Porous Inorganic Membranes for CO2 Capture: Present and Prospects. *Chemical reviews* 2014, *114* (2), 1413–1492.

(3) Aaron, D.; Tsouris, C. Separation of CO2 from Flue Gas: A Review. *Separation science and technology* 2005, *40* (1–3), 321–348.

(4) Sabouni, R. Carbon Dioxide Adsorption by Metal Organic Frameworks (Synthesis, Testing and Modeling).

(5) Rajaram, V.; Siddiqui, F. Z.; Khan, M. E. *From Landfill Gas to Energy: Technologies and Challenges*; CRC press, 2011.

(6) Wilson, S. M. W. Adsorption Separation of CO2 from CO in Syngas: Improving the Conversion of the Reverse Water Gas Shift Reaction.

(7) Wilson, S. Adsorption Separation of CO2 in Low Concentrations for Applications in Direct Air Capture and Excimer Gas Separation.

(8) Shirani, B. Elucidating Adsorption Mechanisms in Carbon Molecular Sieves and Development of New Methodologies for Fast Screening of Gas and Liquid Adsorption Systems, University of New Brunswick., 2016.

(9) Caldwell, S. J. Experimental and Computational Evaluation of Activated Carbons for Carbon Dioxide Capture from High Pressure Gas Mixtures, University of Birmingham, 2015.

(10) Mulgundmath, V. P.; Tezel, F. H.; Saatcioglu, T.; Golden, T. C. Adsorption and Separation of CO2/N2 and CO2/CH4 by 13X Zeolite. *Can. J. Chem. Eng.* 2012, *90* (3), 730–738.

(11) Cavenati, S.; Grande, C. A.; Rodrigues, A. E. Layered Pressure Swing Adsorption for Methane Recovery from CH4/CO2/N2 Streams. *Adsorption* 2005, *11* (S1), 549–554.

(12) Ghoufi, A.; Gaberova, L.; Rouquerol, J.; Vincent, D.; Llewellyn, P. L.; Maurin, G. Adsorption of CO2, CH4 and Their Binary Mixture in Faujasite NaY: A Combination of Molecular Simulations with Gravimetry–Manometry and Microcalorimetry Measurements. *Microporous and Mesoporous Materials* 2009, *119* (1–3), 117–128.

(13) Liu, D.; Yi, H.; Tang, X.; Zhao, S.; Wang, Z.; Gao, F.; Li, Q.; Zhao, B. Adsorption Separation of CO_2 /CH_4 Gas Mixture on Carbon Molecular Sieves Modified by Potassium Carbonate. *J. Chem. Eng. Data* 2016, *61* (7), 2197–2201.

(14) McEwen, J.; Hayman, J.-D.; Ozgur Yazaydin, A. A Comparative Study of CO2, CH4 and N2 Adsorption in ZIF-8, Zeolite-13X and BPL Activated Carbon. *Chemical Physics* 2013, *412*, 72–76.
(15) Cavenati, S.; Grande, C. A.; Rodrigues, A. E. Adsorption Equilibrium of Methane, Carbon Dioxide, and Nitrogen on Zeolite 13X at High Pressures. *J. Chem. Eng. Data* 2004, *49* (4), 1095–1101.
(16) Li, Y.; Yi, H.; Tang, X.; Li, F.; Yuan, Q. Adsorption Separation of CO2/CH4 Gas Mixture on the Commercial Zeolites at Atmospheric Pressure. *Chemical Engineering Journal* 2013, *229*, 50–56.
(17) Zhang, J.; Singh, R.; Webley, P. A. Alkali and Alkaline-Earth Cation Exchanged Chabazite Zeolites for Adsorption Based CO2 Capture. *Microporous and Mesoporous Materials* 2008, *111* (1–3), 478–487.
(18) Grande, C. A.; Rodrigues, A. E. Biogas to Fuel by Vacuum Pressure Swing Adsorption I. Behavior of Equilibrium and Kinetic-Based Adsorbents. 11.
(19) Campo, M. C.; Ribeiro, A. M.; Ferreira, A. F. P.; Santos, J. C.; Lutz, C.; Loureiro, J. M.; Rodrigues, A. E. Carbon Dioxide Removal for Methane Upgrade by a VSA Process Using an Improved 13X Zeolite. *Fuel Processing Technology* 2016, *143*, 185–194.
(20) Delgado, J. A.; Uguina, M. A.; Sotelo, J. L.; Ruíz, B.; Rosário, M. Carbon Dioxide/Methane Separation by Adsorption on Sepiolite. *Journal of Natural Gas Chemistry* 2007, *16* (3), 235–243.
(21) Mofarahi, M.; Gholipour, F. Gas Adsorption Separation of CO2/CH4 System Using Zeolite 5A. *Microporous and Mesoporous Materials* 2014, *200*, 1–10.
(22) Santos, M. P. S.; Grande, C. A.; Rodrigues, A. E. Pressure Swing Adsorption for Biogas Upgrading. Effect of Recycling Streams in Pressure Swing Adsorption Design. *Ind. Eng. Chem. Res.* 2011, *50* (2), 974–985.
(23) Cavenati, S.; Grande, C. A.; Rodrigues, A. E. Separation of CH 4 / CO 2 / N 2 Mixtures by Layered Pressure Swing Adsorption for Upgrade of Natural Gas. *Chemical Engineering Science* 2006, *61* (12), 3893–3906.
(24) Silva, J. A. C.; Cunha, A. F.; Schumann, K.; Rodrigues, A. E. Binary Adsorption of CO2/CH4 in Binderless Beads of 13X Zeolite. *Microporous and Mesoporous Materials* 2014, *187*, 100–107.
(25) Li, P.; Tezel, F. H. Pure and Binary Adsorption Equilibria of Methane and Carbon Dioxide on Silicalite. *Separation Science and Technology* 2007, *42* (14), 3131–3153.
(26) Harlick, P. J. E.; Tezel, F. H. CO2⁄N2 and CO2⁄CH4 Binary Adsorption Isotherms with H-ZSM5: The Importance of Experimental Data Regression with the Concentration Pulse Method. *Can. J. Chem. Eng.* 2001, *79* (2), 236–245.
(27) Rios, R. B.; Stragliotto, F. M.; Peixoto, H. R.; Torres, A. E. B.; Bastos-Neto, M.; Azevedo, D. C. S.; Cavalcante Jr, C. L. Studies on the Adsorption Behavior of CO2-CH4 Mixtures Using Activated Carbon. *Braz. J. Chem. Eng.* 2013, *30* (4), 939–951.
(28) Shao, X.; Feng, Z.; Xue, R.; Ma, C.; Wang, W.; Peng, X.; Cao, D. Adsorption of CO2, CH4, CO2/N2 and CO2/CH4 in Novel Activated Carbon Beads: Preparation, Measurements and Simulation. *AIChE J.* 2011, *57* (11), 3042–3051.
(29) Wu, Y.-J.; Yang, Y.; Kong, X.-M.; Li, P.; Yu, J.-G.; Ribeiro, A. M.; Rodrigues, A. E. Adsorption of Pure and Binary CO_2, CH_4, and N_2 Gas Components on Activated Carbon Beads. *J. Chem. Eng. Data* 2015, *60* (9), 2684–2693.
(30) Peng, X.; Wang, W.; Xue, R.; Shen, Z. Adsorption Separation of CH4/CO2 on Mesocarbon Microbeads: Experiment and Modeling. *AIChE J.* 2006, *52* (3), 994–1003.

(31) Yi, H.; Li, F.; Ning, P.; Tang, X.; Peng, J.; Li, Y.; Deng, H. Adsorption Separation of CO2, CH4, and N2 on Microwave Activated Carbon. *Chemical Engineering Journal* 2013, *215–216*, 635–642. https://doi.org/10.1016/j.cej.2012.11.050.

(32) Peredo-Mancilla, D.; Ghimbeu, C. M.; Ho, B.-N.; Jeguirim, M.; Hort, C.; Bessieres, D. Comparative Study of the CH4/CO2 Adsorption Selectivity of Activated Carbons for Biogas Upgrading. *Journal of Environmental Chemical Engineering* 2019, *7* (5), 103368.

(33) Dreisbach, F.; Staudt, R.; Keller, J. U. High Pressure Adsorption Data of Methane, Nitrogen, Carbon Dioxide and Their Binary and Ternary Mixtures on Activated Carbon. 13.

(34) Grande, C. A.; Blom, R.; Möller, A.; Möllmer, J. High-Pressure Separation of CH4/CO2 Using Activated Carbon. *Chemical Engineering Science* 2013, *89*, 10–20.

(35) Himeno, S.; Komatsu, T.; Fujita, S. High-Pressure Adsorption Equilibria of Methane and Carbon Dioxide on Several Activated Carbons. *J. Chem. Eng. Data* 2005, *50* (2), 369–376.

(36) Nandi, M.; Okada, K.; Dutta, A.; Bhaumik, A.; Maruyama, J.; Derks, D.; Uyama, H. Unprecedented CO2 Uptake over Highly Porous N-Doped Activated Carbon Monoliths Prepared by Physical Activation. *Chem. Commun.* 2012, *48* (83), 10283.

(37) Sabouni, R. Carbon Dioxide Adsorption by Metal Organic Frameworks (Synthesis, Testing and Modeling). 202.

(38) Yuan, B.; Wu, X.; Chen, Y.; Huang, J.; Luo, H.; Deng, S. Adsorption of CO_2, CH_4, and N_2 on Ordered Mesoporous Carbon: Approach for Greenhouse Gases Capture and Biogas Upgrading. *Environ. Sci. Technol.* 2013, *47* (10), 5474–5480.

(39) Hamon, L.; Jolimaître, E.; Pirngruber, G. D. CO_2 and CH_4 Separation by Adsorption Using Cu-BTC Metal–Organic Framework. *Ind. Eng. Chem. Res.* 2010, *49* (16), 7497–7503.

(40) Hamon, L.; Llewellyn, P. L.; Devic, T.; Ghoufi, A.; Clet, G.; Guillerm, V.; Pirngruber, G. D.; Maurin, G.; Serre, C.; Driver, G.; van Beek, W.; Jolimaître, E.; Vimont, A.; Daturi, M.; Férey, G. Co-Adsorption and Separation of CO_2 –CH_4 Mixtures in the Highly Flexible MIL-53(Cr) MOF. *J. Am. Chem. Soc.* 2009, *131* (47), 17490–17499.

(41) Bae, Y.-S.; Mulfort, K. L.; Frost, H.; Ryan, P.; Punnathanam, S.; Broadbelt, L. J.; Hupp, J. T.; Snurr, R. Q. Separation of CO_2 from CH_4 Using Mixed-Ligand Metal–Organic Frameworks. *Langmuir* 2008, *24* (16), 8592–8598. https://doi.org/10.1021/la800555x.

(42) Bárcia, P. S.; Bastin, L.; Hurtado, E. J.; Silva, J. A. C.; Rodrigues, A. E.; Chen, B. Single and Multicomponent Sorption of CO_2, CH_4 and N_2 in a Microporous Metal-Organic Framework. *Separation Science and Technology* 2008, *43* (13), 3494–3521.

(43) Morishige, K. Adsorption and Separation of CO_2 /CH_4 on Amorphous Silica Molecular Sieve. *J. Phys. Chem. C* 2011, *115* (19), 9713–9718.

(44) Zhang, Y.; Chen, K.; Lv, C.; Wu, T.; Wen, Y.; He, H.; Yu, S.; Wang, L. Adsorption Separation of CO2/CH4 from Landfill Gas by Ethanolamine-Modified Silica Gel. *Water Air Soil Pollut* 2021, *232* (2), 64.

(45) Nie, L.; Mu, Y.; Jin, J.; Chen, J.; Mi, J. Recent Developments and Consideration Issues in Solid Adsorbents for CO2 Capture from Flue Gas. *Chinese Journal of Chemical Engineering* 2018, *26* (11), 2303–2317.

(46) Chen, C.; Zhang, S.; Row, K. H.; Ahn, W.-S. Amine–Silica Composites for CO2 Capture: A Short Review. *Journal of Energy Chemistry* 2017, *26* (5), 868–880.

CHAPTER 2

Experimental Analysis and Computational Modelling of Adsorption Separation of Methane and Carbon dioxide on Carbon Molecular Sieve

A. Jahanshahi, F.H. Tezel

University of Ottawa, Department of Chemical and Biological Engineering

161 Louis Pasteur, Ottawa, Ontario, CANADA, K1N 6N5

ABSTRACT

This study provides a comprehensive evaluation of the adsorption separation of methane and carbon dioxide gases using a commercial carbon molecular sieve, CMS(C). The evaluation encompasses experimental measurements and computational modeling with gPROMS software. The experimental measurements include equilibrium measurements of the adsorbent for pure methane and carbon dioxide gases at different temperatures over a pressure range of interest using the gravimetric method and predicting binary isotherms based on temperature dependent isotherm models. The study further examines experimental breakthrough curves at different operating conditions and validates them with simulated breakthrough curves. The effect of different operating conditions (temperature, pressure, and flow rate variations) on the breakthrough curves is discussed to identify optimal operating conditions of the CMS (C) adsorbent for separating carbon dioxide from methane. The analysis of the breakthrough curves indicates that increasing pressure and decreasing temperature and feed flow lead to higher adsorption capacities of both gases for the CMS(C) adsorbent. However, it is observed that the values of adsorption selectivity and the sorbent selection parameter decrease under these conditions. Based on the measurements, the optimal conditions for separating carbon dioxide from methane on CMS(C) were found to be a pressure of 1 atm, temperature of 294K, and a flow rate of 400 ml min^{-1}. These conditions resulted in the highest values of selectivity and the sorbent selection parameter. The examination also showed that, in order to maximize the time for methane purification, it is advantageous to perform breakthrough experiments under increased pressures, lower temperatures, and decreased inlet feed flow rates. As an illustration, the optimum condition was reached at 9 atm pressure, 294 K temperature, and a flow rate of 400 ml/min, resulting in the most extended purification period of 420 seconds.

Keywords: Carbon molecular sieve, gPROMS, Breakthrough, Selectivity, Carbon dioxide, methane

2.1. INTRODUCTION

The swift progression of global warming and increased usage of fossil fuels have led to the prominent issues of resource scarcity and environmental degradation. As a result, the global energy structure has been propelled towards a clean, renewable, and low-carbon direction to address these challenges faced by humanity[1,2]. In modern times, a prevailing belief among scientists is that human-induced greenhouse gas emissions, particularly carbon dioxide and methane, are responsible for altering the climate of the earth. These two gases are commonly present in gas combinations such as natural gas, coalbed methane, biogas, and landfill gas[3]. Carbon dioxide is the primary anthropogenic greenhouse gas that contributes significantly to the warming effect on the planet. The discharge of carbon dioxide into the atmosphere accounts for approximately 60% of the overall global warming impact[4]. Minimizing methane emissions has several noteworthy benefits related to energy, safety, economy, and the environment. Firstly, since methane is a potent greenhouse gas (it has twenty-five times the warming effect of CO_2 over a 100-year period), decreasing methane emissions can make a significant contribution to short-term climate change mitigation efforts. Secondly, methane is the primary component of natural gas and biogas, which indicates that capturing and utilizing methane can serve as a valuable source of clean energy that promotes local economic growth while minimizing environmental pollution. Utilizing methane for energy generation negates the necessity for conventional energy sources, leading to reduced CO_2 and air pollutant emissions from end-users and power plants[5].

A major hurdle for research and technological development is to effectively merge the objective of reducing CO_2 emissions, which is imperative in mitigating global warming, with the mounting global energy demands that contribute significantly to these emissions[6]. Effective removal of carbon dioxide from methane to enhance its value is crucial from an economic standpoint. Several technologies are available to serve this objective, including physical and chemical absorption, cryogenic separation, adsorption, and membrane separation. Adsorption technology is gaining popularity in various industries for gas separation processes. This is primarily because the method offers better cost-effectiveness and reliability than traditional techniques. Adsorption separation demands less energy and has lower costs, making it an attractive option for industries operating under stringent environmental and quality regulations. As a result, adsorption technology has been widely implemented in various industrial applications[7].

The selection of an appropriate adsorbent is crucial for any adsorption separation process. The adsorbent chosen must possess suitable selectivity, capacity, service life, and ease of regeneration[8]. Among the different characteristics that an adsorbent can have, a beneficial one in the separation of carbon dioxide and methane is its non-adsorptive nature towards methane, indicating a greater preference for carbon dioxide over methane. This non-adsorptive quality towards methane and increased selectivity towards carbon dioxide will result in higher CO_2 adsorption, leading to improved methane recovery and purity[9]. An effective approach to achieving selectivity in the adsorbent is to adjust the diameter of the micropores, which enables carbon dioxide to enter while restricting methane diffusion. An effective example of such a kinetic adsorbent is carbon molecular sieve (CMS)[10]. Carbon molecular sieves are microporous materials belonging to the family of activated carbons. The production of CMS adsorbents involves limiting the pore mouth of carbon-based materials to a specific diameter, which serves as a barrier for the diffusion of molecules through the pores[11]. For the application of a CO_2/CH_4 separation, the adsorbent's pores can be modified so that carbon dioxide molecules (with a kinetic diameter of 3.2 Å) can easily penetrate their structure, but bigger methane molecules (with a kinetic diameter of 3.8 Å) are unable to diffuse through them[12]. This can be observed in Figure 2.1.

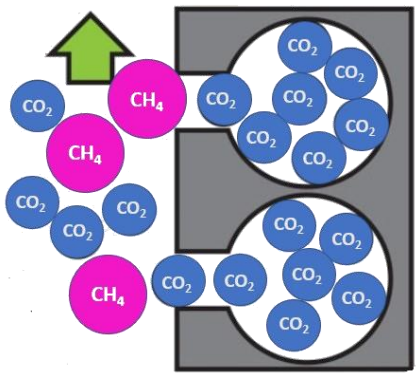

Figure 2.1 Illustration of sieving effect of carbon molecular sieves

Methane and carbon dioxide adsorption equilibrium and kinetics have been studied in various CMS samples, both commercial and laboratory-prepared in the literature [10,13–23]. The equilibrium selectivity towards carbon dioxide is not very good in most of these publications, but the limitations to methane diffusion are a significant reason for the high effective kinetic selectivity.

This study provides a thorough assessment of the adsorption separation of methane and carbon dioxide gases using a commercial carbon molecular sieve incorporating experimental and computational methods. The evaluation includes adsorption equilibrium measurements for pure methane and carbon dioxide gases at various temperatures and pressures, predicting binary isotherms based on pure component data using different mixture adsorption isotherm models, adsorbent characterization and simulating breakthrough curves that are validated with experimental data. The obtained gravimetric and breakthrough data are analyzed and the impact of temperature, pressure, and flow rate variations on the breakthrough curves are studied to identify optimal operating conditions for gas separation via adsorption.

2.2. MATERIALS AND METHODS

2.2.1. MATERIALS

Experiments were performed to measure the adsorption capacity for both pure carbon dioxide and methane gases, as well as their mixture, using gases of high purity (≥99%). High purity helium gas was used in the pressurization stage of the breakthrough experiments, as a carrier gas in the gas chromatograph and for buoyancy correction for the pure component adsorption isotherm experiments carried out in the gravimetric system. All gases were purchased from Messer Canada Inc. (Mississauga, Ontario, Canada). The proprietary sample of the carbon molecular sieve used in this research was provided by Xebec Adsorption Company (Blainville, Quebec, Canada). The sample, which is known as CMS(C), was in the form of cylindrical pellets and its properties are listed in Table 2.1.

Table 2.1 Physical properties of the CMS(C) adsorbent used in this study.

Pellet diameter (mm)	~1.7
Pellet length (mm)	2.1-4.2
Pellet porosity	32-35%
Pellet density (kg/m^3)	1025
Pellet packing density (kg/m^3)	704
BET surface area (m^2/g)	226
Average pore size (nm)	1.6

2.2.2. METHODS

2.2.2.1. Pure component adsorption isotherms

The micrograviметric analyzer from VTI Corp. (Hialeah, Florida, USA) was used to determine single gas methane and carbon dioxide adsorption isotherms with the CMS(C) adsorbent. Prior to the experiments, the sample was regenerated at 200°C for 12 hours under vacuum conditions of around 10^{-8} atm. The adsorbent were then subjected to sample gases at increasing pressures from 0 to 10 atm at various temperatures (10°C, 21°C, 40°C, 60°C). Equilibrium was achieved at each pressure step when the weight change was less than 0.015 wt% for 60 minutes, after which the equilibrium adsorption measurement was recorded. To correct for buoyancy, the sample was also exposed to helium gas at similar pressures and temperatures.

2.2.2.2. Binary gas mixture breakthrough measurements

Binary breakthrough adsorption experiments for a feed gas of 60% CH_4 and 40% CO_2 were conducted in a fixed-bed adsorption column packed with the CMS(C) (approximately 30 g). The fixed-bed column made out of stainless steel has a height of 12 cm and an inner diameter of 2.104 cm. It is equipped with porous plates positioned on both ends of the adsorption column. The experimental breakthrough set up was designed and constructed for a multicomponent gas system during this study. All necessary guidelines were considered for a more efficient experimental design. A schematic diagram of the breakthrough set-up is shown in Figure 2.2. The adsorbent under investigation is fully loaded into the adsorption column. MKS mass flow controllers (MFCs) (Kanata, Ontario, Canada), help in maintaining the desired feed flow rate and composition. The MKS mass flow meter (MFM) measures the flow exiting the adsorption column. A gas chromatograph (GC) GOW-MAC 580 (Bethlehem, Pennsylvania, USA) which is equipped with a thermal conductivity detector (TCD) and a HayeSep Q column is used to analyze the gas concentration leaving the adsorption column. BPR's (back pressure regulators) from Swagelok Central Ontario (Ottawa, Ontario, Canada) are used to control the pressure at the desired level. Different types of valves are used to direct the flow and introduce a step change in concentration at the column inlet. Pressure indicators (PI) are used to keep track of operating pressure and pressure drop across the adsorption column. Type K Thermocouples (TI) are located at inlet, outlet and along the adsorption column length in order to monitor the operating temperature and adsorbent temperature during the breakthrough runs. PIs and TIs were purchased from Omega Sensing Solutions ULC (St-

Eustache, Quebec, Canada). The set-up is also equipped with a needle valve for situations when precise control of gas flow is required.

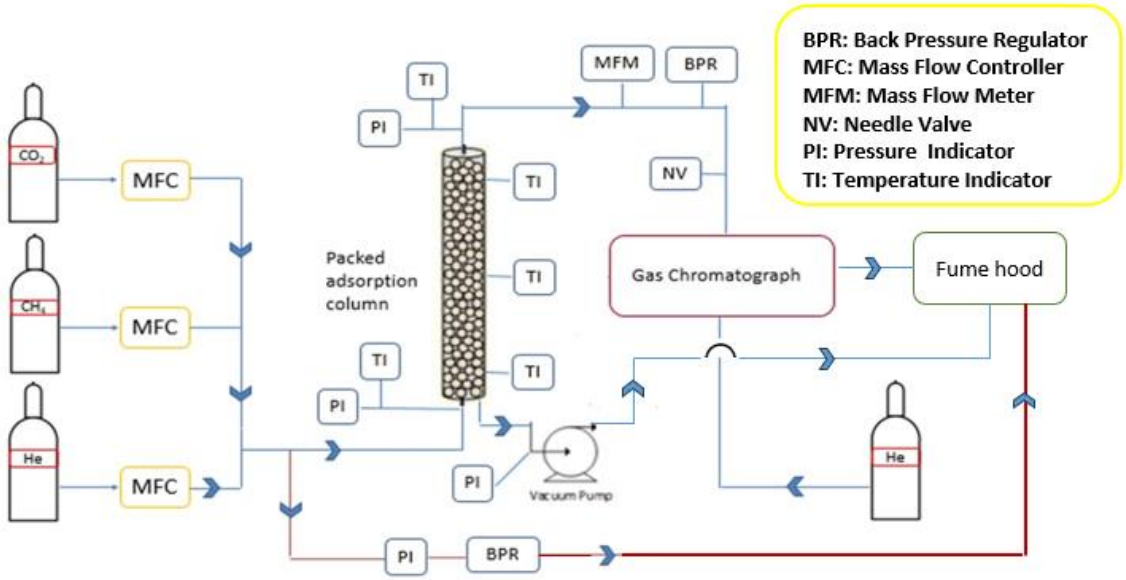

Figure 2.2 Schematic diagram of the breakthrough set-up that is used in this study.

The experimental protocol would begin with instrument calibration followed by dead volume measurement (explained in section 2.2.3.4) and column regeneration before beginning the breakthrough experiments. In this study, each gas was assigned to a mass flow controller calibrated at 25°C and 1 atm by CCR Process Products (Kanata, Ontario, Canada). The gas chromatograph, GOW-MAC 580, underwent calibration for each gas through a trial-and-error approach. The calibration involved adjusting parameters such as amperage, detector temperature, column temperature, injection temperature, and carrier gas (helium) flow rate to produce CO_2 and CH_4 peaks that closely matched the standard peak plots (voltage vs. time) provided by GOW-MAC Instrument Co. (Bethlehem, Pennsylvania, USA). For more effective regeneration, it is recommended that the adsorption column packed with the adsorbent to be slowly heated to the required regeneration temperature and alternately purged with an inert gas and with pulling vacuum. In this study, the regeneration process for the sample packed in the adsorption column was conducted using a ceramic tube furnace purchased from Heaters Controls and Sensors LTD (London, Ontario, Canada). The temperature of the sample was gradually increased at a rate of 8°C per minute. Once the sample reached a temperature of 200°C and stabilized, the regeneration process commenced and continued for 12 hours under vacuum conditions. The sample was weighed to obtain its mass before and after regeneration. Once the regeneration pre-treatment is done and the sample was cooled down, breakthrough

experiments are carried out by initializing (pressurizing) the column and the GC by flowing an inert gas (Helium). For this purpose, the back pressure regulator (BPR) is adjusted to the desired pressure. The initializing stage will continue until the GC baseline stabilizes. The next step is to set the MFCs to the desired flow rate and stabilize their flow without the flow going through the packed column and disturbing the already established baseline of the GC. For this purpose, the flow was stabilized in a separate line (indicated as the red line in Figure 2.2). Once the MFCs have stabilized, at time zero the feed gas is introduced to the column and data is recorded simultaneously via a desktop computer using LabView software. When the signal from the detector reaches a consistently steady value (peaks that appear identical), the bed temperature returns to the initial value (dependent on heat transfer from the sample within the column to the surrounding air, thermal conductivity of the sample etc.), the total outlet flow rate becomes equal to the inlet flow rate and the outlet gas concentration reaches the inlet gas concentration (dependent on mass transfer and diffusivity of the adsorbate etc.), marks the time the adsorbent in the bed is in complete equilibrium with the feed gas composition and the adsorption breakthrough experiment is complete. Note that these experiment completion indicators may not occur simultaneously. In this study, equilibrium was achieved when the flow rate reached its initial value, followed by the gas concentration and bed temperature returning to their initial inlet values. Regeneration is done once again to extract the captured gas and prepare the adsorbent for the next adsorption cycle.

2.2.3. THEORETICAL BACKGROUND

2.2.3.1. Pure component adsorption equilibrium models

To accurately model the experimental adsorption isotherms at different temperatures, it is necessary to have a precise description of the adsorption behavior. In this study, the equilibrium adsorption data was fitted to three isotherm models - Sips, Toth, and Langmuir - as presented in Equations 1 to 3. Sips and Toth isotherms provide greater flexibility than the Langmuir model, as they consider higher heterogeneity and non-uniformity in terms of adsorbent surfaces[24–26]

$$q = \frac{q_s (BP)^{1/n}}{1 + (BP)^{1/n}} \tag{1}$$

$$q = \frac{q_s (BP)}{(1 + (BP)^n)^{1/n}} \tag{2}$$

$$q = \frac{q_s(BP)}{1 + (BP)} \tag{3}$$

In this context, q_s refers to the maximum adsorption capacity, q is the adsorption capacity, P is the pressure, while B is the affinity constant of the Langmuir isotherm model. In the case of the Sips and Toth models, the n parameter is dimensionless and describes the limited availability of adsorption sites at higher surface concentrations.

Considering that adsorption is an exothermic process, it is essential to account for the influence of temperature on adsorption capacity, as the non-isothermal nature of adsorption processes may be affected by any changes in column temperature. Equations 4 to 6 represent the temperature-dependent (TD) Sips and Toth isotherm models, where the q_s, B, and n parameters are expressed as functions of temperature[27].

$$B = B_0 e^{\left(\frac{Q}{RT_0}\left(\frac{T_0}{T} - 1\right)\right)} \tag{4}$$

$$q_s = q_{s0} e^{\left(X\left(1 - \frac{T}{T_0}\right)\right)} \tag{5}$$

$$n = n_0 + a\left(1 - \frac{T}{T_0}\right) \tag{6}$$

In this context, B_0 represents the affinity constant for adsorption at the reference temperature T_0, while q_{s0} indicates the saturation adsorption capacity at the reference temperature T_0 and n_0 represents the n parameter at T_0. Meanwhile, X and α are constant parameters. By substituting Equations 4 to 6 into Equations 1 and 2, six parameter functions are obtained. These functions involve the parameters B_0, Q, q_{s0}, X, n_0, and α. These parameters are determined by performing regression analysis of the model to fit the experimental data obtained at various temperatures[27]

Similarly, the temperature dependent fitting parameters for the Langmuir model are described in Equations 7 and 8[28]

$$B = k_3 e^{\left(\frac{k_4}{T}\right)} \tag{7}$$

$$q_s = k_1 - k_2 T \tag{8}$$

The adsorption strength is influenced by the interactions between the adsorbate and adsorbent at different temperatures and can be measured using the isosteric heat of adsorption, at zero fractional loading. The Langmuir model assumes that ΔH is constant and independent of surface coverage, but in reality, it may vary due to local surface heterogeneity and additional molecular interactions at higher loadings. The Clausius-Clapeyron equation can be used to calculate ΔH directly from experimental isotherms at different temperatures, and this variation can be observed[29].

$$\left[\frac{\Delta H_{iso}}{R}\right] = \left[\frac{\partial lnP}{\partial\left(\frac{1}{T}\right)}\right]_q \tag{9}$$

This equation shows that the logarithmic change of pressure (P) with respect to the inverse of temperature (T) while keeping the adsorption capacity (q) constant is related to the heat of adsorption. The value of ΔH can be obtained from the slope of the plot of ln(P) against $1/T$ at constant q[29].

2.2.3.2. Theoretical models for prediction of multicomponent adsorption

Theoretical models can also be utilized to describe and predict gas mixture adsorption equilibria using pure component experimental data. In the literature, many of them have been carefully tested for accuracy with respect to experimental binary systems[30,31]. In this work, from pure component isotherms of CH_4 and CO_2, the adsorption equilibrium of the gas mixture was described by the Extended Sips model (equation 10)[32] and the Extended Langmuir model (equation 11)[31].

$$q_i = \frac{q_{si}(B_i P_i)^{1/n_i}}{1 + \sum_j^n \left(B_j P_j\right)^{1/n_j}} \tag{10}$$

$$q_i = \frac{q_{si}(B_i P_i)}{1 + \sum_j^n B_j P_j} \tag{11}$$

In this context, q_{si} refers to the maximum adsorption capacity for component i, q_i is the adsorption capacity for component i, $P_{i\ or\ j}$ is partial pressure for component i or j, and $B_{i\ or\ j}$ is the affinity constant of the Sips or the Langmuir isotherm model for component i or j.

2.2.3.3. Assessing gas adsorption separation potential

The selectivity or separation factor for adsorption equilibrium is a measure of the degree of separation between adsorbed and gas phases for the components present in a mixture. It is

calculated by taking the ratio of Langmuir isotherm parameters specified in Equation 3, which is derived from the Extended Langmuir model prediction for a gas mixture, as demonstrated in Equation 12[33].

$$\alpha_{A/B} = \frac{x_A y_B}{x_B y_A} = \frac{q_{sA} B_A}{q_{sB} B_b} \tag{12}$$

The component with stronger adsorption is denoted by the subscript A, while the one with weaker adsorption is labelled with the subscript B. In the case of a gas mixture, the mole fraction in the adsorbed phase is represented by x, while the mole fraction in the gaseous phase is represented by y[33].

Equation 13 is utilized to calculate the sorbent selection parameter, S. This value is obtained by comparing the working capacities of the two components A and B, represented as Δq_A and Δq_B, respectively, which are the differences between the adsorption capacities at the adsorption and desorption pressures[34]. The working capacity is defined as the difference between the amount adsorbed at adsorption (high) pressure and the amount adsorbed at desorption (low) pressure. To determine this parameter, relevant conditions to the separation process are considered In this study, binary adsorption equilibrium data obtained from the TD-Sips model were applied to determine the operational capacities at various total pressures (1, 5, 9 atm) and temperatures (294K, 313K, 333K) for a gas mixture comprising 40% CO2 and 60% CH4. The selection of a desorption pressure of 0.1 atm was made considering the pump's attainable vacuum level at all the adsorption pressures.

$$S = \alpha_{A/B} \frac{\Delta q_A}{\Delta q_B} \tag{13}$$

The small pore size of carbon molecular sieves with narrow channels creates an opportunity for a separation process driven by kinetics. The kinetic selectivity, $K_{A/B}$, is used to estimate the separation efficiency by considering the ratio of kinetic mass transfer coefficients and the ideal adsorption equilibrium separation factor for two different adsorbed components (Equation 14)[35].

$$K_{A/B} = \alpha_{A/B} \sqrt{\frac{k_{LDF,A}}{k_{LDF,B}}} \tag{14}$$

2.2.3.4. Binary gas mixture breakthrough measurements

The ability to evaluate the genuine performance of potential adsorbents for use in gas separations requires a thorough understanding of gas mixture adsorption properties. However,

multicomponent adsorption isotherm measurements are difficult due to the extra complexity of analysing the mixture composition in the adsorbed phase. Several reliable experimental multicomponent adsorption measurement approaches have been developed and are documented in the literature including dynamic systems such as: breakthrough measurements[36–38], differential column analysis[39], zero length column chromatography[40], chromatography[41–43], isotope exchange technique[44]; and static systems such as: gravimetric or volumetric methods[45,46].

As previously stated, the breakthrough approach can be used to measure equilibrium isotherms for binary and pure gases over a wide range of conditions. By integrating breakthrough curves measured in terms of concentration profiles at the exit of the column as a function of time, the molar amount of each compound retained in the bed can be determined. Figure 2.3[47] is a representation of binary breakthrough curves. The molar amount of the weaker component (in our case methane) retained in the bed can be calculated from the area A_1 minus the roll-up area A_2. For the stronger component (in our case carbon dioxide) the molar amount retained in the bed can be calculated from the area A_1+A_3 and is similar to a single component breakthrough. Equation 15 reflects the accumulation of a weaker component inside the column in breakthrough experiments, where $q_{0,B}$ is the amount adsorbed of the weaker component, m_A is the mass of the adsorbent in the column, $\dot{V}_{in}$ is the inlet total flow rate and $c_B and\ c_{0,B}$ are the gas phase concentration of the weaker component at the exit of the column and at the inlet of the column, respectively[47].

$$q_{0,B} m_A = c_{0,B} \times \dot{V}_{in} \times \int_{t=0}^{t_{(c_B=c_{0,B})}} \left(1 - \frac{c_B}{c_{0,B}}\right) dt - c_{0,B} \times \dot{V}_{in} \times \int_{t_{(c_B=c_{0,B})}}^{t_\infty} \left(\frac{c_B}{c_{0,B}} - 1\right) dt \quad (15)$$

Competitive adsorption leads to concentration overshoots for all components, except for the strongest adsorbable adsorbate. The first term on the right-hand side of Equation 15 represents the mass initially adsorbed without influence of competition, whereas the second term represents the mass desorbed due to the subsequent displacement by component 2[47].The material balance equation for the strongly adsorbed component 2, which is not susceptible to a displacement process, is as follows[47]:

$$q_{0,A} m_A = c_{0,A} \times \dot{V}_{in} \times \int_{t=0}^{t_\infty} \left(1 - \frac{c_A}{c_{0,A}}\right) dt \quad (16)$$

where $q_{0,A}$ is the amount adsorbed of the strongly adsorbed component, m_A is the mass of the adsorbent in the column, $\dot{V}_{in}$ is the inlet total flow rate and $c_A \, and \, c_{0,A}$ are the gas phase concentration of the strongly adsorbed component at the exit of the column and at the inlet of the column, respectively[47]. The $\left(\frac{c_i}{c_{0,i}}\right)$ in the integral term in Equations 15, 16 can also be presented in terms of $\frac{y_i(t)\dot{V}(t)}{y_{i,in}\dot{V}_{in}}$ versus time[38,48].

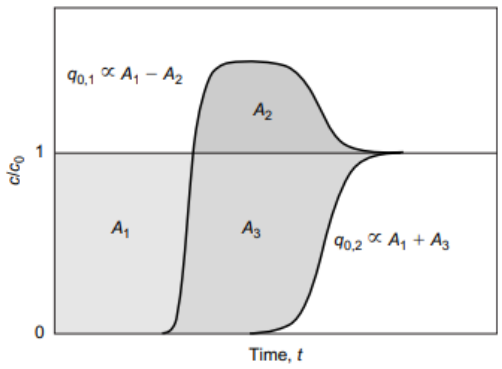

Figure 2.3 Binary breakthrough response for a fixed bed adsorption column[47]

The total dead volume of the system, which includes the adsorption column void volume and the dead volume associated with the tubing, fittings upstream and downstream of the adsorption column, prolongs the time for a breakthrough response, causing an overestimation of the equilibrium capacity computed from the unadjusted column breakthrough response. Additionally, the dead volume impacts the shape and spread of the breakthrough curve, affecting the accuracy of the obtained adsorption kinetics information. Therefore, it is essential to correct the measured breakthrough responses using the blank response to obtain the actual response of the adsorption column. This correction will help to extract reliable equilibrium and kinetic data[38]. Dead volume measurement can be done by conducting breakthrough experiments with a column packed with glass beads the same size of the actual adsorbent (CMS(C)) at the same operational conditions (flow rate, temperature, feed composition, pressure) of the actual experiment, generating a blank response. This blank response (adsorption column packed with glass beads + total dead volume) may be subtracted from the composite response (adsorption column packed with adsorbent + total dead volume), point by point, on a plot of $\frac{C_{(t)}}{C_{in}}$ versus time. Another approach for dead volume correction, which was used in this study, involves a modified version of Equations 15 and 16, by subtracting the terms, $C_{0,i}(\varepsilon_b V_b)$ and $C_{0,i}V_{dead}$ that account for number of moles of component

i in the column void volume and number of moles of component i in the dead volume, respectively. An example of the modified equation for the more strongly adsorbed component (in our case CO_2) is shown as Equation 17[48,49].

$$q = \frac{\left(\dot{V} \times C_0 \times \int_0^{t_{sat}} \left(1 - \frac{C}{C_0}\right) dt\right) - [C_0(\varepsilon_b V_b + V_{dead})]}{m_{adsorbent}} \quad (17)$$

Moles of CO_2 in the column void volume

Moles of CO_2 in dead volume

2.2.3.5. Adsorption breakthrough modeling

Adsorption modeling of packed beds has become very important in the development and design of gas adsorption separation processes. The development of a mathematical model to represent the adsorption kinetics and dynamic behavior and consider all transport phenomena of a packed bed adsorption column with the specified adsorbent is required for the design of an effective adsorption separation process. These mathematical models are required to estimate and predict the adsorption separation process for optimizing design and operational conditions. The lack of an efficient and precise adsorption cycle simulator necessitates the utilisation of data from experimental units to design new processes. This method of designing an adsorption column through extensive experimentation on process development units is both costly and time consuming. In principle, a predictive model based on independently determined equilibrium and kinetic parameters may give a way of predicting column dynamic capacity without extensive experimentation[50].

In general, to predict column dynamic behaviour, a set of coupled partial differential equations (PDEs) describing material and energy balances over a packed bed with the proper initial and boundary conditions must be solved simultaneously. The mechanism by which mass transfer from the fluid to the solid phase occurs has a significant impact on the modelling of transport equations in a packed column. In fact, equilibrium theory is only applicable to systems where the adsorptive selectivity is determined by a difference in equilibrium, and it is not applicable to systems where separation is determined by kinetic selectivity[51]. The separation of a CO_2/CH_4 mixture using a carbon molecular sieve is an example of kinetic

adsorptive separation, in which the separation is achieved by a substantial difference in diffusion rates between the two components[52]. As a result, while modelling a real non-equilibrium packed column, the effects of mass transfer resistance between the fluid and the particle, as well as within the particle, must be taken into account[53]. The mass transfer of adsorbate from gas phase into the solid phase is driven by equilibrium isotherms, whereas the mass balance equation inside the adsorbent particle is dependent on the adsorbent structure. Different mass transfer mechanisms are involved in the diffusion of the adsorbate into the adsorbent particles before adsorption onto the adsorbent surface, at the macroscopic or microscopic level occurs.

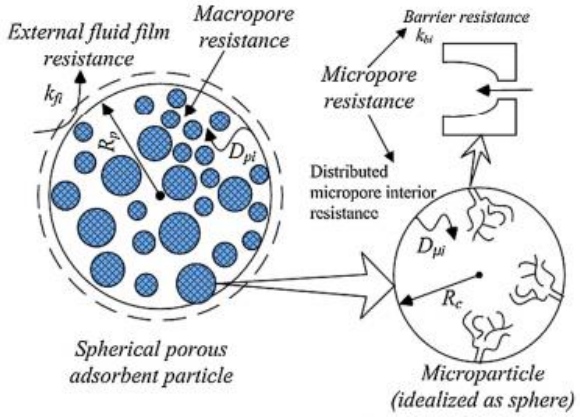

Figure 2.4 Schematic diagram showing different resistances to the transport of adsorbate[50]

As seen in Figure 2.4[50], the adsorbate molecules must first pass the external fluid film encircling each adsorbent particle before diffusing into an adsorbent's porous structure. Depending on the specific system and conditions, any one of the three types of potential mass transfer resistance may be dominant, and more than one resistance may be considerable. External fluid film resistance, macropore diffusional resistance, and micropore diffusional resistance are the three possible resistances. The film transfer and macropore and micropore diffusion can be viewed as sequential steps, and mass conservation assumption can be used[50].

One of the main objectives of the present work is to measure the dynamic adsorption of CO_2/CH_4 gas mixture by the adsorbent and compare and validate predicted breakthrough curves by simulations results with the experimental breakthrough curves. To formulate breakthrough curves for our system, the mathematical model was developed based on the following assumptions: 1) the system runs under non-isothermal conditions; 2) the adsorption equilibrium isotherm is described by the multicomponent Sips temperature dependent

isotherm; 3) the flow pattern is described by the axially dispersed plug flow model; 4) concentration and temperature gradients both exist in the axial direction in the column and the radial direction in the pellet; 5) The gas phase behaves as an ideal gas mixture; 6) both external and internal diffusional resistances to mass and heat transfer are included; 7) the mass transfer rate is represented by a linear driving force (LDF) model.

Under the aforementioned assumptions and considering the majority of particle shapes can be adequately approximated as equivalent spheres, allowing the description of their transport through a diffusion equation formulated in spherical coordinates.[54], the following set of equations and corresponding initial and boundary conditions can be established:

Equation 18[54,55] can be used to represent the gas phase mass balance, which contains the axial dispersion term, convection term, accumulation in the fluid phase, and adsorption term, from left to right, respectively:

$$-D_z\left(\frac{\partial^2 C_g}{\partial z^2}\right)+\frac{\partial\left(vC_g\right)}{\partial z}+\frac{\partial C_g}{\partial t}+\left(\frac{1-\varepsilon_b}{\varepsilon_b}\right)\rho_p\frac{\partial\bar{\bar{q}}}{\partial t}=0 \tag{18}$$

where C_g represents the adsorbate concentration in the gas phase; z is the axial position in the column; ε_b is the bed void fraction; v is the interstitial fluid velocity; t denotes time; ρ_p is pellet density including its voids; $\bar{\bar{q}}$ is the average concentration in the adsorbent particle, which establishes a connection between the fluid and solid-phase mass balance equations; and D_z is the axial dispersion coefficient.

The mass transfer rate over the external film is meant to be equal to the diffusive flux at the particle surface and can be expressed as Equation 19:[16,56–58]

$$\frac{\partial\bar{\bar{q}}}{\partial t}=\frac{3}{R_p}k_f\left(C_g-C_{gp|R=R_p}\right)=\frac{3}{R_p}\varepsilon_p D_{pore}\left(\frac{\partial C_{gp}}{\partial R}\right)_{|R=R_p} \tag{19}$$

where k_f is the external film mass transfer coefficient, R_p is the radius of the pellet, C_{gp} is the adsorbate concentration in the macropore, ε_p is the adsorbent pellet void fraction, D_{pore} is the macropore diffusivity, and R is the radial position in the pellet.

The average concentration in the adsorbent particle can be calculated by integration of the concentration profiles in the macropores and micropores as shown in Equation 20[50,59,60]:

$$\bar{\bar{q}}=\varepsilon_p\frac{3}{{R_p}^3}\int_0^{R_p}C_{gp}R^2dR+(1-\varepsilon_p)\frac{3}{{R_p}^3}\int_0^{R_p}\bar{q}\,R^2dR \tag{20}$$

where:

$$\bar{q} = \frac{3}{{r_c}^3}\int_0^{r_c} q\, r^2 dr \tag{21}$$

$\bar{q}$ is the average adsorbed phase concentration of the adsorbate in the crystals, r_c is the radius of the crystals, r is the radial distance inside the crystals and q is the absolute concentration of the adsorbate in the adsorbed phase.

The mass balance in the pellet can be described by[10,13,16,57]:

$$\frac{\partial C_{gp}}{\partial t} + \frac{\rho_p}{\varepsilon_p}\left(\frac{\partial \bar{q}}{\partial t}\right) = D_{pore}\left[\frac{\partial^2 C_{gp}}{\partial R^2} + \frac{2}{R}\left(\frac{\partial C_{gp}}{\partial R}\right)\right] \tag{22}$$

The mass transfer rate across the micropore mouth can be expressed by the following equation[16,57,58]:

$$\frac{\partial \bar{q}}{\partial t} = k_b\left(q_e - q_{|r=r_c}\right) = \frac{3}{r_c} D_c \left(\frac{\partial q}{\partial r}\right)_{|r=r_c} \tag{23}$$

Where q_e is the adsorbed-phase concentration in equilibrium with the macropore fluid phase concentration (C_{gp}), k_b is the barrier coefficient and D_c is the micropore diffusivity.

The mass balance inside the micropores can be expressed as follows[16,57,59]:

$$\frac{\partial q}{\partial t} = \frac{1}{r^2} D_c \frac{\partial}{\partial r}\left(r^2 \frac{\partial q}{\partial r}\right) \tag{24}$$

Adsorption is an exothermic process, and variations in temperature can modify the adsorption equilibrium relation and adsorption rates. As a result, in order to effectively predict packed column dynamics, the impacts of heat generation and heat transfer in the adsorbent bed must be considered[50]. The heat generated is transmitted to the surface of the particles and then to the gas phase via a convection mechanism. Three distinct control volumes can be considered to account for energy transfer: solid, gas, and column wall[50].

The change of gas temperature with respect to time is caused from the transfer of energy due to the axial conductive solid phase heat flux to the gas phase as well as the energy transfer through convection inside the bed due to the bulk movement of the gas. Hence, the energy balance for the gas phase, including the heat transfer between the flowing fluid and the surface

of the solid adsorbent through the external film, as well as the energy transferred to the wall of the column, can be expressed as in Equation 25: [54,61,62]:

$$\rho_g C_{pg} \frac{\partial T_g}{\partial t} = \boldsymbol{\lambda} \frac{\partial^2 T_g}{\partial z^2} - \rho_g C_{pg} \frac{\partial (v T_g)}{\partial z} - \frac{(1-\varepsilon_b)}{\varepsilon_b} \frac{3}{R_p} h_f \left(T_g - T_{s|R=R_p}\right) - \frac{4 h_w}{\varepsilon_b d_i} \left(T_g - T_w\right) \quad (25)$$

where ρ_g is the gas density, C_{pg} is the gas heat capacity at constant pressure, T_g represents the bulk gas temperature, $\boldsymbol{\lambda}$ is the axial heat dispersion coefficient, $h_f$is the film heat transfer coefficient, T_s is the solid temperature, h_w is the heat transfer coefficient between the gas phase and the column wall, d_i is the inner diameter of the column, T_w denotes the column wall temperature.

The solid phase energy balance can be written as shown in Equation 26[61,63]:

$$\rho_s C_s \frac{\partial T_s}{\partial t} + (H) \frac{\partial \bar{q}}{\partial t} = k_s \left[\frac{\partial^2 T_s}{\partial R^2} + \frac{2}{R} \left(\frac{\partial T_s}{\partial R} \right) \right] \quad (26)$$

where ρ_s is the adsorbent solid density, C_s is the adsorbent heat capacity, H expresses the heat of adsorption and k_s represents the thermal conductivity of the adsorbent.

The column wall energy balance can be expressed as follows:[64]

$$\rho_w C_{pw} \frac{\partial T_w}{\partial t} = k_w \frac{\partial^2 T_w}{\partial z^2} + h_w \frac{2 r_i}{({r_o}^2 - {r_i}^2)} \left(T_g - T_w\right) - h_o \frac{2 r_i}{({r_o}^2 - {r_i}^2)} \left(T_w - T_{amb}\right) \quad (27)$$

where ρ_w is the column wall density, C_{pw} is the column wall heat capacity, k_w expresses the thermal conductivity of the column wall, h_o is the heat transfer coefficient between the column wall and the surrounding fluid, T_{amb} is the ambient temperature and, r_i and r_o represent inner and outer radius of the column, respectively. The corresponding initial and boundary conditions for the mass and energy balances are listed in Table 2.2.

Table 2.2 Corresponding initial and boundary conditions of the mathematical model describing dynamic column breakthroughs.

Mass balance/Energy Balance/Equation No.	**Boundary conditions**	**Initial conditions**
Gas phase mass balance /(18)	$(\frac{\partial C_g}{\partial z})_{z=L} = 0$ $D_{z\|z=0}(\frac{\partial C_g}{\partial z})_{z=0} = \frac{v_s}{\varepsilon_b}(C_{g\|z=0} - C_{gin})$	$C_g = 0\,,\ t = 0$
Mass balance in the pellet /(22)	$(\frac{\partial C_{gp}}{\partial R})_{R=0} = 0$ $\frac{3}{R_p} k_f \left(C_g - C_{gp\|R=R_p}\right) = \frac{3}{R_p} \varepsilon_p D_{pore} (\frac{\partial C_{gp}}{\partial R})_{\|R=R_p}$	$C_{gp} = 0\,,\ t = 0$
Mass balance inside the micropores /(24)	$(\frac{\partial q}{\partial r})_{\|r=0} = 0$ $k_b(q_e - q_{\|r=r_c}) = \frac{3}{r_c} D_c (\frac{\partial q}{\partial r})_{\|r=r_c}$	$q = 0\,,\ t = 0$
Gas phase energy balance /(25)	$\frac{\boldsymbol{\lambda}}{\varepsilon_b}\left(\frac{\partial T_g}{\partial z}\right)_{\|z=0} = \rho_g C_{pg} \upsilon \left(T_{g_{\|z=0}} - T_{gin}\right)$ $\left(\frac{\partial T_g}{\partial z}\right)_{\|z=L} = 0$	$T_g = T_{gin}\,,\ t = 0$
Solid phase energy balance /(26)	$\left(\frac{\partial T_s}{\partial R}\right)_{\|R=0} = 0$ $k_s \left(\frac{\partial T_s}{\partial R}\right)_{\|R=R_p} = h_f \left(T_g - T_{s\|R=R_p}\right)$	$T_s = T_{gin}\,,\ t = 0$
Column wall energy balance /(27)	$T_{w\|z=0} = \frac{T_{gin} + T_{amb}}{2}$ $\left(\frac{\partial T_w}{\partial z}\right)_{\|z=L} = 0$	$T_w = \frac{T_{gin} + T_{amb}}{2}\,,\ t = 0$

2.2.3.6. gPROMS Implementation

The complete adsorption gas separation breakthrough process model includes mass and energy balances with variables that display temporal and spatial distributions. As a result, the comprehensive process model is a combination of partial differential equations, and algebraic equations (PDAEs)[65].

In this study, the mechanistic model is solved by using gPROMS simulation software produced by Process System Enterprise Limited (London, United Kingdom). This is an equation-based software tool capable of solving complex partial differential equations under dynamic conditions for high fidelity predictive modelling. In gPROMS, the adsorption system of PDAEs is solved numerically using the method of lines (MOL). This entails discretizing the distributed equations in the spatial domain, resulting in a mixture of time-dependent differential algebraic equations (DAEs). Using a differential algebraic equation solver (DASOLV) integration code, the DAE system is integrated over time[65].

In this study, a first-order backward finite difference method (BFDM) with 50 number of discretization intervals was used to discretize the spatial domain of the packed column, second- order centered finite difference method (CFDM) with 10 discretization points was used to discretize the spatial domain of the adsorbent pellet and third-order orthogonal collocation finite element method (OCFEM) with 10 number of discretization intervals was used to discretize the spatial domain of micropores inside the adsorbent pellet.

The mathematical model developed and simulated in gPROMS is made up of a number of different entities such as PARAMETERS, VARIABLES, MODELS, PROCESSES, PERFORMED EXPERIMENTS and PARAMETER ESTIMATION. The mathematical equations describing the adsorption system are specified in the MODELS entity which contains parameters, variables and boundary conditions that characterize the system. The input specifics for the simulation are provided in the PROCESS entity. The parameter values, assigned variables, discretization methods, initial conditions for differential variables, operating procedure and solver settings are specified in this entity. The PERFORMED EXPERIMENTS entity is used to specify the full details of a conducted breakthrough experiment. Model validation is done through the PARAMETER ESTIMATION entity where unknown parameters such as diffusion time constant, $\frac{D_c}{r_c^2}$, and mass transfer coefficient at micropore mouth, k_b , are set to be estimated and fitted to experimental data.

2.2.3.6. Parametric studies for process optimization and design

Sensitivity analysis is a study that examines the effects of changes in the parameters of a mathematical model or system on the system's outputs or performance. Sensitivity analysis can be used to observe changes in a system's outputs to distinct sources of uncertainty in its inputs. To do this, one of the system parameters is modified by a particular percentage while all other parameters remain fixed, the model is run, and the percentage change of the predetermined performance indicator is monitored[66].

In an adsorption breakthrough system, a parameter sensitivity analysis is presented in order to identify which parameters have the most impact on the adsorption process and therefore, should be the focus of adsorption breakthrough system optimization and design. In other words, the purpose of this analysis is investigating which properties of the adsorbent material, bed characteristics and physical and transport properties of the gases have the most impact on breakthrough curves, both in terms of breakthrough time and curve shape. It is obvious that a long breakthrough time (in the context of CO_2) and a steep breakthrough curve (both CO_2 and CH_4) are desirable for a particular system, as this maximizes the usage of the bed. Based on sensitivity analysis results, dynamic optimization can be carried out for adsorption breakthrough process under consideration.

This study examined the sensitivity of the separation system for the physical and transport characteristics of the feed gas (such as pressure, temperature, and flow rate. The aim was to understand how changes in these factors influence breakthrough curves. Through this analysis, the optimal operational conditions (pressure, temperature, and flow rate) for achieving the highest performance of CO_2 adsorption separation from CH_4 using CMS(C) were determined.

2.3. RESULTS AND DISCUSSION

2.3.1. Pure component and binary adsorption isotherms

The adsorption isotherms of pure carbon dioxide and methane at different temperatures (283, 294, 313 and 333 K: for CO_2 and 283, 294 and 308 K: for CH_4) were obtained experimentally for the CMS(C) adsorbent for pressures up to 10 atm. These isotherms together with the representation of the data with the temperature dependent Sips (TD-Sips) and temperature dependent Langmuir (TD-Langmuir) models are shown in Figures 2.5 and 2.6 respectively. Both models represent the isothermal experimental data very well.

As the pressure in the system increases, the equilibrium adsorbed amounts for both CO_2 and CH_4 increase, as expected. However, at higher pressures, the slope of the isotherm

decreases as the adsorption sites approach saturation. The adsorption isotherms also indicate that, under similar operating conditions of pressure and temperature, CO_2 is significantly more adsorbed compared to CH_4. This difference can be attributed to the large quadrupole moment of CO_2 in comparison to CH_4, as CH_4 does not possess a quadrupole moment. This property results in a stronger electrostatic interaction between CO_2 and the adsorbent, leading to an enhanced uptake of CO_2.

The influence of temperature on the equilibrium adsorption capacity at a given pressure is clearly observed in Figures 2.5 and 2.6. In an adsorptive separation process, the temperature increases during the adsorption step due to the exothermic nature of adsorption, while it decreases during desorption, which is an endothermic process. The figures 3.5 and 3.6 represent the breakthrough capacities (BC) marked by symbols. These capacities are plotted at their corresponding partial pressures, which are P_{CO2}=0.4 atm and P_{CH4}=0.6 atm when P_{total}=1 atm, P_{CO2}=2 atm and P_{CH4}=3 atm when P_{total}=5 atm, and P_{CO2}=3.6 atm and P_{CH4}=5.4 atm when P_{total}=9 atm. On the other hand, pure adsorption isotherms are plotted as a function of the total pressure.

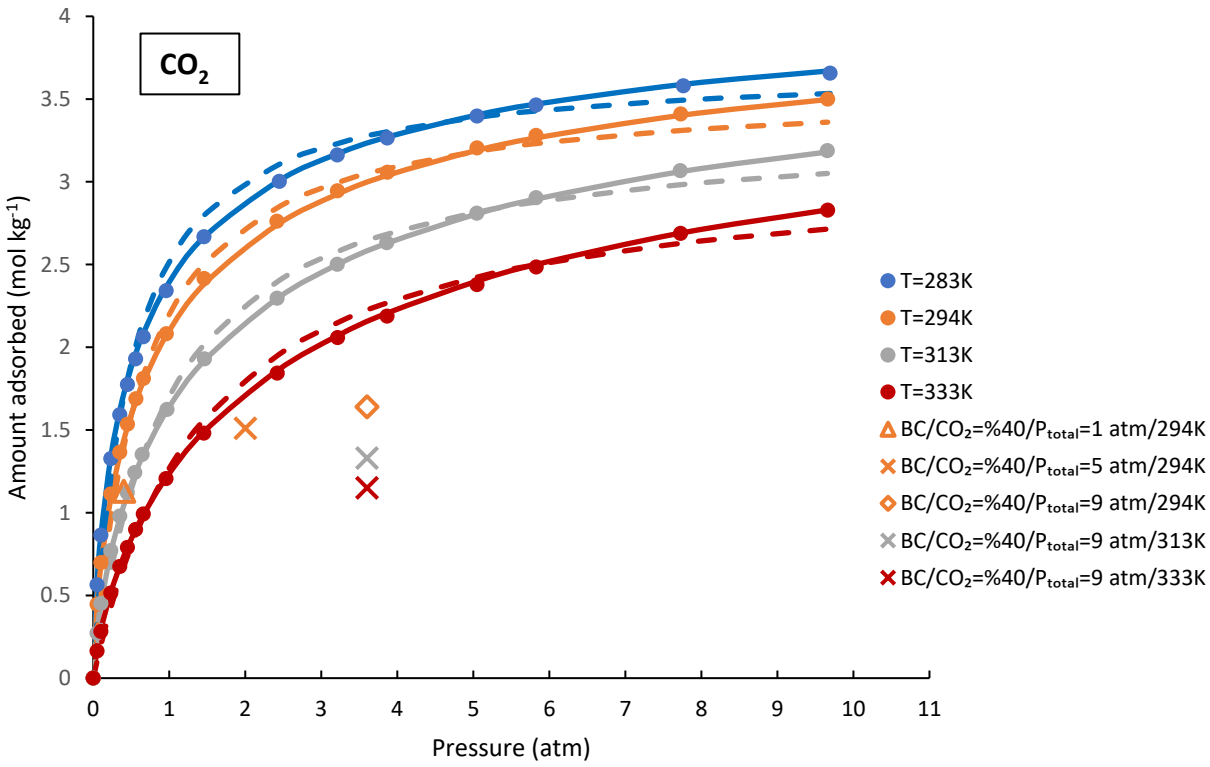

Figure 2.5 Adsorption isotherms of carbon dioxide at 283, 294, 313 K on CMS(C). Solid lines represent the TD-Sips model and dashed line represent the TD-Langmuir. BC= Breakthrough Capacity. The symbols representing the breakthrough capacities (BC) are graphed at their respective partial pressures: P_{CO2}=0.4 atm when P_{total}=1 atm, P_{CO2}=2 atm when P_{total}=5 atm, and P_{CO2}=3.6 atm when P_{total}=9 atm.

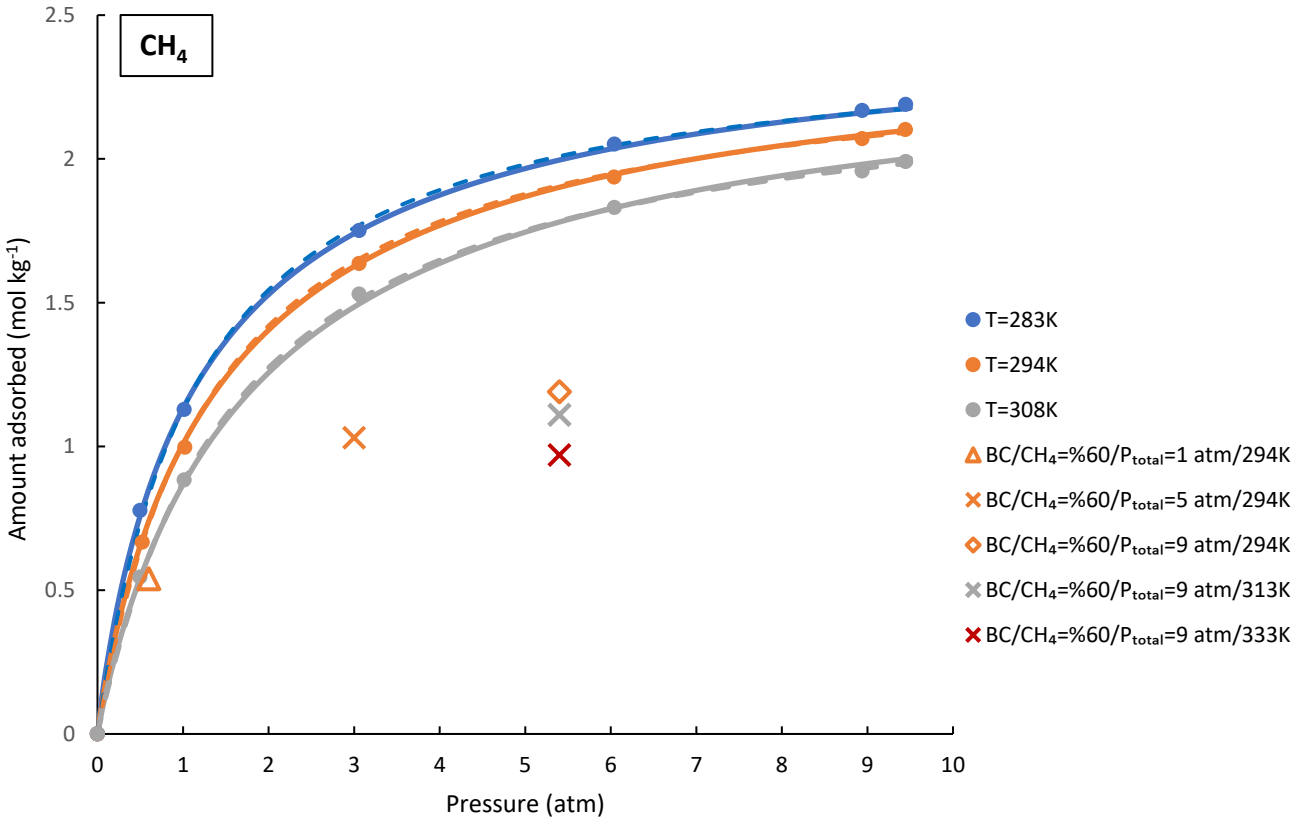

Figure 2.6 Adsorption isotherms of methane at 283, 294 and 308 K on CMS (C). Solid lines represent the TD-Sips model and dashed line represent the TD-Langmuir. BC= Breakthrough Capacity. The symbols representing the breakthrough capacities (BC) are graphed at their respective partial pressures: P_{CH4}=0.6 atm when P_{total}=1 atm, P_{CH4}=3 atm when P_{total}=5 atm, and P_{CH4}=5.4 atm when P_{total}=9 atm.

Table 2.3 and Table 2.4 display the regression parameters for the TD-Sips and TD-Langmuir isotherm models.

Table 2.3 Regression parameters of the temperature dependent TD-Sips isotherm model for CO_2 and CH_4 with CMS(C)

Component	q_{s0}	X	n_0	α	B_0	$\frac{Q}{RT_0}$
CO_2	4.23	0.39	1.41	0.31	1.44	9.41
CH_4	2.50	0.36	1.08	0.32	0.80	5.03

Table 2.4 Regression parameters of the temperature dependent TD-Langmuir isotherm model for CO_2 and CH_4 with CMS(C)

Component	k_1	k_2	k_3	k_4
CO_2	7.0008	0.0117	0.00116	2125.59
CH_4	3.6618	0.0043	0.01008	1259.22

The analysis of the isosteric heat of adsorption was conducted using the Clausius-Clapeyron equation and is depicted in Figure 2.7. Isosteric heats of adsorption for both gases show a slight decrease as the component loading increases. The average heat of adsorption value for CO_2 and CH_4 on the CMS(C) adsorbent were determined to be approximately 27.5 kJ/mol and 14.4 kJ/mol, respectively, within the experimental conditions considered.

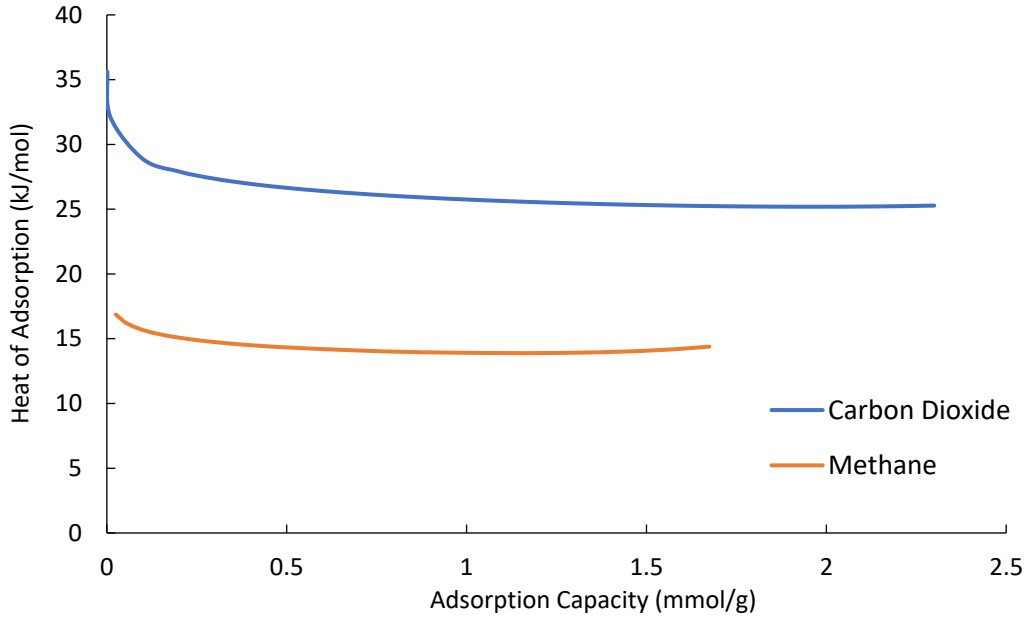

Figure 2.7 Isosteric heat of adsorption values of methane and carbon dioxide for CMS (C).

Predicted adsorption data of CO_2-CH_4 mixtures at total pressures of 1 and 9 atm for different molar compositions at 294 K and at temperatures of 313 and 333 K for different molar compositions at 9 atm are shown in Figure 2.8.

The binary adsorption isotherms were estimated using the multicomponent temperature dependent Langmuir and Sips equations. Across all the pressures and temperatures investigated in this study, the total amount of adsorption and the amount of carbon dioxide increased as the CO_2 composition in the gas phase increased, while the amount of methane adsorbed decreased. This suggests competition for adsorption sites and further confirms the preferential adsorption of carbon dioxide over methane. The primary reason for this trend is the considerably higher critical temperature of CO_2 relative to CH_4[67]. CO_2 exhibits behavior closer to that of a condensable vapor than a supercritical gas, resulting in reduced volatility and increased adsorption.

Additionally, CO_2 possesses higher polarizability and a quadrupole moment, facilitating stronger interactions with the solid surface and enhanced attractive forces[67]. In

Section 2.3.2.4, we explore the difference between the predicted adsorption capacities and the breakthrough capacities, along with the pure component adsorption capacities.

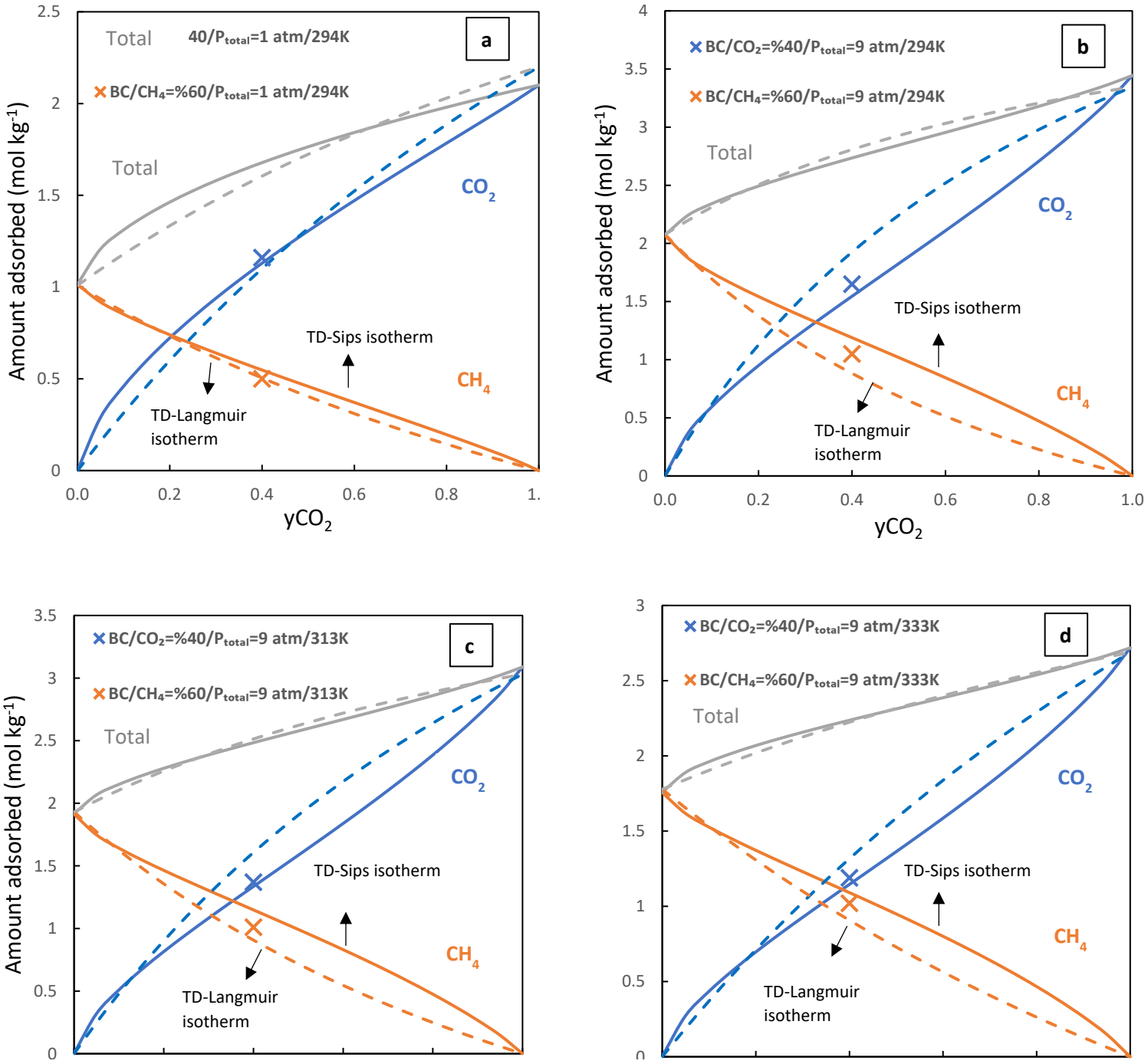

Figure 2.8 Predicted binary isotherms of CO_2/CH_4 gas mixture at 294K and 1 atm (a), 294K and 9 atm (b), 313K and 9 atm (c), 333K and 9 atm (d) with CMS(C). Solid lines represent the TD-Sips model and dashed lines represent the TD-Langmuir model. BC= Breakthrough Capacity.

Figure 2.9 depicts the binary CO_2-CH_4 adsorption phase diagrams for the examined adsorbent at 294K and 9 atm, 294 K and 1 atm, 313K and 9 atm, 333K and 9 atm. These diagrams were derived from the predicted binary adsorption isotherms. It was observed that lower pressure and lower temperature data yielded superior separation due to the phase diagram curves being farther away from the 45° line at the lower pressure. This outcome aligns with the shapes of the CO_2 and CH_4 isotherms. Furthermore, Figure 2.9 demonstrates a good alignment between the breakthrough data and the phase diagrams predicted by the temperature-dependent Sips model.

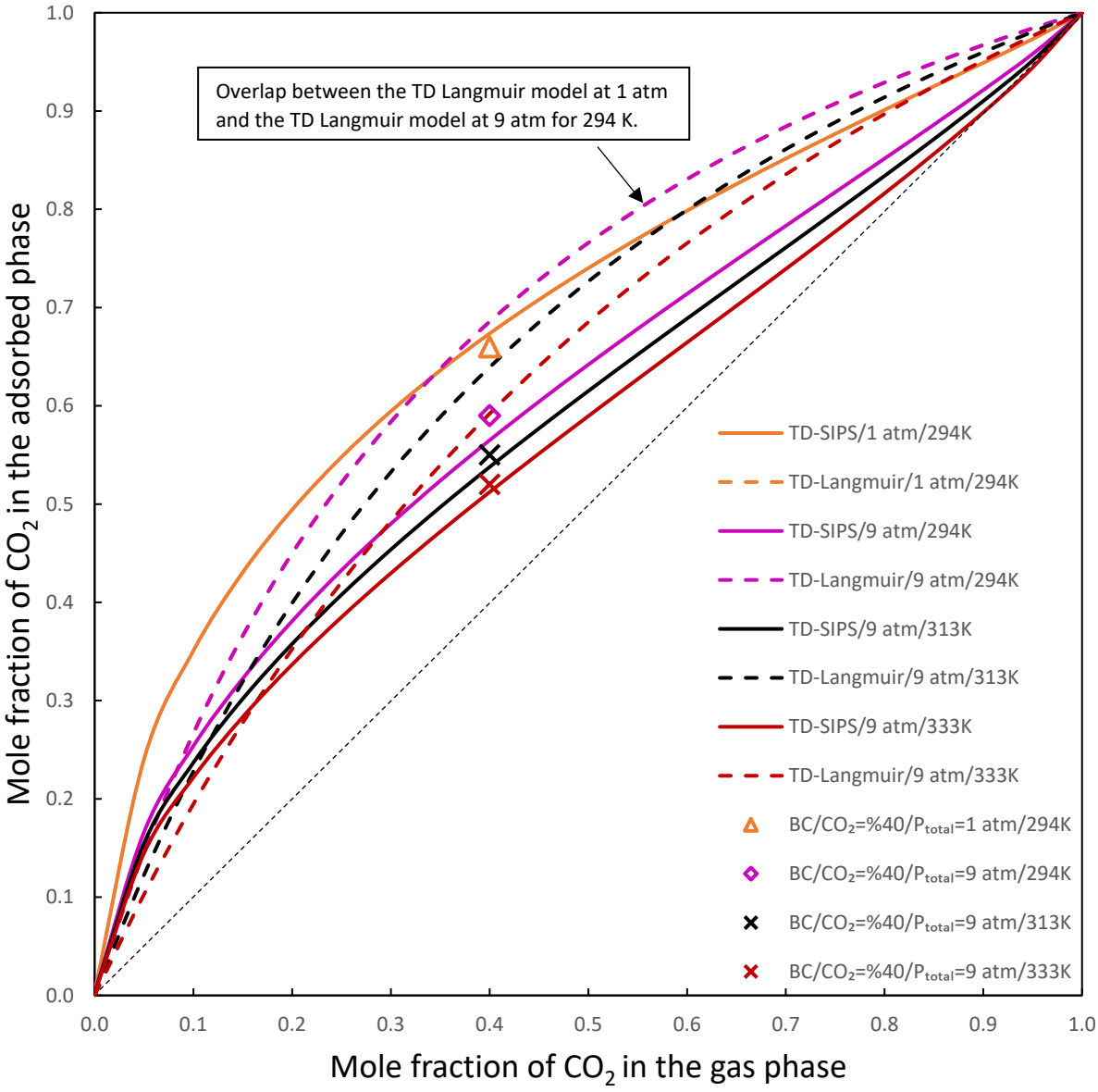

Figure 2.9 *x-y* phase diagrams for CO_2/CH_4 binary adsorption system at 294K and 1 atm, 294 K and 9 atm, 313K and 9 atm, 333K and 9 atm with CMS(C). Solid lines represent the TD-Sips model and dashed lines represent the TD-Langmuir model. BC= Breakthrough Curve. Note: in the figure, there is an overlap between the TD Langmuir model at 1 atm and the TD Langmuir model at 9 atm for 294 K.

2.3.2. Adsorption binary breakthrough experiments and simulations

A set of breakthrough experiments representing the dynamic behavior of an inlet mixture containing 40% CO_2 and 60% CH_4 in a fixed bed packed with CMS(C) adsorbent was conducted to examine the influences of different operating conditions on adsorption selectivity. The experiments were carried out at various total pressures, temperatures, and feed flow rates. Table 2.5 provides the details of the experimental conditions of the breakthrough experiments. The selection of operating conditions for conducting breakthrough experiments was determined by the maximum operational limitations of the devices used within the experimental breakthrough setup. Additionally, the decision to conduct breakthrough experiments specifically at high pressures is driven by the expectation that the adsorption performance of carbon materials at an industrial scale will be enhanced under such conditions, resulting in improved bulk separation and removal of CO_2 from CH_4.

Table 2.5 Breakthrough experiments' operating conditions.

Operating conditions	
Feed gas composition	40% CO_2 and 60% CH_4
Adsorption pressure (atm)	1, 5, 9
Feed temperature (K)	294, 313, 333
Feed flow rate (at 1 atm, 294 K) (ml min^{-1})	400, 600, 1000

2.3.2.1 Effect of pressure

The effect of pressure on the breakthrough curves at a constant temperature (294 K) and feed flow rate (400 ml min^{-1}) are illustrated in Figure 2.10. As shown in the figure, both of the breakthrough times for CO_2 and CH_4 increase as pressure increases, as expected, since the adsorption capacity increases as pressure increases. The equilibrium dynamic capacity is obtained from the breakthrough curve. Adsorption breakthrough capacity increases with pressure and the highest values for both gases are obtained at 9 atm. Comparison of these mixture adsorption capacities are compared to the predicted ones, as well as the pure component ones and discussed in Section 2.3.2.4.

The amounts adsorbed for CO_2 and CH_4, selectivity and the sorbent selection parameter are shown in Table 2.6. As the pressure increases, a slightly more co-adsorption of CH_4 with CO_2 on the CMS(C) adsorbent is observed. This co-adsorption phenomenon restricts the separation efficiency of CO_2/CH_4 as shown in table with reduced values of selectivity because of increase in pressure. The time difference between the CH_4 and CO_2 breakthrough curves

could act as an indicator of the fixed bed's separation performance. A larger disparity in breakthrough times between the two adsorbates can imply a greater effectiveness of the separation process.

Figure 2.10 also indicates as the pressure increases, the length of the mass-transfer zone, proportional to the difference between breakthrough and saturation times, becomes slightly wider, which indicates longer mass transfer zone. In the adsorption column, the distance across which concentration variations occur is referred to as the mass transfer zone. Higher axial dispersion and other higher mass transfer resistances during the adsorption lead to slower mass transfer. A narrow mass-transfer zone is preferred to optimize the utilization of the adsorbent. When the mass-transfer zone is narrow compared to the bed length, the breakthrough curve becomes steeper, and a larger portion of the solid capacity is utilized at the breakthrough point. This can be observed in figure 2.10 as the pressure decreases from 9 to 1 atm.

A strong agreement between the experimental data and simulation results for breakthrough curves is observed in Figure 2.10. This observation confirms the accuracy of the mathematical model and the model parameters. In this figure, one can also observe the duration for which only pure methane exits the adsorption column. The key factor influencing methane purity is the moment when carbon dioxide initially begins to emerge from the adsorbent bed within the gas mixture. The greater the adsorption of carbon dioxide, the more methane becomes enriched (purified) as it exits the adsorption column. As evident from this figure, an increase in pressure leads to a higher level of methane purification until the point of carbon dioxide breakthrough, attributable to the improved adsorption of carbon dioxide. Illustrated in the graph, when the pressure rises from 1 atm to 9 atm, the time gap between the breakthroughs of methane and carbon dioxide increases (at 1 atm, Δt=195 sec; at 5 atm, Δt=385 sec; at 9 atm, Δt=420 sec), providing a greater duration for methane purification at the exit of the adsorption column.

Table 2.6 Amounts adsorbed of CH_4, CO_2, working capacity, selectivity and sorbent selection parameter values as a function of total inlet pressure for the separation of 60%CH_4 - 40%CO_2 on CMS(C) at 294K and inlet flow rate of 400 ml/min.

Feed composition of 60%CH_4 - 40%CO2 on CMS(C) at 294K and inlet flow rate of 400 ml/min							
Adsorbent	Pressure (atm)	Component	Adsorption breakthrough capacity (mol/kg)	Working capacity (mol/kg)	Adsorption equilibrium selectivity (-)	Adsorption kinetic selectivity (-)	Sorbent selection parameter *S* (-)
CMS(C)	1	CO_2	1.13	0.67	3.09 (1 atm)	100.7 (1 atm)	7.76 (1 atm)
CMS(C)	5	CO_2	1.51	1.31	2.20 (5atm)	54.5 (5atm)	4.32 (5 atm)
CMS(C)	9	CO_2	1.54	1.42	1.94 (9 atm)	56.4 (9 atm)	3.41 (9 atm)
CMS(C)	1	CH_4	0.54	0.26			
CMS(C)	5	CH_4	1.03	0.66			
CMS(C)	9	CH_4	1.19	0.81			

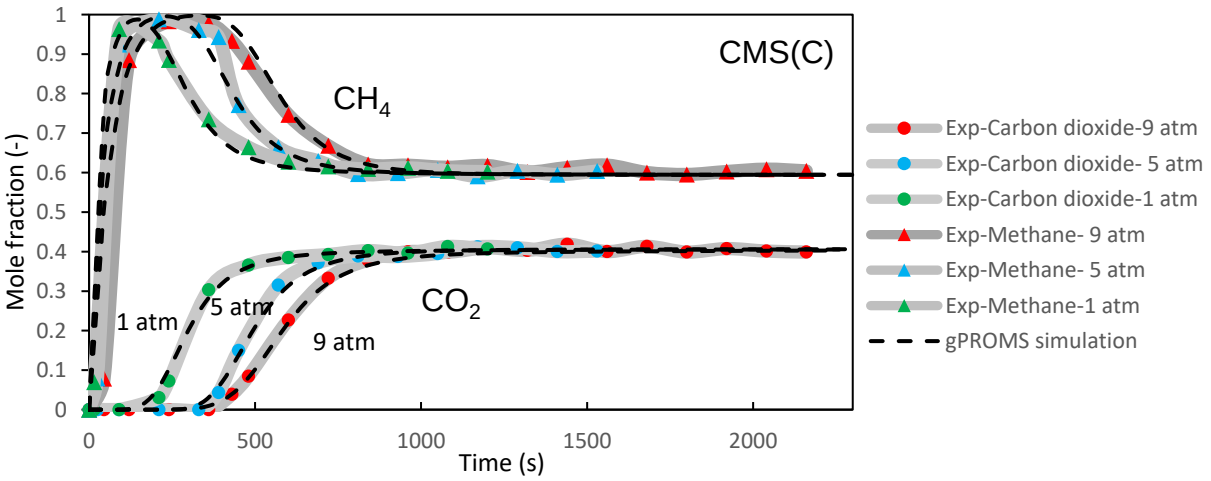

Figure 2.10 Breakthrough curves of 60% CH_4 and 40% CO_2 in CMS (C) at 294 K and inlet flow rate of 400 ml/min for total pressures of 1, 5, 9 atm. Dashed lines correspond to the simulation.

2.3.2.2 Effect of temperature

The effect of temperature on the breakthrough curves at a constant pressure of 9 atm and a feed flow rate of 400 ml min^{-1} are illustrated in Figure 2.11. On one hand, As shown in the figure, both the breakthrough times for CO_2 and CH_4 decrease as temperature increases, as expected, since adsorption capacity decreases with increase in temperature, which decreases the breakthrough time. The reason for this is that adsorption is exothermic, which is a process that releases heat, tends to be more favorable at lower temperatures. On the other, when the

temperature rises under a specific pressure (as depicted in Figure 2.11), it promotes the transfer of mass. As a result, the breakthrough curve becomes steeper, and the zone for mass transfer becomes narrower, enhancing column efficiency by reducing the length of unused bed[49]. The amounts adsorbed of CO_2 and CH_4, selectivity and the sorbent selection parameter values at different temperatures are shown in Table 2.7. Comparison of these mixture adsorption capacities are compared to the predicted ones, as well as the pure component ones and discussed in Section 2.3.2.4.

As shown in Table 2.7, as temperature increases both the separation factor and the sorbent selection parameter decrease.

Just like pressure as discussed in the previous section, temperature can similarly influence methane purification, as well as the duration of producing pure methane. The key factor that dictates methane purity is the moment when carbon dioxide initially begins to emerge from the adsorbent bed. In the case of a gas mixture, the greater the adsorption of carbon dioxide, which causes carbon dioxide to breakthrough later, the more enriched (purified) the methane becomes at the exit of the adsorption column. As evident from Figure 2.11, as temperature decreases, a greater quantity of pure methane will be produced, until the point of carbon dioxide breakthrough is reached. As shown in the figure, as the temperature drops from 333K to 294K, the time interval between the moments when methane and carbon dioxide breakthrough events happen increases (at 333K, Δt=185 seconds; at 313K, Δt=340 seconds; at 294K, Δt=420 seconds), allowing for a prolonged period for methane purification at the outlet of the adsorption column.

Table 2.7Amounts adsorbed of CH_4, CO_2, working capacity, selectivity and sorbent selection parameter values as a function of feed temperature for the separation of 60%CH_4 - 40%CO_2 on CMS(C) at 9 atm and inlet flow rate of 400 ml/min.

Feed composition of 60%CH_4 - 40%CO2 on CMS(C) at 9 atm and inlet flow rate of 400 ml/min							
Adsorbent	Temperature (K)	Component	Adsorption breakthrough capacity (mol/kg)	Working capacity (mol/kg)	Adsorption equilibrium selectivity (-)	Adsorption kinetic selectivity (-)	Sorbent selection parameter *S* (-)
CMS(C)	294	CO_2	1.54	1.42	1.94 (294 K)	56.4 (294 K)	1.94 (294 K)
CMS(C)	313	CO_2	1.33	1.22	1.74 (313 K)	44 (313 K)	1.74 (313 K)
CMS(C)	333	CO_2	1.15	1.05	1.57 (333 K)	45.6 (333 K)	1.57 (333 K)
CMS(C)	294	CH_4	1.19	0.81			
CMS(C)	313	CH_4	1.14	0.79			
CMS(C)	333	CH_4	1.09	0.76			

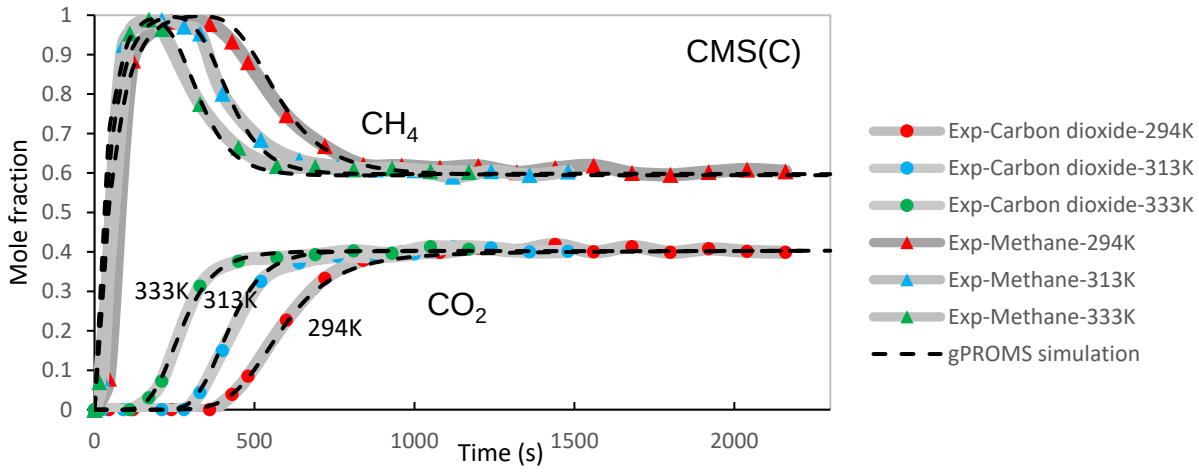

Figure 2.11 Breakthrough curves of 60% CH_4 and 40% CO_2 in CMS (C) at 9 atm and inlet flow rate of 400 ml/min and different temperatures: 294, 313, 333 K. Dashed lines correspond to the simulation.

2.3.2.3 Effect of feed flow rate

The effect of feed flow rate on the breakthrough curves at a constant pressure (9 atm) and temperature (294 K) are illustrated in Figure 2.12. The CH_4 breakthrough in the adsorption bed is immediate due to its extremely slow diffusion rate within the CMS(C) micropores. The same phenomena was also seen across different pressures and temperatures while conducting

breakthrough experiments with CMS(C). The breakthrough curves for CH_4 and CO_2 demonstrate that higher feed flowrates led to a decrease in breakthrough time and a more rapid increase in concentration. This can be explained by the decrease in contact time between the gas mixture and the surface of the CMS (C) as the flowrate was increased. For example, the breakthrough time for CO_2 becomes longer as the feed flowrate decreases, and it exhibits non-linear behavior with changing flowrate. Specifically, when the feed flowrate decreases from 1000 ml min^{-1} to 400 ml min^{-1}, the breakthrough time for CO_2 increases from 190 s to 410 s. This is because a lower feed flowrate requires more time to saturate the adsorption bed, and the resulting longer residence time enhances the mass transfer of CO_2 between the gas phase and the solid phase.

The amounts adsorbed of CO_2 and CH_4, selectivity and the sorbent selection parameters are shown in Table 2.8. These mixture adsorption capacities are compared to the predicted ones, as well as the pure component ones and discussed in Section 2.3.2.4. As a general expectation, the amount adsorbed should remain constant when only the flow rate is changed at the same temperature and total pressure, and all other parameters are kept constant, which is the case here. The slight deviation observed in the amounts adsorbed can be attributed to slight errors associated with the devices responsible for maintaining flow and pressure during these experiments. With this in mind, we took into account the average selectivity values. Figure 2.12 also illustrates the duration when only pure methane exits the adsorption column for each flow rate. The primary factor influencing methane purity is the point at which carbon dioxide initially begins to emerge from the adsorbent bed. In the case of a gas mixture, the higher the adsorption of carbon dioxide, the greater the enrichment (purification) of methane at the outlet of the adsorption column. As can be observed in this figure, a decrease in flow rate results in a larger quantity of pure methane coming out of the column until the point of carbon dioxide breakthrough occurs. As shown in the graph, as the input flow rate decreases from 1000 ml/min to 400 ml/min, the time lag between the instances of methane and carbon dioxide breakthroughs widens (at 1000 ml/min, Δt=160 seconds; at 600 ml/min, Δt=330 seconds; and at 400 ml/min, Δt=420 seconds). This prolonged time frame allows for an increased chance for methane to be purified at the exit of the adsorption column.

Table 2.8 Amounts adsorbed of CH_4, CO_2, selectivity and sorbent selection parameter values as a function of feed flow rate for the separation of 60%CH_4 - 40%CO_2 on CMS(C) at 9 atm and 294 K. The table below displays the percentage deviation (PD) of the measured adsorption equilibrium selectivity values at flow rates of 400 ml/min, 600 ml/min, and 1000 ml/min in comparison to the average adsorption equilibrium selectivity.

		Feed composition of 60%CH_4 - 40%CO2 on CMS(C) at 9 atm and 294K				
Adsorbent	Flow rate (ml/min)	Gas	Adsorption breakthrough capacity (mol/kg)	Adsorption equilibrium selectivity (-)	Average (with respect different flow rates) Adsorption equilibrium selectivity (-)	Sorbent selection parameter (-)
CMS(C)	400	CO_2	1.54	1.94 (PD: +%3.19) (at 400 ml/min)	1.88±0.64	3.41±0.24
CMS(C)	600	CO_2	1.49	1.847 (PD: -%1.76) (at 600 ml/min)		
CMS(C)	1000	CO_2	1.44	1.878 (PD: -%0.11) (at 1000 ml/min)		
CMS(C)	400	CH_4	1.19			
CMS(C)	600	CH_4	1.21			
CMS(C)	1000	CH_4	1.15			

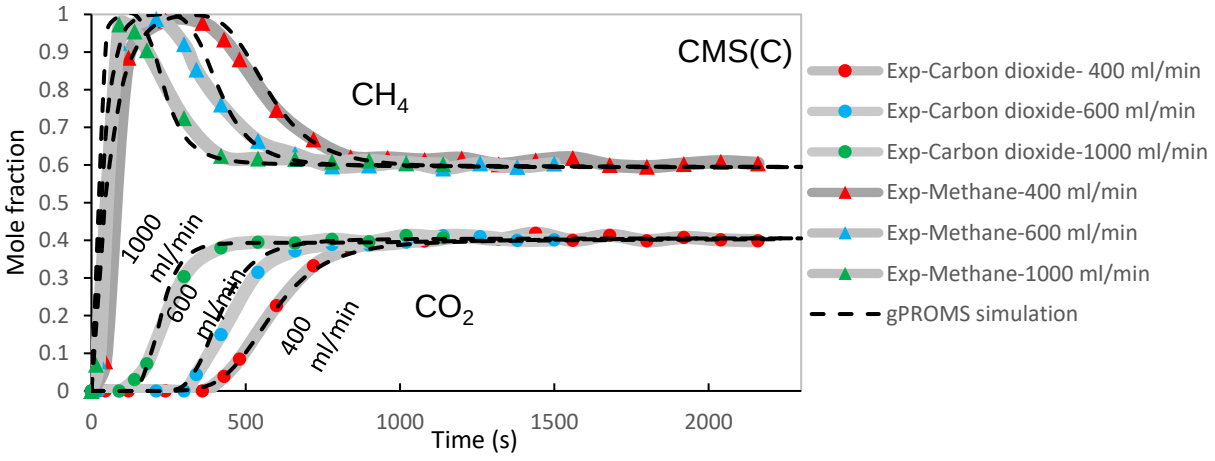

Figure 2.12 Breakthrough curves of 60% CH_4 and 40% CO_2 in CMS (C) at 9 atm and 294K and feed flow rates: 400, 600, 1000 ml/min. Dashed lines correspond to the simulation.

2.3.2.4 Comparison of breakthrough capacity to pure and binary equilibrium capacity

The breakthrough capacities measured at different operating condition, reported in Tables 2.6, 2.7, 2.8, and indicated by cross symbols, were compared to both pure component and predicted binary capacities, as illustrated in Figures 2.5, 2.6, and 2.8. It is evident that the breakthrough capacities closely match the predicted binary capacities, particularly those predicted using TD-Sips. However, there is a significant difference between the breakthrough capacities and the pure component capacities, with the breakthrough capacities being notably lower. The reduction of the breakthrough capacities can be attributed to the nature of competitive co-adsorption of methane and carbon dioxide within the material and the extent of this reduction can be attributed to non-ideal behavior of the CO_2/CH_4 mixtures**.**

2.4. CONCLUSIONS

In this study a comprehensive analysis of pure and binary adsorption equilibria of CO_2 and CH_4 on a commercial carbon molecular sieve (CMS(C)) was carried out at static and dynamic conditions via experiments and simulations based on mechanistic modelling. The adsorption equilibrium data of pure gases were measured gravimetrically at different temperatures over a pressure range of interest and fitted to temperature dependent Sips and Langmuir models and successfully used to predict pure and multicomponent data. Adsorption breakthrough experiments for a feed mixture of 60% CH_4- 40% CO_2 were conducted in a packed bed adsorption column at various operational conditions (different total pressures, different temperatures, different feed flow rates). A mechanistic model representing the kinetics and dynamics of a breakthrough adsorption system was developed within gPROMS simulation software and validated with the experimental breakthrough curves. The predicted simulation results are in good agreement with the experimental data. From breakthrough curves, adsorption capacities, selectivity and adsorbent selection parameter were determined to assess gas adsorption separation potential of the CMS(C) adsorbent. The most favorable performance is associated with the highest calculated selectivity for CO_2 and the sorbent selection parameter, *S*. The examination of the breakthrough curves indicates that to maximize the duration for methane purification, it is most favorable to conduct the breakthrough experiments at higher pressures, lower temperatures, and reduced inlet feed flow rates. For instance, an optimal condition is achieved at a pressure of 9 atm, a temperature of 294 K, and a flow rate of 400 ml min^{-1} which led to the most extended purification duration of 420 seconds.

The analysis also demonstrates that as pressure increases and temperature decreases, the adsorption capacity of both gases on the CMS(C) adsorbent rises. Moreover, the analysis highlights that lower pressures and cooler temperatures result in the highest levels of selectivity and the *S* parameter with the ideal corresponding operational condition for the separation of carbon dioxide from methane on CMS (C) being at a pressure of 1 atm, temperature of 294 K and a flow rate of 400 ml min^{-1}. These elements (including selectivity, *S* parameter, adsorption capacity, and time required for methane purification) prove highly valuable for the initial assessment of the gas separation capabilities of the adsorbent material. Considering these elements, along with other aspects like operational expenses, adsorbent characteristics, adsorption kinetics etc., along with the aid of simulations and pilot scale testing can result in an improved and more optimal adsorption separation process.

2.5 NOMENCLATURE

a	Empirically TD-Sips parameter	[dimensionless]
B	Adsorption affinity constant	[atm^{-1}]
B_0	Adsorption affinity constant at reference temperature	[atm^{-1}]
C_0	Inlet concentration of the gas phase	[$mol.m^{-3}$]
C_g	Concentration of the gas phase	[$mol.m^{-3}$]
C_{gin}	Feed concentration of the gas phase	[$mol.m^{-3}$]
C_{gp}	Concentration of the gas phase inside macropores	[$mol.m^{-3}$]
C_{pg}	Gas phase heat capacity	[$J.kg^{-1}.K^{-1}$]
C_{pw}	Column wall heat capacity	[$J.kg^{-1}.K^{-1}$]
C_s	Solid heat capacity	[$J.kg^{-1}.K^{-1}$]
D_c	Micropore diffusivity	[$m^2.s^{-1}$]
d_i	Column inner diameter	[m]
D_{pore}	Effective macropore diffusivity	[$m^2.s^{-1}$]
h_f	External film heat transfer coefficient	[$W.m^{-2}.K^{-1}$]
h_o	Heat transfer coefficient between column wall and ambient air	[$W.m^{-2}.K^{-1}$]
h_w	Heat transfer coefficient between the gas and the column wall	[$W.m^{-2}.K^{-1}$]
k_1	TD-Langmuir parameter	[$mmol.g^{-1}$]
k_2	TD-Langmuir parameter	[$mmol.g^{-1}\ K^{-1}$]
k_3	TD-Langmuir parameter	[atm^{-1}]
k_4	TD-Langmuir parameter	[K]
k_b	Mass transfer coefficient at the micropore mouth	[$m.s^{-1}$]
k_f	External film mass transfer coefficient	[$m.s^{-1}$]

k_{LDF}	Kinetic rate constant	[s^{-1}]
k_s	Thermal conductivity of the solid	[$W.m^{-1}.K^{-1}$]
k_w	Column wall thermal conductivity	[$W.m^{-1}.K^{-1}$]
$K_{A/B}$	Kinetic selectivity	[dimensionless]
L	Length of the adsorption column	[m]
m_A	Mass of adsorbent	[kg]
n	Sips parameter	[dimensionless]
n_0	TD-Sips reference parameter	[dimensionless]
P	Adsorption pressure	[atm]
q	Adsorption capacity in micropores	[$mmol.g^{-1}$]
Q	Empirical TD-Sips heat of adsorption	[$kJ.mol^{-1}$]
$\overline{q}$	Average adsorbed phase concentration in crystals	[$mmol.g^{-1}$]
$\overline{\overline{q}}$	Average adsorption capacity in the pellet	[$mmol.g^{-1}$]
q_e	Adsorbed amount in equilibrium with the gas in macropore	[$mmol.g^{-1}$]
q_s	Adsorption capacity at saturation	[$mmol.g^{-1}$]
q_{so}	Saturation adsorption capacity at reference temperature	[$mmol.g^{-1}$]
R	Universal gas constant	[$m^3.Pa.K^{-1}.mol^{-1}$]
R	Radial distance coordinate of adsorbent pellet	[m]
r	Radial distance coordinate of the micropore	[m]
r_c	Radius of the crystals	[m]
R_p	Radius of the pellet	[m]
S	Sorbent selection parameter	[dimensionless]
T	Temperature	[K]
T_0	Reference temperature	[K]
T_g	Gas phase temperature	[K]
T_s	Solid phase temperature	[K]
T_w	Column wall temperature	[K]
t	Time	[s]
v	Interstitial velocity	[$m.s^{-1}$]
$\dot{V}$	Total volumetric flow rate	[$m^3.s^{-1}$]
$\dot{V}_{in}$	Total inlet volumetric flow rate	[$m^3.s^{-1}$]
V_b	Volume of adsorption bed	[m^3]
V_{dead}	Dead volume of adsorption breakthrough system associated with tubing and fittings upstream as well as downstream of the adsorption column	[m^3]

X	TD-Sips constant	[dimensionless]
x_i	Mole fraction of component i in the adsorbed phase	[dimensionless]
y_i	Mole fraction of component i in the gas phase	[dimensionless]
z	Axial position in the column	[m]

Subscripts

1	Component 1
2	Component 2
A	Component with stronger adsorption
B	Component with weaker adsorption

Greek Symbols

$\alpha_{A/B}$	Gas selectivity	[dimensionless]
ΔH	Heat of adsorption	[kJ.kg^{-1}]
λ	Axial heat dispersion coefficient	[W.m^{-1}.K^{-1}]
ε_b	Bed porosity	[dimensionless]
ε_p	Pellet porosity	[dimensionless]
μ	Mean retention time	[s]
ρ_g	Gas density	[kg.m^{-3}]
ρ_p	Pellet density	[kg.m^{-3}]
ρ_s	Pellet solid density	[kg.m^{-3}]

Abbreviations

$BFDM$	Backward finite difference method
BPR	Back pressure regulator
$CFDM$	Centered finite difference method
CMS	Carbon molecular sieve
CPM	Concentration pulse method
DAE	Differential algebraic equations
$DASOLV$	Differential algebraic equation solver
DSL	Dual site Langmuir model
EIA	Energy information administration

ELM	Extended Langmuir model
GC	Gas chromatograph
IEA	International energy agency
LDF	Linear driving force
MFC	Mass flow controller
MFM	Mass flow meter
MOL	Methods of lines
$OCFEM$	Orthogonal collocation finite element method
$PDAE$	Partial differential and algebraic equations
PDE	Partial differential equations
PSA	Pressure swing adsorption
TCD	Thermal conductivity detector
TD	Temperature dependent
VSA	Vacuum swing adsorption

2.6. REFERENCES

(1) Shen, Y.; Niu, Z.; Zhang, R.; Zhang, D. Vacuum Pressure Swing Adsorption Process with Carbon Molecular Sieve for CO2 Separation from Biogas. *Journal of CO2 Utilization* 2021, *54*, 101764.

(2) Energy, Global. "CO2 status report." *IEA (International Energy Agency): Paris, France* 1030 (2019): 1031.

(3) Álvarez-Gutiérrez, N.; Gil, M. V.; Rubiera, F.; Pevida, C. Adsorption Performance Indicators for the CO2/CH4 Separation: Application to Biomass-Based Activated Carbons. *Fuel Processing Technology* 2016, *142*, 361–369.

(4) Sabouni, Rana. *Carbon dioxide adsorption by metal organic frameworks (Synthesis, Testing and Modeling)*. PhD diss., The University of Western Ontario (Canada), 2013.

(5) Rajaram, V.; Siddiqui, F. Z.; Khan, M. E. *From Landfill Gas to Energy: Technologies and Challenges*; CRC press, 2011.

(6) Rainone, F.; D'Agostino, O.; Erto, A.; Balsamo, M.; Lancia, A. Biogas Upgrading by Adsorption onto Activated Carbon and Carbon Molecular Sieves: Experimental and Modelling Study in Binary CO2/CH4 Mixture. *Journal of Environmental Chemical Engineering* 2021, *9* (5), 106256.

(7) Wilson, Sean MW. "Adsorption Separation of CO2 from CO in Syngas: Improving the Conversion of the Reverse Water Gas Shift Reaction." PhD diss., Université d'Ottawa/University of Ottawa, 2015.

(8) Rocha, L. A. M.; Andreassen, K. A.; Grande, C. A. Separation of CO 2 /CH 4 Using Carbon Molecular Sieve (CMS) at Low and High Pressure. *Chemical Engineering Science* 2017, *164*, 148–157. https://doi.org/10.1016/j.ces.2017.01.071.

(9) Cavenati, S.; Grande, C. A.; Rodrigues, A. E. Separation of Methane and Nitrogen by Adsorption on Carbon Molecular Sieve. *Separation Science and Technology* 2005, *40* (13), 2721–2743.
(10) Canevesi, Rafael LS, Kari A. Andreassen, Edson A. Da Silva, Carlos E. Borba, and Carlos A. Grande. "Pressure swing adsorption for biogas upgrading with carbon molecular sieve." *Industrial & Engineering Chemistry Research* 57, no. 23 (2018): 8057-8067..
(11) O'koye, I. P.; Benham, M.; Thomas, K. M. Adsorption of Gases and Vapors on Carbon Molecular Sieves. *Langmuir* 1997, *13* (15), 4054–4059.
(12) Grande, Carlos A. "Biogas upgrading by pressure swing adsorption." *Biofuel's engineering process technology* (2011): 65-84.
(13) Cavenati, Simone, Carlos A. Grande, and Alírio E. Rodrigues. "Upgrade of methane from landfill gas by pressure swing adsorption." *Energy & fuels* 19, no. 6 (2005): 2545-2555. .
(14) Kapoor, A.; Yang, R. T. Kinetic Separation of Methane—Carbon Dioxide Mixture by Adsorption on Molecular Sieve Carbon. *Chemical Engineering Science* 1989, *44* (8), 1723–1733.
(15) Jayaraman, A.; Chiao, A. S.; Padin, J.; Yang, R. T.; Munson, C. L. Kinetic Separation of Methane/Carbon Dioxide by Molecular Sieve Carbons. *Separation Science and Technology* 2002, *37* (11), 2505–2528.
(16) Qinglin, Huang, S. M. Sundaram, and S. Farooq. "Revisiting transport of gases in the micropores of carbon molecular sieves." *Langmuir* 19, no. 2 (2003): 393-405.
(17) Rutherford, S. W.; Nguyen, C.; Coons, J. E.; Do, D. D. Characterization of Carbon Molecular Sieves Using Methane and Carbon Dioxide as Adsorptive Probes. *Langmuir* 2003, *19* (20), 8335–8342.
(18) Kim, M.-B.; Bae, Y.-S.; Choi, D.-K.; Lee, C.-H. Kinetic Separation of Landfill Gas by a Two-Bed Pressure Swing Adsorption Process Packed with Carbon Molecular Sieve: Nonisothermal Operation. *Ind. Eng. Chem. Res.* 2006, *45* (14), 5050–5058.
(19) Bae, Y.-S.; Lee, C.-H. Sorption Kinetics of Eight Gases on a Carbon Molecular Sieve at Elevated Pressure. *Carbon* 2005, *43* (1), 95–107.
(20) Wahby, A.; Ramos-Fernández, J. M.; Martínez-Escandell, M.; Sepúlveda-Escribano, A.; Silvestre-Albero, J.; Rodríguez-Reinoso, F. High-Surface-Area Carbon Molecular Sieves for Selective CO2 Adsorption. *ChemSusChem* 2010, *3* (8), 974–981.
(21) Silvestre-Albero, J.; Wahby, A.; Sepúlveda-Escribano, A.; Martínez-Escandell, M.; Kaneko, K.; Rodríguez-Reinoso, F. Ultrahigh CO2 Adsorption Capacity on Carbon Molecular Sieves at Room Temperature. *Chem. Commun.* 2011, *47* (24), 6840.
(22) Arya, A.; Divekar, S.; Rawat, R.; Gupta, P.; Garg, M. O.; Dasgupta, S.; Nanoti, A.; Singh, R.; Xiao, P.; Webley, P. A. Upgrading Biogas at Low Pressure by Vacuum Swing Adsorption. *Ind. Eng. Chem. Res.* 2015, *54* (1), 404–413.
(23) Qinglin, H.; Farooq, S.; Karimi, I. A. Binary and Ternary Adsorption Kinetics of Gases in Carbon Molecular Sieves. *Langmuir* 2003, *19* (14), 5722–5734..
(24) Langmuir, I. The Adsorption of Gases on Plane Surfaces of Glass, Mica and Platinum. *Journal of the American Chemical society* 1918, *40* (9), 1361–1403.
(25) Sips, R. On the Structure of a Catalyst Surface. *The journal of chemical physics* 1948, *16* (5), 490–495.
(26) Toth, J. State Equation of the Solid-Gas Interface Layers. *Acta chim. hung.* 1971, *69*, 311–328.
(27) Li, P.; Handan Tezel, F. Pure and Binary Adsorption of Methane and Nitrogen by Silicalite. *Journal of Chemical & Engineering Data* 2009, *54* (1), 8–15.

(28) Kikkinides, E. S.; Yang, R. T.; Cho, S. H. Concentration and Recovery of Carbon Dioxide from Flue Gas by Pressure Swing Adsorption. *Industrial & Engineering Chemistry Research* 1993, *32* (11), 2714–2720.
(29) Kennedy, D. A.; Mujčin, M.; Abou-Zeid, C.; Tezel, F. H. Cation Exchange Modification of Clinoptilolite–Thermodynamic Effects on Adsorption Separations of Carbon Dioxide, Methane, and Nitrogen. *Microporous and Mesoporous Materials* 2019, *274*, 327–341.
(30) Harlick, P. J. E.; Tezel, F. H. Adsorption of Carbon Dioxide, Methane, and Nitrogen: Pure and Binary Mixture Adsorption by ZSM-5 with SiO_2/Al_2O_3 Ratio of 30. *Separation Science and Technology* 2002, *37* (1), 33–60.
(31) Malek, A.; Farooq, S. Comparison of Isotherm Models for Hydrocarbon Adsorption on Activated Carbon. *AIChE J.* 1996, *42* (11), 3191–3201.
(32) Ghalandari, V.; Hashemipour, H.; Bagheri, H. Experimental and Modeling Investigation of Adsorption Equilibrium of CH4, CO2, and N2 on Activated Carbon and Prediction of Multi-Component Adsorption Equilibrium. *Fluid Phase Equilibria* 2020, *508*, 112433.
(33) Ruthven, D. M.; Farooq, S.; Knaebel, K. S. *Pressure Swing Adsorption*; John Wiley & Sons, 1996.
(34) Rege, S. U.; Yang, R. T. A Simple Parameter for Selecting an Adsorbent for Gas Separation by Pressure Swing Adsorption. *Separation science and technology* 2001, *36* (15), 3355–3365.
(35) Ruthven, D. M. Molecular Sieve Separations. *Chemie Ingenieur Technik* 2011, *83* (1-2), 44–52.
(36) Wu, Y.-J.; Yang, Y.; Kong, X.-M.; Li, P.; Yu, J.-G.; Ribeiro, A. M.; Rodrigues, A. E. Adsorption of Pure and Binary CO_2, CH_4, and N_2 Gas Components on Activated Carbon Beads. *J. Chem. Eng. Data* 2015, *60* (9), 2684–2693.
(37) Silva, J. A. C.; Cunha, A. F.; Schumann, K.; Rodrigues, A. E. Binary Adsorption of CO2/CH4 in Binderless Beads of 13X Zeolite. *Microporous and Mesoporous Materials* 2014, *187*, 100–107.
(38) Wilkins, N. S.; Rajendran, A.; Farooq, S. Dynamic Column Breakthrough Experiments for Measurement of Adsorption Equilibrium and Kinetics. *Adsorption* 2021, *27* (3), 397–422.
(39) Shirani, B.; Eic, M. Novel Differential Column Method for Measuring Multicomponent Gas Adsorption Isotherms in NaY Zeolite. *Ind. Eng. Chem. Res.* 2017, *56* (4), 1008–1018.
(40) Brandani, F.; Ruthven, D. Measurement of Adsorption Equilibria by the Zero Length Column (ZLC) Technique Part 2: Binary Systems. *Ind. Eng. Chem. Res.* 2003, *42* (7), 1462–1469.
(41) Ruthven, D. M.; Kumar, R. An Experimental Study of Single-Component and Binary Adsorption Equilibria by a Chromatographic Method. *Ind. Eng. Chem. Fund.* 1980, *19* (1), 27–32.
(42) Kennedy, D. A.; Mujčin, M.; Alenko, T.; Tezel, F. H. Pure and Mixture Adsorption Equilibria of Methane and Nitrogen onto Clinoptilolite: Effects of Cs+ and Fe 3+ Exchanged Cations on Separation Performance. *Adsorption* 2019, *25*, 135–158.
(43) Harlick, P. J. E.; Tezel, F. H. Use of Concentration Pulse Chromatography for Determining Binary Isotherms: Comparison with Statically Determined Binary Isotherms. *Adsorption* 2003, *9*, 275–286.
(44) Rynders, R. M.; Rao, M. B.; Sircar, S. Isotope Exchange Technique for Measurement of Gas Adsorption Equilibria and Kinetics. *AIChE J.* 1997, *43* (10), 2456–2470.
(45) Bakhtyari, A.; Mofarahi, M. Pure and Binary Adsorption Equilibria of Methane and Nitrogen on Zeolite 5A. *J. Chem. Eng. Data* 2014, *59* (3), 626–639.

(46) Heymans, N.; Alban, B.; Moreau, S.; De Weireld, G. Experimental and Theoretical Study of the Adsorption of Pure Molecules and Binary Systems Containing Methane, Carbon Monoxide, Carbon Dioxide and Nitrogen. Application to the Syngas Generation. *Chemical Engineering Science* 2011, *66* (17), 3850–3858.
(47) Worch, E. *Adsorption Technology in Water Treatment: Fundamentals, Processes, and Modeling*; De Gruyter: Berlin ; Boston, 2012.
(48) Wilkins, N. S.; Sawada, J. A.; Rajendran, A. Measurement of Competitive CO 2 and H 2 O Adsorption on Zeolite 13X for Post-Combustion CO 2 Capture. *Adsorption* 2020, *26* (5), 765–779.
(49) Garcia, S.; Gil, M. V.; Martín, C. F.; Pis, J. J.; Rubiera, F.; Pevida, C. Breakthrough Adsorption Study of a Commercial Activated Carbon for Pre-Combustion CO2 Capture. *Chemical Engineering Journal* 2011, *171* (2), 549–556.
(50) Shafeeyan, M. S.; Wan Daud, W. M. A.; Shamiri, A. A Review of Mathematical Modeling of Fixed-Bed Columns for Carbon Dioxide Adsorption. *Chemical Engineering Research and Design* 2014, *92* (5), 961–988.
(51) Hassan, M. M.; Ruthven, D. M.; Raghavan, N. S. Air Separation by Pressure Swing Adsorption on a Carbon Molecular Sieve. *Chemical Engineering Science* 1986, *41* (5), 1333–1343.
(52) Diagne, D.; Gotob, M.; Hiroseb, T. Numerical Analysis of a Dual Refluxed PSA Process during Simultaneous Removal and Concentration of Carbon Dioxide Dilute Gas from Air. 10.
(53) Hwang, K. S.; Jun, J. H.; Lee, W. K. Fixed-Bed Adsorption for Bulk Component System. Non-Equilibrium, Non-Isothermal and Non-Adiabatic Model. *Chemical Engineering Science* 1995, *50* (5), 813–825.
(54) Ruthven, D. M. *Principles of Adsorption and Adsorption Processes*; John Wiley & Sons, 1984.
(55) Ko, D.; Siriwardane, R.; Biegler, L. T. Optimization of Pressure Swing Adsorption and Fractionated Vacuum Pressure Swing Adsorption Processes for CO_2 Capture. *Ind. Eng. Chem. Res.* 2005, *44* (21), 8084–8094.
(56) Farooq, S.; Qinglin, H.; Karimi, I. A. Identification of Transport Mechanism in Adsorbent Micropores from Column Dynamics. *Ind. Eng. Chem. Res.* 2002, *41* (5), 1098–1106.
(57) Jin, X.; Malek, A.; Farooq, S. Production of Argon from an Oxygen−Argon Mixture by Pressure Swing Adsorption. *Ind. Eng. Chem. Res.* 2006, *45* (16), 5775–5787.
(58) LeVan, M. D.; Carta, G.; Yon, C. M. Adsorption and Ion Exchange. 67.
(59) Khalighi, M.; Farooq, S.; Karimi, I. A. Nonisothermal Pore Diffusion Model for a Kinetically Controlled Pressure Swing Adsorption Process. *Ind. Eng. Chem. Res.* 2012, *51* (32), 10659–10670.
(60) Qinglin, H.; Farooq, S.; Karimi, I. A. Prediction of Binary Gas Diffusion in Carbon Molecular Sieves at High Pressure. *AIChE J.* 2004, *50* (2), 351–367.
(61) Yang, R. T. *Gas Separation by Adsorption Processes*; Butterworths: Boston, 1987.
(62) Rezaei, F.; Grahn, M. Thermal Management of Structured Adsorbents in CO_2 Capture Processes. *Ind. Eng. Chem. Res.* 2012, *51* (10), 4025–4034.
(63) Gholami, M.; Talaie, M. R. Investigation of Simplifying Assumptions in Mathematical Modeling of Natural Gas Dehydration Using Adsorption Process and Introduction of a New Accurate LDF Model. *Ind. Eng. Chem. Res.* 2010, *49* (2), 838–846.
(64) Goyal, P.; Purdue, M. J.; Farooq, S. Adsorption and Diffusion of Moisture and Wet Flue Gas on Silica Gel. *Chemical Engineering Science* 2020, *227*, 115890.

(65) Harun, N.; Nittaya, T.; Douglas, P. L.; Croiset, E.; Ricardez-Sandoval, L. A. Dynamic Simulation of MEA Absorption Process for CO2 Capture from Power Plants. *International Journal of Greenhouse Gas Control* 2012, *10*, 295–309.
(66) Balaman, Ş. Y. Uncertainty Issues in Biomass-Based Production Chains. In *Decision-Making for Biomass-Based Production Chains*; Elsevier, 2019; pp 113–142.
(67) Rios, R. B.; Stragliotto, F. M.; Peixoto, H. R.; Torres, A. E. B.; Bastos-Neto, M.; Azevedo, D. C. S.; Cavalcante Jr, C. L. Studies on the Adsorption Behavior of CO2-CH4 Mixtures Using Activated Carbon. *Brazilian journal of chemical engineering* 2013, *30*, 939–951.

CHAPTER 3

Experimental Analysis and Computational Modelling of Adsorption Separation of Methane and Carbon dioxide on Activated Carbon

A. Jahanshahi, F.H. Tezel

University of Ottawa, Department of Chemical and Biological Engineering

161 Louis Pasteur, Ottawa, Ontario, CANADA, K1N 6N5

ABSTRACT

This study presents a comprehensive assessment of the adsorption separation of methane and carbon dioxide gases using a commercial activated carbon, AC(B). The evaluation includes a combination of experimental measurements and computational modeling through gPROMS software. Experimental equilibrium measurements for pure methane and carbon dioxide gases were conducted using the gravimetric method at various temperatures and pressures within the targeted range. Additionally, binary isotherms were predicted based on temperature-dependent isotherm models. The study delves into experimental breakthrough curves under different operating conditions to validate the simulated breakthrough curves. The impact of various operating conditions, such as temperature, pressure, and flow rate variations, on the breakthrough curves is carefully examined to identify the optimal operating conditions for the AC(B) adsorbent in separating carbon dioxide from methane gases. The analysis of the breakthrough curves reveals that increasing pressure and decreasing temperature and feed flow result in longer breakthrough time and higher adsorption capacity of both gases for the AC(B) absorbent. However, it is observed that these conditions lead to decreased values of adsorption selectivity and the sorbent selection parameter. Based on the measurements, this study has identified the optimal parameters for separating carbon dioxide from methane using AC(B) in terms of selectivity and the sorbent selection parameter. These conditions were found to be the most effective at a pressure of 1 atm, a temperature of 294 K, and a flow rate of 400 ml min^{-1}. Under these specific conditions, the adsorbent exhibits its highest values, rendering it a more favorable choice for the intended gas separation process. Additionally, in the context of methane purification during the separation process, it was observed that higher pressures, lower temperatures, and lower inlet feed flow rates, extended the duration for methane purification as it exits the adsorption column. The most favorable conditions were attained

at 9 atm pressure, 294 K temperature, and a flow rate of 400 ml/min, leading to an extended purification period of 220 seconds.

Keywords: Activated carbon, gPROMS, Breakthrough, Selectivity, Carbon dioxide adsorption, Methane adsorption

3.1. INTRODUCTION

The rapid advancement of global warming and increased use of fossil fuels have resulted in significant problems of limited resources and damage to the environment. Consequently, there has been a global shift towards a clean, renewable, and low-carbon energy systems to address these challenges faced by humanity[1,2]. Nowadays, scientists widely believe that human activities, particularly the release of greenhouse gases like carbon dioxide and methane, are responsible for the changing climate on Earth. These gases are commonly found in gas mixtures such as natural gas, coalbed methane, biogas, and landfill gas [3]. Carbon dioxide is the primary man-made greenhouse gas that has a substantial impact on global warming. Its emissions into the atmosphere account for approximately 60% of the overall warming effect [4]. Taking measures to reduce methane emissions offers several notable benefits in terms of energy, safety, the economy, and the environment. Firstly, since methane is a potent greenhouse gas (with a warming effect twenty-five times greater than that of CO_2 over a 100-year period), decreasing methane emissions can significantly contribute to short-term efforts to mitigate climate change. Secondly, methane is the main component of natural gas and biogas, indicating that capturing and using methane can provide a valuable source of clean energy that supports local economic growth while minimizing environmental pollution. By utilizing methane for energy generation, there is less need for traditional energy sources, resulting in reduced CO_2 and air pollutant emissions from end-users and power plants[5].

One of the main challenges in research and technological development is finding a way to effectively balance the need to reduce CO_2 emissions, which is crucial for addressing global warming, with the growing global energy demands that contribute significantly to these emissions[6]. It is economically important to find ways to efficiently remove carbon dioxide from methane and increase its value. Various technologies are available to achieve this goal, including physical and chemical absorption, cryogenic separation, adsorption, and membrane separation. Among these technologies, adsorption has gained popularity in different industries for gas separation processes. This is primarily because it offers better cost-effectiveness and

reliability compared to traditional methods. Adsorption separation requires less energy and has lower costs, making it an appealing choice for industries that operate under strict environmental and quality regulations. Consequently, adsorption technology has been widely adopted in various industrial applications [7].

Choosing the right adsorbent is essential for any adsorption separation process. The selected adsorbent should have the appropriate selectivity, capacity, durability, and ease of regeneration[8]. Activated carbons are derivatives of carbonaceous materials that show high carbon content via activation process. Activated carbons have been widely reported as competitive adsorbents for the separation of carbon dioxide from methane thanks to their extensive surface area, high micropore volume, appropriate pore size distribution, being easier to regenerate (low regeneration energy, low regeneration temperature), low production cost, having a high raw material availability and thermal stability, receptive to surface modification for adsorption and hydrophobic nature[3,6,9,10]. Many studies have looked into using activated carbon as an adsorbent to separate carbon dioxide from its mixture with methane by physical adsorption separation processes[11–23]. Figure 3.1 illustratues an example of activated carbon pellets.

Figure 3.1 Activated carbon pellets[24].

According to the literature, activated carbons exhibit a lower CO_2 adsorption capacity than zeolites and MOFs at low pressures. This is because the uniform electrical potential of their surface lacks surface cations, which play a role in promoting CO_2 capture, as observed in zeolites. However, activated carbon compensates for this with their high surface area and porosity, leading to high adsorption capacities at high pressures. Additionally, activated carbons offer advantages over zeolites and MOFs, such as a smaller decrease in performance during adsorption/desorption cycles, greater stability in the presence of water, and a lower regeneration temperature [25–28].

This study comprehensively examines the adsorption separation of methane and carbon dioxide using commercially available activated carbon. The research incorporates a combination of experimental and computational methods. The assessment involves measuring the equilibrium of pure methane and carbon dioxide gases at different temperatures and pressures and predicting binary isotherms based on pure component equilibrium data and multicomponent adsorption isotherm models. Adsorption breakthrough experiments are conducted at different operating conditions and the impact of temperature, pressure, and flow rate variations on the breakthrough curves are examined. Breakthrough curve mechanistic models for mass and energy balances are developed using gPROMS simulation software and they were compared to experimental data to validate the models developed. Gravimetric and breakthrough data are analyzed to identify the most ideal operating conditions of the adsorption process for the separation of carbon dioxide from methane.

3.2. MATERIALS AND METHODS

3.2.1. MATERIALS

To measure the adsorption of carbon dioxide and methane gases, as well as their mixture, a series of experiments were conducted using high purity gases (≥99%). In the pressurization phase of the breakthrough experiments, helium gas with high purity was utilized. Additionally, helium served as a carrier gas in the gas chromatograph and facilitated buoyancy correction during the gravimetric system's pure component adsorption isotherm experiments. All gases were sourced from Messer Canada Inc in Mississauga, Ontario, Canada. The specific activated carbon sample used in this research, known as AC(B), was provided by Xebec Adsorption Company in Blainville, Quebec, Canada. The AC(B) sample consisted of cylindrical pellets, and its properties can be found in Table 3.1.

Table 3.1 Physical properties of AC(B) adsorbent

Pellet diameter (mm)	~2.1
Pellet length (mm)	2.7-4.4
Pellet porosity	31-36%
Pellet density (kg/m^3)	711
Pellet packing density (kg/m^3)	458
BET surface area (m^2/g)	949
Average pore size (nm)	0.43

3.2.2. METHODS

3.2.2.1. Pure component adsorption isotherms

The AC(B) adsorbent's single gas methane and carbon dioxide adsorption isotherms were determined using the micrograviметric analyzer purchased from VTI Corp. (Hialeah, Florida, USA). Before conducting the experiments, the sample underwent regeneration for 12 hours at a temperature of 200°C under high vacuum conditions. The adsorbent was then exposed to sample gases at increasing pressures ranging from 0 to 10 atm at various temperatures (10°C, 21°C, 40°C, 60°C). Equilibrium was considered to be reached at each pressure step when the weight change remained below 0.015 wt% for a duration of 60 minutes, and the equilibrium adsorption measurement was recorded accordingly. To account for buoyancy effects, the sample was also exposed to helium gas at similar pressures and temperatures.

3.2.2.2. Binary gas mixture breakthrough measurements

The experimental setup involved conducting binary breakthrough adsorption experiments using a feed gas consisting of 60% CH_4 and 40% CO_2. These experiments were performed in a fixed-bed adsorption column packed with approximately 21 g of AC(B). The column, made out of stainless steel, had a height of 12 cm and an inner diameter of 2.104 cm. Porous plates were positioned on both ends of the column to keep the adsorbent in place in the column. During this study, an experimental breakthrough set up was designed and constructed for a multicomponent gas system. The design of the breakthrough set-up considered guidelines for an efficient experimental setup, and the schematic diagram of the set-up can be seen in Figure 3.2.

The adsorption column was fully loaded with the AC(B) adsorbent, and MKS mass flow controllers (MFCs) from Kanata, Ontario, Canada, were utilized to maintain the desired feed flow rate and composition. The flow exiting the column was measured using an MKS mass flow meter (MFM). Gas concentration analysis of the effluent leaving the column was performed using a gas chromatograph (GC) (GOW-MAC 580 (Bethlehem, Pennsylvania, USA)) equipped with a thermal conductivity detector (TCD) and a HayeSep Q column. The pressure was controlled using back pressure regulators (BPR) from Swagelok Central Ontario in Ottawa, Ontario, Canada. Different valves were employed to control the flow and introduce step changes in concentration at the column inlet. Pressure indicators (PI) were used to monitor operating pressure and pressure drop across the column, while Type K Thermocouples (TI) were placed at the inlet, outlet, and along the column length to monitor the operating and

adsorbent temperatures during the breakthrough runs. PI and TI were purchased from Omega Sensing Solutions ULC in St-Eustache, Quebec, Canada. The setup is additionally fitted with a needle valve, which allows for precise control of gas flow when needed.

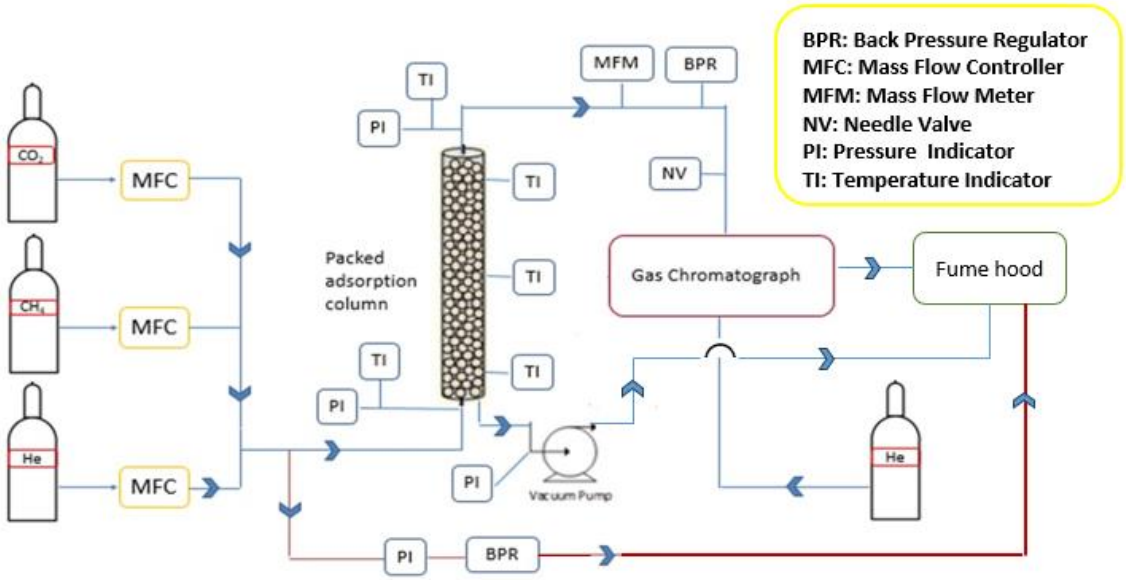

Figure 3.2 Schematic diagram of the breakthrough set-up that is used in this study.

The experimental procedure involved instrument calibration, measuring the dead volume, and regenerating the column before conducting the breakthrough experiments. During this study, individual gases were allocated to different mass flow controllers (MFC's) and MFC's were calibrated at 25°C and 1 atm by CCR Process Products (Kanata, Ontario, Canada). The gas chromatograph, GOW-MAC 580, underwent calibration for each gas using a trial and error approach, where adjustments were made to the amperage, detector temperature, column temperature, injection temperature, and carrier gas (helium) flow rate. This calibration process aimed to produce CO_2 and CH_4 peaks that closely resembled the standard peak plots (voltage vs. time) provided by GOW-MAC Instrument Co. (Bethlehem, Pennsylvania, USA). For effective regeneration, it was recommended to gradually heat the adsorption column packed with the adsorbent to the required regeneration temperature while purging it alternately with an inert gas and vacuum. In this study, the regeneration of the sample packed in the adsorption column was performed using a ceramic tube furnace supplied by Heaters Controls and Sensors LTD (London, Ontario, Canada). The sample's temperature was gradually raised at a rate of 8°C per minute. Once it reached a stable temperature of 200°C, the regeneration process commenced and lasted for 12 hours under vacuum conditions. The sample was weighed before and after regeneration to determine its mass. After the regeneration pre-treatment, the breakthrough experiments were initiated by pressurizing the column and flowing an inert gas

(helium) through the GC. The desired pressure was set using the BPR. The initialization stage continued until the GC reached a stable baseline. The subsequent phase involves adjusting the MFCs to the desired flow rate and allowing their flow to stabilize without passing through the packed column or disrupting the established GC baseline. To achieve this, the flow was stabilized in a separate line (red line). Once the MFCs stabilized, the feed gas was introduced to the column at time zero, and data were simultaneously recorded using a computer using LabView software. The breakthrough experiment was considered complete when the GC reached a stable constant value, the bed temperature returned to its initial value (dependent on heat transfer from the sample within the column to the surrounding air, thermal conductivity of the sample etc.), the total outlet flow rate matched the inlet flow rate, and the outlet gas concentration matched the inlet gas concentration (dependent on mass transfer and diffusivity of the adsorbate). Experiment completion indicators mentioned earlier may not coincide. In this study, equilibrium was attained the earliest when the flow rate returned to its initial value. This was followed by the gas concentration and bed temperature returning to their initial inlet values. Afterwards, the regeneration was performed again to desorb the captured gas and prepare the adsorbent for the next adsorption cycle.

3.2.3. THEORETICAL BACKGROUND

3.2.3.1. Pure component adsorption equilibrium models

To accurately model the adsorption behavior observed in the experimental data at different temperatures, a precise understanding of the adsorption behavior is crucial. In this study, three isotherm models - Sips, Toth, and Langmuir - were used to fit the equilibrium adsorption data, as described by Equations 1 to 3, respectively. Sips and Toth isotherm models offer greater flexibility compared to the Langmuir model, as they incorporate heterogeneity and non-uniformity of adsorbent surfaces[29–31].

$$q = \frac{q_s (BP)^{1/n}}{1 + (BP)^{1/n}} \tag{1}$$

$$q = \frac{q_s (BP)}{(1 + (BP)^n)^{1/n}} \tag{2}$$

$$q = \frac{q_s (BP)}{1 + (BP)} \tag{3}$$

In Equations 1 to 3, the parameters q_s, q, P, and B represent the maximum adsorption capacity at the isotherm temperature, adsorption capacity, pressure, and affinity constant, respectively. For the Sips and Toth isotherm models, the parameter n describes the limited availability of adsorption sites at higher surface concentrations and is dimensionless.

Since adsorption is an exothermic process, it is important to account for the effect of temperature on the adsorption capacity, as the non-isothermal nature of adsorption processes can be affected by changes in column temperature. Equations 4 to 6 represent the temperature-dependent Sips and Toth models, where the parameters q_s, B, and n are written as functions of temperature[32].

$$B = B_0 e^{\left(\frac{Q}{RT_0}\left(\frac{T_0}{T}-1\right)\right)} \tag{4}$$

$$q_s = q_{s0} e^{\left(X\left(1-\frac{T}{T_0}\right)\right)} \tag{5}$$

$$n = n_0 + a\left(1-\frac{T}{T_0}\right) \tag{6}$$

In Equations 4 to 6, B_0 is the affinity constant for adsorption at the reference temperature T_0, q_{s0} and n_0 are the saturation adsorption capacity and the n parameter at the reference temperature T_0. The parameters X and α are constant parameters and are not functions of temperature. By substituting Equations 4 to 6 into Equations 1 and 2, six parameter functions are obtained for temperature dependent Sips and temperature dependent Toth isotherms, respectively. These functions would include the B_0, Q, q_{s0}, X, n_0, and α parameters and the value of these parameters are determined by performing a regression analysis to do a curve-fit to the experimental data obtained at different temperatures[32].

For the Langmuir model, Equations 7 and 8 can be used to describe the temperature-dependent fitting parameters B and q_s for this isotherm model [33].

$$B = k_3 e^{\left(\frac{k_4}{T}\right)} \tag{7}$$

$$q_s = k_1 - k_2 T \tag{8}$$

The strength of adsorption is effected by the interactions between the adsorbate and adsorbent at different temperatures. The isosteric heat of adsorption at zero fractional loading can be used to measure these interactions. Although the Langmuir model assumes that the heat

of adsorption (ΔH) is constant and independent of surface coverage, but in reality, it may vary due to local surface heterogeneity and additional molecular interactions at higher loadings. The Clausius-Clapeyron equation can be employed to directly calculate ΔH from experimentally determined isotherms at different temperatures, providing insight into this variation[34].

$$\left[\frac{\Delta H_{iso}}{R}\right] = \left[\frac{\partial lnP}{\partial\left(\frac{1}{T}\right)}\right]_q \tag{9}$$

The Clausius-Clapeyron equation relates the logarithmic change in pressure (P) with respect to the inverse of temperature (T) while keeping the adsorption capacity (q) constant. The value of the heat of adsorption, ΔH, can be determined at different adsorption capacities, q, from the slope of the plot of ln(P) against 1/ T [34].

3.2.3.2. Theoretical models for prediction of multicomponent adsorption

Theoretical models have been developed to describe and predict the equilibrium adsorption of gas mixtures based on experimental data for different components. These models have been extensively tested in the literature to ensure their accuracy when applied to binary systems[35,36]. In this study, the adsorption equilibrium of the gas mixture was described using the Extended Sips model (Equation 10) [37] and the Extended Langmuir model (Equation 11)[36] based on the pure component isotherms of CH_4 and CO_2.

$$q_i = \frac{q_{si}(B_i P_i)^{1/n_i}}{1 + \sum_j^n \left(B_j P_j\right)^{1/n_j}} \tag{10}$$

$$q_i = \frac{q_{si}(B_i P_i)}{1 + \sum_j^n B_j P_j} \tag{11}$$

In Equations 10 and 11, q_{si} represents the maximum adsorption capacity of component i at the isotherm temperature, q_i indicates the adsorption capacity of component i, $P_{i\ or\ j}$ represents the partial pressure of component i or j, and $B_{i\ or\ j}$ represents the affinity constant of the Sips or the Langmuir isotherm model of component i or j.

3.2.3.3. Assessing gas adsorption separation potential

The selectivity or separation factor in adsorption equilibrium quantifies the degree of separation between the adsorbed and gas phases for the components present in a mixture. This factor is defined by taking the ratio of the Langmuir isotherm parameters as defined in Equation

3 that is derived from the Extended Langmuir model for gas mixtures, as shown in Equation 12[38].

$$\alpha_{A/B} = \frac{x_A y_B}{x_B y_A} = \frac{q_{sA} B_A}{q_{sB} B_b} \tag{12}$$

In this equation, the component with stronger adsorption is represented by the subscript A, and the one with weaker adsorption is denoted by the subscript B. For a gas mixture, x denotes the mole fraction of the adsorbed phase, and y represents the mole fraction of the gaseous phase mixture[38].

To calculate the sorbent selection parameter, Equation 13 is utilized. This parameter is defined by comparing the working capacities (represented as Δq_A and Δq_B) of the components A and B, respectively. The working capacities are the differences between the adsorption capacities at the adsorption and desorption pressures[39]. The working capacity is characterized by the difference between the amount adsorbed at adsorption (high) pressure and desorption (low) pressure. To calculate this parameter, corresponding conditions related to the separation process are taken into account. In this study, binary adsorption equilibrium information from the TD-Sips model was employed to determine working capacities at varying total pressures (1, 5, 9 atm) and temperatures (294K, 313K, 333K) for a gas mixture consisting of 40% CO_2 and 60% CH_4. The selection of a desorption pressure of 0.1 atm was based on the vacuum level attainable by the pump across all the adsorption pressures.

$$S = \alpha_{A/B} \frac{\Delta q_A}{\Delta q_B} \tag{13}$$

The kinetic selectivity, $K_{A/B}$, is also employed to estimate the separation efficiency. It considers the ratio of kinetic mass transfer coefficients and the adsorption equilibrium selectivity for the two adsorbates, as expressed in Equation 14[40].

$$K_{A/B} = \alpha_{A/B} \sqrt{\frac{k_{LDF,A}}{k_{LDF,B}}} \tag{14}$$

3.2.3.4. Binary gas mixture breakthrough measurements

To accurately evaluate the performance of potential adsorbents for gas separations, a comprehensive understanding of the adsorption properties of gas mixtures is necessary. However, measuring multicomponent adsorption isotherms is challenging due to the complexity of analyzing the composition of the adsorbed phase. Few reliable experimental approaches for multicomponent adsorption measurements have been developed and

documented in the literature. These include dynamic systems such as breakthrough measurements[13,41,42], differential column analysis[43], zero length column chromatography[44], chromatography[45–47] and isotope exchange technique[48] as well as static systems such as gravimetric or volumetric methods[49,50]. The breakthrough approach is one method that can be used to measure equilibrium isotherms for mixed and pure gases across a wide range of conditions. By integrating breakthrough curves, which represent concentration at the exit of the column over time, it is possible to determine the amount of each component retained in the bed. Figure 3.3[51] provides an illustration of binary breakthrough curves. The amount of the weakly adsorbed component (in this case, methane) retained in the bed can be calculated by subtracting area A_2 from area A_1. For the strongly adsorbed component (in this case, carbon dioxide), the amount retained in the bed can be calculated by adding the areas A_1 and A_3. Equation 15 describes the accumulation of the weakly adsorbed component inside the column during the breakthrough experiments. Here, $q_{0,B}$ represents the amount adsorbed of the weakly adsorbed component, m_A is the mass of the adsorbent in the column, $\dot{V}_{in}$ is the inlet total flow rate, and c_B and $c_{0,B}$ are the gas phase concentrations of the weakly adsorbed component at the exit and at the inlet of the column, respectively[51].

$$q_{0,B} m_A = c_{0,B} \times \dot{V}_{in} \times \int_{t=0}^{t_{(c_B = c_{0,B})}} \left(1 - \frac{c_B}{c_{0,B}}\right) dt - c_{0,B} \times \dot{V}_{in} \times \int_{t_{(c_1 = c_{0,1})}}^{t_\infty} \left(\frac{c_B}{c_{0,B}} - 1\right) dt \quad (15)$$

During the breakthrough experiments, competitive adsorption results in concentration overshoots for all components except for the most strongly adsorbed component. For the weakly adsorbed component, the first term on the right-hand side of Equation 15 represents the mass initially adsorbed without competition, while the second term accounts for the mass desorbed due to displacement of that component by the more strongly adsorbed component[51].The amount adsorbed for the strongly adsorbed component A, which is not susceptible to displacement for the breakthrough experiments, can be written as follows:[51]:

$$q_{0,A} m_A = c_{0,2} \times \dot{V}_{in} \times \int_{t=0}^{t_\infty} \left(1 - \frac{c_A}{c_{0,A}}\right) dt \quad (16)$$

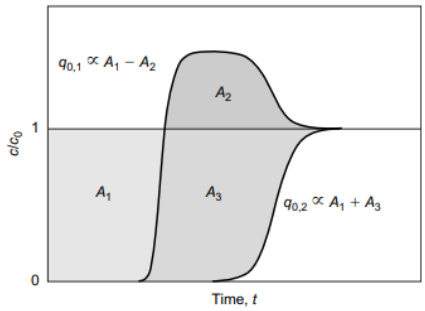

Figure 3.3 Binary breakthrough response for a fixed bed adsorption column[51]

In this equation, $q_{0,A}$ represents the amount adsorbed of the strongly adsorbed component A, m_A is the mass of the adsorbent in the column, $\dot{V}_{in}$ is the inlet total flow rate, and c_A and $c_{0,A}$ are the gas phase concentrations of the strongly adsorbed component at the exit and at the inlet of the column, respectively[51]. The $\left(\frac{c_i}{c_{0,i}}\right)$ in the integral term in Equations 15 and 16 can also be expressed in terms of $\frac{y_i(t)\dot{V}(t)}{y_{i,in}\dot{V}_{in}}$ versus time[42].

For the breakthrough set-up, the total system dead volume comprises the void volume within the adsorption column and the dead volume corresponding to the tubing and fittings positioned either before or after the adsorption column. It delays the breakthrough response and can lead to an overestimation of the equilibrium capacity calculated from the unadjusted breakthrough response. Moreover, the dead volume affects the shape and spread of the breakthrough curve, impacting the accuracy of the obtained adsorption kinetics information. Therefore, it is crucial to correct the measured breakthrough response with respect to the blank response of the column to isolate the actual response of the column related to the adsorption alone. This correction ensures the extraction of reliable equilibrium and kinetic data for adsorption. Dead volume measurements can be conducted by performing breakthrough experiments with a column packed with glass beads of similar size as the actual adsorbent (AC(B)). The experiments should be conducted under the same operating conditions (flow rate, temperature, feed composition, pressure) as the actual experiments, generating a blank response. This blank response (adsorption column packed with glass beads + total dead volume) can be subtracted from the composite response (adsorption column packed with adsorbent + total dead volume) point by point on a plot of $\frac{C_{(t)}}{C_{in}}$ versus time. In this study, another approach for dead volume correction was used, which involves using a modified version of Equations 15 and 16, subtracting the combined terms $C_{0,i}(\varepsilon_b V_b)$ and $C_{0,i}V_{dead}$, which account for the number of moles of component i in the column void volume and the number of moles of component i in the dead volume, respectively. Equation 17 illustrates a modified equation for the component that exhibits stronger adsorption, specifically CO_2 in our study.[10,52].

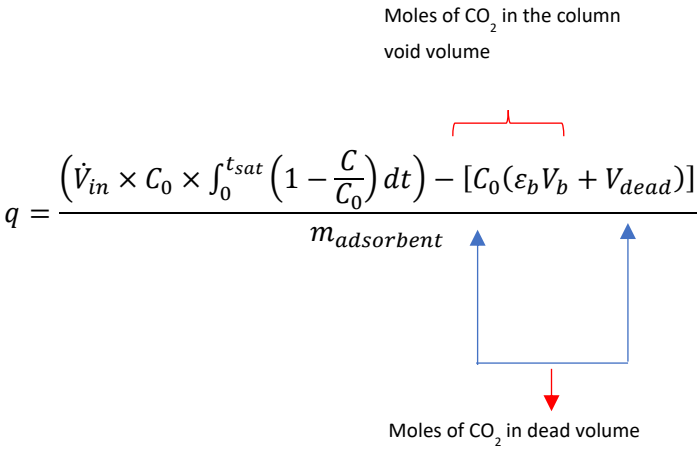

$$q = \frac{\left(\dot{V}_{in} \times C_0 \times \int_0^{t_{sat}} \left(1 - \frac{C}{C_0}\right) dt\right) - [C_0(\varepsilon_b V_b + V_{dead})]}{m_{adsorbent}} \quad (17)$$

3.2.3.5. Adsorption breakthrough modeling

The modeling of adsorption in packed beds has become crucial for the development and design of gas adsorption separation processes. To effectively design an adsorption separation process, it is necessary to develop a mechanistic model that accounts for the adsorption kinetics, dynamic behavior, and all transport phenomena occurring in a packed bed adsorption column with a specific adsorbent. These mathematical models are essential for estimating and predicting the adsorption separation process, optimizing design and operating conditions. However, the lack of an efficient and accurate adsorption cycle simulator requires the utilization of data from experiments for process design. This approach, which involves extensive experimentation on process development units, is expensive and time-consuming. Ideally, a predictive model based on independently determined equilibrium and kinetic parameters can offer a way to predict column dynamic capacity without the need for extensive experimentation[53].

To predict the dynamic behavior of a column, a set of coupled partial differential equations (PDEs) that describe material and energy balances over a packed bed, along with appropriate initial and boundary conditions, must be solved simultaneously. The mass transfer mechanism from the fluid phase to the solid phase significantly influences the modeling of transport equations in a packed column. Equilibrium theory is applicable only to systems where the adsorptive selectivity is determined by differences in equilibrium, and it is not suitable for systems where separation is controlled by kinetic selectivity[54]. The mass transfer of the adsorbate from the gas phase into the solid phase is driven by equilibrium isotherms, while the mass balance equation inside the adsorbent particle depends on the structure of the adsorbent.

Different mass transfer mechanisms are involved in the diffusion of the adsorbate into the adsorbent particles, either at the macroscopic or microscopic level.

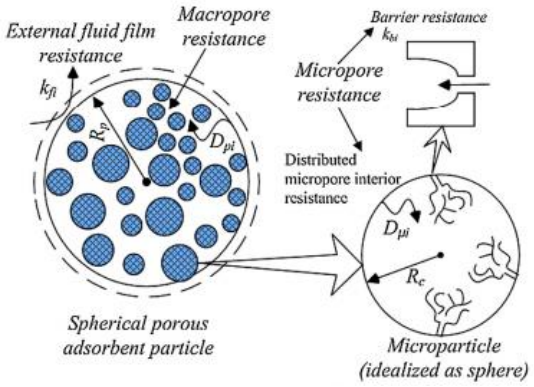

Figure 3.4 Schematic diagram showing different resistances to the transport of adsorbate[53]

As depicted in Figure 3.4[53], the adsorbate molecules first need to pass through the external fluid film surrounding each adsorbent particle before diffusing into the porous structure of the adsorbent. Depending on the specific system and conditions, any of the three types of potential mass transfer resistance - external fluid film resistance, macropore diffusional resistance, and micropore diffusional resistance - may dominate, and more than one resistance can be significant. The transfer processes through the film, macropores, and micropores can be considered as sequential steps, and the assumption of mass conservation can be applied[53].

One of the primary objectives of this study is to measure the dynamic adsorption of CO_2/CH_4 mixtures by the adsorbent experimentally and compare and validate the modelled breakthrough curves with the experimental ones. The mechanistic model for the breakthrough curves was developed under the following assumptions: 1) the system operates under non-isothermal conditions; 2) the adsorption equilibrium isotherm follows the multicomponent Sips temperature-dependent model; 3) the flow pattern is described by the axially dispersed plug flow model; 4) there are concentration and temperature gradients in both the axial direction within the column and the radial direction in the adsorbent pellet; 5) the gas phase behaves as an ideal gas mixture; 6) both external and internal diffusional resistances to mass and heat transfer are taken into account; 7) the mass transfer rate is represented by a linear driving force (LDF) model. With these assumptions, and considering that for most particle shapes, it is acceptable to approximate them as equivalent spheres, enabling their transport to be described by a diffusion equation formulated in spherical coordinates[55], a set of equations and corresponding initial and boundary conditions can be established:

The following equation[55,56] can be used to represent the gas phase mass balance, which considers the axial dispersion term, convection term, accumulation in the fluid phase, and adsorption term, from left to right, respectively :

$$-D_z\left(\frac{\partial^2 C_g}{\partial z^2}\right)+\frac{\partial\left(vC_g\right)}{\partial z}+\frac{\partial C_g}{\partial t}+\left(\frac{1-\varepsilon_b}{\varepsilon_b}\right)\rho_p\frac{\partial\bar{\bar{q}}}{\partial t}=0 \tag{18}$$

Here, C_g represents the adsorbate concentration in the gas phase, z is the axial position in the column, ε_b is the bed void fraction, v is the interstitial fluid velocity, t is time, ρ_p is the pellet bulk density, $\bar{\bar{q}}$ is the average concentration in the adsorbent particle, and D_z is the axial dispersion coefficient.

The mass transfer rate across the external film is equal to the diffusive flux at the particle surface and is given by:[57–60]

$$\frac{\partial\bar{\bar{q}}}{\partial t}=\frac{3}{R_p}k_f\left(C_g-C_{gp|R=R_p}\right)=\frac{3}{R_p}\varepsilon_p D_{pore}\left(\frac{\partial C_{gp}}{\partial R}\right)_{|R=R_p} \tag{19}$$

Here, k_f is the external film mass transfer coefficient, R_p is the pellet radius, C_{gp} is the adsorbate concentration in the macropore, ε_p is the adsorbent pellet void fraction, D_{pore} is the macropore diffusivity, and R is the radial position in the pellet.

The average concentration in the adsorbent particle is determined by integrating the concentration profiles in the macropores and micropores [53,61,62]:

$$\bar{\bar{q}}=\varepsilon_p\frac{3}{{R_p}^3}\int_0^{R_p}C_{gp}R^2dR+(1-\varepsilon_p)\frac{3}{{R_p}^3}\int_0^{R_p}\bar{q}\,R^2dR \tag{20}$$

where:

$$\bar{q}=\frac{3}{{r_c}^3}\int_0^{r_c}q\,r^2dr \tag{21}$$

where $\bar{q}$ is the average concentration of adsorbate in the crystals, r_c is the crystal radius, r is the radial distance within the crystals, and q is the distributed concentration of the adsorbate in the adsorbed phase.

The mass balance inside the pellet can be described by [57,59,63,64]:

$$\frac{\partial C_{gp}}{\partial t}+\frac{\rho_p}{\varepsilon_p}\left(\frac{\partial\bar{q}}{\partial t}\right)=D_{pore}\left[\frac{\partial^2 C_{gp}}{\partial R^2}+\frac{2}{R}\left(\frac{\partial C_{gp}}{\partial R}\right)\right] \tag{22}$$

The mass transfer rate across the micropores is given by the following equation[57,59,60]:

$$\frac{\partial \bar{q}}{\partial t} = \frac{3}{r_c} D_c \left(\frac{\partial q}{\partial r}\right)_{|r=r_c} \tag{23}$$

where q_e is the adsorbed-phase concentration in equilibrium with the macropore fluid phase concentration (C_{gp}) and D_c is the micropore diffusivity.

The mass balance inside the micropores is expressed as [57,59,61]:

$$\frac{\partial q}{\partial t} = \frac{1}{r^2} D_c \frac{\partial}{\partial r}\left(r^2 \frac{\partial q}{\partial r}\right) \tag{24}$$

Since adsorption is an exothermic process, temperature variations can affect the adsorption equilibrium and rates. Therefore, for accurate prediction of packed column dynamics, the effects of heat generation and transfer within the adsorbent bed must be considered [53]. Energy transfer is accounted for in three distinct control volumes: solid, gas, and column wall [53].

The change in gas temperature over time is influenced by energy transfer due to axial conductive solid phase heat flux to the gas phase and convection within the bed. The energy balance equation for the gas phase in the column, including heat transfer between the flowing fluid and the surface of the solid adsorbent and energy transmitted to the column wall, can be expressed as [55,65,66]:

$$\rho_g C_{pg} \frac{\partial T_g}{\partial t} = \frac{\boldsymbol{\lambda}}{\varepsilon_b} \frac{\partial^2 T_g}{\partial z^2} - \rho_g C_{pg} \frac{\partial (v T_g)}{\partial z} - \frac{(1-\varepsilon_b)}{\varepsilon_b} \frac{3}{R_p} h_f \left(T_g - T_{s|_{R=R_p}}\right) - \frac{4 h_w}{\varepsilon_b d_i} \left(T_g - T_w\right) \tag{25}$$

Where ρ_g is the gas density, C_{pg} is the gas heat capacity at constant pressure, T_g is the bulk gas temperature, $\boldsymbol{\lambda}$ is the axial heat dispersion coefficient, h_f is the film heat transfer coefficient, T_s is the solid temperature, h_w is the heat transfer coefficient between the gas phase and the column wall, d_i is the inner diameter of the column, and T_w is the column wall temperature.

The energy balance equation for the solid phase is given by[65,67]:

$$\rho_s C_s \frac{\partial T_s}{\partial t} + (H)\frac{\partial \bar{q}}{\partial t} = k_s \left[\frac{\partial^2 T_s}{\partial R^2} + \frac{2}{R}\left(\frac{\partial T_s}{\partial R}\right)\right] \tag{26}$$

where ρ_s is the adsorbent solid density, C_s is the adsorbent heat capacity, H represents the heat of adsorption, and k_s is the thermal conductivity of the adsorbent.

The energy balance equation for the column wall is expressed as[68]:

$$\rho_w C_{pw} \frac{\partial T_w}{\partial t} = k_w \frac{\partial^2 T_w}{\partial z^2} + h_w \frac{2r_i}{({r_o}^2 - {r_i}^2)}(T_g - T_w) - h_o \frac{2r_i}{({r_o}^2 - {r_i}^2)}(T_w - T_{amb}) \tag{27}$$

where ρ_w is the column wall density, C_{pw} is the column wall heat capacity, k_w is the thermal conductivity of the column wall, h_o is the heat transfer coefficient between the column wall and the surrounding fluid, T_{amb} is the ambient temperature, r_i is the inner radius of the column, and r_o is the outer radius of the column. The corresponding initial and boundary conditions for the mass and energy balances are provided in Table 3.2

Table 3.2 Corresponding initial and boundary conditions of the mechanistic model describing dynamic column breakthrough curves.

Mass balance/Energy balance/Equation No.	**Boundary conditions**	**Initial conditions**
Gas phase mass balance/18	$(\frac{\partial C_g}{\partial z})_{z=L} = 0$ $D_{z\|z=0}(\frac{\partial C_g}{\partial z})_{z=0} = \frac{v_s}{\varepsilon_b}(C_{g\|z=0} - C_{gin})$	$C_g = 0\,,\ t = 0$
Mass balance inside the pellet/22	$(\frac{\partial C_{gp}}{\partial R})_{R=0} = 0$ $\frac{3}{R_p}k_f\left(C_g - C_{gp\|R=R_p}\right) = \frac{3}{R_p}\varepsilon_p D_{pore}\,(\frac{\partial C_{gp}}{\partial R})_{\|R=R_p}$	$C_{gp} = 0\,,\ t = 0$
Mass balance inside the micropores/24	$(\frac{\partial q}{\partial r})_{\|r=0} = 0$ $(q_{\|r=r_c}) = f(C_{gp})\,, q_e = \ f(C_{gp})$	$q = 0\,,\ t = 0$
Gas phase energy balance/25	$\frac{\boldsymbol{\lambda}}{\varepsilon_b}\left(\frac{\partial T_g}{\partial z}\right)_{\|z=0} = \rho_g C_{pg} v\left(T_{g_{\|z=0}} - T_{gin}\right)$ $\left(\frac{\partial T_g}{\partial z}\right)_{\|z=L} = 0$	$T_g = T_{gin}\,,\ t = 0$
Solid phase energy balance/26	$\left(\frac{\partial T_s}{\partial R}\right)_{\|R=0} = 0$ $k_s\left(\frac{\partial T_s}{\partial R}\right)_{\|R=R_p} = h_f\left(T_g - T_{s\|R=R_p}\right)$	$T_s = T_{gin}\,,\ t = 0$
Column wall energy balance/27	$T_{w\|z=0} = \frac{T_{gin} + T_{amb}}{2}$ $\left(\frac{\partial T_w}{\partial z}\right)_{\|z=L} = 0$	$T_w = \frac{T_{gin} + T_{amb}}{2}$, $t = 0$

3.2.3.6. gPROMS Implementation

The comprehensive model for the adsorption gas separation process involves mass and energy balances with variables that exhibit temporal and spatial distributions. This model is formulated as a combination of partial differential equations and algebraic equations (PDAEs). In this study, the developed mechanistic model is solved using gPROMS simulation software, developed by Process System Enterprise Limited (London, UK). This software is capable of solving complex PDAEs under dynamic conditions, enabling high-fidelity predictive modeling.[69].

In gPROMS, the adsorption system, represented by PDAEs, is numerically solved using the method of lines (MOL). This involves discretizing the distributed equations in the spatial domain, resulting in a system of time-dependent differential algebraic equations (DAEs). The DAE system is then integrated over time using a differential algebraic equation solver (DASOLV) integration code[69].

In this study, specific discretization methods were applied to different spatial domains. The packed column's spatial domain was discretized using a first-order backward finite difference method (BFDM) with 50 discretization intervals. The adsorbent pellet's spatial domain was discretized using a second-order centered finite difference method (CFDM) with 10 discretization points. The micropores inside the adsorbent pellet were discretized using a third-order orthogonal collocation finite element method (OCFEM) with 10 discretization intervals.

The mathematical model developed and simulated in gPROMS comprises various entities, including PARAMETERS, VARIABLES, MODELS, PROCESSES, PERFORMED EXPERIMENTS, and PARAMETER ESTIMATION. The MODELS entity specifies the mathematical equations describing the adsorption system, along with the parameters, variables, and boundary conditions. The PROCESS entity provides input details for the simulation, such as parameter values, assigned variables, discretization methods, initial conditions for differential variables, operating procedures, and solver settings. The PERFORMED EXPERIMENTS entity contains the complete details of conducted breakthrough experiments. Model validation is carried out through the PARAMETER ESTIMATION entity, where unknown such as diffusion time constant, $\frac{D_c}{r_c^2}$, are estimated and fitted to experimental data.

2.2.3.6. Parametric studies for process optimization and design

Sensitivity analysis is a technique used to examine how changes in the parameters of a mathematical model or system affect the system's outputs or performance. It enables the observation of how variations in inputs impact the system's outputs. In this analysis, a specific parameter is adjusted by a certain percentage while keeping all other parameters constant. The model is then executed, and the resulting percentage change in the selected performance indicator is monitored[70].

In the context of an adsorption breakthrough system, a sensitivity analysis is conducted to identify the parameters that significantly influence the adsorption process. This information is crucial for optimizing and designing the adsorption breakthrough system. The analysis aims to determine the properties of the adsorbent material, bed characteristics, and physical and transport properties of the gases that have the greatest impact on breakthrough curves. The desired outcomes are a short breakthrough time for CH_4 and a long breakthrough time for CO_2 to increase the concentration of CH_4 coming out of the column, as well as a steep breakthrough curve for both CO_2 and CH_4, which would maximize the utilization of the bed. By studying the results of the sensitivity analysis, dynamic optimization techniques can be applied to the adsorption breakthrough process under consideration.

This study concentrated on conducting a sensitivity analysis for operating conditions including pressure, temperature, and feed flow rate. The primary objective was to investigate how alterations in these parameters influence the breakthrough curves. This exploration aimed to pinpoint these operating conditions under which AC(B) exhibits optimal efficiency for the process of adsorption separation, effectively isolating CO_2 from CH_4.

3.3. RESULTS AND DISCUSSION

3.3.1. Pure component and binary adsorption isotherms

Experimental adsorption equilibrium isotherms for pure carbon dioxide and methane gases were obtained for the AC(B) adsorbent at various temperatures (283, 294, 313, and 333 K) for CO_2 and CH_4 for pressures up to 10 atm. These isotherms, along with the fitted representations using the temperature-dependent Sips (TD-SIPS) and temperature-dependent Langmuir (TD-Langmuir) models, are presented in Figures 3.5 and 3.6, for CO_2 and CH_4, respectively. Both temperature dependent models exhibit good agreement with the experimental isotherm data.

With increasing pressure in the system, the adsorbed amounts of both CO_2 and CH_4 increased. However, the rate of increase decreased at higher pressures as the adsorption sites approached saturation. The adsorption isotherms revealed that, under similar pressure and temperature conditions, CO_2 exhibited significantly higher adsorption compared to CH_4. This disparity can be attributed to the larger quadrupole moment of CO_2 compared to CH_4, as CH_4 is non-polar. The stronger electrostatic interaction between CO_2 and the adsorbent led to a higher uptake of CO_2.The impact of temperature on the equilibrium adsorption capacity at a given pressure was clearly observed in Figures 3.5 and 3.6. In an adsorptive separation process, the temperature typically increases during adsorption due to the exothermic nature of the adsorption process and decreases during desorption due to the endothermic nature of desorption. These thermal effects tend to decrease the adsorbent's performance by reducing the equilibrium capacity during adsorption and increasing it during regeneration. The breakthrough capacities (BC) indicated as symbols in figures 3.5 and 3.6 are plotted at their respective partial pressures (P_{CO2}=0.4 atm and P_{CH4}=0.6 atm for P_{total}=1 atm, P_{CO2}=2 atm and P_{CH4}=3 atm for P_{total}=5 atm, P_{CO2}=3.6 atm and P_{CH4}=5.4 atm for P_{total}=9 atm), whereas pure adsorption isotherms are plotted as a function of total pressure.

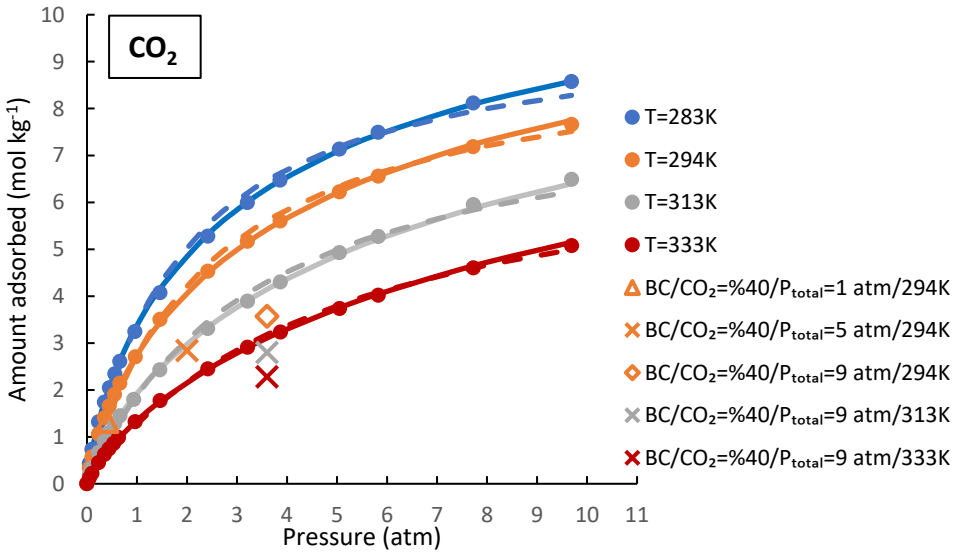

Figure 3.5 Adsorption isotherms of carbon dioxide at 283, 294, 313 and 333 K on AC(B). Solid lines represent the TD-Sips model and dashed line represent the TD-Langmuir model fits to the experimental data. BC= Breakthrough Capacity. The symbols denoting the breakthrough capacities (BC) are graphed at their corresponding partial pressures, which are P_{CO2}=0.4 atm when P_{total}=1 atm, P_{CO2}=2 atm when P_{total}=5 atm, and P_{CO2}=3.6 atm when P_{total}=9 atm.

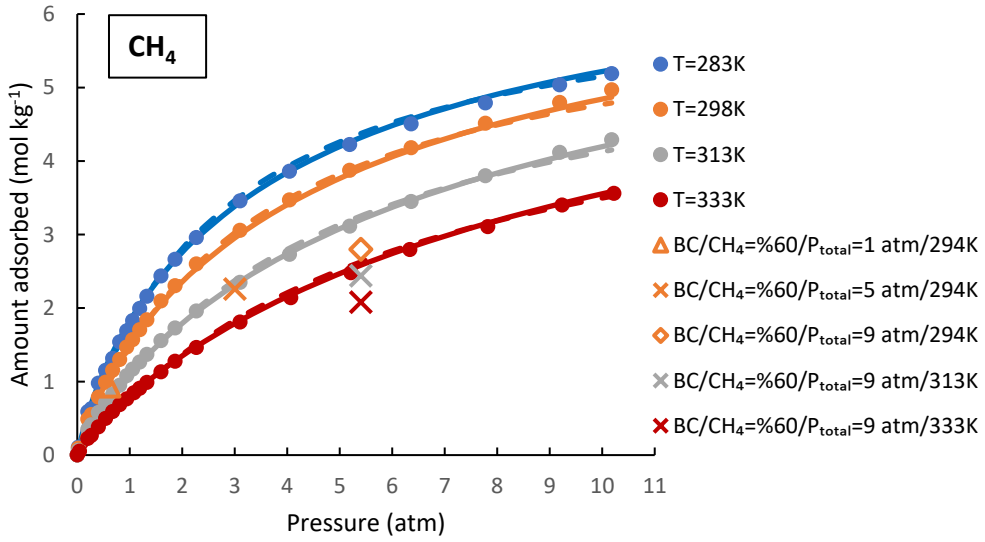

Figure 3.6 Adsorption isotherms of methane at 283, 298, 313 and 333K on AC (B). Solid lines represent the TD-Sips model and dashed line represent the TD-Langmuir model fits to the experimental data. BC= Breakthrough Capacity. The symbols denoting the breakthrough capacities (BC) are graphed at their corresponding partial pressures, which are P_{CH4}=0.6 atm when P_{total}=1 atm, P_{CH4}=3 atm when P_{total}=5 atm, and P_{CH4}=5.4 atm when P_{total}=9 atm.

Table 3.3 and Table 3.4 display the regression parameters for the TD-Sips and TD-Langmuir isotherm models.

Table 3.3 Regression parameters of the temperature dependent Sips isotherm model of CO_2 and CH_4 on AC(B).

Component	q_{s0}	X	n_0	α	B_0	$\frac{Q}{RT_0}$
CO_2	12.42	0.59	1.26	0.11	0.28	8.11
CH_4	7.42	0.0001	1.16	0.13	0.27	7.29

Table 3.4 Regression parameters of the temperature dependent Langmuir isotherm model of CO_2 and CH_4 on AC(B).

Component	k_1	k_2	k_3	k_4
CO_2	23.44	0.0477	0.00097	1775.12
CH_4	10.97	0.0157	0.00106	1662.04

The isosteric heat of adsorption were analyzed using the Clausius-Clapeyron equation, and the results are shown in Figure 3.7 for CO_2 and CH_4. The isosteric heats of adsorption for both gases exhibit a slight decrease as the loadings of both components increase. Within the experimental conditions considered, the average heat of adsorption for CO_2 with the AC(B) adsorbent was approximately 22.5 kJ/mol, while for CH_4 it was around 18.1 kJ/mol.

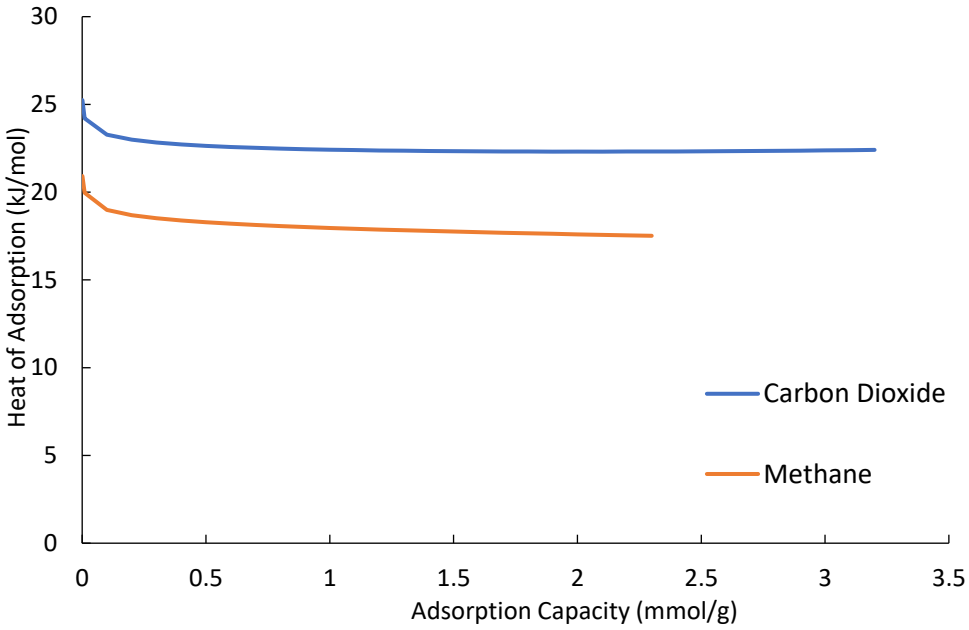

Figure 3.7 Isosteric heat of adsorption values of methane and carbon dioxide with AC(B).

The predicted adsorption data for CO_2-CH_4 mixtures, considering different mole fractions of CO_2 are depicted in Figure 3.8. These data correspond to total pressures of 1 and 9 atm at 294 K, as well as temperatures of 313 and 333 K at a fixed total pressure of 9 atm. The binary adsorption isotherms were predicted through the utilization of multicomponent, temperature-dependent Langmuir and Sips models. Throughout the range of pressures and temperatures investigated within this study, the overall adsorption and the quantity of carbon dioxide captured both increased with higher CO_2 composition in the gas phase. Conversely, the quantity of methane adsorbed experienced a reduction. This observation points toward a competitive process for adsorption sites, thus providing additional evidence for the preferential adsorption of carbon dioxide over methane. CO_2 has higher polarizability and a quadrupole moment, leading to stronger interactions with the solid surface and enhanced attractive forces[71]. In Section 3.3.2.4, we delve into the comparison of the predicted adsorption capabilities and

the breakthrough capacities, in addition to the adsorption capacities of individual pure components.

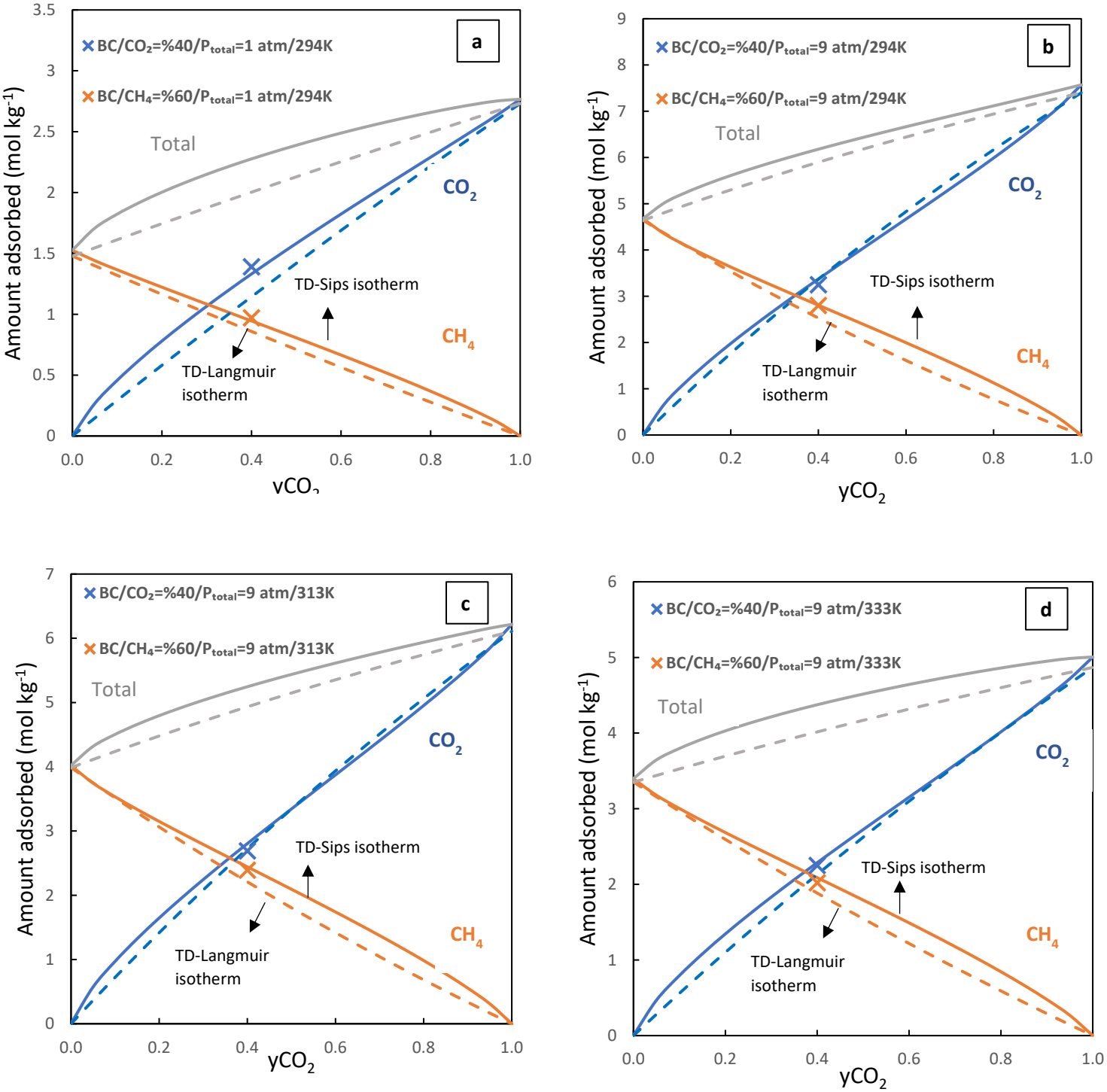

Figure 3.8 Predicted binary isotherms of CO_2/CH_4 gas mixture at (a) 294K and 1 atm,, (b) 294K and 9 atm, (c) 313K and 9 atm,, (d) 333K and 9 atm with AC(B). Solid lines represent the TD-Sips model and dashed lines represent the TD-Langmuir model. BC= Breakthrough Capacity.

Figure 3.9 illustrates the binary adsorption phase diagrams of CO_2-CH_4 for the investigated adsorbent under various conditions: 294 K and 1 atm, 294 K and 9 atm, 313 K and 9 atm, and 333 K and 9 atm. These diagrams were generated based on the predicted binary adsorption isotherms. Notably, it was observed that the data obtained at lower pressures and temperatures exhibited enhanced separation performance. This advantage stemmed from the phase diagram curves being positioned farther away from the 45° line, particularly at lower to pressures and temperatures. Moreover, Figure 3.9 illustrates a strong correlation between the breakthrough data and the phase diagrams projected by the temperature-dependent Sips model.

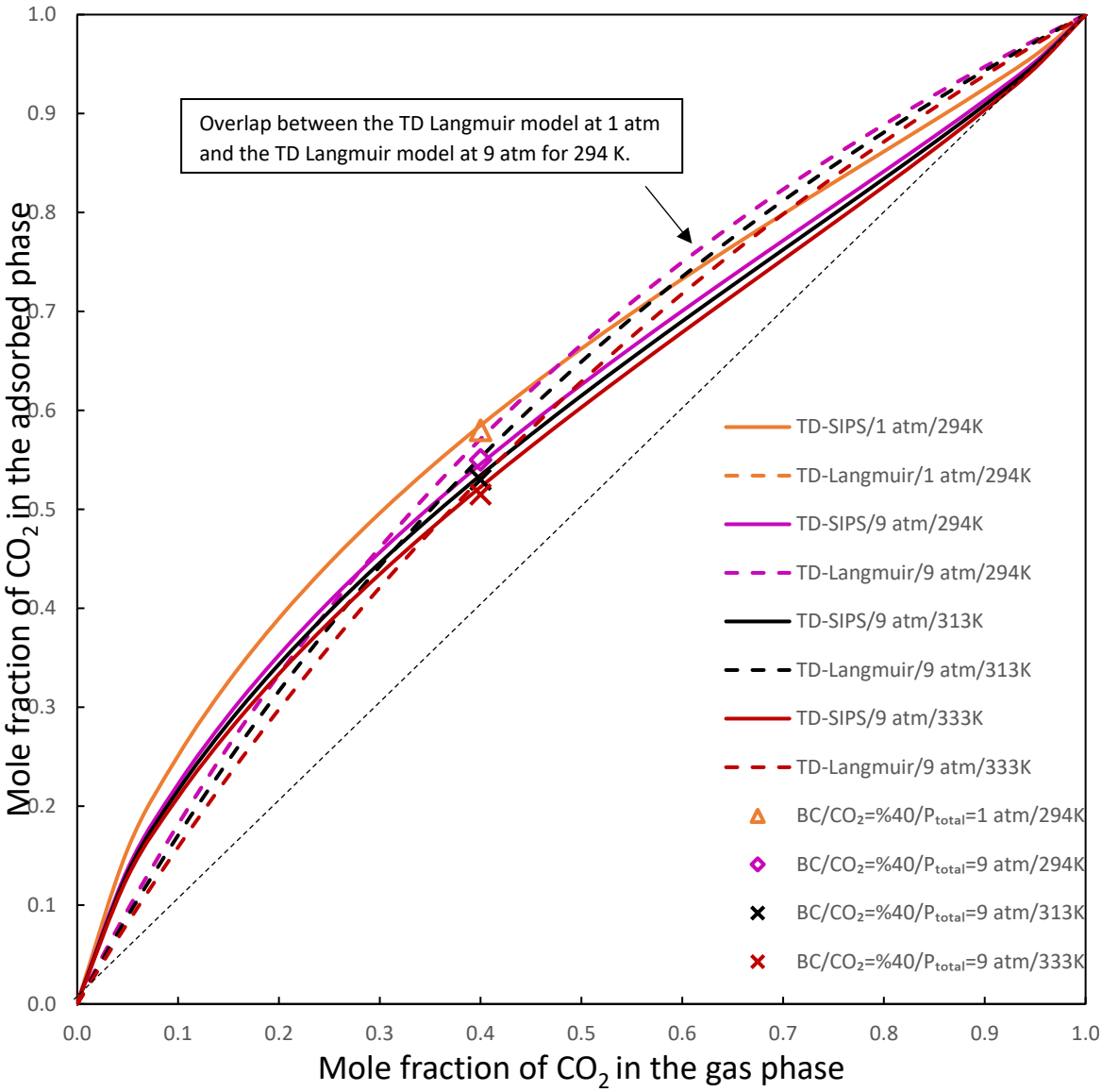

Figure 3.9 *x-y* phase diagrams for CO_2/CH_4 binary adsorption system at 294 K and 1 atm, 294K and 9 atm, 313K and 9 atm, 333K and 9 atm with AC(B). Solid lines represent the TD-Sips model and dashed lines represent the TD-Langmuir model. Note: in the figure, there is an overlap between the TD Langmuir model at 1 atm and the TD Langmuir model at 9 atm for 294 K.

3.3.2. Adsorption binary breakthrough experiments and simulations

A series of breakthrough experiments were performed to investigate the dynamic behavior of a mixture comprising 40% CO_2 and 60% CH_4 in a fixed bed filled with AC(B) adsorbent. These experiments aimed to analyze the effects of different operating parameters on adsorption selectivity. The experimental conditions, including total pressures, feed temperatures, and feed flow rates, were varied, and the specifics of the breakthrough experiments are provided in Table 3.5. The selection of operating conditions for conducting experiments was influenced by the maximum operational limitations of the devices used within the experimental breakthrough setup. Furthermore, the decision to conduct breakthrough experiments specifically at high pressures is grounded in the expectation that carbon materials' adsorption performance, leading to improved bulk separation and removal of CO_2 from CH_4, will be more effective at higher pressures when applied at an industrial scale.

Table 3.5 Breakthrough experiments operational conditions.

Operational conditions	
Feed gas composition	40% CO_2 and 60% CH_4
Adsorption pressure (atm)	1, 5, 9
Feed temperature (K)	294, 313, 333
Feed flow rate (at 1 atm, 294 K) (ml min^{-1})	400, 600, 1000

3.3.2.1 Effect of pressure

The impact of pressure on the breakthrough curves was examined at a constant temperature of 294 K and a feed flow rate of 400 ml/min, as depicted in Figure 3.10. It can be observed from this figure that the breakthrough times for both CO_2 and CH_4 increase with higher pressures, as expected. The equilibrium dynamic capacity, which represents the adsorption breakthrough capacity, also rises with increasing pressure, with the highest values achieved at 9 atm total pressure. The contrast between these adsorption capacities for mixtures is evaluated against both the predicted mixture values as well as the capacities for pure components. This analysis and its implications are elaborated upon in Section 3.3.2.4. The quantities adsorbed for CO_2 and CH_4, selectivity, and the sorbent selection parameter are presented in Table 3.6. With increasing pressure, a slight increase in the co-adsorption of CH_4 with CO_2 on the AC(B) adsorbent is observed. This co-adsorption phenomenon hampers the separation efficiency of CO_2/CH_4, as evident in the table with reduced selectivity and sorbent selection values due to the pressure increment. The time difference between the CH_4 and CO_2

breakthrough curves may serve as an indicator of the solid bed's separation performance. Furthermore, a larger difference in breakthrough times between the two adsorbates can suggest a higher level of effectiveness in the separation process. Figure 3.10 also illustrates that with an increase in pressure, the extent of the mass-transfer zone, which is relative to the difference between breakthrough and saturation times, widens slightly. This widening suggests a stretched mass transfer zone. Within the adsorption column, the region across which concentrations experience changes is known as the mass transfer zone. Slower mass transfer is a result of higher axial dispersion and other increased mass transfer obstacles during the adsorption process. In order to optimize the utilization of the adsorbent, a narrower mass-transfer zone is preferred in adsorption separation processes. When the mass-transfer zone is narrower in comparison to the bed length, the breakthrough curve becomes steeper, and a greater portion of the solid capacity is utilized at the point of breakthrough. This trend can be observed in Figure 3.10 as the pressure decreases from 9 to 1 atm, since the breakthrough curve is observed to be steeper.

A strong alignment between the experimental data and simulation outcomes for breakthrough curves is evident in Figure 3.10. This correspondence confirms the precision of the mathematical model and the associated parameters. In this figure, one can also observe the period during which only pure methane is discharged from the adsorption column. The primary factor that influences the purity of methane after it breaks through and ultimately reaches its maximum purity level is the point at which carbon dioxide initially begins to appear from the adsorbent bed within the gas mixture. To put it differently, the more significant the adsorption of carbon dioxide occurs after methane breaks through the column and reaches its highest level of purity, the more time methane has to undergo enrichment (purification) as it exits the adsorption column. As shown in the figure, as the pressure increases from 1 atm to 9 tam the time difference between the occurance of methane and carbon dioxide breakthrough increases (Δt=100 sec at 1 atm, Δt=210 sec at 5 tam and Δt=220 sec at 9 atm) allowing more time for methane to be purified at the outlet of the adsorption column.

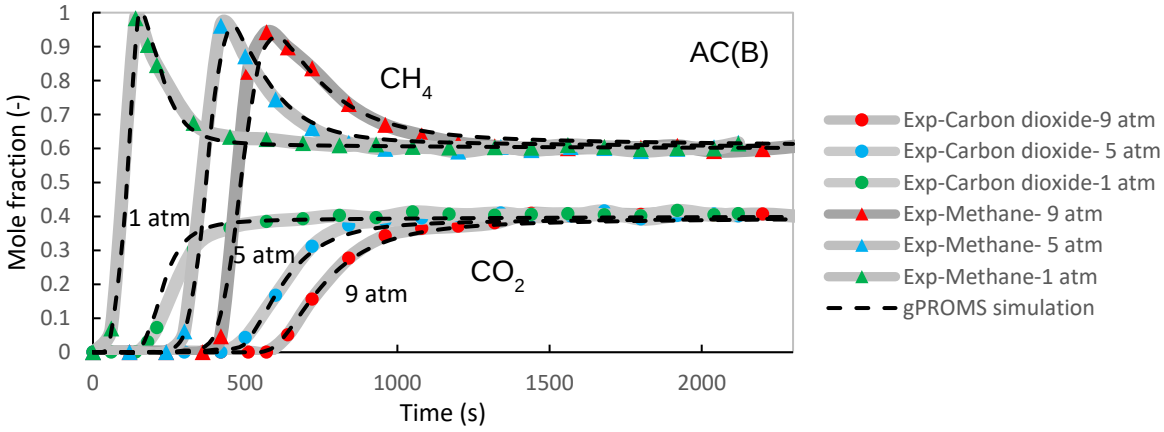

Figure 3.10 Breakthrough curve of 60% CH_4 and 40% CO_2 with AC (B) at 294K and inlet flow rate of 400 ml/min for 1, 5, 9 atm total pressures. Dashed lines correspond to the simulation.

Table 3.6 Amounts adsorbed for CH_4, CO_2, working capacity, selectivity and sorbent selection parameter values as a function of total inlet pressure for the separation of 60%CH_4 - 40%CO_2 with AC(B) at 294K and inlet flow rate of 400 ml/min**.**

Feed composition of 60%CH_4 - 40%CO2 on AC(B) at 294K and inlet flow rate of 400 ml/min							
Adsorbent	Pressure (atm)	Gas	Adsorption breakthrough capacity (mol/kg)	Working capacity (mol/kg)	Adsorption equilibrium selectivity (-)	Adsorption kinetic selectivity (-)	Sorbent selection parameter *S* (-)
AC(B)	1	CO_2	1.33	0.87	2.11 (1atm)	3.61 (1atm)	4.01 (1 atm)
AC(B)	5	CO_2	2.84	2.55	1.88 (5atm)	2.61 (5atm)	3.25 (5 atm)
AC(B)	9	CO_2	3.37	3.17	1.80 (9atm)	2.53 (9atm)	3.00 (9 atm)
AC(B)	1	CH_4	0.94	0.46			
AC(B)	5	CH_4	2.26	1.47			
AC(B)	9	CH_4	2.80	1.90			

3.3.2.2 Effect of temperature

The impact of temperature on the breakthrough curves was examined at a constant pressure of 9 atm and a feed flow rate of 400 ml/min, as depicted in Figure 3.11. It can be observed from the figure that the breakthrough times for both CO_2 and CH_4 decrease as temperature increases, as expected, since adsorption capacity decreases at higher temperatures. This is attributed to the exothermic nature of the adsorption process, which becomes less favorable at elevated temperatures. However, under a specific pressure, increasing the temperature promotes mass transfer. This leads to a steeper breakthrough curve and a narrower mass transfer zone, resulting in improved column efficiency by reducing the length of unused

bed. Table 3.7 presents the quantities adsorbed for CO_2 and CH_4, selectivity, and the sorbent selection parameter at different temperatures.

The comparison between the adsorption capacities of these mixtures is conducted with respect to both the predicted mixture values as well as the capacities of pure components. This analysis is elaborated upon in Section 3.3.2.4. As shown in Table 3.7, as temperature increases, both the selectivity and the sorbent selection parameter decrease. In addition to the pressure effects covered in the previous section, it's important to note that temperature also plays a role in determining how long methane purification with AC(B) takes. As depicted in Figure 3.11, when the temperature decreases from 333K to 294K, the time gap between the points at which methane and carbon dioxide breakthrough occur increases (at 333K, Δt=145 sec; at 313K, Δt=160 sec; at 294K, Δt=220 sec), providing an extended duration for methane purification at the exit of the adsorption column.

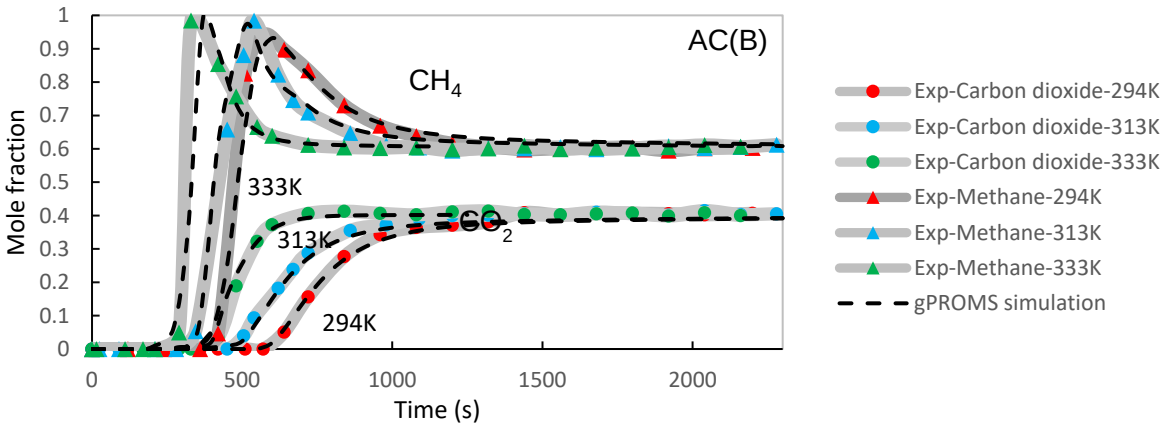

Figure 3.11 Breakthrough curves of 60% CH_4 and 40% CO_2 with AC (B) at 9 atm and inlet flow rate of 400 ml/min for different temperatures: 294, 313, 333 K. Dashed lines correspond to the simulation.

Table 3.7 Amounts adsorbed for CH_4, CO_2, working capacity, selectivity and sorbent selection parameter values as a function of feed temperature for the separation of 60%CH_4 - 40%CO_2 with AC(B) at 9 atm and inlet flow rate of 400 ml/min.

Feed composition of 60%CH_4 - 40%CO2 on AC(B) at 9 atm and inlet flow rate of 400 ml/min							
Adsorbent	Temperature (K)	Gas	Adsorption breakthrough capacity (mol/kg)	Working capacity (mol/kg)	Adsorption equilibrium selectivity (-)	Adsorption kinetic selectivity (-)	Sorbent selection parameter *S* (-)
AC(B)	294	CO_2	3.37	3.17	1.80 (294 K)	2.53 (294 K)	3.00 (294 K)
AC(B)	313	CO_2	2.80	2.63	1.72 (313 K)	2.496 (313 K)	2.73 (313 K)
AC(B)	333	CO_2	2.28	2.15	1.64 (333 K)	2.490 (333 K)	2.48 (333 K)
AC(B)	294	CH_4	2.80	1.90			
AC(B)	313	CH_4	2.44	1.65			
AC(B)	333	CH_4	2.08	1.42			

3.3.2.2 Effect of feed flow rate

Figure 3.12 illustrates the impact of varying feed flow rate on breakthrough curves under constant pressure (9 atm) and temperature (294 K). The breakthrough patterns of CH_4 and CO_2 reveal that higher feed flow rates prompt shorter breakthrough times and a faster concentration rise. This outcome arises from reduced contact time between the gas mixture and AC(B) surface at elevated flow rates. Conversely, the CO_2 breakthrough time extends as feed flow rate decreases. Specifically, decreasing the feed flow rate from 1000 ml/min to 400 ml/min increases the CO_2 breakthrough time from 190 s to 530 s. This result stems from the need for more time to saturate the adsorption bed at lower flow rates, thus prolonging residence time.

Table 3.8 presents CO_2 and CH_4 adsorption amounts, selectivity, and sorbent selection parameter at different flow rates.

Comparisons between the observed mixture adsorption capacities, predicted mixture values, and pure component capacities are discussed in Section 3.3.2.4. Under the same temperature and total pressure conditions while keeping other parameters constant, adsorption amounts should remain consistent with changing flow rates – as observed here. Slight deviations in adsorption amounts would arise from minor deviations in flow and pressure control equipment during the experiments. Given this fact, average values of selectivity were considered.

Beyond the effects of pressure and temperature discussed in the earlier sections, it's worth mentioning that the flow rate also exerts an influence on the duration of methane purification with AC(B). As depicted in the figure, when the inlet flow rate reduces from 1000 ml/min to 400 ml/min, there is an increase in the time gap between the occurrences of methane and carbon dioxide breakthrough (Δt=90 sec at 1000 ml/min, Δt=110 sec at 600 ml/min, and Δt=220 sec at 400 ml/min). This extension in time provides a greater opportunity for methane to undergo purification at the exit of the adsorption column.

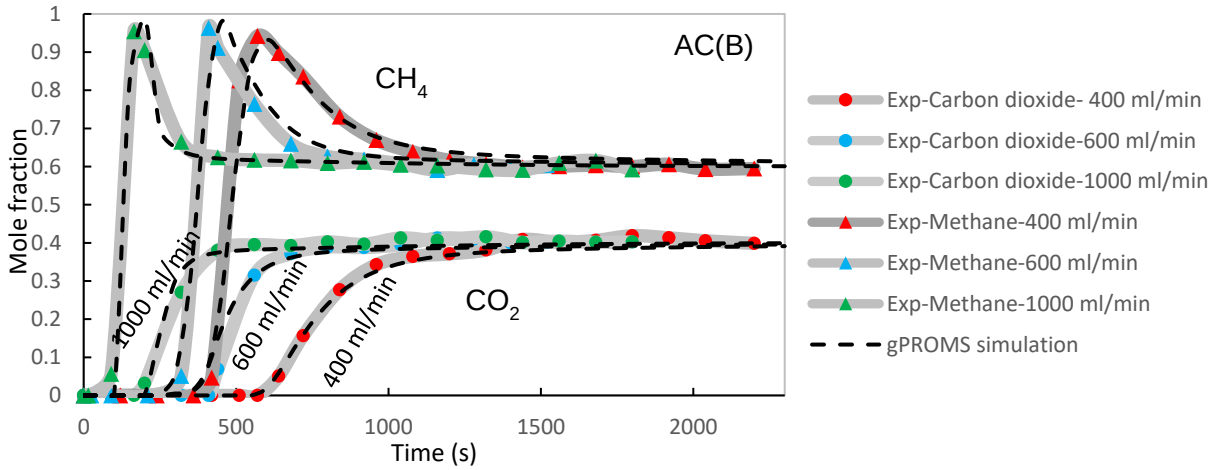

Figure 3.12 Breakthrough curve of 60% CH_4 and 40% CO_2 with AC (B) at 9 atm and 294K for feed flow rates of 400, 600, 100 ml/min. Dashed lines correspond to the simulation.

Table 3.8 Amounts adsorbed for CH_4, CO_2, selectivity, and sorbent selection parameter values as a function of feed flow rate for the separation of 60%CH_4 - 40%CO_2 with AC(B) at 9 atm and 294 K. Percent deviation (PD) of the measured values of adsorption equilibrium selectivity at 400 ml.min^{-1} , 600 ml.min^{-1} and 1000 ml.min^{-1} compared to average adsorption equilibrium selectivity are shown as PD in the table below.

Feed composition of 60%CH_4 - 40%CO2 on AC(B) at 9 atm and 294K						
Adsorbent	Flow rate (ml/min)	Gas	Adsorption breakthrough capacity (mol/kg)	Adsorption equilibrium selectivity (-)	Average (with respect different flow rates) Adsorption equilibrium selectivity (-)	Sorbent selection parameter (-)
AC(B)	400	CO_2	3.37	1.80 (PD: +%2.32) (at 400 ml/min)	1.764±0.37	3.00±0.24
AC(B)	600	CO_2	3.42	1.762 (PD: -%0.11) (at 600 ml/min)		
AC(B)	1000	CO_2	3.31	1.723 (PD: -%2.29) (at 1000 ml/min)		
AC(B)	400	CH_4	2.80			
AC(B)	600	CH_4	2.91			
AC(B)	1000	CH_4	2.88			

3.3.2.4 Comparison of breakthrough capacity to pure and binary equilibrium capacity

The breakthrough capacities, which were measured under various operating conditions and are presented in Tables 3.6, 3.7, and 3.8 and represented by cross symbols, were compared to both the capacities of individual components and the capacities predicted in binary mixtures, as depicted in Figures 3.5, 3.6, and 3.8. It's clear that the breakthrough capacities closely align with the predicted binary capacities, particularly those forecasted using TD-Sips. However, a notable difference exists between the breakthrough capacities and the capacities of the pure components, with the breakthrough capacities being considerably lower. The decrease in the breakthrough capacities can be attributed to the competitive co-adsorption of methane and

carbon dioxide within the material, and the extent of this reduction can be ascribed to the non-ideal behavior of CO_2/CH_4 mixtures.

3.4. CONCLUSIONS

This study conducted a thorough examination of the adsorption equilibria of pure and mixed CO_2 and CH_4 gases on an activated carbon AC(B). The analysis involved both experimental and simulation methods under static and dynamic conditions. Gravimetric measurements were used to determine the adsorption equilibrium data for pure gases at different temperatures and pressures, which were then fitted to temperature-dependent Sips and Langmuir models. These models were successfully employed to predict adsorption data for both pure gases and mixed components.

To assess the adsorption separation potential of the AC(B) adsorbent, breakthrough experiments were performed using a feed mixture consisting of 60% CH_4 and 40% CO_2 in a packed bed adsorption column. Various operating conditions, such as pressure, temperature, and feed flow rates, were tested. A mechanistic model representing the kinetics and dynamics of the breakthrough column was developed using gPROMS simulation software and validated with experimental breakthrough curves. The simulation results aligned well with the experimental data.

The evaluation of AC(B) adsorbent's gas separation potential involved in the determination of adsorption capacities, selectivity, sorbent selection parameter (S parameter), and the time required for methane purification at the exit of the adsorption column, from the breakthrough curves. Optimal performance was linked to the highest calculated selectivity for CO_2, sorbent selection parameter, and the duration of methane purification.

The examination of breakthrough curves revealed that to maximize the duration of methane purification, it is most favorable to conduct breakthrough experiments at higher pressures, lower temperatures, and reduced inlet feed flow rates. For example, the best condition was achieved at 9 atm pressure, 294 K temperature, and a flow rate of 400 ml/min, resulting in the longest purification time of 220 seconds.

The analysis also demonstrated that as pressure increased and temperature decreased, the adsorption capacity of both gases on the AC(B) adsorbent increased. Furthermore, the analysis highlighted that lower pressures and lower temperatures led to the highest levels of selectivity and the S parameter with the ideal corresponding operating conditions for separating

carbon dioxide from methane on AC(B) were found to be at 1 atm pressure, 294K temperature, and a flow rate of 400 ml/min.

These parameters, including selectivity, the S parameter, adsorption capacity, and purification time for methane, are valuable for the initial assessment of the adsorbent's gas separation capabilities. By considering these factors, along with operational costs, adsorbent characteristics, adsorption kinetics, and conducting simulations and pilot-scale testing, it's possible to enhance and optimize the adsorption separation process.

3.5 NOMENCLATURE

a	Empirically TD-Sips parameter	[dimensionless]
B	Adsorption affinity constant	[atm^{-1}]
B_0	Adsorption affinity constant at reference temperature	[atm^{-1}]
C_0	Inlet concentration of the gas phase	[$mol.m^{-3}$]
C_g	Concentration of the gas phase	[$mol.m^{-3}$]
C_{gin}	Feed concentration of the gas phase	[$mol.m^{-3}$]
C_{gp}	Concentration of the gas phase inside macropores	[$mol.m^{-3}$]
C_{pg}	Gas phase heat capacity	[$J.kg^{-1}.K^{-1}$]
C_{pw}	Column wall heat capacity	[$J.kg^{-1}.K^{-1}$]
C_s	Solid heat capacity	[$J.kg^{-1}.K^{-1}$]
D_c	Micropore diffusivity	[$m^2.s^{-1}$]
d_i	Column inner diameter	[m]
D_{pore}	Effective macropore diffusivity	[$m^2.s^{-1}$]
h_f	External film heat transfer coefficient	[$W.m^{-2}.K^{-1}$]
h_o	Heat transfer coefficient between column wall and ambient air	[$W.m^{-2}.K^{-1}$]
h_w	Heat transfer coefficient between the gas and the column wall	[$W.m^{-2}.K^{-1}$]
k_1	TD-Langmuir parameter	[$mmol.g^{-1}$]
k_2	TD-Langmuir parameter	[$mmol.g^{-1}\ K^{-1}$]
k_3	TD-Langmuir parameter	[atm^{-1}]
k_4	TD-Langmuir parameter	[K]
k_b	Mass transfer coefficient at the micropore mouth	[$m.s^{-1}$]
k_f	External film mass transfer coefficient	[$m.s^{-1}$]
k_{LDF}	Kinetic rate constant	[s^{-1}]
k_s	Thermal conductivity of the solid	[$W.m^{-1}.K^{-1}$]
k_w	Column wall thermal conductivity	[$W.m^{-1}.K^{-1}$]
$K_{A/B}$	Kinetic selectivity	[dimensionless]

L	Length of the adsorption column	[m]
m_A	Mass of adsorbent	[kg]
n	Sips parameter	[dimensionless]
n_0	TD-Sips reference parameter	[dimensionless]
P	Adsorption pressure	[atm]
q	Adsorption capacity in micropores	[mmol.g^{-1}]
Q	Empirical TD-Sips heat of adsorption	[kJ.mol^{-1}]
$\overline{q}$	Average adsorbed phase concentration in crystals	[mmol.g^{-1}]
$\overline{\overline{q}}$	Average adsorption capacity in the pellet	[mmol.g^{-1}]
q_e	Adsorbed amount in equilibrium with the gas in macropore	[mmol.g^{-1}]
q_s	Adsorption capacity at saturation	[mmol.g^{-1}]
q_{so}	Saturation adsorption capacity at reference temperature	[mmol.g^{-1}]
R	Universal gas constant	[m^3.Pa.K^{-1}.mol^{-1}]
R	Radial distance coordinate of adsorbent pellet	[m]
r	Radial distance coordinate of the micropore	[m]
r_c	Radius of the crystals	[m]
R_p	Radius of the pellet	[m]
S	Sorbent selection parameter	[dimensionless]
T	Temperature	[K]
T_0	Reference temperature	[K]
T_g	Gas phase temperature	[K]
T_s	Solid phase temperature	[K]
T_w	Column wall temperature	[K]
t	Time	[s]
v	Interstitial velocity	[m.s^{-1}]
$\dot{V}$	Total volumetric flow rate	[m^3.s^{-1}]
$\dot{V}_{in}$	Total inlet volumetric flow rate	[m^3.s^{-1}]
V_b	Volume of adsorption bed	[m^3]
V_{dead}	Dead volume of adsorption breakthrough system associated with tubing and fittings upstream as well as downstream of the adsorption column	[m^3]
X	TD-Sips constant	[dimensionless]
x_i	Mole fraction of component *i* in the adsorbed phase	[dimensionless]
y_i	Mole fraction of component *i* in the gas phase	[dimensionless]
z	Axial position in the column	[m]

Subscripts

A	Component with stronger adsorption
B	Component with weaker adsorption

Greek Symbols

$\alpha_{A/B}$	Gas selectivity	[dimensionless]
ΔH	Heat of adsorption	[kJ.kg^{-1}]
λ	Axial heat dispersion coefficient	[W.m^{-1}.K^{-1}]
ε_b	Bed porosity	[dimensionless]
ε_p	Pellet porosity	[dimensionless]
μ	Mean retention time	[s]
ρ_g	Gas density	[kg.m^{-3}]
ρ_p	Pellet density	[kg.m^{-3}]
ρ_s	Pellet solid density	[kg.m^{-3}]

Abbreviations

AC	Activated Carbon
$BFDM$	Backward finite difference method
$CFDM$	Centered finite difference method
CPM	Concentration pulse method
DAE	Differential algebraic equations
$DASOLV$	Differential algebraic equation solver
DSL	Dual site Langmuir model
EIA	Energy information administration
ELM	Extended Langmuir model
GC	Gas chromatograph
IEA	International energy agency
LDF	Linear driving force
MFC	Mass flow controller
MFM	Mass flow meter

MOL	Methods of lines
$OCFEM$	Orthogonal collocation finite element method
$PDAE$	Partial differential and algebraic equations
PDE	Partial differential equations
PSA	Pressure swing adsorption
TCD	Thermal conductivity detector
VSA	Vacuum swing adsorption

3.6. REFERENCES

(1) Shen, Y.; Niu, Z.; Zhang, R.; Zhang, D. Vacuum Pressure Swing Adsorption Process with Carbon Molecular Sieve for CO2 Separation from Biogas. *Journal of CO2 Utilization* 2021, *54*, 101764.

(2) Energy, Global. "CO2 status report." *IEA (International Energy Agency): Paris, France* 1030 (2019): 1031.

(3) Álvarez-Gutiérrez, N.; Gil, M. V.; Rubiera, F.; Pevida, C. Adsorption Performance Indicators for the CO2/CH4 Separation: Application to Biomass-Based Activated Carbons. *Fuel Processing Technology* 2016, *142*, 361–369.

(4) Sabouni, Rana. *Carbon dioxide adsorption by metal organic frameworks (Synthesis, Testing and Modeling)*. PhD diss., The University of Western Ontario (Canada), 2013.

(5) Rajaram, V.; Siddiqui, F. Z.; Khan, M. E. *From Landfill Gas to Energy: Technologies and Challenges*; CRC press, 2011.

(6) Rainone, F.; D'Agostino, O.; Erto, A.; Balsamo, M.; Lancia, A. Biogas Upgrading by Adsorption onto Activated Carbon and Carbon Molecular Sieves: Experimental and Modelling Study in Binary CO2/CH4 Mixture. *Journal of Environmental Chemical Engineering* 2021, *9* (5), 106256.

(7) Wilson, Sean MW. "Adsorption Separation of CO2 from CO in Syngas: Improving the Conversion of the Reverse Water Gas Shift Reaction." PhD diss., Université d'Ottawa/University of Ottawa, 2015

(8) Rocha, L. A. M.; Andreassen, K. A.; Grande, C. A. Separation of CO 2 /CH 4 Using Carbon Molecular Sieve (CMS) at Low and High Pressure. *Chemical Engineering Science* 2017, *164*, 148–157.

(9) Peredo-Mancilla, D.; Ghimbeu, C. M.; Ho, B.-N.; Jeguirim, M.; Hort, C.; Bessieres, D. Comparative Study of the CH4/CO2 Adsorption Selectivity of Activated Carbons for Biogas Upgrading. *Journal of Environmental Chemical Engineering* 2019, *7* (5), 103368.

(10) Garcia, S.; Gil, M. V.; Martín, C. F.; Pis, J. J.; Rubiera, F.; Pevida, C. Breakthrough Adsorption Study of a Commercial Activated Carbon for Pre-Combustion CO2 Capture. *Chemical Engineering Journal* 2011, *171* (2), 549–556.

(11) Rios, R. B.; Stragliotto, F. M.; Peixoto, H. R.; Torres, A. E. B.; Bastos-Neto, M.; Azevedo, D. C. S.; Cavalcante Jr, C. L. Studies on the Adsorption Behavior of CO2-CH4 Mixtures Using Activated Carbon. *Braz. J. Chem. Eng.* 2013, *30* (4), 939–951.

(12) Shao, X.; Feng, Z.; Xue, R.; Ma, C.; Wang, W.; Peng, X.; Cao, D. Adsorption of CO2, CH4, CO2/N2 and CO2/CH4 in Novel Activated Carbon Beads: Preparation, Measurements and Simulation. *AIChE J.* 2011, *57* (11), 3042–3051. https://doi.org/10.1002/aic.12515.
(13) Wu, Y.-J.; Yang, Y.; Kong, X.-M.; Li, P.; Yu, J.-G.; Ribeiro, A. M.; Rodrigues, A. E. Adsorption of Pure and Binary CO_2, CH_4, and N_2 Gas Components on Activated Carbon Beads. *J. Chem. Eng. Data* 2015, *60* (9), 2684–2693.
(14) Peng, X.; Wang, W.; Xue, R.; Shen, Z. Adsorption Separation of CH4/CO2 on Mesocarbon Microbeads: Experiment and Modeling. *AIChE J.* 2006, *52* (3), 994–1003.
(15) Yi, H.; Li, F.; Ning, P.; Tang, X.; Peng, J.; Li, Y.; Deng, H. Adsorption Separation of CO2, CH4, and N2 on Microwave Activated Carbon. *Chemical Engineering Journal* 2013, *215*–
(16) Peredo-Mancilla, D.; Ghimbeu, C. M.; Ho, B.-N.; Jeguirim, M.; Hort, C.; Bessieres, D. Comparative Study of the CH4/CO2 Adsorption Selectivity of Activated Carbons for Biogas Upgrading. *Journal of Environmental Chemical Engineering* 2019, *7* (5), 103368.
(17) Dreisbach, F.; Staudt, R.; Keller, J. U. High Pressure Adsorption Data of Methane, Nitrogen, Carbon Dioxide and Their Binary and Ternary Mixtures on Activated Carbon. 13.
(18) Grande, C. A.; Blom, R.; Möller, A.; Möllmer, J. High-Pressure Separation of CH4/CO2 Using Activated Carbon. *Chemical Engineering Science* 2013, *89*, 10–20.
(19) Himeno, S.; Komatsu, T.; Fujita, S. High-Pressure Adsorption Equilibria of Methane and Carbon Dioxide on Several Activated Carbons. *J. Chem. Eng. Data* 2005, *50* (2), 369–376.
(20) Nandi, M.; Okada, K.; Dutta, A.; Bhaumik, A.; Maruyama, J.; Derks, D.; Uyama, H. Unprecedented CO2 Uptake over Highly Porous N-Doped Activated Carbon Monoliths Prepared by Physical Activation. *Chem. Commun.* 2012, *48* (83), 10283.
(21) Zhang, X.-X.; Xiao, P.; Chen, G.-J.; Sun, C.-Y.; Yang, L.-Y. Separation of Methane and Carbon Dioxide Gas Mixtures Using Activated Carbon Modified with 2-Methylimidazole. *Chem. Eng. Technol.* 2018, *41* (9), 1818–1825.
(22) Abdullah, A.; Idris, I.; Shamsudin, I. K.; Kim, J.; Othman, M. R. Carbon Dioxide Separation from Carbon Dioxide-Methane Gas Mixture Using PSA Utilizing Inorganic and Organic Adsorbents; Penang, Malaysia, 2019; p 020058.
(23) Grande, C. A.; Blom, R.; Möller, A.; Möllmer, J. High-Pressure Separation of CH4/CO2 Using Activated Carbon. *Chemical Engineering Science* 2013, *89*, 10–20.
(24) *Professional Coal-based Spherical/Pellet Activated Carbon for Water Treatment Material(id:10767527). Buy China Water Treatment Material, High Quality Activated Carbon, Pellet Activated Carbon - EC21*. EC21, Global B2B Marketplace - Connecting Global Buyers with Manufacturers, Suppliers, Exporters worldwide. https://www.ec21.com/product-details/Professional-Coal-based-Spherical-Pellet--10767527.html (accessed 2023-07-16).
(25) Kacem, M.; Pellerano, M.; Delebarre, A. Pressure Swing Adsorption for CO 2 /N 2 and CO 2 /CH 4 Separation: Comparison between Activated Carbons and Zeolites Performances. *Fuel Processing Technology* 2015, *138*, 271–283.
(26) Chue, K. T.; Kim, J. N.; Yoo, Y. J.; Cho, S. H.; Yang, R. T. Comparison of Activated Carbon and Zeolite 13X for CO2 Recovery from Flue Gas by Pressure Swing Adsorption. *Ind. Eng. Chem. Res.* 1995, *34* (2), 591–598.
(27) Siriwardane, R. V.; Shen, M.-S.; Fisher, E. P.; Poston, J. A. Adsorption of CO_2 on Molecular Sieves and Activated Carbon. *Energy Fuels* 2001, *15* (2), 279–284.

(28) Choi, S.; Drese, J. H.; Jones, C. W. Adsorbent Materials for Carbon Dioxide Capture from Large Anthropogenic Point Sources. *ChemSusChem: Chemistry & Sustainability Energy & Materials* 2009, *2* (9), 796–854.
(29) Langmuir, I. The Adsorption of Gases on Plane Surfaces of Glass, Mica and Platinum. *Journal of the American Chemical society* 1918, *40* (9), 1361–1403.
(30) Sips, R. On the Structure of a Catalyst Surface. *The journal of chemical physics* 1948, *16* (5), 490–495.
(31) Toth, J. State Equation of the Solid-Gas Interface Layers. *Acta chim. hung.* 1971, *69*, 311–328.
(32) Li, P.; Handan Tezel, F. Pure and Binary Adsorption of Methane and Nitrogen by Silicalite. *Journal of Chemical & Engineering Data* 2009, *54* (1), 8–15.
(33) Kikkinides, E. S.; Yang, R. T.; Cho, S. H. Concentration and Recovery of Carbon Dioxide from Flue Gas by Pressure Swing Adsorption. *Industrial & Engineering Chemistry Research* 1993, *32* (11), 2714–2720.
(34) Kennedy, D. A.; Mujčin, M.; Abou-Zeid, C.; Tezel, F. H. Cation Exchange Modification of Clinoptilolite–Thermodynamic Effects on Adsorption Separations of Carbon Dioxide, Methane, and Nitrogen. *Microporous and Mesoporous Materials* 2019, *274*, 327–341.
(35) Harlick, P. J. E.; Tezel, F. H. Adsorption of Carbon Dioxide, Methane, and Nitrogen: Pure and Binary Mixture Adsorption by ZSM-5 with SiO_2/Al_2O_3 Ratio of 30. *Separation Science and Technology* 2002, *37* (1), 33–60.
(36) Malek, A.; Farooq, S. Comparison of Isotherm Models for Hydrocarbon Adsorption on Activated Carbon. *AIChE J.* 1996, *42* (11), 3191–3201.
(37) Ghalandari, V.; Hashemipour, H.; Bagheri, H. Experimental and Modeling Investigation of Adsorption Equilibrium of CH4, CO2, and N2 on Activated Carbon and Prediction of Multi-Component Adsorption Equilibrium. *Fluid Phase Equilibria* 2020, *508*, 112433.
(38) Ruthven, D. M.; Farooq, S.; Knaebel, K. S. *Pressure Swing Adsorption*; John Wiley & Sons, 1996.
(39) Rege, S. U.; Yang, R. T. A Simple Parameter for Selecting an Adsorbent for Gas Separation by Pressure Swing Adsorption. *Separation science and technology* 2001, *36* (15), 3355–3365.
(40) Ruthven, D. M. Molecular Sieve Separations. *Chemie Ingenieur Technik* 2011, *83* (1-2), 44–52.
(41) Silva, J. A. C.; Cunha, A. F.; Schumann, K.; Rodrigues, A. E. Binary Adsorption of CO2/CH4 in Binderless Beads of 13X Zeolite. *Microporous and Mesoporous Materials* 2014, *187*, 100–107.
(42) Wilkins, N. S.; Rajendran, A.; Farooq, S. Dynamic Column Breakthrough Experiments for Measurement of Adsorption Equilibrium and Kinetics. *Adsorption* 2021, *27* (3), 397–422.
(43) Shirani, B.; Eic, M. Novel Differential Column Method for Measuring Multicomponent Gas Adsorption Isotherms in NaY Zeolite. *Ind. Eng. Chem. Res.* 2017, *56* (4), 1008–1018.
(44) Brandani, F.; Ruthven, D. Measurement of Adsorption Equilibria by the Zero Length Column (ZLC) Technique Part 2: Binary Systems. *Ind. Eng. Chem. Res.* 2003, *42* (7), 1462–1469.
(45) Ruthven, D. M.; Kumar, R. An Experimental Study of Single-Component and Binary Adsorption Equilibria by a Chromatographic Method. *Ind. Eng. Chem. Fund.* 1980, *19* (1), 27–32.

(46) Kennedy, D. A.; Mujčin, M.; Alenko, T.; Tezel, F. H. Pure and Mixture Adsorption Equilibria of Methane and Nitrogen onto Clinoptilolite: Effects of Cs+ and Fe 3+ Exchanged Cations on Separation Performance. *Adsorption* 2019, *25*, 135–158.
(47) Harlick, P. J. E.; Tezel, F. H. Use of Concentration Pulse Chromatography for Determining Binary Isotherms: Comparison with Statically Determined Binary Isotherms. *Adsorption* 2003, *9*, 275–286.
(48) Rynders, R. M.; Rao, M. B.; Sircar, S. Isotope Exchange Technique for Measurement of Gas Adsorption Equilibria and Kinetics. *AIChE J.* 1997, *43* (10), 2456–2470.
(49) Bakhtyari, A.; Mofarahi, M. Pure and Binary Adsorption Equilibria of Methane and Nitrogen on Zeolite 5A. *J. Chem. Eng. Data* 2014, *59* (3), 626–639.
(50) Heymans, N.; Alban, B.; Moreau, S.; De Weireld, G. Experimental and Theoretical Study of the Adsorption of Pure Molecules and Binary Systems Containing Methane, Carbon Monoxide, Carbon Dioxide and Nitrogen. Application to the Syngas Generation. *Chemical Engineering Science* 2011, *66* (17), 3850–3858.
(51) Worch, E. *Adsorption Technology in Water Treatment: Fundamentals, Processes, and Modeling*; De Gruyter: Berlin ; Boston, 2012.
(52) Wilkins, N. S.; Sawada, J. A.; Rajendran, A. Measurement of Competitive CO 2 and H 2 O Adsorption on Zeolite 13X for Post-Combustion CO 2 Capture. *Adsorption* 2020, *26* (5), 765–779.
(53) Shafeeyan, M. S.; Wan Daud, W. M. A.; Shamiri, A. A Review of Mathematical Modeling of Fixed-Bed Columns for Carbon Dioxide Adsorption. *Chemical Engineering Research and Design* 2014, *92* (5), 961–988.
(54) Hassan, M. M.; Ruthven, D. M.; Raghavan, N. S. Air Separation by Pressure Swing Adsorption on a Carbon Molecular Sieve. *Chemical Engineering Science* 1986, *41* (5), 1333–1343.
(55) Ruthven, D. M. *Principles of Adsorption and Adsorption Processes*; John Wiley & Sons, 1984.
(56) Ko, D.; Siriwardane, R.; Biegler, L. T. Optimization of Pressure Swing Adsorption and Fractionated Vacuum Pressure Swing Adsorption Processes for CO_2 Capture. *Ind. Eng. Chem. Res.* 2005, *44* (21), 8084–8094.
(57) Qinglin, H.; Sundaram, S. M.; Farooq, S. Revisiting Transport of Gases in the Micropores of Carbon Molecular Sieves. 13.
(58) Farooq, S.; Qinglin, H.; Karimi, I. A. Identification of Transport Mechanism in Adsorbent Micropores from Column Dynamics. *Ind. Eng. Chem. Res.* 2002, *41* (5), 1098–1106.
(59) Jin, X.; Malek, A.; Farooq, S. Production of Argon from an Oxygen−Argon Mixture by Pressure Swing Adsorption. *Ind. Eng. Chem. Res.* 2006, *45* (16), 5775–5787.
(60) LeVan, M. D.; Carta, G.; Yon, C. M. Adsorption and Ion Exchange. 67.
(61) Khalighi, M.; Farooq, S.; Karimi, I. A. Nonisothermal Pore Diffusion Model for a Kinetically Controlled Pressure Swing Adsorption Process. *Ind. Eng. Chem. Res.* 2012, *51* (32), 10659–10670.
(62) Qinglin, H.; Farooq, S.; Karimi, I. A. Prediction of Binary Gas Diffusion in Carbon Molecular Sieves at High Pressure. *AIChE J.* 2004, *50* (2), 351–367.
(63) Cavenati, S.; Grande, C. A.; Rodrigues, A. E. Upgrade of Methane from Landfill Gas by Pressure Swing Adsorption. *Energy Fuels* 2005, *19* (6), 2545–2555.
(64) Canevesi, R. L. S.; Andreassen, K. A.; da Silva, E. A.; Borba, C. E.; Grande, C. A. Pressure Swing Adsorption for Biogas Upgrading with Carbon Molecular Sieve. *Ind. Eng. Chem. Res.* 2018, *57* (23), 8057–8067.

(65) Yang, R. T. *Gas Separation by Adsorption Processes*; Butterworths: Boston, 1987.
(66) Rezaei, F.; Grahn, M. Thermal Management of Structured Adsorbents in CO_2 Capture Processes. *Ind. Eng. Chem. Res.* 2012, *51* (10), 4025–4034.
(67) Gholami, M.; Talaie, M. R. Investigation of Simplifying Assumptions in Mathematical Modeling of Natural Gas Dehydration Using Adsorption Process and Introduction of a New Accurate LDF Model. *Ind. Eng. Chem. Res.* 2010, *49* (2), 838–846.
(68) Lefebvre, D.; Amyot, P.; Ugur, B.; Tezel, F. H. Adsorption Prediction and Modeling of Thermal Energy Storage Systems: A Parametric Study. *Industrial & Engineering Chemistry Research* 2016, *55* (16), 4760–4772.
(69) Harun, N.; Nittaya, T.; Douglas, P. L.; Croiset, E.; Ricardez-Sandoval, L. A. Dynamic Simulation of MEA Absorption Process for CO2 Capture from Power Plants. *International Journal of Greenhouse Gas Control* 2012, *10*, 295–309.
(70) Balaman, Ş. Y. Uncertainty Issues in Biomass-Based Production Chains. In *Decision-Making for Biomass-Based Production Chains*; Elsevier, 2019; pp 113–142.
(71) Rios, R. B.; Stragliotto, F. M.; Peixoto, H. R.; Torres, A. E. B.; Bastos-Neto, M.; Azevedo, D. C. S.; Cavalcante Jr, C. L. Studies on the Adsorption Behavior of CO2-CH4 Mixtures Using Activated Carbon. *Brazilian journal of chemical engineering* 2013, *30*, 939–951.

CHAPTER 4

Kinetic Analysis and an Initial Gas Separation Assessment of Methane and Carbon Dioxide with Carbon Molecular Sieve and Activated Carbon

A. Jahanshahi, F.H. Tezel

University of Ottawa, Department of Chemical and Biological Engineering

161 Louis Pasteur, Ottawa, Ontario, CANADA, K1N 6N5

ABSTRACT

This study investigates the kinetic behavior of methane and carbon dioxide using a commercial carbon molecular sieve CMS(C), and an activated carbon AC(B), under different temperature and pressure conditions. Moreover, it assesses the initial adsorbent performance indicator (API) for these adsorbents at various operating conditions for the removal of CO_2 from CH_4.

To determine mass uptake, measurements were conducted at different pressures and temperatures using the gravimetric method. The adsorption transport diffusivity was calculated by applying a kinetic model to the experimental mass uptake data, leading to the determination of mass transfer and diffusion coefficients. Different kinetic models were considered and fitted to the experimental mass uptake data. Through regression analysis to match the mass uptake data at different pressure intervals and temperatures, the mass transfer and diffusion coefficients of methane and carbon dioxide were obtained.

The results indicate that the carbon dioxide uptake rates were higher than methane for both adsorbents, consistently observed across various temperatures and pressures. Diffusivity and mass transfer of carbon dioxide and methane occurred at a faster rate for activated carbon compared to carbon molecular sieve. The kinetic analysis revealed that for the CMS(C), both the micropore mouth barrier and interior micropore resistance were the dominant factors affecting methane diffusion, while diffusion resistance within the pores was more dominant for CO_2. As for the AC(B), the controlling mass transfer resistance for both gases was the micropore resistance. AC(B) had the best performance for the separation of CO_2 from CH_4, at operating conditions of 9 atm, 294 K, and 400 ml/min, achieving the highest API value of 0.11.

Keywords: Kinetic analysis, adsorption mass uptake, Adsorption Performance Indicator, carbon dioxide adsorption, methane adsorption

4.1. INTRODUCTION

As global warming continues to escalate, accompanied by an accelerated depletion of fossil fuel resources, the foremost challenges confronting humanity revolve around resource scarcity and environmental degradation. Consequently, this pressing situation has served as a catalyst for steering the global energy landscape towards a cleaner, low-carbon, and renewable trajectory[1,2]. Presently, a widely held view among scientists is that the shifting climate of our planet is being influenced by human-generated greenhouse gas emissions, with carbon dioxide and methane being the primary culprits. These gases are commonly found in various gas mixtures, including natural gas, coalbed methane, biogas, and landfill gas[3]. Currently, a key objective in the global shift towards a low-carbon future involves the separation of carbon dioxide from methane, and subsequently, the storage and utilization of both gases to create valuable products. This serves as a short-term measure to address the pressing issue.

In recent decades, significant advancements in adsorption processes and the emergence of novel nanoporous materials have made physical adsorption a highly efficient and cost-effective method for separating and purifying various fluid mixtures. This includes its application in removing carbon dioxide from methane. To ensure the effective design of an adsorption separation unit and optimize system efficiency, a crucial aspect is the prior understanding of equilibrium and kinetic data for each sorbate-sorbent system. The kinetics of adsorption and desorption play a significant role in determining the duration of the adsorption/desorption cycle in a fixed-bed system, the overall efficiency of the device, and the quantity of adsorbent needed[4]. In other words, fast kinetics results in a steep breakthrough curve, while slower kinetics produces a broader breakthrough curve. A broader breakthrough curve results in a lower degree of utilization of the adsorption column and consequently increasing the length of unused adsorption unit. Addressing the impact of a broader breakthrough curve can be achieved by introducing additional adsorbent at the product end or extending the cycle time, yet with a reduced throughput per unit of adsorbent. However, both of these options necessitate an increase in the quantity of adsorbent used. Another approach to counteracting slow diffusion involves using smaller particles, but this comes with the drawback of increased pressure drop[5]. Figure 4.1[6] demonstrates the connection between mass transfer rate and adsorption breakthrough curves. The black breakthrough curve in the figure has a mass transfer coefficient 10 times lower than the green curve, 100 times lower than the blue curve, and 1000 times lower compared to the red curve. As sorption rates decrease, the breakthrough curves progressively flatten, and when the coefficient drops below a specific threshold, a spontaneous breakthrough occurs, as evidenced by the black curve.

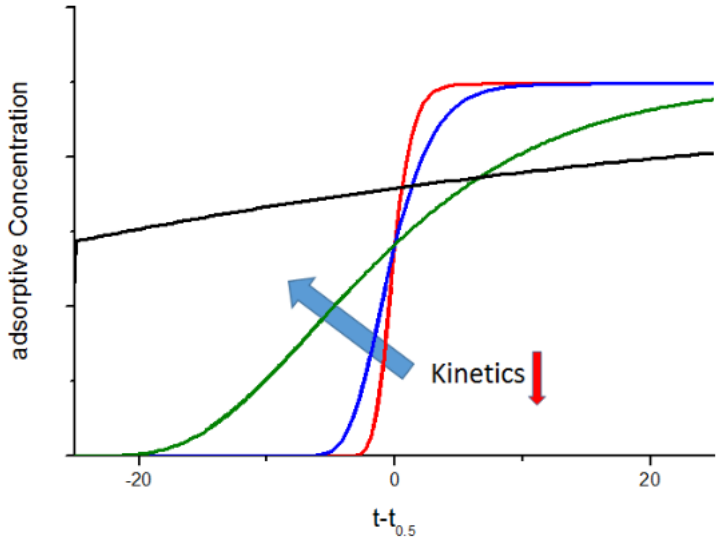

Figure 4. 1 Effect of mass transfer rate on adsorption breakthrough curves[5]

In any adsorption separation process, the choice of a suitable adsorbent is of primary importance. The selected adsorbent should exhibit appropriate selectivity, capacity, service life, and ease of regeneration[7]. Carbon-based adsorbents, such as activated carbons and carbon molecular sieves, are among the most frequently utilized materials for carbon dioxide capture. Their popularity stems from various advantages, including extensive surface areas, high micropore volumes, appropriate pore size distributions, ease of regeneration (requiring low energy and temperature), cost-effectiveness in production, abundant raw material availability, thermal stability, and responsiveness to surface modifications to enhance adsorption and hydrophobic properties[3,4,8,9]. A number of studies have reported the kinetics of methane and carbon dioxide on these adsorbents for different industrial applications[4,10–22]. When employing an adsorption separation process to separate a gas mixture, two fundamental control mechanisms come into play: equilibrium-based and kinetically based[23]. The equilibrium-based separation relies on the difference in adsorption affinities of gases on the chosen adsorbent. An example of such an adsorbent is activated carbon (AC). On the other hand, the kinetically based separation occurs due to variations in gas diffusion rates within the adsorbent. Carbon molecular sieves (CMS) serve as well-known adsorbents with distinct uptake rates for methane and carbon dioxide. Notably, carbon molecular sieve materials exhibit substantially higher carbon dioxide adsorption rates compared to methane, resulting in a kinetic effect during the adsorption separation process, facilitating the enrichment of the light product with methane[24].

Another important aspect for accurately designing, simulating, and developing an adsorption separation process is the preliminary assessment of the gas separation capabilities of the adsorbents. This evaluation should be based on readily available adsorption data, allowing for an appropriate initial selection of adsorbents. Subsequently, more extensive tests can be conducted to further explore their potential[3]. To achieve this objective, an adsorbent performance indicator (API) can be utilized, which takes into account and balances three crucial parameters: selectivity, working capacity, and the isosteric heat of adsorption[3]. The adsorbent that exhibits the most promising performance is identified based on having the highest value of API.

This study evaluates the kinetic behavior of methane and carbon dioxide on commercial carbon molecular sieve and activated carbon provided by Xebec Adsorption Inc (Blainville, Quebec, Canada) at different temperatures and over a pressure range of interest and the initial assessment of gas separation potential of the mentioned adsorbents at different operating conditions. The gravimetric method was employed to conduct mass uptake measurements at various pressures steps and temperatures. To derive the adsorption transport diffusivity from the experimental mass uptake data, a kinetic model is utilized to calculate the mass transfer and diffusion coefficients. In this study, three different kinetic models were taken into consideration and fitted to the experimental mass uptake data. By regressing the models to match the experimental mass uptake data at various pressure intervals and temperatures, the mass transfer and diffusion coefficients were determined. The obtained mass transfer and diffusivity parameters are analyzed and compared for a thorough understanding of the mass transfer mechanism and diffusion rates of the CO_2 and CH_4 within the adsorbents. API values were obtained at different operating conditions based on adsorption data reported in our previous studies (chapter 2 and 3 of this document) for adsorption equilibrium analysis and to identify the most promising adsorbent and corresponding operating conditions for the separation of carbon dioxide from methane.

4.2. METHODOLOGY

4.2.1 ADSORPTION KINETIC MEASUREMENTS

The adsorption kinetic measurements were carried out using a micro-gravimetric analyzer from VTI Corp. (Hialeah, Florida, USA). The kinetic parameters were derived from the mass uptake curves (at different pressure steps and temperatures) for pure gases, which were obtained from the generated experimental adsorption isotherm data. The experiments were conducted using a Cahn microbalance with an accuracy of ±1 μg, placed within a

stainless-steel chamber. The experimental temperature was maintained using a jacketed water bath surrounding the adsorption chamber and monitored with a thermocouple having an accuracy of ±0.01K. To regenerate the samples, high vacuum conditions were applied using a high vacuum turbo molecular pump at 573K for 12 hours.

After regeneration, the adsorbents were exposed to the sample gas and evaluated at increasing pressure levels ranging from 0 to 10 atm at various temperatures (283K, 294K, 313K, 333K). Throughout the pressure changes, the dynamic adsorption uptake was continuously monitored, and the change in sample weight over time was recorded. Equilibrium was determined to be achieved when the weight change was less than 0.015 wt%. To assess the reversibility of the adsorption process, desorption isotherms were carried out, and the sample weight change was observed during decreasing pressure steps. To correct for buoyancy, the experimental sample weight was adjusted by exposing the sample to high-purity helium at similar pressures and temperatures.

4.3 THEORETICAL BACKGROUND

4.3.1 ADSORPTION KINETIC MODELS

Adsorption kinetics is an essential element to consider when assessing adsorbent performance. The physical adsorption from the gas phase to the adsorbed phase within the solid material is restricted because of three main resistances: external surface film, macro/meso-pore resistance in the secondary pore structure and micro-pore resistance (surface barrier and pore diffusion) in the primary pore structure[22]. Drawing from previous examinations[22,25–27], it was assumed that the gas concentration within the carbon porous pellets remained consistent. Therefore, the resistance to diffusion in macro/mesopores was considered insignificant, and as a result, the surface barrier at the micropore entrance and the interior resistance within the micropores was identified as the key factor regulating the overall mass transfer rate. Utilising equilibrium adsorption data and assuming CMS and AC as a collection of identical microcrystals, multiple kinetic models were applied to match the experimental uptake data, aiming to describe the kinetic behavior of gases[22]. Models such as the linear driving force model (LDF) [28–31], Fickian diffusion model[27,32,33], and combination surface resistance/Fickian diffusion model[29,31,34,35] are used to evaluate the diffusivity of the sorbates inside the pores of the adsorbent.

4.3.1.1 Linear Driving Force Model

The linear driving force (LDF) technique, was first suggested by Gleuckauf and Coates[36]. This approach is based on the assumption of a homogeneous adsorbent medium, where the mass transfer coefficient, k_{LDF}, remains unaffected by the adsorbate concentration. To implement the LDF model, we observe the experimental pressure step change response, monitoring the average amount adsorbed, $\bar{q}(t)$ at various times t. Analyzing the change in $\bar{q}$ with respect to time yields the slope, $\frac{\overline{dq}}{dt}$, which is then plotted against $\bar{q}(t)$ for different time points. Utilizing the known value of q^* (amount adsorbed at equilibrium at the end of the step change), we can determine the specific k_{LDF}, value for the system at the specific step change.

The LDF model uses Equation 1 to relate the rate of adsorption of a single adsorbate into the particle LDF mass transfer coefficient (k_{LDF}) for the gravimetric system.

$$\frac{d\bar{q}}{dt} = k_{LDF}(q^* - \bar{q}(t)) \tag{1}$$

To compute k_{LDF} from the adsorption equilibrium data obtained from the gravimetric system, the uptake $f(t)$ for the adsorbent must be calculated from the change in weight of the sample over time as the system achieves equilibrium (Equation 2).

$$f(t) = \frac{\bar{q}(t) - q_0}{q^* - q_0} \tag{2}$$

where q^* is the adsorbate's equilibrium concentration in the adsorbed phase and q_0 is the adsorbate's concentration in the adsorbed phase before the pressure step. Equation 2 is related to Equation 3 in terms of the effective LDF mass transfer coefficient, k_{LDF}, for a constant pressure experiment. By integrating Equation 1 and changing the adsorbed phase concentration ratio to mass ratio, the following equation is derived (Equation 3):

$$f(t) = \frac{\bar{q}(t) - q_0}{q^* - q_0} = \frac{M_t}{M_\infty} = 1 - e^{(-k_{LDF}t)} \tag{3}$$

where M_t and M_∞ are the uptake amounts at time t and equilibrium, respectively. The LDF model's kinetic mass transfer coefficient, k_{LDF}, solely describes the overall particle surface resistance as a mass transfer barrier, which can be evaluated from the slope of $\ln(1 - \frac{M_t}{M_\infty})$

plotted against time according to Equation 3. In order to reflect the diffusion within the macropores and micropores of the sorbent, the LDF model may be described as an extension of the Gleuckauf approximation[32] (Equation 4).

$$\frac{1}{k_{LDF}} = \frac{R_p K}{3k_f} + \frac{R_p^2 K}{15\varepsilon_p D_p} + \frac{r_c^2}{15D_c} \tag{4}$$

where K is the Henry's law constant at low concentrations, R_p is the radius of the pellet, r_c is the radius of the crystals, k_f is the external film mass transfer coefficient, D_p is the effective macropore diffusivity, D_c is the micropore diffusivity and ε_p is the pellet void fraction. The LDF diffusion model is valid in the fractional uptake region of $\left(\frac{M_t}{M_\infty}\right) > 0.6$.

4.3.1.2 Fickian Diffusion Model

The diffusion process can also be governed by the concentration gradient through the particle according to Fick's second law that applies for unsteady state conditions. For isothermal diffusion into a spherical particle, Fick's law can be expressed as follows[31]:

$$\frac{\partial q}{\partial t} = \frac{1}{r^2}\frac{\partial}{\partial r}\left(D_c r^2 \frac{\partial q}{\partial r}\right) \tag{5}$$

The corresponding initial and boundary conditions are as follows:

$$\left(\frac{\partial q}{\partial r}\right)_{|r=0} = 0 \quad , \quad \left(q_{|r=r_c}\right) = \left(q_{e_{|r=r_c}}\right) \quad , \quad q = 0\,,\ t = 0 \tag{6}$$

Solving Equation 5 with the boundary conditions described in equation 6 results in the following solution for isothermal diffusion into a homogeneous sphere[27,31,32,37]:

$$\frac{M_t}{M_\infty} = 1 - \frac{6}{\pi^2}\sum_{n=1}^{n=\infty} \frac{e^{\left(-n^2\pi^2\frac{D_c}{r_c^2}t\right)}}{n^2} \tag{7}$$

The series in Equation 7 converges rapidly, and only a few terms can be taken as a good approximation. In the long-time region, $\left(\frac{M_t}{M_\infty}\right) > 0.6$, only the first term in the series is needed and this allows to estimate the diffusivity from a semi-logarithmic plot of $1 - \left(\frac{M_t}{M_\infty}\right)$ as a function of time.

4.3.1.3 Combined Surface Barrier/Fickian Diffusion Model

A combined surface barrier/Fickian diffusion model (CBFDM) can also be employed to examine uptake measurement findings for adsorbents with surface barrier resistance followed by diffusion inside the crystal[29,31,35]. The combined surface barrier-Fickian diffusion model can be expressed by solving Equation 5 with the following boundary condition at the crystal surface, r_c, together with other boundary conditions given at $r = 0$ and at $t = 0$ as shown in Equation 6:

$$(\frac{\partial q}{\partial r})_{|r=0} = 0 \quad , \qquad k_b(q^*(r_c,t) - q(r_c,t)) = D_c\frac{\partial q}{\partial r}(r_c,t) \quad , \quad q = 0\,,\ t = 0 \tag{8}$$

where k_b is the barrier coefficient at the micropore mouth. The solution of Equation 5 with these boundary conditions results in fractional uptake that can be expressed as follows[29,31,33,38]:

$$\frac{M_t}{M_\infty} = 1 - \sum\nolimits_{n=1}^{n=\infty} \frac{6L^2 \times e^{(-\beta_n^2\frac{D_c}{r_c^2}t)}}{\beta_n^2(\beta_n^2 + L(L-1))} \tag{9}$$

where β_n are the nonzero roots of the equation $\beta_n cot\beta_n + L - 1 =,0$ and $L = \frac{r_c^2 k_b}{3D_c}$.

In this study, $\frac{D_c}{r_c^2}$, k_{LDF}, k_b values are obtained by regressing the kinetic models to fit the uptake data at different temperatures and pressure steps. The obtained kinetic parameters are compared to gain insight into the nature of the mass transfer rate controlling mechanisms and a better understanding of interactions between sorbate molecules and active pore surfaces.

4.3.2 INITIAL GAS SEPARATION ASSESSMENT

No single parameter alone can accurately identify the best adsorbent for the specific application of CO_2/CH_4 separation. Hence, it is essential to establish a straightforward method for assessing and comparing adsorbents based on readily available adsorption data. This initial selection will then allow more extensive tests to be carried out[3]. The ideal adsorbent should possess high selectivity, a large capacity, and a low adsorption enthalpy. However, in reality, the selection of adsorbents often involves a trade-off among these factors, making it more challenging to compare them effectively. For a preliminary evaluation based on equilibrium adsorption data, it is beneficial to define a simple parameter. Therefore, the following adsorbent performance indicator (API)[39] has been estimated, which balances the three aforementioned

parameters (equilibrium selectivity, $\alpha_{A/B}$, working capacity, WC, and isosteric heat of adsorption, ΔH)[3,39].

$$API = \frac{(\alpha_{A/B}-1)^{a} WC_A{}^{b}}{|\Delta H_A|^{c}} \quad (10)$$

In Eq. 10, the subscript "A" represents the most adsorbed species (in our case CO_2). The working capacity is determined by subtracting the quantity adsorbed at high-pressure adsorption from the quantity adsorbed at low-pressure desorption. The reason why the isosteric heat of adsorption of the strongly adsorbed component, ΔH_A, is in the denominator is that the heat generated during adsorption negatively impacts the process performance. To customize the API (adsorbent performance indicator) for each separation process, exponents (a, b, and c) were introduced as real numbers to adjust the relative significance of each factor. Initially, all exponents are set to 1, and then they can be fine-tuned based on the objectives of the separation process. The authors[39] that proposed the API parameter suggested different values for the exponents based on different scenarios. They have suggested , where CO_2 is present in large mole fractions and the primary goal is bulk removal, the working capacity holds greater importance therefore b=2 ,a=0.5 and c=1, whereas in situations where the goal is to achieve a high purity and recovery rate for CH_4, selectivity ,working capacity and heat of adsorption all become important. hence in this scenario a= b=c=1[39] .

In this study, one important objective is to identify the adsorbent that has better capabilities of bulk removal of CO_2 from CH_4 and achieving a high purity and recovery rate for methane and ease of regeneration; thus, having a good working capacity and a high selectivity and low heat of adsorption are all important. In this scenario, as suggested by the authors that proposed the API parameter[39], values of 1 have been applied to all three exponents. The exponents (a, b, c) are not constrained within a specific range, and, ultimately, the user has the discretion to assign values to them based on their specific application.

4.4. RESULTS AND DISCUSSION

Mass uptakes were measured at different temperatures (283, 294, 313, and 333 K) and pressure steps (0.35-0.45, 1.4-2.4, 3.2-3.8, 5.8-7.7, 7.7-9.6 atm) for CMS(C) and AC(B) for CO_2 and CH_4 gases. An example of the experimental mass uptakes and fitted kinetic models for carbon dioxide and methane on CMS(C) and AC(B) at ΔP= 5.8 – 7.7 atm and 294 K can be seen in figure 4.2. Results indicate that the uptake rate of carbon dioxide is faster than

methane with both carbon molecular sieve and activated carbon as it reaches equilibrium more rapidly. The same was observed at different pressure steps and temperatures.

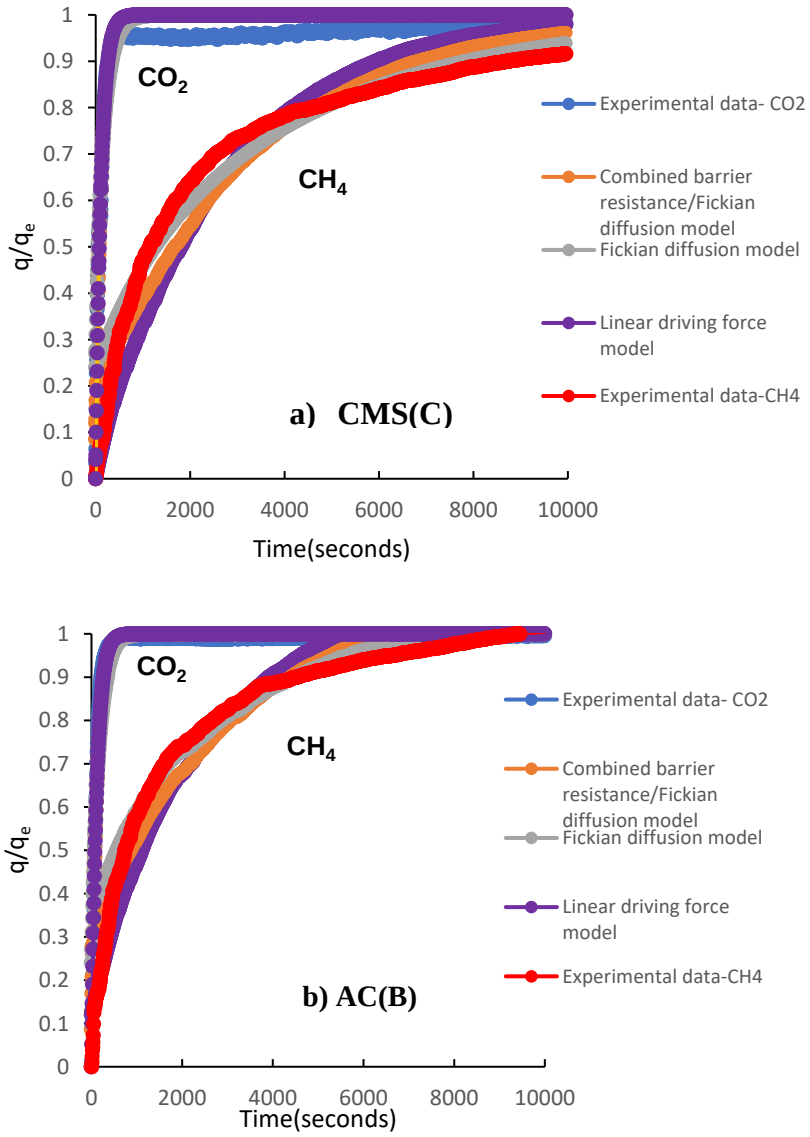

Figure 4.2 Experimental mass uptakes and fitted kinetic models of carbon dioxide and methane on (a) CMS(C) and (b) AC(B) at ΔP= 5.8 – 7.7 atm and 294 K. Note: in the figure, there is an overlap between the different kinetic models specifically for CO_2.

The CMS(C) sample exhibited a very slow methane adsorption rate at every pressure step, leading to a significant amount of time required to achieve equilibrium, particularly at low pressures where it took more than 120 hours to reach equilibrium. This slow diffusion rate of methane is evident in Figure 4.2 (a), as equilibrium was not fully attained after 10,000 seconds. In contrast, carbon dioxide reached equilibrium much more rapidly. Knowing that

mass transfer mechanism is kinetically controlled within the carbon molecular sieves, the variation in adsorption rates can be attributed to the difference in the size of molecules and micropore mouths(acting as a barrier and limiting methane diffusion), as well as the influence of electrostatic properties and molecular shape, affecting sorption kinetics[18]. Similar trends were observed for carbon dioxide and methane on the activated carbon sample, but with diffusion rates of a greater magnitude when compared to the carbon molecular sieve. This higher rate of diffusion for AC(B) can be observed by comparing Figure 4.2 (a) and (b) as both methane and carbon dioxide reach equilibrium faster and within the time interval of 0 to 10000 seconds for this adsorbent. As depicted in Figure 4.2, the kinetic models displayed a reasonably good fit to the experimental mass uptake data at lower fractional coverage. However, as the fractional coverage increased, specifically for CH_4, the models tended to deviate more from the experimental data. The models predict CH_4 reaching equilibrium earlier than what is actually observed in the experiments. These results suggests that more resistance is happening within the micropores that the models were not able to predict.

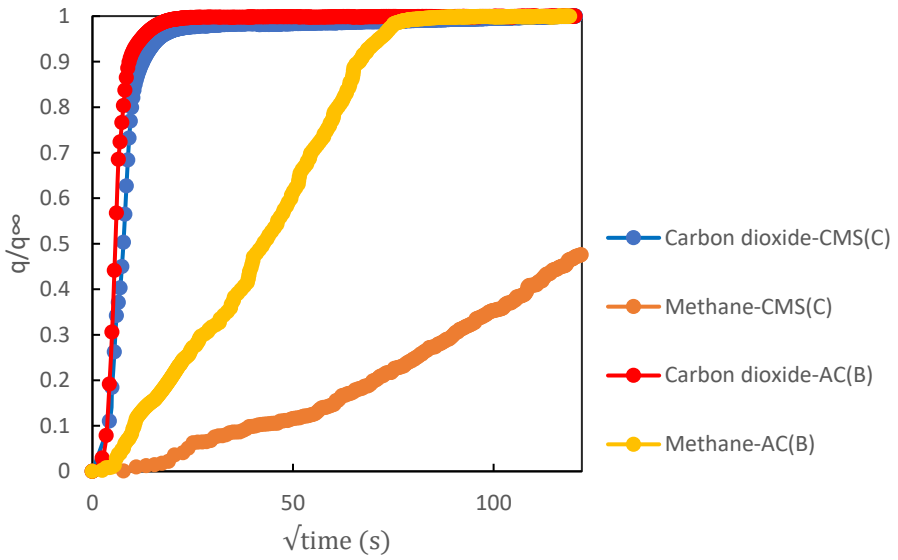

Figure 4.3 Experimental mass uptakes as function of square root of time of carbon dioxide and methane on CMS(C) and AC(B) at ΔP= 1.4 – 2.4 atm and 294 K

The uptake curves can be graphed against the square root of time to provide a clearer depiction of the initial uptake behavior[7,38,40]. This graph enables a qualitative assessment of mass transfer resistance: in a micropore-controlled system, the initial uptake will exhibit a linear trend and convex upward for the entire range when plotted against the square root of time, whereas a system with substantial barrier resistance (whether it's a surface barrier resistance or a combined surface barrier and a micropore resistance) experiences a shift in shape from being concave to becoming convex (sigmoidal shape). [40,41].

An example of this can be seen in Figure 4.3, illustrating the kinetic behavior of methane and carbon dioxide on CMS(C) and AC(B) for a pressure change of going from 1.4 to 2.4 atm at 294 K. Within the CMS(C) adsorbent, we observe that the initial uptake of CO_2 follows a linear trend, signifying that micropore resistance plays a more dominant role than the barrier resistance at the micropore entrance. This is further substantiated by examining the larger values of $\frac{D_c}{r_c^2}$ and k_b for CO_2 in Figure 4.4(c), (e), and (g), which indicate that CO_2 can diffuse through the CMS(C) structure with relatively less restriction to its movement. In contrast, the initial uptake curve for CH_4 adsorption exhibits a sigmoidal tendency, with a small slope followed by a turning point, indicating the presence of a strong barrier resistance. This is also supported by the lower k_b values for CH_4 compared to CO_2, as evident in Figures 4.4(g) and (h). The existence of a barrier resistance suggests that the adsorbent contains a constriction approximately the size of the methane molecular diameter (3.8 Å), significantly impeding the rate of diffusion. As the fractional uptake increases, the curve transitions towards linearity, indicating a growing influence of micropore resistance as the adsorbent approaches' saturation. Overall, the diffusion of methane is affected by both micropore resistance and the surface barrier at the micropore entrance.

Regarding the AC(B) sample, As can be seen from figure 4.3, the uptakes of both CO_2 and CH_4 follow a linear trend, indicating that controlling mass transfer resistance for both gases is the micropore resistance. This suggests that there are no surface barriers for either methane or carbon dioxide as they diffuse into the micropores of the adsorbent. This was further confirmed by observing high values of k_b for both gases on the AC(B). Additionally, another contributing factor is that AC(B) functions as an equilibrium-based adsorbent, which differs from CMS(C). Unlike CMS(C), the micropore entrances in AC(B) are not specifically designed to restrict the passage of methane or carbon dioxide. As a result, both adsorbates can diffuse through the micropores of the adsorbent without any restrictions at the micropore entrance. This can be confirmed with higher amounts of methane and carbon dioxide adsorbed on AC(B) compared to CMS(C) shown in pure adsorptions isotherms in chapters 2 and 3.

Linear driving force mass transfer coefficient (k_{LDF}), diffusional time constant ($\frac{D_c}{r_c^2}$), and mass transfer coefficient at the micropore mouth (k_b) of methane and carbon dioxide for different kinetic models were obtained at different temperatures and pressure steps and can be seen in Figure 4.4 for CMS(C) and ($\frac{D_c}{r_c^2}$) and k_{LDF} values for activated carbon in Figure 4.5.

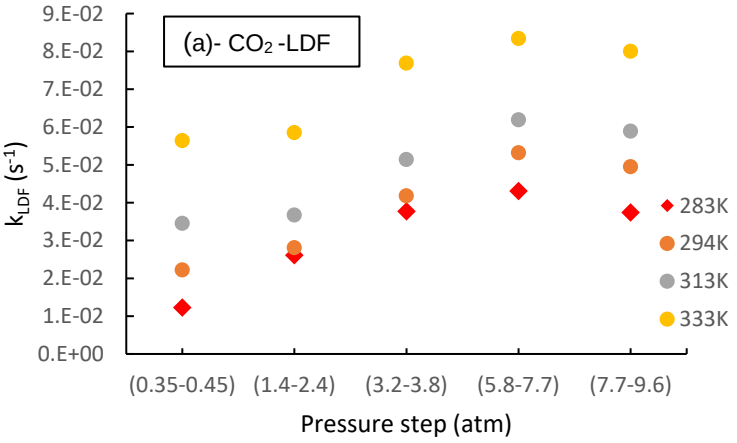
(a)- CO2 -LDF
9.E-02
8.E-02
7.E-02
6.E-02
5.E-02
4.E-02
3.E-02
2.E-02
1.E-02
0.E+00
kLDF (s-1)
283K
294K
313K
333K
(0.35-0.45)
(1.4-2.4)
(3.2-3.8)
(5.8-7.7)
(7.7-9.6)
Pressure step (atm)

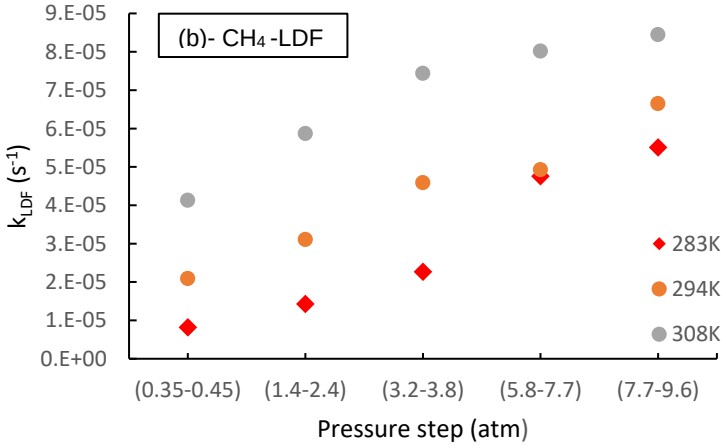
(b)- CH4 -LDF
9.E-05
8.E-05
7.E-05
6.E-05
5.E-05
4.E-05
3.E-05
2.E-05
1.E-05
0.E+00
kLDF (s-1)
283K
294K
308K
(0.35-0.45)
(1.4-2.4)
(3.2-3.8)
(5.8-7.7)
(7.7-9.6)
Pressure step (atm)

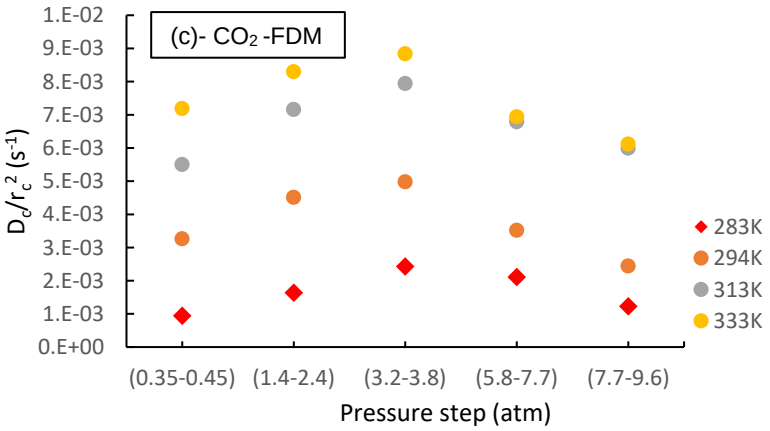
(c)- CO2 -FDM
1.E-02
9.E-03
8.E-03
7.E-03
6.E-03
5.E-03
4.E-03
3.E-03
2.E-03
1.E-03
0.E+00
Dc/rc2 (s-1)
283K
294K
313K
333K
(0.35-0.45)
(1.4-2.4)
(3.2-3.8)
(5.8-7.7)
(7.7-9.6)
Pressure step (atm)

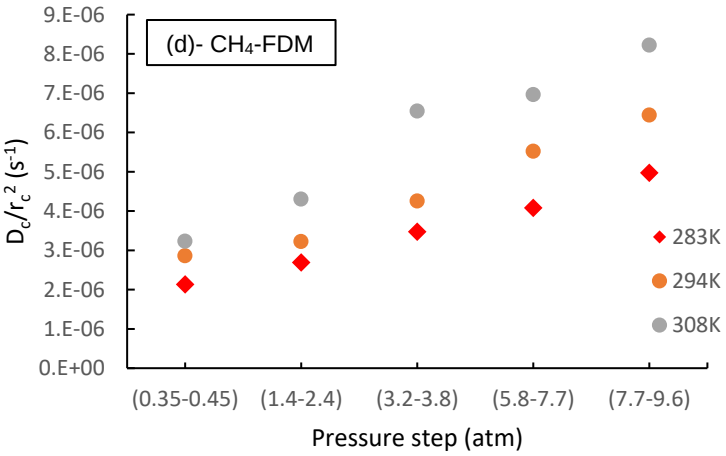
(d)- CH4-FDM
9.E-06
8.E-06
7.E-06
6.E-06
5.E-06
4.E-06
3.E-06
2.E-06
1.E-06
0.E+00
Dc/rc2 (s-1)
283K
294K
308K
(0.35-0.45)
(1.4-2.4)
(3.2-3.8)
(5.8-7.7)
(7.7-9.6)
Pressure step (atm)

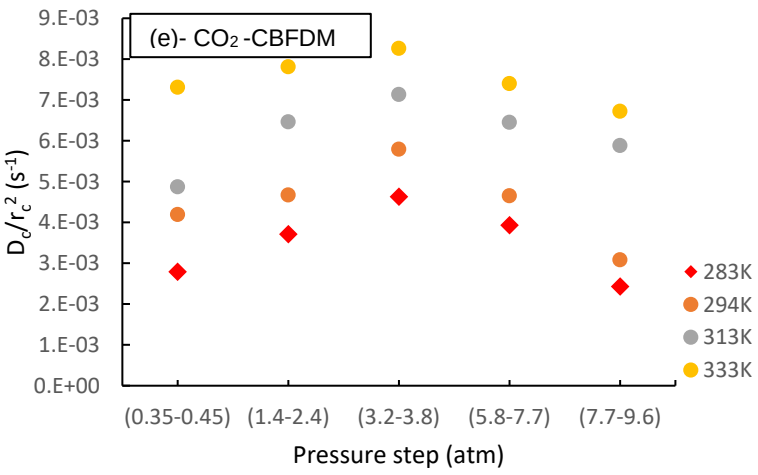
(e)- CO2 -CBFDM
9.E-03
8.E-03
7.E-03
6.E-03
5.E-03
4.E-03
3.E-03
2.E-03
1.E-03
0.E+00
Dc/rc2 (s-1)
283K
294K
313K
333K
(0.35-0.45)
(1.4-2.4)
(3.2-3.8)
(5.8-7.7)
(7.7-9.6)
Pressure step (atm)

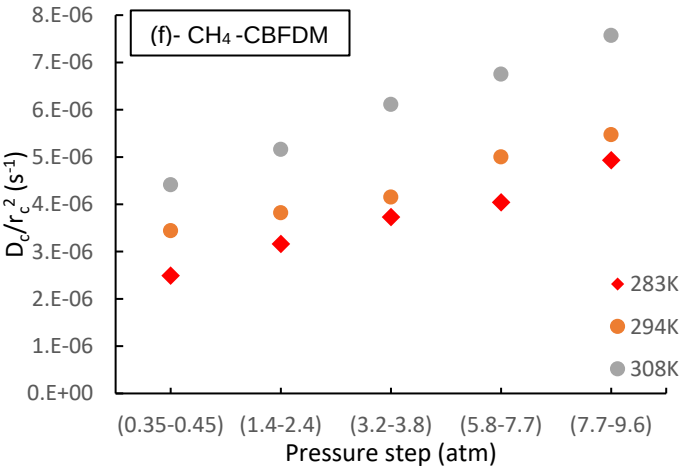
(f)- CH4 -CBFDM
8.E-06
7.E-06
6.E-06
5.E-06
4.E-06
3.E-06
2.E-06
1.E-06
0.E+00
Dc/rc2 (s-1)
283K
294K
308K
(0.35-0.45)
(1.4-2.4)
(3.2-3.8)
(5.8-7.7)
(7.7-9.6)
Pressure step (atm)

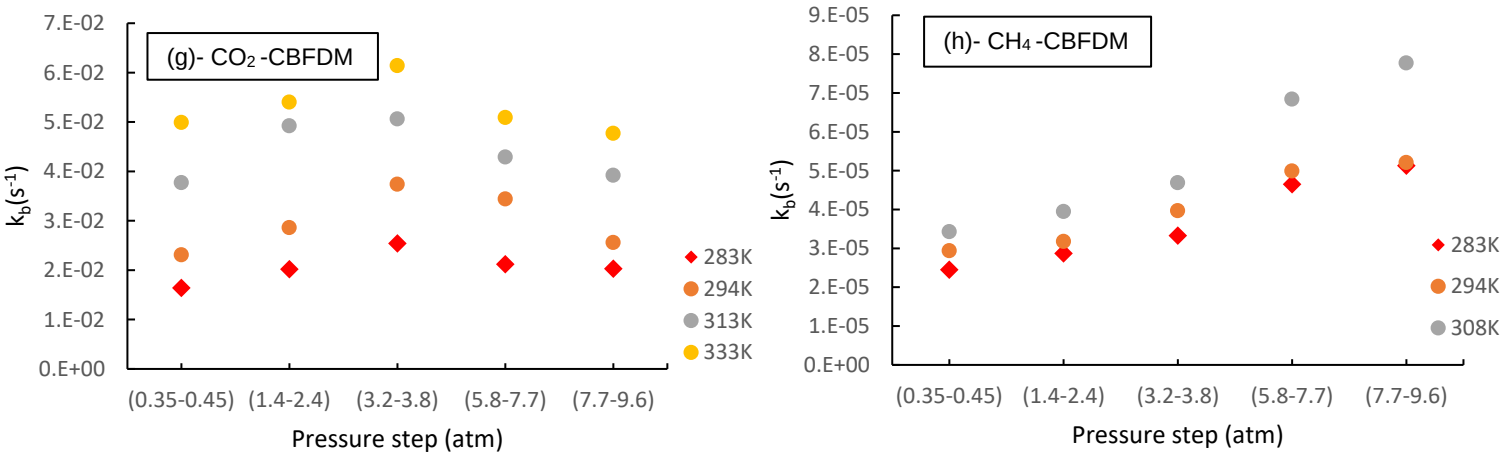

Figure 4.4 Linear driving force mass transfer coefficient (a: CO_2 and b: CH_4), Diffusional time constant for Fickian diffusion model (c: CO_2 and d: CH_4), Diffusional time constant for Combined surface barrier/Fickian diffusion model (e: CO_2 and f: CH_4) and mass transfer coefficient at the micropore mouth (g: CO_2 and h: CH_4) for combined surface barrier/Fickian diffusion model of methane and carbon dioxide on carbon molecular sieve at different pressure steps and temperatures.

The findings reveal that the mass transfer and diffusional parameters for carbon dioxide on CMS increase until approximately 4 atm, after which they start declining indicating that the adsorbent is approaching its saturation limit. Consequently, both the surface and pore diffusion resistance are increased, leading to a more restricted mass transfer of the CO_2 molecules into and within the pores. Furthermore, the results indicate that these parameters increase with rising temperatures. For methane it was observed that the mass transfer and diffusion parameters increase steadily with the increase in pressure and temperature. At elevated temperatures, methane molecules possess greater kinetic energy, allowing them to pass through the energy barrier at the pore mouth with reduced resistance and enabling faster diffusion into the pores[21].

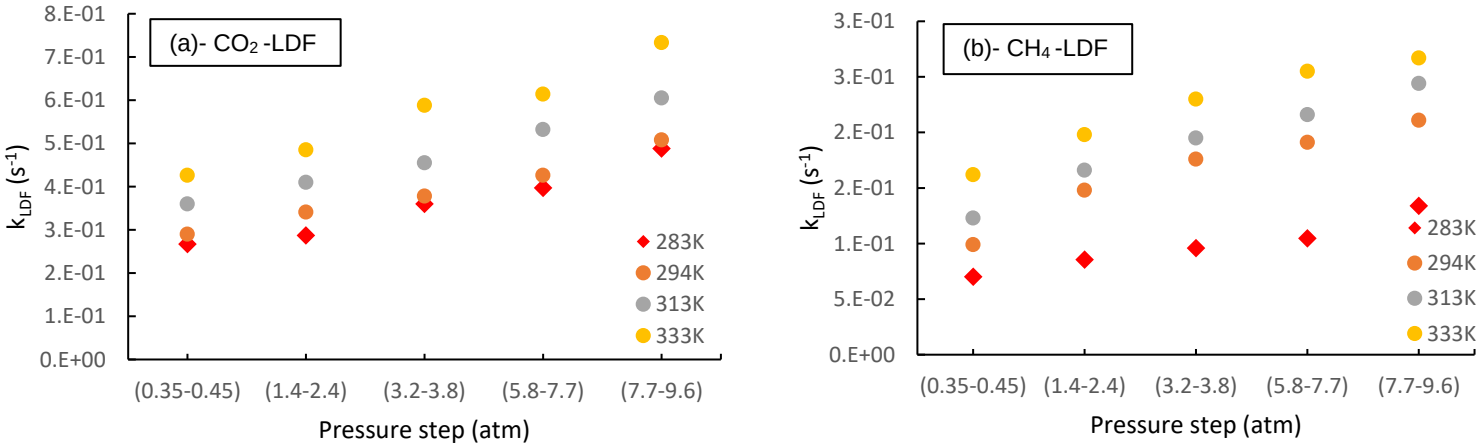

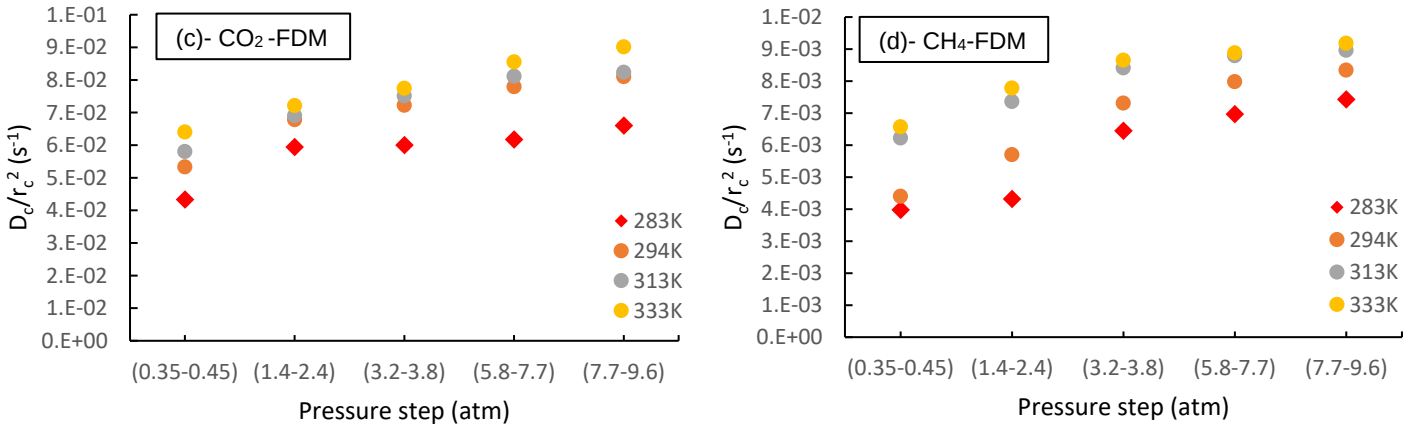

Figure 4.5 Linear driving force mass transfer coefficient (a: CO_2 and d: CH_4) and diffusional time constant for Fickian diffusion model (c: CO_2 and d: CH_4) of methane and carbon dioxide on activated carbon at different temperatures and pressure steps.

The activated carbon sample was subjected to the same analysis, and the outcomes reveal an increase in the mass transfer and diffusivity parameters ($\frac{D_c}{r_c^2}$, k_{LDF}) for both carbon dioxide and methane as the pressure and temperature increased. As previously mentioned, observing high values of k_b for both CO_2 and CH_4 led to this conclusion that entrance of the micropores of AC(B) do not act as resistance for mass transfer, and therefore combined surface barrier/Fickian diffusion model was not considered for evaluation for this adsorbent and not shown in the figures. Upon evaluating the mass uptake data and the extracted mass transfer and diffusivity parameters, it was observed that the diffusivity and mass transfer of carbon dioxide and methane occurred at a faster rate in activated carbon compared to carbon molecular sieves. As a result, activated carbon proves to be a more suitable adsorbent for reducing the time taken for adsorption/desorption cycles in industrial adsorption separation processes.

The API parameter values were calculated based on data obtained from our adsorption breakthrough and gravimetric experiments and from simulations, in our previous studies and are reported in tables 4.1, 4.2 and 4.3. The average heat of adsorption values reported in Chapters 2 and 3, for CO_2 with the CMS(C) and AC(B) adsorbents were 27.5 kJ/mol and 22.5 kJ/mol, respectively, while for CH_4, the average heat of adsorption with CMS(C) and AC(B) were 14.4 1 kJ/mol and 18.1 kJ/mol, respectively. This study utilized binary adsorption equilibrium data from the TD-Sips model to calculate working capacities across at total pressures of (1, 5, 9 atm) and temperatures of (294K, 313K, 333K) for a gas mixture composition of 40% CO_2 and 60% CH_4. The desorption pressure of 0.1 atm was chosen based on the achievable vacuum level of the pump for all the adsorption pressures.

Table 4.1 Amounts adsorbed of CH_4, CO_2, working capacity, equilibrium selectivity and API parameter values at different pressures for the separation of 60%CH_4 - 40%CO_2 on CMS(C) and AC(B) at 294K and inlet flow rate of 400 ml/min.
AC(B): red frame, CMS(C): blue frame

Feed composition of 60%CH_4 - 40%CO2 at 294K and inlet flow rate of 400 ml/min						
Adsorbent	Pressure (atm)	Component	Adsorption breakthrough capacity (mol/kg)	Working capacity (mol/kg)	Adsorption equilibrium selectivity (-)	API
CMS(C)	1	CO_2	1.13	0.67	3.09 (1 atm)	0.052 (1 atm)
CMS(C)	5	CO_2	1.51	1.31	2.20 (5atm)	0.059 (5atm)
CMS(C)	9	CO_2	1.54	1.42	1.94 (9 atm)	0.05 (9 atm)
CMS(C)	1	CH_4	0.54	0.26	---	---
CMS(C)	5	CH_4	1.03	0.66	---	---
CMS(C)	9	CH_4	1.19	0.81	---	---
AC(B)	1	CO_2	1.33	0.87	2.11 (1atm)	0.04 (1 atm)
AC(B)	5	CO_2	2.84	2.55	1.88 (5atm)	0.09 (5atm)
AC(B)	9	CO_2	3.37	3.17	1.80 (9atm)	0.11 (9 atm)
AC(B)	1	CH_4	0.94	0.46	---	---
AC(B)	5	CH_4	2.26	1.47	---	---
AC(B)	9	CH_4	2.80	1.90	---	---

Table 4.2 Amounts adsorbed of CH_4, CO_2, working capacity, equilibrium selectivity and API parameter values at different temperatures pressure for the separation of 60%CH_4 - 40%CO_2 on CMS(C) and AC(B) at 9 atm and inlet flow rate of 400 ml/min. AC(B): red frame, CMS(C): blue frame

Feed composition of 60%CH_4 - 40%CO2 at 9 atm and inlet flow rate of 400 ml/min						
Adsorbent	Temperature (K)	Component	Adsorption breakthrough capacity (mol/kg)	Working capacity (mol/kg)	Adsorption equilibrium selectivity (-)	API
CMS(C)	294	CO_2	1.54	1.42	1.94 (294 K)	0.050 (294 K)
CMS(C)	313	CO_2	1.33	1.22	1.74 (313 K)	0.033 (313 K)
CMS(C)	333	CO_2	1.15	1.05	1.57 (333 K)	0.022 (333 K)
CMS(C)	294	CH_4	1.19	0.81	---	---
CMS(C)	313	CH_4	1.14	0.79	---	---
CMS(C)	333	CH_4	1.09	0.76	---	---
AC(B)	294	CO_2	3.37	3.17	1.80 (294 K)	0.11 (294 K)
AC(B)	313	CO_2	2.80	2.63	1.72 (313 K)	0.083 (313 K)
AC(B)	333	CO_2	2.28	2.15	1.64 (333 K)	0.060 (333 K)
AC(B)	294	CH_4	2.80	1.90	---	---
AC(B)	313	CH_4	2.44	1.65	---	---
AC(B)	333	CH_4	2.08	1.42	---	---

According to the API values reported in these tables and given the fact the most promising separation performance corresponds to the adsorbent with the highest calculated API values, it was found that the AC(B) with operating conditions of 9 atm, 294 K, 400 ml/min had the best performance for the separation of CO_2 from CH_4 with an API value of 0.11. Álvarez-Gutiérrez et al[3], obtained API parameter for two activated carbon, namely CS-CO2 and CS-H2O with the highest value of 1.27 obtained for a binary mixture of 50% CO_2 and 50% CH_4 at 303K , 30 mL/min (STP) ,and 1000kPA with exponents given a value of : a=1, b=2, c=1.

After initially identifying the most effective adsorbent based on API values, more thorough testing, and computational modeling can be carried out to examine the influence of additional factors such as the production cost of the adsorbent, energy requirements for

regeneration and pressurization, diffusivity etc. to have a more detailed comparison of the materials.

4.4. CONCLUSIONS

This research examines the kinetic behavior of methane and carbon dioxide using commercial carbon molecular sieve and activated carbon under varying temperatures and pressure steps. Additionally, the initial gas separation potential of the mentioned adsorbents is evaluated under different operational conditions for the separation of CO_2 from CH_4.

Mass uptake measurements were conducted at various pressures using the gravimetric method. The adsorption transport diffusivity was determined by applying a kinetic model to the experimental mass uptake data, which allowed for the calculation of mass transfer and diffusion coefficients. Three different kinetic models (linear driving force, Fickian diffusion and combined surface barrier/Fickian diffusion) were considered and fitted to the experimental mass uptake data. Through regression analysis to match the mass uptake data at different temperatures and pressure intervals, the mass transfer and diffusion coefficients were determined.

The obtained mass transfer and diffusivity parameters are thoroughly analyzed and compared to gain a comprehensive understanding of the mass transfer mechanism and diffusion rates of CO_2 and CH_4 within the adsorbents. Results reveal that uptake rates of carbon dioxide were higher than methane with both adsorbents considered in this work. This was consistent throughout different temperatures and pressures. Mass transfer and diffusivity parameters (k_{LDF}, ($\frac{D_c}{r_c^2}$), and k_b) of methane and carbon dioxide increased with the increase in pressure and temperature for both adsorbents with the exception of CO_2 for CMS(C) as these parameters increased to a certain pressure then showed a decreasing trend confirming that the adsorbent is reaching saturation. Diffusivity and mass transfer rates of carbon dioxide and methane were faster in activated carbon compared to carbon molecular sieves, making AC(B) a more ideal adsorbent for reduced adsorption/desorption time cycles in adsorption separation processes. The kinetic analysis also demonstrated that in the CMS(C), both micropore mouth barrier and micropore resistance was the dominant resistance to methane diffusion and diffusion resistance inside the pores was the more dominant for the CO_2. As for the AC(B), the controlling mass transfer resistance for both gases was the micropore resistance. To initially evaluate the gas separation potential of the adsorbents, API values were obtained at various operational conditions based on adsorption data from our previous studies and the results were compared

to identify the more promising adsorbent with the corresponding operational conditions for the separation of carbon dioxide from methane. It was found that AC(B) with an operating condition of 9 atm, 294 K, 400 ml/min had the best performance for the separation of CO_2 from CH_4 , as it achieved the highest API value of 0.11 in this study.

.

4.5 NOMENCLATURE

$\boldsymbol{D_c}$	Micropore diffusivity	[$m^2.s^{-1}$]
$\boldsymbol{D_{pore}}$	Effective macropore diffusivity	[$m^2.s^{-1}$]
$\boldsymbol{k_b}$	Mass transfer coefficient at the micropore mouth	[$m.s^{-1}$]
$\boldsymbol{k_f}$	External film mass transfer coefficient	[$m.s^{-1}$]
$\boldsymbol{k_{LDF}}$	Kinetic rate constant for linear driving force model	[s^{-1}]
$\boldsymbol{K}$	Henry's law constant at low concentrations	[dimensionless]
$\boldsymbol{M_t}$	Uptake amount at time t	[$mmol.g^{-1}$]
$\boldsymbol{M_\infty}$	Uptake amount at equilibrium	[$mmol.g^{-1}$]
$\boldsymbol{q}$	Adsorption capacity in micropores	[$mmol.g^{-1}$]
$\boldsymbol{\bar{q}}$	Average amount adsorbed within the adsorbent	[$mmol.g^{-1}$]
$\boldsymbol{q^*}$	Average amount adsorbed at equilibrium	[$mmol.g^{-1}$]
$\boldsymbol{q_0}$	Amount adsorbed before the pressure step	[$mmol.g^{-1}$]
$\boldsymbol{r}$	Radial distance coordinate of the micropore	[m]
$\boldsymbol{r_c}$	Radius of the crystals	[m]
$\boldsymbol{Rp}$	Radius of the pellet	[m]
$\boldsymbol{t}$	Time	[s]

Greek Symbols

$\boldsymbol{\alpha_{A/B}}$	Gas selectivity	[dimensionless]
$\boldsymbol{\Delta H}$	Heat of adsorption	[$kJ.kg^{-1}$]
$\boldsymbol{\Delta q}$	Working Capacity	[$mol.kg^{-1}$]
$\boldsymbol{\varepsilon_p}$	Pellet porosity	[dimensionless]

Abbreviations

AC	Activated carbon
API	Adsorbent performance indicator
$CBFDM$	Combined surface barrier/Fickian diffusion model
CMS	Carbon molecular sieve
FDM	Fickian diffusion model
LDF	Linear driving force

4.6. REFERENCES

(1) Shen, Y.; Niu, Z.; Zhang, R.; Zhang, D. Vacuum Pressure Swing Adsorption Process with Carbon Molecular Sieve for CO2 Separation from Biogas. *Journal of CO2 Utilization* 2021, *54*, 101764.

(2) IEA, I. Global Energy & CO2 Status Report. *Technical Report* 2019.

(3) Álvarez-Gutiérrez, N.; Gil, M. V.; Rubiera, F.; Pevida, C. Adsorption Performance Indicators for the CO2/CH4 Separation: Application to Biomass-Based Activated Carbons. *Fuel Processing Technology* 2016, *142*, 361–369.

(4) Rainone, F.; D'Agostino, O.; Erto, A.; Balsamo, M.; Lancia, A. Biogas Upgrading by Adsorption onto Activated Carbon and Carbon Molecular Sieves: Experimental and Modelling Study in Binary CO2/CH4 Mixture. *Journal of Environmental Chemical Engineering* 2021, *9* (5), 106256.

(5) Knaebel, K. S. Adsorbent Selection. *Accessed on* 2011, *6* (8).

(6) *Kinetics | Dynamic Sorption, Breakthrough Curve Measurement, mixSorb, dynaSorb BT*. https://www.dynamicsorption.com/dynamic-sorption-method/kinetics/ (accessed 2023-07-20).

(7) Rocha, L. A. M.; Andreassen, K. A.; Grande, C. A. Separation of CO 2 /CH 4 Using Carbon Molecular Sieve (CMS) at Low and High Pressure. *Chemical Engineering Science* 2017, *164*, 148–157. https://doi.org/10.1016/j.ces.2017.01.071.

(8) Peredo-Mancilla, D.; Ghimbeu, C. M.; Ho, B.-N.; Jeguirim, M.; Hort, C.; Bessieres, D. Comparative Study of the CH4/CO2 Adsorption Selectivity of Activated Carbons for Biogas Upgrading. *Journal of Environmental Chemical Engineering* 2019, *7* (5), 103368.

(9) Garcia, S.; Gil, M. V.; Martín, C. F.; Pis, J. J.; Rubiera, F.; Pevida, C. Breakthrough Adsorption Study of a Commercial Activated Carbon for Pre-Combustion CO2 Capture. *Chemical Engineering Journal* 2011, *171* (2), 549–556.

(10) Qinglin, H.; Sundaram, S. M.; Farooq, S. Revisiting Transport of Gases in the Micropores of Carbon Molecular Sieves. 13.

(11) Grande, C. A.; Lopes, F. V.; Ribeiro, A. M.; Loureiro, J. M.; Rodrigues, A. E. Adsorption of Off-gases from Steam Methane Reforming (H2, CO2, CH4, CO and N2) on Activated Carbon. *Separation Science and Technology* 2008, *43* (6), 1338–1364.

(12) Reid, C. R.; Thomas, K. M. Adsorption of Gases on a Carbon Molecular Sieve Used for Air Separation: Linear Adsorptives as Probes for Kinetic Selectivity. *Langmuir* 1999, *15* (9), 3206–3218.

(13) Jribi, S.; Miyazaki, T.; Saha, B. B.; Pal, A.; Younes, M. M.; Koyama, S.; Maalej, A. Equilibrium and Kinetics of CO2 Adsorption onto Activated Carbon. *International Journal of Heat and Mass Transfer* 2017, *108*, 1941–1946.

(14) Shen, C.; Grande, C. A.; Li, P.; Yu, J.; Rodrigues, A. E. Adsorption Equilibria and Kinetics of CO2 and N2 on Activated Carbon Beads. *Chemical Engineering Journal* 2010, *160* (2), 398–407.

(15) Lopes, F. V.; Grande, C. A.; Ribeiro, A. M.; Loureiro, J. M.; Evaggelos, O.; Nikolakis, V.; Rodrigues, A. E. Adsorption of H2, CO2, CH4, CO, N2 and H2O in Activated Carbon and Zeolite for Hydrogen Production. *Separation Science and Technology* 2009, *44* (5), 1045–1073.

(16) Saha, D.; Deng, S. Adsorption Equilibrium and Kinetics of CO2, CH4, N2O, and NH3 on Ordered Mesoporous Carbon. *Journal of colloid and interface science* 2010, *345* (2), 402–409.

(17) Park, Y.; Moon, D.-K.; Park, D.; Mofarahi, M.; Lee, C.-H. Adsorption Equilibria and Kinetics of CO2, CO, and N2 on Carbon Molecular Sieve. *Separation and Purification Technology* 2019, *212*, 952–964.

(18) Canevesi, R. L. S.; Andreassen, K. A.; da Silva, E. A.; Borba, C. E.; Grande, C. A. Pressure Swing Adsorption for Biogas Upgrading with Carbon Molecular Sieve. *Ind. Eng. Chem. Res.* 2018, *57* (23), 8057–8067. https://doi.org/10.1021/acs.iecr.8b00996.

(19) Bae, Y.-S.; Lee, C.-H. Sorption Kinetics of Eight Gases on a Carbon Molecular Sieve at Elevated Pressure. *Carbon* 2005, *43* (1), 95–107.

(20) Grande, C. A.; Rodrigues, A. E. Biogas to Fuel by Vacuum Pressure Swing Adsorption I. Behavior of Equilibrium and Kinetic-Based Adsorbents. *Industrial & engineering chemistry research* 2007, *46* (13), 4595–4605.

(21) Shirani, B.; Eic, M. Equilibrium and Kinetics of Methane and Ethane Adsorption in Carbon Molecular Sieve. *International Journal of Chemical Reactor Engineering* 2016, *14* (4), 887–898.

(22) Shirani, B.; Eic, M. Kinetic Behaviours of Carbon Dioxide and Carbon Monoxide on Carbon Molecular Sieve. *The Canadian Journal of Chemical Engineering* 2016, *94* (10), 2023–2034.

(23) Kapoor, A.; Yang, R. T. Kinetic Separation of Methane—Carbon Dioxide Mixture by Adsorption on Molecular Sieve Carbon. *Chemical Engineering Science* 1989, *44* (8), 1723–1733. https://doi.org/10.1016/0009-2509(89)80014-4.

(24) Erden, L. Methane Separation and Purification via Pressure Swing Adsorption, University of South Carolina, 2016.

(25) Rutherford, S. W.; Do, D. D. Characterization of Carbon Molecular Sieve 3A. *Langmuir* 2000, *16* (18), 7245–7254.

(26) Chagger, H. K.; Ndaji, F. E.; Sykes, M. L.; Thomas, K. M. Kinetics of Adsorption and Diffusional Characteristics of Carbon Molecular Sieves. *Carbon* 1995, *33* (10), 1405–1411.

(27) Reid, C. R.; Thomas, K. M. Adsorption Kinetics and Size Exclusion Properties of Probe Molecules for the Selective Porosity in a Carbon Molecular Sieve Used for Air Separation. *J. Phys. Chem. B* 2001, *105* (43), 10619–10629. https://doi.org/10.1021/jp0108263.

(28) Braymer, T. A.; Coe, C. G.; Farris, T. S.; Gaffney, T. R.; Schork, J. M.; Armor, J. N. Granular Carbon Molecular Sieves. *Carbon* 1994, *32* (3), 445–452. https://doi.org/10.1016/0008-6223(94)90165-1.

(29) Liu, H.; Ruthven, D. M. Diffusion in Carbon Molecular Sieves. In *Fundamentals of Adsorption*; LeVan, M. D., Ed.; The Kluwer International Series in Engineering and Computer Science; Springer US: Boston, MA, 1996; Vol. 356, pp 529–536. https://doi.org/10.1007/978-1-4613-1375-5_66.
(30) Chagger, H. K.; Ndaji, F. E.; Sykes, M. L.; Thomas, M. KINETICS OF ADSORPTION AND DIFFUSIONAL CHARACTERISTICS OF CARBON MOLECULAR SIEVES. 7.
(31) Shirani, B.; Eic, M. Kinetic Behaviours of Carbon Dioxide and Carbon Monoxide on Carbon Molecular Sieve. *Can. J. Chem. Eng.* 2016, *94* (10), 2023–2034. https://doi.org/10.1002/cjce.22585.
(32) Ruthven, D. M. *Principles of Adsorption and Adsorption Processes*; John Wiley & Sons, 1984.
(33) Reid, C. R.; Thomas, K. M. Adsorption of Gases on a Carbon Molecular Sieve Used for Air Separation: Linear Adsorptives as Probes for Kinetic Selectivity. *Langmuir* 1999, *15* (9), 3206–3218. https://doi.org/10.1021/la981289p.
(34) Crank, J. *The Mathematics of Diffusion*, 2d ed.; Clarendon Press: Oxford, [Eng], 1975.
(35) Loughlin, K. F.; Hassan, M. M.; Fatehi, A. I.; Zahur, M. Rate and Equilibrium Sorption Parameters for Nitrogen and Methane on Carbon Molecular Sieve. *Gas Separation & Purification* 1993, *7* (4), 264–273. https://doi.org/10.1016/0950-4214(93)80028-U.
(36) Glueckauf, E.; Coates, J. I. 241. Theory of Chromatography. Part IV. The Influence of Incomplete Equilibrium on the Front Boundary of Chromatograms and on the Effectiveness of Separation. *Journal of the Chemical Society (Resumed)* 1947, 1315–1321.
(37) Wang, J.-Y.; Mangano, E.; Brandani, S.; Ruthven, D. M. A Review of Common Practices in Gravimetric and Volumetric Adsorption Kinetic Experiments. *Adsorption* 2021, *27* (3), 295–318. https://doi.org/10.1007/s10450-020-00276-7.
(38) Jin, X.; Malek, A.; Farooq, S. Production of Argon from an Oxygen−Argon Mixture by Pressure Swing Adsorption. *Ind. Eng. Chem. Res.* 2006, *45* (16), 5775–5787. https://doi.org/10.1021/ie060113c.
(39) Wiersum, A. D.; Chang, J.-S.; Serre, C.; Llewellyn, P. L. An Adsorbent Performance Indicator as a First Step Evaluation of Novel Sorbents for Gas Separations: Application to Metal–Organic Frameworks. *Langmuir* 2013, *29* (10), 3301–3309.
(40) Wilkins, N. S.; Sawada, J. A.; Rajendran, A. Diffusion of CH4 and N2 in Barium-Exchanged Reduced Pore Zorite (Ba-RPZ) and Zeolite 4A. *Industrial & Engineering Chemistry Research* 2021, *60* (29), 10777–10790.
(41) Qinglin, H.; Sundaram, S. M.; Farooq, S. Revisiting Transport of Gases in the Micropores of Carbon Molecular Sieves. *Langmuir* 2003, *19* (2), 393–405.

CHAPTER 5

CONCLUSIONS AND RECOMMENDATIONS FOR FUTURE WORK

5.1. CONCLUSIONS

Addressing the consequences of climate change is of high importance due to the observable daily impacts. Many scientists now attribute Earth's changing climate to human-driven emissions of greenhouse gases, particularly carbon dioxide. Concurrently, global energy demand is swiftly transforming. Thus, it becomes crucial to adopt a sustainable approach that harmonizes economic growth with social and environmental accountability for a lasting strategy.

Both carbon dioxide (CO_2) and methane (CH_4) are prevalent in gas mixtures like natural gas, landfill gas, coalbed methane, and biogas. It is vital to decrease emissions of these gases and explore cleaner energy options to combat climate change. One current focus involves isolating CO_2 from CH_4 and utilizing both gases to create high-value products as a short-term solution.

The application of physical adsorption separation techniques has proven effective in separating carbon dioxide from methane. The primary aim of this study is to perform a detailed evaluation of the process that separates methane and carbon dioxide gases using adsorption. This will be achieved using two readily accessible materials: CMS(C), which is a commercially available carbon molecular sieve, and AC(B), a form of activated carbon. This is achieved through a comprehensive examination of the adsorption equilibria of pure and binary adsorption of CO_2 and CH_4 on commercial carbon molecular sieve (CMS(C)) and activated carbon AC(B). This analysis includes both static and dynamic conditions, utilizing experiments and mechanistic modeling.

In this study, the adsorption equilibrium data for pure gases were obtained through gravimetric measurements at different temperatures at 0-10 atm. pressure range. These data were fitted to temperature-dependent Sips and Langmuir isotherm models, successfully predicting mixed gas adsorption. Breakthrough experiments involving a feed mixture of 60% CH_4 and 40% CO_2 were conducted using a packed bed adsorption column under various operating conditions (differing pressures, temperatures, and feed flow rates). A mechanistic

model capturing the kinetics and dynamics of breakthrough adsorption was developed and validated, showing good agreement with experimental breakthrough data.

From the breakthrough curves, pure and predicted binary adsorption equilibria data, parameters like adsorption capacities, selectivity, sorbent selection parameter and the adsorbent performance indicator (API) were determined to assess the initial gas adsorption separation potential of adsorbents CMS(C) and AC(B) under different operating conditions. The analysis of the breakthrough curves highlights that increasing pressure, decreasing temperature and feed flow rate led to increased breakthrough time and adsorption breakthrough capacity for both gases on CMS(C) and AC(B), as expected. The most favorable performance was associated with the highest calculated values of selectivity for CO_2, sorbent selection parameter (S), API and the time duration that methane is purified. At a pressure of 1 atm, a temperature of 294 K, and a flow rate of 400 ml min^{-1}, the highest levels of selectivity and the S parameter were observed for both adsorbents. Among the two, CMS (C) exhibited the highest values. Regarding the API parameter, the AC(B) sample yielded the highest value under conditions of 9 atm pressure, a temperature of 294 K, and a flow rate of 400 ml min^{-1}. Because the API considers a broader range of factors in comparison to other gas separation indicators studied here, such as selectivity and sorbent selection parameter, it is regarded as the more practical parameter for assessing the initial gas separation potential. Furthermore, the breakthrough analysis emphasizes that between the two adsorbents, CMS(C) proved to be the superior choice for methane purification. It exhibited faster methane breakthrough and a longer duration during which methane was enriched (purified) as it exited the adsorption column, extending until the breakthrough of carbon dioxide occurred. The optimal conditions for this scenario are attained at a pressure of 9 atm, a temperature of 294 K, and a flow rate of 400 ml min^{-1}, which resulted in the longest purification time lasting 420 seconds.

This research also delves into the kinetic behavior of methane and carbon dioxide using commercial carbon molecular sieve and activated carbon across varying temperatures and pressure ranges. Mass uptake measurements were carried out using the gravimetric method at different pressures, allowing determination of mass transfer and diffusion parameters. Three kinetic models were applied to the data to obtain these parameters. The obtained parameters were analyzed and compared to comprehend the mass transfer mechanism and diffusion rates of CO_2 and CH_4 within the adsorbents.

Results revealed that carbon dioxide exhibited faster uptake rates than methane in both adsorbents across different temperatures and pressures. Mass transfer and diffusivity

parameters (($\frac{D_c}{r_c^2}$), k_{LDF} and k_b) of methane and carbon dioxide increased with rising pressure and temperature in both adsorbents, with an exception for CO_2 on CMS(C) where these parameters exhibited an initial increase followed by a decrease, indicating saturation.

The kinetic analysis showcased that for CMS(C), micropore mouth barrier and interior pore resistance dominated methane diffusion, while diffusion resistance inside the pores was more significant for CO_2. For AC(B), interior pore resistance was the controlling mass transfer resistance for both gases. Furthermore, diffusivity and mass transfer rates of both gases were faster in activated carbon compared to carbon molecular sieves, rendering AC(B) more suitable for reducing adsorption/desorption cycle times in separation processes.

These factors (comprising selectivity, the S parameter, adsorption capacity, and the duration needed for methane purification) are of significant value when initially evaluating the gas separation potential of the adsorbent material. Taking these factors into consideration, along with additional aspects such as operational costs, adsorbent properties, adsorption kinetics, and employing simulations and pilot-scale testing, can lead to an enhanced and more efficient adsorption separation process.

The analysis of the outcomes in this study, when compared with findings from existing literature, indicates a logical and aligned progression. It was challenging to locate adsorption breakthrough experiments in the literature that precisely matched the operational conditions and characteristics of the adsorption column in our study. This made quantitative comparisons difficult; hence, a more suitable approach was to conduct a qualitative analysis.

Shen et al.[1] conducted and modeled breakthrough experiments using a gas composition of 55% methane and 45% carbon dioxide at various pressures (2, 4, and 4 bar) and feed flow rates (2, 4, and 6 SLPM). The temperature was set at 303.15 K, and a carbon molecular sieve sample was utilized for biogas upgrading applications. Their findings indicated that lower feed flow rates and higher pressures improved methane purification, while higher pressures led to decreased equilibrium selectivity values. Parametric studies on the adsorption breakthroughs of CO_2/CH_4 gas mixtures with an MOF by Gomez et al.[2] and a study on zeolite 13X by Silva et al.[3] also demonstrated that adsorption separation performance, in terms of equilibrium selectivity, was better at lower temperatures and pressures. The results obtained in our study align with those in the literature mentioned here.

Rainone et al.[4] experimentally investigated one commercial activated carbon and two commercial carbon molecular sieves using a gas composition of 60% methane and 40% carbon dioxide, as well as other feed compositions, at P=1 atm and T=30 °C. Their findings revealed

that activated carbon outperforms carbon molecular sieves in terms of adsorption capacity for both CO_2 and CH_4. Additionally, activated carbon exhibited superior kinetic performance, characterized by higher bed usage efficiency and shorter desorption times. In contrast, carbon molecular sieves displayed significantly lower CH_4 adsorption capacity but demonstrated much higher selectivity in separating CO_2/CH_4 mixtures. The results obtained in our study perfectly align with these findings.

Diffusivity and mass transfer values calculated in our study for carbon molecular sieve and activated carbon were in the same order of magnitude as reported in the research conducted by Canevesi et al.[5], Qinglin et al.[6], and Grande et al[7]. Additionally, these studies reported faster diffusion for carbon dioxide than methane within the carbon materials, which was consistent with the findings of our study.

5.2. RECOMMENDATIONS FOR FUTURE WORK

- Evaluating the potential of other carbon-based materials such as carbon nano tubes and graphene for the removal of CO_2 from CH_4 and comparing their potential with activated carbon and carbon molecular sieve**.**
- Improving the low selectivity associated with carbon-based materials compared to other commercial adsorbents such as zeolites and MOF's by increasing the basicity to improve interactions between the carbon surface and the acidic carbon dioxide adsorbate via different surface modification methods.
- Evaluating raw and surface modified flax shives as a potential adsorbent material for CO_2 removal from CH_4.
- Potential modification of the API parameter (including cost of the adsorbent, energy requirements for regeneration and pressurization, diffusivity etc.) which can result in a more effective assessment of gas separation potential of adsorbents.
- Evaluating the effects of variations in other parameters (inlet feed gas concentrations, bed diameter, particle size, regeneration temperature and time, axial dispersion coefficient, etc.) on the separation performance through experiments and simulations.

.

5.3 NOMENCLATURE

$\frac{D_c}{r_c^2}$	Diffusion time constant	[s^{-1}]
k_b	Mass transfer coefficient at the micropore mouth	[$m.s^{-1}$]
k_{LDF}	Linear driving force mass transfer coefficient	[s^{-1}]

Abbreviations

AC	Activated carbon
API	Adsorbent performance indicator
CMS	Carbon molecular sieve
LDF	Linear driving force

5.4 NOMENCLATURE

(1) Shen, Y.; Niu, Z.; Zhang, R.; Zhang, D. Vacuum Pressure Swing Adsorption Process with Carbon Molecular Sieve for CO2 Separation from Biogas. *Journal of CO2 Utilization* 2021, *54*, 101764.

(2) Gomez, L. F., Zacharia, R., Bénard, P., & Chahine, R. (2015). Simulation of binary CO_2/CH_4 mixture breakthrough profiles in MIL-53 (Al). Journal of Nanomaterials, 16(1), 424-424.

(3) Silva, J. A., Cunha, A. F., Schumann, K., & Rodrigues, A. E. (2014). Binary adsorption of CO_2/CH_4 in binderless beads of 13X zeolite. Microporous and Mesoporous Materials, 187, 100-107.

(4) Rainone, F.; D'Agostino, O.; Erto, A.; Balsamo, M.; Lancia, A. Biogas Upgrading by Adsorption onto Activated Carbon and Carbon Molecular Sieves: Experimental and Modelling Study in Binary CO_2/CH_4 Mixture. *Journal of Environmental Chemical Engineering* 2021, *9* (5), 106256.

(5) Canevesi, R. L., Andreassen, K. A., Da Silva, E. A., Borba, C. E., & Grande, C. A. (2018). Pressure swing adsorption for biogas upgrading with carbon molecular sieve. Industrial & Engineering Chemistry Research, 57(23), 8057-8067.

(6) Qinglin, Huang, S. M. Sundaram, and S. Farooq. "Revisiting transport of gases in the micropores of carbon molecular sieves." Langmuir 19.2 (2003): 393-405.).

(7) Grande, C. A., Lopes, F. V., Ribeiro, A. M., Loureiro, J. M., & Rodrigues, A. E. (2008). Adsorption of off-gases from steam methane reforming (H_2, CO_2, CH_4, CO and N_2) on activated carbon. Separation Science and Technology, 43(6), 1338-1364.

APPENDIX A – Additional equations

In addition to the core equations (which include adsorption isotherm equations, mass, and energy balances) mentioned in chapters 2 and 3, the following equations used in the adsorption breakthrough modeling are as follows:

THERMOPHYSICAL PROPERTIES OF THE FLUID

*Gas density

Pure component[1]:

$$\rho = \frac{(yP)MW}{RT}$$

Gas mixture[1]:

$$\rho_{mixture} = \sum_{i=1}^{n} y_i \rho_i$$

* Gas viscosity

Pure component[1–3]:

$$\eta = 40.785 \frac{F_c (MW \times T)^{0.5}}{V_c^{2/3} \Omega_v}$$

$$\Omega_v = [1.16145(T^*)^{-0.14874}] + 0.52487[exp(0.77320T^*)] + +2.16178[exp(2.43787T^*)]$$

$$T^* = 1.2593 T_r$$

$$T_r = \frac{T}{T_c}$$

$$F_c = 1 - 0.275\omega + 0.059035\mu_r^4 + \kappa$$

Gas mixture[1,4]:

$$\eta_{mixture} = \sum_{i=1}^{n} \frac{y_i \eta_i}{\sum_{j=1}^{n} y_j \emptyset_{ij}}$$

$$\emptyset_{ij} = \frac{\left[1 + \left(\frac{\eta_i}{n_j}\right)^{0.5} \left(\frac{MW_j}{MW_i}\right)^{0.25}\right]^2}{\left[8\left(1 + \frac{MW_i}{MW_j}\right)\right]^{0.5}}$$

$$\emptyset_{ji} = \left(\frac{\eta_j}{n_i}\right)\left(\frac{MW_i}{MW_j}\right)\emptyset_{ij}$$

* Gas heat capacity at constant pressure

Pure component[1]:

$$C_p = (A_0 + A_1 T + A_2 T^2 + A_3 T^3 + A_4 T^4)R$$

"Values are of A_0, A_1, A_2, A_3, A_4 for different gases are reported in Appendix A of the following reference":

Poling, Bruce E., John M. Prausnitz, and John P. O'connell. *Properties of gases and liquids*. McGraw-Hill Education, 2001.

Gas mixture[1]:

$$C_{p_{mixture}} = \sum_{i=1}^{n} y_i C_{p,i}$$

*Gas heat capacity at constant volume

Pure component[1]:

$$C_v = C_p - R$$

Gas mixture[1]:

$$C_{v_{mixture}} = \sum_{i=1}^{n} y_i C_{v,i}$$

* Gas thermal conductivity

Pure component[1–3]:

$$\lambda_{ThC} = \frac{3.75\eta C_v \psi}{MW\left(\frac{C_v}{R}\right)}$$

$$\psi = 1 + \alpha\left[\left(\frac{(0.215 + 0.28288\alpha - 1.061\beta + 0.26665Z)}{(0.6366 + \beta Z + 1.061\alpha\beta)}\right)\right]$$

$$\alpha = \left(\frac{C_v}{R}\right) - {}^3/_2$$

$$\beta = 0.7862 - 0.7109\omega + 1.3168\omega^2$$

$$Z = 2 + 10.5T_r^2$$

Gas mixture[1,4,5]:

$$\lambda_{ThC,mixture} = \sum_{i=1}^{n} \frac{y_i \lambda_i}{\sum_{j=1}^{n} y_j A_{ij}}$$

$$A_{ij} = \emptyset_{ij} \ , A_{ji} = \emptyset_{ji}$$

$$\emptyset_{ij} = \frac{\left[1 + \left(\frac{\eta_i}{n_j}\right)^{0.5} \left(\frac{MW_j}{MW_i}\right)^{0.25}\right]^2}{\left[8\left(1 + \frac{MW_i}{MW_j}\right)\right]^{0.5}}$$

$$\emptyset_{ji} = \left(\frac{\eta_j}{n_i}\right)\left(\frac{MW_i}{MW_j}\right)\emptyset_{ij}$$

GAS DIFFUSIVITY RELATIONS

***Molecular Diffusivity between A and B**[6,7]

$$D_m = 0.0018583 \times \frac{T^{\frac{3}{2}}(\frac{1}{MW_A} + \frac{1}{MW_B})^{\frac{1}{2}}}{P\sigma_{AB}^2 \Omega_{AB}}$$

$$\Omega_{AB} = \frac{1.06036}{(T^*)^{0.15610}} + \frac{0.19300}{e^{0.47635T^*}} + \frac{1.03587}{e^{1.52996T^*}} + \frac{1.76474}{e^{3.89411T^*}}$$

$$T^* = \frac{T}{\sqrt{\frac{\varepsilon_A}{k}\frac{\varepsilon_B}{k}}}$$

$$\sigma_{AB} = \frac{1}{2}(\sigma_A + \sigma_B)$$

***Molecular Diffusivity of component *i* in gas mixture**

$$D_{m,i} = \frac{1 - y_i}{\sum_{i \neq j} \frac{y_j}{D_{ij}}}$$

***Knudsen Diffusivity**[8,9]

$$D_k = 9.7 \times 10^3 r_p (\frac{T}{MW_i})^{\frac{1}{2}}$$

*** Effective Macropore Diffusivity**[8]

$$D_e = \frac{\varepsilon_p D}{\tau}$$

$$D = \frac{1}{\frac{1}{D_m} + \frac{1}{D_k}}$$

MASS TRANSFER RELATIONS

*** Axial dispersion coefficient of component *i***[10]

$$D_z = \frac{D_m}{\varepsilon_b}(20 + 0.5\text{ReSc})$$

*** Reynolds, Schmidt and Sherwood number**[10]

$$Re = \frac{d_p v_s \rho}{\eta}$$

$$Sc = \frac{\eta}{\rho D_m}$$

$$Sh = 2 + 1.1 Sc^{1/3} Re^{0.6}$$

*** Film mass transfer coefficient for packed bed**[10]

$$k_f = \frac{D_m Sh}{d_p}$$

HEAT TRANSFER RELATIONS (INSIDE ADSORPTION COLUMN)

*** Axial heat dispersion coefficient**[8]

$$\lambda = \frac{(7 + 0.5 PrRe)}{\lambda_{ThC}}$$

*** Prandtl number**[11]

$$Pr = \frac{C_p \eta}{\lambda_{ThC}}$$

*** Nusselt number between fluid and adsorbent**[11]

$$Nu_{inside} = 2 + 1.1Pr^{1/3}Re^{0.6}$$

*** Convective film heat transfer coefficient between fluid and adsorbent**[11]

$$h_f = \frac{Nu_{inside}\lambda_{ThC}}{d_p}$$

*** Nusselt number inside column between fluid and column wall**[12,13]

$$Nu_w = 12.5 + 0.048Re$$

*** Convective heat transfer coefficient between fluid and column wall**[13]

$$h_w = \frac{Nu_w\lambda_{ThC}}{d_p}$$

HEAT TRANSFER RELATIONS (OUTSIDE ADSORPTION COLUMN)

*** Rayleigh number outside column**[14,15]

$$RA_{outside} = \frac{g(T_w - T_{amb})d_o^3}{T_{amb}Nu_{amb}\nu_{amb}}$$

*** Nusselt number outside column**[16]

$$Nu_o = 0.68 + \frac{0.67Ra_{outside}^{1/4}}{\left[1 + \left(\frac{0.492}{Pr_{amb}}\right)^{9/16}\right]^{4/9}}$$

Convective heat transfer coefficient between column wall and ambient air[16]

$$h_o = \frac{k_{amb}Nu_o}{d_0}$$

MOMENTUM BALANCE (ERGUN EQUATION)[17]

$$-\frac{\partial P}{\partial z} = \frac{150\eta(1-\varepsilon_b)^2 v}{\varepsilon_b^3 d_p} + \frac{1.75(1-\varepsilon_b)\rho v^2}{\varepsilon_b^3 d_p}$$

Nomenclature

$\boldsymbol{A}$	Parameter used in gas mixture thermal conductivity calculation	[dimensionless]
$\boldsymbol{C_p}$	Gas phase heat capacity at constant pressure	[J.kg^{-1}.K^{-1}]

C_v	Gas phase heat capacity at constant volume	[J.kg^{-1}.K^{-1}]
D	Total molecular diffusivity	[m^2.s^{-1}]
D_c	Micropore diffusivity	[m^2.s^{-1}]
D_e	Effective Macropore diffusivity	[m^2.s^{-1}]
d_i	Column inner diameter	[m]
D_m	Molecular diffusivity	[m^2.s^{-1}]
d_o	Column outer diameter	[m]
d_p	Pellet diameter	[m]
D_k	Knudesen diffusivity	[m^2.s^{-1}]
D_z	Axial dispersion coefficient	[m^2.s^{-1}]
F_c	Factor accounting molecular shapes and polarities of dilute gases	[dimensionless]
g	Gravitational acceleration	[m.s^{-2}]
h_f	External film heat transfer coefficient	[W.m^{-2}.K^{-1}]
h_o	Heat transfer coefficient between column wall and ambient air	[W.m^{-2}.K^{-1}]
h_w	Heat transfer coefficient between the gas and the column wall	[W.m^{-2}.K^{-1}]
k	Boltzmann's constant	[J.K^{-1}]
k_f	External film mass transfer coefficient	[m.s^{-1}]
MW	Molecular weight	[kg.mol^{-1}]
P	Total pressure	[atm]
R	Universal gas constant	[m^3.Pa.K^{-1}.mol^{-1}]
T	Temperature	[K]
T^*	Parameter used in gas viscosity calculation	[K]
T_c	Critical temperature	[K]
T_r	Reduced temperature	[K]
T_w	Column wall temperature	[K]
ν_{amb}	Thermal diffusivity of air	[m^2.s^{-1}]
v	Interstitial velocity	[m.s^{-1}]
v_s	Superficial velocity	[m.s^{-1}]
V_c	Critical volume	[cm^3.mol^{-1}]
y	Mole fraction in the gas phase	[dimensionless]
z	Axial position in the column	[m]

Subscripts

A	Component with stronger adsorption

$\boldsymbol{B}$	Component with weaker adsorption	

Greek Symbols

$\boldsymbol{\Omega_{AB}}$	Collision integral	[dimensionless]
$\boldsymbol{\Omega_{v}}$	Viscosity collision integral	[dimensionless]
$\boldsymbol{\alpha}$	Correlation used in gas thermal conductivity calculation	[dimensionless]
$\boldsymbol{\beta}$	Correlation used in gas thermal conductivity calculation	[dimensionless]
$\boldsymbol{\varepsilon}$	Dispersion energy (Lennard-Jones parameter)	[J]
$\boldsymbol{\varepsilon_b}$	Bed porosity	[dimensionless]
$\boldsymbol{\varepsilon_p}$	Pellet porosity	[dimensionless]
$\boldsymbol{\eta}$	Gas viscosity	[$kg.m^{-1}.s^{-1}$]
$\boldsymbol{\lambda}$	Axial heat dispersion coefficient	[$W.m^{-1}.K^{-1}$]
$\boldsymbol{\lambda_{ThC}}$	Gas thermal conductivity	[$W.m^{-1}.K^{-1}$]
$\boldsymbol{\mu_r}$	Dimensionless dipole moment	[dimensionless]
$\boldsymbol{\rho}$	Gas density	[$kg.m^{-3}$]
$\boldsymbol{\sigma_{AB}}$	Constant in Lennard-Jones potential-energy function	[Å]
$\boldsymbol{\tau}$	Tortuosity factor	[dimensionless]
$\boldsymbol{\omega}$	Acentric factor	[dimensionless]
$\emptyset$	Parameter used in gas mixture viscosity calculation	[dimensionless]
$\boldsymbol{\psi}$	Correlation used in gas thermal conductivity calculation	[dimensionless]
$\boldsymbol{Z}$	Number of collisions required to interchange a quantum of rotational energy with translational energy	[dimensionless]

DIMENSIONLESS NUMBERS

$\boldsymbol{Nu}$	Nusselt number
$\boldsymbol{Pr}$	Prandtl number
$\boldsymbol{Ra}$	Rayleigh number
$\boldsymbol{Re}$	Reynolds number
$\boldsymbol{Sc}$	Schmidt number
$\boldsymbol{Sh}$	Sherwood number

REFERENCES

(1) Poling, B. E.; Prausnitz, J. M.; O'connell, J. P. *Properties of Gases and Liquids*; McGraw-Hill Education, 2001.

(2) Chung, T. H.; Lee, L. L.; Starling, K. E. Applications of Kinetic Gas Theories and Multiparameter Correlation for Prediction of Dilute Gas Viscosity and Thermal Conductivity. *Industrial & engineering chemistry fundamentals* **1984**, *23* (1), 8–13.

(3) Chung, T. H.; Ajlan, M.; Lee, L. L.; Starling, K. E. Generalized Multiparameter Correlation for Nonpolar and Polar Fluid Transport Properties. *Industrial & engineering chemistry research* **1988**, *27* (4), 671–679.

(4) Wilke, C. R. A Viscosity Equation for Gas Mixtures. *The journal of chemical physics* **1950**, *18* (4), 517–519.

(5) Mason, E. A.; Saxena, S. C. Approximate Formula for the Thermal Conductivity of Gas Mixtures. *The Physics of fluids* **1958**, *1* (5), 361–369.

(6) Chapman, S.; Cowling, T. G. *The Mathematical Theory of Non-Uniform Gases: An Account of the Kinetic Theory of Viscosity, Thermal Conduction and Diffusion in Gases*; Cambridge university press, 1990.

(7) Hirschfelder, J. O. cF Curtiss, and RB Bird. *Molecular theory of gases and liquids* **1954**, 5–11.

(8) Yang, R. T. *Gas Separation by Adsorption Processes*; World Scientific, 1997; Vol. 1.

(9) Kauzmann, W. *Kinetic Theory of Gases*; Courier Corporation, 2012.

(10) Wakao, N.; Funazkri, T. Effect of Fluid Dispersion Coefficients on Particle-to-Fluid Mass Transfer Coefficients in Packed Beds: Correlation of Sherwood Numbers. *Chemical Engineering Science* **1978**, *33* (10), 1375–1384.

(11) Wakao, N.; Kaguei, S.; Funazkri, T. Effect of Fluid Dispersion Coefficients on Particle-to-Fluid Heat Transfer Coefficients in Packed Beds: Correlation of Nusselt Numbers. *Chemical engineering science* **1979**, *34* (3), 325–336.

(12) Shafeeyan, M. S.; Daud, W. M. A. W.; Shamiri, A. A Review of Mathematical Modeling of Fixed-Bed Columns for Carbon Dioxide Adsorption. *Chemical engineering research and design* **2014**, *92* (5), 961–988.

(13) Dantas, T. L.; Luna, F. T.; Silva Jr, I. J.; Torres, A. E.; De Azevedo, D. C. S.; Rodrigues, A. E.; Moreira, R. de F. P. M. Modeling of the Fixed-Bed Adsorption of Carbon Dioxide and a Carbon Dioxide-Nitrogen Mixture on Zeolite 13X. *Brazilian Journal of Chemical Engineering* **2011**, *28*, 533–544.

(14) Bhowmik, H.; Gharibi, A.; Yaarubi, A.; Alawi, N. Transient Natural Convection Heat Transfer Analyses from a Horizontal Cylinder. *Case Studies in Thermal Engineering* **2019**, *14*, 100422.

(15) Xu, X.; Yu, Z.; Hu, Y.; Fan, L.; Cen, K. A Numerical Study of Laminar Natural Convective Heat Transfer around a Horizontal Cylinder inside a Concentric Air-Filled Triangular Enclosure. *International journal of heat and mass transfer* **2010**, *53* (1–3), 345–355.

(16) Cavenati, S.; Grande, C. A.; Rodrigues, A. E. Separation of CH4/CO2/N2 Mixtures by Layered Pressure Swing Adsorption for Upgrade of Natural Gas. *Chemical engineering science* **2006**, *61* (12), 3893–3906.

(17) Macdonald, I. F.; El-Sayed, M. S.; Mow, K.; Dullien, F. A. L. Flow through Porous Media-the Ergun Equation Revisited. *Industrial & Engineering Chemistry Fundamentals* **1979**, *18* (3), 199–208.

APPENDIX B – gPROMS codes (Distribution domains: axial direction in the column the radial direction in the pellet, the radial direction in of the crystals)

Case study:

* Adsorption breakthrough modeling for a feed composition of 60%CH_4 - 40%CO2 on CMS(C) at a total pressure of 9 atm, bed temperature of 294K and inlet flow rate of 400 ml/min (T= 294K and P=1 atm)

* Concentration and temperature gradients exist in the axial direction in the column the radial direction in the pellet, the radial direction in of the crystals

Codes:

PARAMETER

```
Components AS ORDERED_SET
# Components i of the gas mixture
Species AS ORDERED_SET
# Species j of the gas mixture
PI AS REAL DEFAULT 3.1416
# pi number
g  AS REAL DEFAULT 9.81
# m/s^2; gravitational constant
R  AS REAL DEFAULT 8.3144621
# Pa.m^3/mol.K; ideal gas constant
R_Latm AS REAL DEFAULT 8.205745*(10^(-5))
# m^3.atm/mol.K; ideal gas constant

# Pellet Characteristics
#-------------------------------------------------------------------------
dp AS REAL DEFAULT 0.00142
# m; mean pellet diameter
Rp AS REAL DEFAULT dp/2
# m; mean pellet radius
rhos AS REAL DEFAULT 875
# kg/m^3; skeletal density of pellet
Cps AS REAL DEFAULT 680
# J/kg.K; specific heat capacity of pellet
rhop AS REAL DEFAULT 1025.938098
# kg/m^3; particle density of pellet
ep AS REAL DEFAULT 0.33
# -; particle void fraction
Cpp AS REAL DEFAULT 880
```

```
# J/kg.K; specific heat capacity of pellet
ksg AS REAL DEFAULT 0.7
# W/m.K; effective thermal conductivity of pellet
rc AS REAL DEFAULT 3.7*(10^(-6))
# m; mean radius of crystals
rpore_avg AS REAL DEFAULT  4*(10^(-8))
# cm; mean pore radius
tortuosityfactor  AS REAL DEFAULT 3
# -; tortuosityfactor


# Column Characteristics
#--------------------------------------------------------------------------------
H AS REAL DEFAULT 0.22
# m; column length
di AS REAL DEFAULT 0.02064
# m; column internal diameter
ri AS REAL DEFAULT di/2
# m; column internal radius
wall AS REAL DEFAULT 0.00431
# m; column wall thickness
do_ AS REAL DEFAULT 0.02535
# m; column external diameter
ro AS REAL DEFAULT do_/2
# m; column external radius
Area AS REAL DEFAULT (PI/4) * ((di)^2)
# m^2; cross sectional area of the column
eb AS REAL DEFAULT 0.296324633
# -; column void fraction


# Flow Characteristics
#--------------------------------------------------------------------------------

Tamb AS REAL DEFAULT 294.36
# K; ambient temperature
MW AS ARRAY(Components) OF REAL
# g/mol; molecular weight
MW_prime AS ARRAY(Components) OF REAL
# kg/mol; molecular weight
V_c AS ARRAY(Components) OF REAL
# cm^3 /mol; critical volume
T_c AS ARRAY(Components) OF REAL
# K; critical temperature
W_c AS ARRAY(Components) OF REAL
# -; acentric factor
Y_in AS ARRAY(Components) OF REAL
```

```
# -; feed mole fraction of component i in gas mixture
Pfeed AS REAL DEFAULT 9
# atm; feed pressure
Tfeed AS REAL DEFAULT 294.76
# K; inlet gas temperature
Qin AS REAL DEFAULT 7.407741E-7
# m^3/s; feed volumetric flow rate
cginlet AS ARRAY(Components) of REAL
# mol/m^3; feed concentration of component i


#% Column Wall Characteristics
#-------------------------------------------------------------------------------
rhow AS REAL DEFAULT 8000
# kg/m^3; density of stainless steel column
Cpw AS REAL DEFAULT 500
# J/kg.K; heat capacity of stainless steel column
kw AS REAL DEFAULT 12.1
# W/m.K; thermal conductivity of stainless steel column


#% Mass and Thermal Transfer Characteristics of Air
#-------------------------------------------------------------------------------
nuamb AS REAL DEFAULT 0.00001517
# m^2/s; air kinetic viscosity at 294.36 K
kamb AS REAL DEFAULT 0.0259
# W/m.K; thermal conductivity of air  at 294.36 K
Pramb AS REAL DEFAULT 0.71
# -; Prandlt number of ambient air outside column
Alphamb AS REAL DEFAULT (15.57+(22.07-15.67)*(Tamb-250)/50)*(10^(-6))
#% m^2/s; thermal diffusivity of air:


# Mass Transfer and Diffusivity coefficients (Micropore Diffusion)
#-------------------------------------------------------------------------------
kb AS ARRAY(Components) OF REAL
# 1/s; mass transfer coefficient at micropore mouth
Dc AS ARRAY(Components) OF REAL
# m^2/s; Micropore diffusivity

# Temperature Dependant SIPS Isotherm Parameters
#-------------------------------------------------------------------------------
T0 AS REAL DEFAULT 283.15
#°K; reference temperature
b0 AS ARRAY(Components) OF REAL
# atm^-1; adsorption affinity constant at some reference temperature
```

```
Heat_RTg AS ARRAY(Components) OF REAL
# -; constant parameter of toth isotherm model
qm0 AS ARRAY(Components) OF REAL
# mol/kg; adsorption saturation capacity at some reference temperature
DeltaH AS ARRAY(Components) OF REAL
# J/mol; isosteric heat
X AS ARRAY(Components) OF REAL
# -; constant parameter of SIPS isotherm model
n0 AS ARRAY(Components) OF REAL
# -; adsorption exponents or number of active sites at some reference temperature
alfa AS ARRAY(Components) OF REAL
# -; constant parameter of SIPS isotherm model

b0_CH4 AS REAL DEFAULT 0.808900568215052
# atm^-1; adsorption affinity constant at some reference temperature
b0_CO2 AS REAL DEFAULT 1.44733512515504
# atm^-1; adsorption affinity constant at some reference temperature
b0_He AS REAL DEFAULT 0.1
# atm^-1; adsorption affinity constant at some reference temperature
Heat_RTg_CH4 AS REAL DEFAULT 5.03955811380626
# -; constant parameter of toth isotherm model
Heat_RTg_CO2 AS REAL DEFAULT 9.41333325056097
# -; constant parameter of toth isotherm model
Heat_RTg_He AS REAL DEFAULT 0.1
# -; constant parameter of toth isotherm model
n0_CH4 AS REAL DEFAULT 1.08594777550726
# -; adsorption exponents or number of active sites at some reference temperature
n0_CO2 AS REAL DEFAULT 1.4164472249844
# -; adsorption exponents or number of active sites at some reference temperature
n0_He AS REAL DEFAULT 0.1
# -; adsorption exponents or number of active sites at some reference temperature
alfa_methane AS REAL DEFAULT 0.322732007064096
# -; constant parameter of toth isotherm model
alfa_CarbonDioxide AS REAL DEFAULT 0.318706297307062
# -; constant parameter of toth isotherm model
alfa_Helium AS REAL DEFAULT 0.1
# -; constant parameter of toth isotherm model


# Molecular Diffusivity Parameters
#-------------------------------------------------------------------------
MWi AS ARRAY(Components) OF REAL
# g/mol; molecular weight of component i
MWj AS ARRAY(Species) OF REAL
# g/mol; molecular weight of species j
epsiloni AS ARRAY(Components) OF REAL
```

-,Lennard-Jones characteristic energy parameter of component i
epsilonj AS ARRAY(Species) OF REAL
-,Lennard-Jones characteristic energy parameter of species j
sigmai AS ARRAY(Components) OF REAL
Å,Lennard-Jones characteristic length parameter of component i
sigmaj AS ARRAY(Species) OF REAL
Å,Lennard-Jones characteristic length parameter of species j
Y_in_j AS ARRAY(Species) OF REAL
-; feed mole fraction of species j in gas mixture

DISTRIBUTION_DOMAIN

Axial AS [0 : H]
Axial_BFDM AS [0 : H]
Axial_FFDM AS [0 : H]

axial distance coordinate of the column
RADIAL as [0 : Rp]
radial distance coordinate of adsorbent pellet
RADIAL_Micro as [0 : rc]
radial distance coordinate of the micropore

VARIABLE

cgendnorm AS ARRAY(Components) OF Dimensionless2
-; Normalized gas phase concentration at the outlet of the column
cg AS DISTRIBUTION (Components,Axial_BFDM) OF GasConcentration
mol/m^3; concentration of component i in the gas phase
Ctotal AS DISTRIBUTION (Axial) OF GasConcentration
mol/m^3; total concentration in the gas phase
cgp AS DISTRIBUTION (Components,Axial,RADIAL) OF GasConcentration
mol/m^3; concentration of component i in the macropores
q AS DISTRIBUTION(Components,Axial,RADIAL,RADIAL_Micro) OF
SolidConcentration
mol/kg; adsorption capacity of component i in micropores
qm AS DISTRIBUTION (Components,Axial) OF SolidConcentration
mol/kg; adsorption saturation capacity
n AS DISTRIBUTION (Components,Axial) OF Dimensionless2
-; adsorption exponents or number of active sites
rhog AS DISTRIBUTION (Axial) OF Density
kg/m^3; density of gas mixture
vs, v_interstitial AS DISTRIBUTION(Axial_BFDM) OF Velocity
m/s; superficial and interstitial gas velocity

Cpg_CH4, Cpg_CO2, Cpg_He, Cpg, Cvg_CH4, Cvg_CO2,Cvg_He,Cvg AS DISTRIBUTION (Axial) OF HeatCapacity
J/mol.K; molar heat capacity at constant pressure and constant volume for component i and gas mixture
mug, Mu_CH4, Mu_CO2, Mu_He AS DISTRIBUTION (Axial) OF DynamicViscosity
kg/m.s = N.s/m2 = Pa.s ; dynamic viscosity of component i and gas mixture
Re AS DISTRIBUTION (Axial) OF Dimensionless2#notype_gtzero
-; Reynolds number
Sc, Sh AS DISTRIBUTION (Components,Axial) OF Dimensionless2
-; schmidt and sherwood number
Dpore,Dk,Dz AS DISTRIBUTION (Components,Axial) OF Diffusivity
m^2/s; effective pore diffusivity, knudesn diffusivity, axial dispersion coefficient
hi, ho, hw AS DISTRIBUTION (Axial) OF HeatTransferCoeff
W/m^2.K; heat transfer coefficient between fluid and adsorbent,between fluid and column wall and outside column
kL,kg,Lambda_CH4,Lambda_CO2,Lambda_He AS DISTRIBUTION (Axial) OF ThermalConductivity
J/s.m.k = W/m.k; effective axial heat dispersion, thermal conductivity of gas mixture and component i
b AS DISTRIBUTION (Components,Axial) OF Molar_Volume
m^3/mol; Langmuir constant
P AS DISTRIBUTION (Axial_ffdm) OF Pressure
atm; pressure
kf AS DISTRIBUTION (Components,Axial) OF MassTransferCoeff
m/s; film mass transfer coefficient from fluid to particle surface
qe AS DISTRIBUTION (Components,Axial,RADIAL) OF SolidConcentration
mol/kg; adsorbed amount in equilibrium with the macropore gas
#qe AS DISTRIBUTION (Components,Axial) OF SolidConcentration
mol/kg; adsorbed amount in equilibrium with the macropore gas
Tg, Tw AS DISTRIBUTION (Axial_BFDM) OF Temperature
K; gas temperature, temperature of column wall
Ts AS DISTRIBUTION (Axial,RADIAL) OF Temperature
K; solid temperature
Pr, Nui, Nuw, Nuo AS DISTRIBUTION (Axial) OF Dimensionless2
-; prandlt number, nusselt between fluid and adsorbent,between fluid and column wall and outside column
Rao AS DISTRIBUTION (Axial) OF Dimensionless2
-; Rayleight number outside column
Fc_CH4, Fc_CO2,Fc_He AS Dimensionless2
-; factor acoounting molecular shapes and polarities of dilute gases of component i
Tstar_visc_CH4, Tstar_visc_CO2, Tstar_visc_He AS DISTRIBUTION(Axial) of Dimensionless2
-; parameter used in gas viscosity calculation of component i
Omega_visc_CH4, Omega_visc_CO2,Omega_visc_He AS DISTRIBUTION(Axial) of Dimensionless2
-; viscosity collision integral of component i

phi_12, phi_21, phi_13, phi_23, phi_31, phi_32 AS DISTRIBUTION(Axial) of Dimensionless2
-; parameter used in gas mixture viscosity calculation of component i and species j
Betaa_CH4, Betaa_CO2,Betaa_He AS Dimensionless2
-; empirical correlation used in gas thermal conductivity calculation of component i
alfa_CH4, alfa_CO2,alfa_He AS DISTRIBUTION(Axial) of Dimensionless2
-; parameter used in gas thermal conductivity calculation of component i
Z_CH4, Z_CO2,Z_He AS DISTRIBUTION(Axial) of Dimensionless2
-; number of collisions required to interchange a quantum of rotational energy with translational energy of component i
Psi_CH4, Psi_CO2,Psi_He AS DISTRIBUTION(Axial) of Dimensionless2
-; empirical correlation used in gas thermal conductivity calculation of component i
MW_Final AS Array(Species,Components) OF Molecular_Weight
g/mol; parameter used in molecular diffusivity calculation of component i and species j
Tstar AS Distribution(Species,Components,Axial) OF NoType
-; parameter used in molecular diffusivity calculation of component i and species j
Omega AS Distribution(Species,Components,Axial) OF NoType
-; collision integral for diffusion of component i and species j
Sigmaa AS Array(Species,Components) OF Collision_Diameter
Å; collision diameter of component i and species j
D_molecular AS Distribution(Species,Components,Axial) OF Diffusivity
m^2/s; molecular diffusivity of component i and species j
Dm_comp_in_mix AS Distribution(Components,Axial) OF Diffusivity
m^2/s; molecular diffusivity of component i and gas mixture
Qvol AS DISTRIBUTION(Axial) OF VolumetricFlowrate
m^3/s; volumetric flow rate
A_erg, B_erg AS Dimensionless2
-; Constant for Ergun equation (momentum balance)
MW_avg AS DISTRIBUTION(Axial) OF Molecular_Weight
g/mol; molecular weight of gas mixture
MW_avg_prime AS DISTRIBUTION(Axial) OF Molecular_Weight_Prime
kg/mol; molecular weight of gas mixture
Y AS DISTRIBUTION(Components,Axial_BFDM) OF MoleFraction
-; mole fraction of component i
Y_out_CO2 AS MoleFraction
-; outlet mole fraction of component CO2
Y_out_CH4 AS MoleFraction
-; outlet mole fraction of component CH4

SELECTOR
cal_mode AS (initialize, calculate) DEFAULT calculate

BOUNDARY

Boundary Conditions for Gas-Phase Component Mass Balance
#---

```
FOR i in Components DO

PARTIAL(cg(i,0),Axial_BFDM) = (-vs(0) * (cginlet(i) - cg(i,0)))/ Dz(i,0)/eb ;
PARTIAL(cg(i,H),Axial_BFDM) = 0 ;

END

# Boundary Conditions for Macropore Diffusion
#-------------------------------------------------------------------------

FOR i in Components DO
FOR z := 0 TO H DO
  PARTIAL(cgp(i,z,0),RADIAL) = 0 ;
  kf(i,z) * (cg(i,z) - cgp(i,z,Rp)) = ep * Dpore(i,z) * PARTIAL(cgp(i,z,Rp),RADIAL) ;
END
END

# Boundary Conditions for Micropore Diffusion
#-------------------------------------------------------------------------

FOR i in Components DO
FOR z := 0 TO H DO
FOR w := 0 TO Rp DO
  PARTIAL(q(i,z,w,0),RADIAL_Micro)/100 = 0 ;
  kb(i) * (qe(i,z,w) - q(i,z,w,rc)) = 3/rc * Dc(i) * PARTIAL(q(i,z,w,rc),RADIAL_Micro) ;
END
END
END

# Boundary Conditions for Gas-Phase Energy Balance
#-------------------------------------------------------------------------

PARTIAL(Tg(0),Axial_BFDM) = (rhog(0)*Cpg(0)*vs(0)*(Tg(0) - Tfeed))/kL(0)/eb;
PARTIAL(Tg(H),Axial_BFDM) = 0 ;

# Boundary Conditions for Energy Balance of Column Wall
#-------------------------------------------------------------------------

Tw(0) = (Tfeed+Tamb)/2 ;
PARTIAL(Tw(H),Axial_BFDM) = 0 ;

# Boundary Conditions for Solid-Phase Energy Balance
#-------------------------------------------------------------------------

FOR z := 0 TO H DO
  PARTIAL(Ts(z,0),RADIAL) = 0 ;
```

```
  hi(z) * (Tg(z) - Ts(z,Rp)) = ksg * PARTIAL(Ts(z,Rp),RADIAL) ;

END

# Boundary Conditions for Momentum balance
#-------------------------------------------------------------------------------
P(H) = Pfeed ;

# Velocity Boundary Conditions for the Overall Mass Balance
#-------------------------------------------------------------------------------
vs(0) = Qin / Area  ;
PARTIAL(Ctotal(H)*vs(H), Axial_BFDM) = 0 ;
```

EQUATION

```
# Molecular Weight
#-------------------------------------------------------------------------------

# Gas Mixture
#-------------------------------------------------------------------------------

FOR z := 0 TO H DO
  CASE cal_mode OF
    WHEN initialize:
      MW_avg(z) = ((MW('CH4') * Y_in('CH4')) + (MW('CO2') * Y_in('CO2')) + (MW('He')
* Y_in('He'))) ;
      # g/mol;

    WHEN calculate:
      MW_avg(z) = ((MW('CH4') * Y('CH4',z)) + (MW('CO2') * Y('CO2',z)) + (MW('He') *
Y('He',z))) ;
      # g/mol;

  END

   MW_avg_prime(z) = MW_avg(z)*1E-3 ;
   # kg/mol;

END

# Thermophysical Properties of the Fluid
#-------------------------------------------------------------------------------

# Viscosity
```

```
#-------------------------------------------------------------------------------

# Pure Component Gas
#-------------------------------------------------------------------------------


 Fc_CH4 = 1 -(0.2756*W_c('CH4')) ;
 Fc_CO2 = 1 -(0.2756*W_c('CO2')) ;
 Fc_He = 1 -(0.2756*W_c('He')) ;

 FOR z := 0 TO H DO
   CASE cal_mode OF
     WHEN initialize:
        Tstar_visc_CH4(z) = 1.2593 *(Tfeed/T_c('CH4')) ;
        Tstar_visc_CO2(z) = 1.2593 *(Tfeed/T_c('CO2')) ;
        Tstar_visc_He(z) = 1.2593 *(Tfeed/T_c('He')) ;
        Mu_CH4(z) = ((40.785*Fc_CH4*(MW('CH4')*Tfeed)^0.5)/((V_c('CH4'))^0.66666667
* Omega_visc_CH4(z)))*(10^(-7)) ;
        Mu_CO2(z) = ((40.785*Fc_CO2*(MW('CO2')*Tfeed)^0.5)/((V_c('CO2'))^0.66666667
* Omega_visc_CO2(z)))*(10^(-7)) ;
        Mu_He(z) = ((40.785*Fc_He*(MW('He')*Tfeed)^0.5)/((V_c('He'))^0.66666667 *
Omega_visc_He(z)))*(10^(-7)) ;

     WHEN calculate:
        Tstar_visc_CH4(z) = 1.2593 *(Tg(z)/T_c('CH4')) ;
        Tstar_visc_CO2(z) = 1.2593 *(Tg(z)/T_c('CO2')) ;
        Tstar_visc_He(z) = 1.2593 *(Tg(z)/T_c('He')) ;
        Mu_CH4(z) = ((40.785*Fc_CH4*(MW('CH4')*Tg(z))^0.5)/((V_c('CH4'))^0.66666667
* Omega_visc_CH4(z)))*(10^(-7)) ;
        Mu_CO2(z) = ((40.785*Fc_CO2*(MW('CO2')*Tg(z))^0.5)/((V_c('CO2'))^0.66666667
* Omega_visc_CO2(z)))*(10^(-7)) ;
        Mu_He(z) = ((40.785*Fc_He*(MW('He')*Tg(z))^0.5)/((V_c('He'))^0.66666667 *
Omega_visc_He(z)))*(10^(-7)) ;
   END
 Omega_visc_CH4(z) = (1.16145/(Tstar_visc_CH4(z))^0.14874)+ (0.52487*(EXP((-
0.7732)*Tstar_visc_CH4(z))))+ (2.16178*(EXP((-2.43787)*Tstar_visc_CH4(z)))) ;
 Omega_visc_CO2(z) = (1.16145/(Tstar_visc_CO2(z))^0.14874)+ (0.52487*(EXP((-
0.7732)*Tstar_visc_CO2(z))))+ (2.16178*(EXP((-2.43787)*Tstar_visc_CO2(z)))) ;
 Omega_visc_He(z) = (1.16145/(Tstar_visc_He(z))^0.14874)+ (0.52487*(EXP((-
0.7732)*Tstar_visc_He(z))))+ (2.16178*(EXP((-2.43787)*Tstar_visc_He(z)))) ;
 END



# Gas Mixture
#-------------------------------------------------------------------------------
```

```
FOR z := 0 TO H DO

 phi_12(z) = (1 + (Mu_CH4(z)/Mu_CO2(z))^0.5 * (MW('CO2')/MW('CH4'))^0.25)^2/(8 * (1
+ (MW('CH4')/MW('CO2'))))^0.5 ;
 phi_21(z) = (Mu_CO2(z)/Mu_CH4(z)) * (MW('CH4')/MW('CO2')) * phi_12(z) ;
 phi_13(z) = (1 + (Mu_CH4(z)/Mu_He(z))^0.5 * (MW('He')/MW('CH4'))^0.25)^2/(8 * (1 +
(MW('CH4')/MW('He'))))^0.5 ;
 phi_31(z) = (Mu_He(z)/Mu_CH4(z)) * (MW('CH4')/MW('He')) * phi_13(z) ;
 phi_23(z) = (1 + (Mu_CO2(z)/Mu_He(z))^0.5 * (MW('He')/MW('CO2'))^0.25)^2/(8 * (1 +
(MW('CO2')/MW('He'))))^0.5 ;
 phi_32(z) = (Mu_He(z)/Mu_CO2(z)) * (MW('CO2')/MW('He')) * phi_23(z) ;


   CASE cal_mode OF
    WHEN initialize:
       mug(z) = ((Y_in('CH4')*Mu_CH4(z))/(Y_in('CH4') + (Y_in('CO2')*phi_12(z)) +
(Y_in('He')*phi_13(z))))
              + ((Y_in('CO2')*Mu_CO2(z))/(Y_in('CO2') + (Y_in('CH4')*phi_21(z)) +
(Y_in('He')*phi_23(z))))
              + ((Y_in('He')*Mu_He(z))/(Y_in('He') + (Y_in('CH4')*phi_31(z)) +
(Y_in('CO2')*phi_32(z)))) ;


    WHEN calculate:
       mug(z) = ((Y('CH4',z)*Mu_CH4(z))/(Y('CH4',z) + (Y('CO2',z)*phi_12(z)) +
(Y('He',z)*phi_13(z))))
              + ((Y('CO2',z)*Mu_CO2(z))/(Y('CO2',z) + (Y('CH4',z)*phi_21(z)) +
(Y('He',z)*phi_23(z))))
              + ((Y('He',z)*Mu_He(z))/(Y('He',z) + (Y('CH4',z)*phi_31(z)) +
(Y('CO2',z)*phi_32(z)))) ;

   END

END

# Density
#-------------------------------------------------------------------------------

# Gas Mixture
#-------------------------------------------------------------------------------

FOR z := 0 TO H DO

   CASE cal_mode OF
    WHEN initialize:
```

```
      rhog(z) = ((Pfeed * ((MW_prime('CH4') * Y_in('CH4')) + (MW_prime('CO2') *
Y_in('CO2')) + (MW_prime('He') * Y_in('He'))))/(R_Latm * Tfeed))   ;

    WHEN calculate:
      rhog(z) = ((P(z) * ((MW_prime('CH4') * Y('CH4',z)) + (MW_prime('CO2') *
Y('CO2',z)) + (MW_prime('He') * Y('He',z))))/(R_Latm * Tg(z)))   ;

  END

END

# Heat Capacity at Contant Pressure
#-------------------------------------------------------------------------

# Pure Component Gas
#-------------------------------------------------------------------------

FOR z := 0 TO H DO

  CASE cal_mode OF
    WHEN initialize:
      Cpg_CH4(z) = ((4.568 +((-8.975*10^(-3))*Tfeed)+((3.631*10^(-5))*(Tfeed)^(2))+((-
3.407*10^(-8))*(Tfeed)^(3))+((1.091*10^(-11))*(Tfeed)^(4)))* R)/MW_prime('CH4') ;
      Cpg_CO2(z) = ((3.259 +((1.356*10^(-3))*Tfeed)+((1.502*10^(-5))*(Tfeed)^(2))+((-
2.374*10^(-8))*(Tfeed)^(3))+((1.056*10^(-11))*(Tfeed)^(4)))* R)/MW_prime('CO2') ;
      Cpg_He(z) = ((20.78603 +((4.850638*10^(-10))*(10^(-3))*Tfeed)+((-1.582916*10^(-
10))*(10^(-3))*(Tfeed)^(2))+((1.525102*10^(-11))*(10^(-
3))*(Tfeed)^(3))+(((3.196347*10^(-11)))/((Tfeed)^(2))*10^(-3))))/(MW_prime('He')) ;

      Cpg(z) = (Y_in('CH4') * Cpg_CH4(z)) + (Y_in('CO2') * Cpg_CO2(z)) + (Y_in('He') *
Cpg_He(z));
    WHEN calculate:
      Cpg_CH4(z) = ((4.568 +((-8.975*10^(-3))*Tg(z))+((3.631*10^(-5))*(Tg(z))^(2))+((-
3.407*10^(-8))*(Tg(z))^(3))+((1.091*10^(-11))*(Tg(z))^(4)))* R)/MW_prime('CH4') ;
      Cpg_CO2(z) = ((3.259 +((1.356*10^(-3))*Tg(z))+((1.502*10^(-5))*(Tg(z))^(2))+((-
2.374*10^(-8))*(Tg(z))^(3))+((1.056*10^(-11))*(Tg(z))^(4)))* R)/MW_prime('CO2') ;
      Cpg_He(z) = ((20.78603 +((4.850638*10^(-10))*(10^(-3))*Tg(z))+((-1.582916*10^(-
10))*(10^(-3))*(Tg(z))^(2))+((1.525102*10^(-11))*(10^(-
3))*(Tg(z))^(3))+(((3.196347*10^(-11)))/((Tg(z))^(2))*10^(-3))))/(MW_prime('He')) ;

      Cpg(z) = (Y('CH4',z) * Cpg_CH4(z)) + (Y('CO2',z) * Cpg_CO2(z)) + (Y('He',z) *
Cpg_He(z)) ;
  END

END
```

```
# Heat Capacity at Contant Volume
#-------------------------------------------------------------------------------

# Pure Component Gas
#-------------------------------------------------------------------------------

FOR z := 0 TO H DO

 Cvg_CH4(z) = Cpg_CH4(z) - (R/MW_prime('CH4')) ;
 Cvg_CO2(z) = Cpg_CO2(z) - (R/MW_prime('CO2')) ;
 Cvg_He(z) = Cpg_He(z) - (R/MW_prime('He')) ;

END

# Gas Mixture
#-------------------------------------------------------------------------------


FOR z := 0 TO H DO

   CASE cal_mode OF
     WHEN initialize:
        Cvg(z) = (Y_in('CH4') * Cvg_CH4(z)) + (Y_in('CO2') * Cvg_CO2(z)) + (Y_in('He') *
Cvg_He(z)) ;
     WHEN calculate:
        Cvg(z) = (Y('CH4',z) * Cvg_CH4(z)) + (Y('CO2',z) * Cvg_CO2(z)) + (Y('He',z) *
Cvg_He(z)) ;
   END

END


# Thermal Conductivity
#-------------------------------------------------------------------------------

# Pure Component Gas
#-------------------------------------------------------------------------------

Betaa_CH4 = 0.7862 - (0.7109*W_c('CH4')) + (1.3168*(W_c('CH4'))^2) ;
Betaa_CO2 = 0.7862 - (0.7109*W_c('CO2')) + (1.3168*(W_c('CO2'))^2) ;
Betaa_He = 0.7862 - (0.7109*W_c('He')) + (1.3168*(W_c('He'))^2) ;

FOR z := 0 TO H DO

alfa_CH4(z) = ((Cvg_CH4(z)*MW_prime('CH4'))/R) - 1.5 ;
```

```
alfa_CO2(z) = ((Cvg_CO2(z)*MW_prime('CO2'))/R) - 1.5 ;
#alfa_He(z) = ((Cvg_He(z)*MW_prime('He'))/R) - 1.5 ;
#alfa_He(z) = ((Cvg_He(z)*MW_prime('He'))/R) - 1.5 ;

alfa_He(z) = alfa_CO2(z);#((Cvg_He(z)*MW_prime('He'))/R) - 1.5 ;

  CASE cal_mode OF
    WHEN initialize:
      Z_CH4(z) = 2 + (10.5*(Tfeed/T_c('CH4'))^2) ;
      Z_CO2(z) = 2 + (10.5*(Tfeed/T_c('CO2'))^2) ;
      Z_He(z) = 2 + (10.5*(Tfeed/T_c('He'))^2) ;
    WHEN calculate:
      Z_CH4(z) = 2 + (10.5*(Tg(z)/T_c('CH4'))^2) ;
      Z_CO2(z) = 2 + (10.5*(Tg(z)/T_c('CO2'))^2) ;
      Z_He(z) = 2 + (10.5*(Tg(z)/T_c('He'))^2) ;

  END

Psi_CH4(z) = 1 + alfa_CH4(z)*(((0.215 + 0.28288*alfa_CH4(z)) - (1.061*Betaa_CH4) +
(0.26665*Z_CH4(z)))/(0.6366 + (Betaa_CH4*Z_CH4(z)) +
(1.061*Betaa_CH4*alfa_CH4(z)))) ;
Psi_CO2(z) = 1 + alfa_CO2(z)*(((0.215 + 0.28288*alfa_CO2(z)) - (1.061*Betaa_CO2) +
(0.26665*Z_CO2(z)))/(0.6366 + (Betaa_CO2*Z_CO2(z)) +
(1.061*Betaa_CO2*alfa_CO2(z)))) ;
Psi_He(z) = 1 + alfa_He(z)*(((0.215 + 0.28288*alfa_He(z)) - (1.061*Betaa_He) +
(0.26665*Z_He(z)))/(0.6366 + (Betaa_He*Z_He(z)) + (1.061*Betaa_He*alfa_He(z)))) ;
Lambda_CH4(z) =
(3.75*Cvg_CH4(z)*MW_prime('CH4')*Psi_CH4(z)*(Mu_CH4(z)))/(((Cvg_CH4(z)*MW_pr
ime('CH4'))/R)*MW_prime('CH4')) ;
Lambda_CO2(z) =
(3.75*Cvg_CO2(z)*MW_prime('CO2')*Psi_CO2(z)*(Mu_CO2(z)))/(((Cvg_CO2(z)*MW_pr
ime('CO2'))/R)*MW_prime('CO2')) ;
Lambda_He(z) =
(3.75*Cvg_He(z)*MW_prime('He')*Psi_He(z)*(Mu_He(z)))/(((Cvg_He(z)*MW_prime('He'
))/R)*MW_prime('He')) ;

END

# Gas Mixture
#-------------------------------------------------------------------------

FOR z := 0 TO H DO

  CASE cal_mode OF
    WHEN initialize:
```

```
      kg(z) = ((Y_in('CH4')*Lambda_CH4(z))/(Y_in('CH4') + (Y_in('CO2')*phi_12(z)) +
(Y_in('He')*phi_13(z))))
              + ((Y_in('CO2')*Lambda_CO2(z))/(Y_in('CO2') + (Y_in('CH4')*phi_21(z)) +
(Y_in('He')*phi_23(z))))
              + ((Y_in('He')*Lambda_He(z))/(Y_in('He') + (Y_in('CH4')*phi_31(z)) +
(Y_in('CO2')*phi_32(z)))) ;

    WHEN calculate:
      kg(z) = ((Y('CH4',z)*Lambda_CH4(z))/(Y('CH4',z) + (Y('CO2',z)*phi_12(z)) +
(Y('He',z)*phi_13(z))))
              + ((Y('CO2',z)*Lambda_CO2(z))/(Y('CO2',z) + (Y('CH4',z)*phi_21(z)) +
(Y('He',z)*phi_23(z))))
              + ((Y('He',z)*Lambda_He(z))/(Y('He',z) + (Y('CH4',z)*phi_31(z)) +
(Y('CO2',z)*phi_32(z)))) ;

  END
END


# Diffusivity Relations
#-------------------------------------------------------------------------------

# Molecular Diffusivity
#-------------------------------------------------------------------------------

FOR j in Species DO
FOR i in Components DO

MW_Final(j,i) = ((1/MWi(i))+(1/MWj(j))) ;

END
END

FOR j in Species DO
FOR i in Components DO
FOR z := 0 TO H DO

  CASE cal_mode OF
    WHEN initialize:
      Tstar(j,i,z) = Tfeed/(epsiloni(i) * epsilonj(j))^0.5 ;
    WHEN calculate:
      Tstar(j,i,z) = Tg(z)/(epsiloni(i) * epsilonj(j))^0.5 ;
  END

END
END
```

```
END

FOR j in Species DO
FOR i in Components DO
FOR z := 0 TO H DO

Omega(j,i,z) = (1.06036/(Tstar(j,i,z))^0.15610) + ( 0.19300/EXP(0.47635*Tstar(j,i,z))) +
(1.03587/EXP(1.52996*Tstar(j,i,z))) + (1.76474/EXP(3.89411*Tstar(j,i,z))) ;


END
END
END

FOR j in Species DO
FOR i in Components DO

sigmaa(j,i) = 0.5 * (sigmai(i) + sigmaj(j)) ;

END
END

FOR j in Species DO
FOR i in Components DO
FOR z := 0 TO H DO

  CASE cal_mode OF
   WHEN initialize:
     D_molecular(j,i,z) = ((0.0018583)*(((Tfeed)^3)*MW_Final(j,i))^0.5 /
(Pfeed*((sigmaa(j,i))^2)*Omega(j,i,z)))/10000 ;
   WHEN calculate:
     D_molecular(j,i,z) = ((0.0018583)*(((Tg(z))^3)*MW_Final(j,i))^0.5 /
(P(z)*((sigmaa(j,i))^2)*Omega(j,i,z)))/10000 ;
  END

END
END
END


FOR i in Components DO
FOR z := 0 TO H DO

  CASE cal_mode OF
   WHEN initialize:
```

```
      Dm_comp_in_mix(i,z) = (1 - Y_in(i)) / ((SIGMA(Y_in()/D_molecular(,i,z)))-
(Y_in(i)/D_molecular(i,i,z))) ;
    WHEN calculate:
      Dm_comp_in_mix(i,z) = (1 - Y(i,z)) / ((SIGMA(Y(,z)/D_molecular(,i,z)))-
(Y(i,z)/D_molecular(i,i,z))) ;
  END
#
#
END
END

# Knudsen Diffusivity
#-------------------------------------------------------------------------

FOR i in Components DO
FOR z := 0 TO H DO

  CASE cal_mode OF
    WHEN initialize:
      Dk(i,z) = (9700 * rpore_avg * (Tfeed/MW(i))^0.5)/10000 ;
    WHEN calculate:
      Dk(i,z) = (9700 * rpore_avg * (Tg(z)/MW(i))^0.5)/10000 ;
  END

END
END

# Effective Macropore Diffusivity
#-------------------------------------------------------------------------

FOR i in Components DO
FOR z := 0 TO H DO

Dpore(i,z) = ((ep * Dk(i,z) * Dm_comp_in_mix(i,z)) / (tortuosityfactor * (Dk(i,z) +
Dm_comp_in_mix(i,z)))) ;

END
END


# Mass Transfer Relations
#-------------------------------------------------------------------------

FOR z := 0 TO H DO

#Re(z) =  rhog(z)*vs(z)*dp/(mug(z)) ;
```

```
Re(z) =  rhog(z)*MAX(1E-5,vs(z))*dp/(mug(z)) ;
# -; Reynolds number
END

FOR i in Components DO
FOR z := 0 TO H DO


Sc(i,z) =    (mug(z))/(rhog(z)*Dm_comp_in_mix(i,z));
# -; Schimdt number
Dz(i,z) =   (Dm_comp_in_mix(i,z)/eb)*(20 + 0.5*Re(z)*Sc(i,z)) ;
# m^2/s; axial dispersion coefficient
Sh(i,z) =    2 + 1.1*(ABS(Sc(i,z)+1E-5)^(1/3))*(ABS(Re(z)+1E-5)^0.6);
# -; Sherwood number
kf(i,z) =    Sh(i,z)*Dm_comp_in_mix(i,z)/dp;
# m/s; film mass transfer coefficient from fluid to particle surface

END
END



# Heat Transfer Relations (Inside Column)
#-------------------------------------------------------------------------

FOR z := 0 TO H DO

Pr(z) =   (Cpg(z) * mug(z))/ kg(z) ;
# -; Prandlt number
#Nui(z) =   2 + 1.1*(Pr(z)^(1/3))*(Re(z)^0.6);
Nui(z) =   2 + 1.1*(ABS(Pr(z)+1E-5)^(1/3))*(ABS(Re(z)+1E-5)^0.6);
# -; Nusselt number between fluid and adsorbent
hi(z)  =   kg(z)*Nui(z)/dp;
# W/m^2.K; convective film heat transfer coefficient between fluid and adsorbent
Nuw(z) =   12.5 + 0.048*Re(z);
# -; Nusselt number inside column between fluid and column wall
hw(z)  =   kg(z)*Nuw(z)/di;
# W/m^2.K; internal convective heat transfer coefficient between fluid and column wall
kL(z) =    kg(z)*(7 + (0.5*Pr(z)*Re(z))) ;
# J/s.m.k; effective axial heat dispersion inside column
END

# Heat Transfer Relations (Outside Column)
#-------------------------------------------------------------------------

FOR z := 0 TO H DO
```

```
Rao(z)= ABS((Tw(z) - Tamb)*g*(do_^3)/Tamb/nuamb/Alphamb) ;
# -; Rayleight number outside column
Nuo(z)= 0.68 + (0.67*(ABS(Rao(z)+1E-5)^(1/4)))/(1 + (0.492/Pramb)^(9/16))^(4/9) ;
# -; Nusselt number outside column
ho(z) = kamb*Nuo(z)/do_ ;
# W/m^2.K; heat transfer coefficient outside column

END

#Multicomponent Temperature Dependent SIPS Isotherm
#-------------------------------------------------------------------------

FOR i in Components DO
FOR z := 0 TO H DO
b(i,z) = (b0(i)*EXP(Heat_RTg(i)*((T0/Tg(z))-1))) ; #atm^-1
qm(i,z) = (qm0(i)*EXP(X(i)*(1-(Tg(z)/T0))))  ;      #mol/kg
n(i,z) = (n0(i)+(alfa(i)*(1-(T0/Tg(z))))) ;        #dimensionless
END
END

FOR i in Components - "He" DO
FOR z := 0 TO H DO
FOR w := 0 TO Rp DO

CASE cal_mode OF
    WHEN initialize:
        qe(i,z,w) =
(qm(i,z)*(b(i,z)*((cgp(i,z,w)*R_Latm*Tfeed)))^(1/n(i,z)))/(1+((b0_CH4*EXP(Heat_RTg_C
H4*((T0/Tfeed)-1)))*(cgp('CH4',z,w)*R_Latm*Tfeed))^(1/(n0_CH4+(alfa_methane*(1-
(T0/Tfeed)))))+ ((b0_CO2*EXP(Heat_RTg_CO2*((T0/Tfeed)-
1)))*(cgp('CO2',z,w)*R_Latm*Tfeed))^(1/(n0_CO2+(alfa_CarbonDioxide*(1-
(T0/Tfeed)))))+ ((b0_He*EXP(Heat_RTg_He*((T0/Tfeed)-
1)))*(cgp('He',z,w)*R_Latm*Tfeed))^(1/(n0_He+(alfa_Helium*(1-(T0/Tfeed))))) ;
    WHEN calculate:
        qe(i,z,w) = (qm(i,z)*ABS(b(i,z)*((cgp(i,z,w)*R_Latm*Tg(z)))+1E-
5)^(1/n(i,z)))/(1+ABS((b0_CH4*EXP(Heat_RTg_CH4*((T0/Tg(z))-
1)))*(cgp('CH4',z,w)*R_Latm*Tg(z))+1E-5)^(1/(n0_CH4+(alfa_methane*(1-(T0/Tg(z))))))+
ABS((b0_CO2*EXP(Heat_RTg_CO2*((T0/Tg(z))-
1)))*(cgp('CO2',z,w)*R_Latm*Tg(z))+1E-5)^(1/(n0_CO2+(alfa_CarbonDioxide*(1-
(T0/Tg(z))))))+ ABS((b0_He*EXP(Heat_RTg_He*((T0/Tg(z))-
1)))*(cgp('He',z,w)*R_Latm*Tg(z))+1E-5)^(1/(n0_He+(alfa_Helium*(1-(T0/Tg(z)))))) ;

  END

END
```

```
END
END

qe("He",,) = 0 ;

#% Mass Balances
#-------------------------------------------------------------------------

# Gas-Phase Component Mass Balance
#-------------------------------------------------------------------------

FOR i in Components DO
FOR z := 0|+ TO H|- DO



$cg(i,z) = Dz(i,z)*PARTIAL(cg(i,z),Axial_BFDM,Axial_BFDM)
        -
((1/eb)*((vs(z)*PARTIAL(cg(i,z),Axial_BFDM))+(cg(i,z)*PARTIAL(vs(z),Axial_BFDM))))
        - ((3/Rp)*((1-eb)/eb)*kf(i,z)*(cg(i,z)- cgp(i,z,Rp))) ;
END
END

# Diffusion in Macropores
#-------------------------------------------------------------------------

FOR i in Components DO
 FOR z := 0 TO H DO
  FOR w := 0|+ TO Rp|- DO

     $cgp(i,z,w) = (1/(w^2)) * PARTIAL((w^2) * Dpore(i,z) *
PARTIAL(cgp(i,z,w),RADIAL),RADIAL) - (kb(i)*(rhop/ep)*(qe(i,z,w)- q(i,z,w,rc)));

   END
  END
END


# Diffusion in Micropores
#-------------------------------------------------------------------------

FOR i in Components - "He" DO
 FOR z := 0 TO H DO
  FOR w := 0 TO Rp DO
   FOR e := 0|+ TO rc|- DO
```

```
    $q(i,z,w,e) =  (1/(e^2)) * PARTIAL((e^2) * Dc(i) *
PARTIAL(q(i,z,w,e),RADIAL_Micro),RADIAL_Micro);

  END
 END
END
END

q("He",,,0|+:rc|-) = 0 ;

#Energy Balances
#-------------------------------------------------------------------------

# Gas-Phase Energy Balance
#-------------------------------------------------------------------------

FOR z := 0|+ TO H|- DO


$Tg(z) = kL(z)*PARTIAL(Tg(z),Axial_BFDM,Axial_BFDM)/rhog(z)/Cpg(z)/eb
       - ((1/eb)*((vs(z)*PARTIAL(Tg(z),Axial_BFDM))+
(Tg(z)*PARTIAL(vs(z),Axial_BFDM))))
       - 2*hw(z)*(Tg(z) - Tw(z))/eb/ri/rhog(z)/Cpg(z)
       - ((1-eb)/eb)*hi(z)*(3/rp)*(Tg(z)-Ts(z,Rp))/rhog(z)/Cpg(z) ;

END

# Solid Phase Energy Balance
#-------------------------------------------------------------------------

FOR z := 0 TO H DO
 FOR w := 0|+ TO Rp|- DO
  $Ts(z,w) = (ksg * (PARTIAL(PARTIAL(Ts(z,w), RADIAL), RADIAL) + 2/w *
PARTIAL(Ts(z,w), RADIAL)) - (rhop * SIGMA(DeltaH()*(kb()*(qe(,z,w)- q(,z,w,rc))))))/
rhop/Cpp  ;
 END
END

# Energy Balance for Column Wall
#-------------------------------------------------------------------------

FOR z := 0|+ TO H|- DO

$Tw(z) = kw*PARTIAL(Tw(z),Axial_BFDM,Axial_BFDM)/(rhow*Cpw)
       + 2*ri*hi(z)/((ro^2 - ri^2)*rhow*Cpw)*(Tg(z) - Tw(z))
       - 2*ro*ho(z)/((ro^2 - ri^2)*rhow*Cpw)*(Tw(z) - Tamb) ;
```

```
END

# Momentum Balance
#-------------------------------------------------------------------------

A_erg = 150 ;
B_erg = 1.75 ;

FOR z := 0 TO H|- DO

-PARTIAL(P(z), Axial_FFDM)*101325 = (A_erg * (mug(z)) * (1 - eb)^2 * vs(z) /(eb^3 *
dp^2)
                + B_erg * (1-eb) / ((dp) * (eb)^3) * vs(z) * ABS(vs(z)) * rhog(z)) ;
END




# Normalized gas phase concentration at the outlet of the column
#-------------------------------------------------------------------------

FOR i in Components DO

cgendnorm(i) = cg(i,H)/SIGMA(cg(,H)) ;

END

# Total Concentration in the Gas Phase
#-------------------------------------------------------------------------

FOR z := 0 TO H DO

Ctotal(z) = (P(z)/(R_Latm*Tg(z))) ;

END


# Overall Mass Balance
#-------------------------------------------------------------------------

FOR z := 0|+ TO H|- DO

Ctotal(z) = SIGMA(cg(,z));

END
```

```
# Volumetric Flow Rate
#-------------------------------------------------------------------------------
FOR z := 0 TO H DO

v_interstitial(z) = vs(z)/eb ;
Qvol(z) = Area * v_interstitial(z) * eb ;

END


# Mole Fraction of component i
#-------------------------------------------------------------------------------

FOR i in Components - Components.last DO
FOR z := 0 TO H DO

  Y(i,z) = cg(i,z)/Ctotal(z) ;

 END
END

FOR z := 0 TO H DO

  SIGMA(Y(,z)) = 1 ;

 END

Y_out_CO2 = Y('CO2',H) ;
Y_out_CH4 = Y('CH4',H) ;


INITIALISATION_PROCEDURE init
START
  cal_mode := initialize ;
END
NEXT
  JUMP_TO
    cal_mode := calculate ;
  END
END
```

APPENDIX C – gPROMS codes (Distribution domain: axial direction in the column)

Case study:

* Adsorption breakthrough modeling for a feed composition of 60%CH_4 - 40%CO2 on CMS(C) at a total pressure of 9 atm, bed temperature of 294K and inlet flow rate of 400 ml/min (T= 294K and P=1 atm)

* Concentration and temperature gradients exist in the axial direction in the column

Codes:

PARAMETER

```
Components AS ORDERED_SET
# Components i of the gas mixture
Species AS ORDERED_SET
# Species j of the gas mixture
PI AS REAL DEFAULT 3.1416
# pi number
g  AS REAL DEFAULT 9.81
# m/s^2; gravitational constant
R  AS REAL DEFAULT 8.3144621
# Pa.m^3/mol.K; ideal gas constant
R_Latm AS REAL DEFAULT 8.205745*(10^(-5))
# m^3.atm/mol.K; ideal gas constant

# Pellet Characteristics
#-------------------------------------------------------------------------------
#dp AS REAL DEFAULT 0.00142
# m; mean pellet diameter
Rp AS REAL DEFAULT dp/2
#% m; mean pellet radius
rhos AS REAL DEFAULT 875
# kg/m^3; skeletal density of pellet
Cps AS REAL DEFAULT 680
# J/kg.K; specific heat capacity of pellet
rhop AS REAL DEFAULT 1025.938098
# kg/m^3; particle density of pellet
ep AS REAL DEFAULT 0.33
# -; particle void fraction
Cpp AS REAL DEFAULT 880
```

```
# J/kg.K; specific heat capacity of pellet
ksg AS REAL DEFAULT 0.7
# W/m.K; effective thermal conductivity of pellet
rc AS REAL DEFAULT 3.7*(10^(-6))
# m; mean radius of crystals
rpore_avg AS REAL DEFAULT  4*(10^(-8))
# cm; mean pore radius
tortuosityfactor  AS REAL DEFAULT 3
# -; tortuosityfactor

# Column Characteristics
#-------------------------------------------------------------------------
H AS REAL DEFAULT 0.25
# m; column length
di AS REAL DEFAULT 0.02104
# m; column internal diameter
ri AS REAL DEFAULT di/2
# m; column internal radius
wall AS REAL DEFAULT 0.00431
# m; column wall thickness
do_ AS REAL DEFAULT 0.02535
# m; column external diameter
ro AS REAL DEFAULT do_/2
# m; column external radius
Area AS REAL DEFAULT (PI/4) * ((di)^2)
# m^2; cross sectional area of the column
eb AS REAL DEFAULT 0.296324633
# -; column void fraction



# Flow Characteristics
#-------------------------------------------------------------------------

Tamb AS REAL DEFAULT 294.36
# K; ambient temperature
MW AS ARRAY(Components) OF REAL
# g/mol; molecular weight
MW_prime AS ARRAY(Components) OF REAL
# kg/mol; molecular weight
V_c AS ARRAY(Components) OF REAL
# cm^3 /mol; critical volume
T_c AS ARRAY(Components) OF REAL
# K; critical temperature
W_c AS ARRAY(Components) OF REAL
# -; acentric factor
```

```
Y_in AS ARRAY(Components) OF REAL
# -; feed mole fraction of component i in gas mixture
Pfeed AS REAL DEFAULT 9
# atm; feed pressure
Tfeed AS REAL DEFAULT 294.76
# K; inlet gas temperature
Qin AS REAL DEFAULT 7.40741E-07
# m^3/s; feed volumetric flow rate
cginlet AS ARRAY(Components) of REAL
# mol/m^3; feed concentration of component i
Ctotal_inlet AS REAL DEFAULT 372.0968082669
# mol/m^3; feed concentration of component i



#% Column Wall Characteristics
#-------------------------------------------------------------------------------
rhow AS REAL DEFAULT 8000
# kg/m^3; density of stainless steel column
Cpw AS REAL DEFAULT 500
# J/kg.K; heat capacity of stainless steel column
kw AS REAL DEFAULT 16.7
# W/m.K; thermal conductivity of stainless steel column


#% Mass and Thermal Transfer Characteristics of Air
#-------------------------------------------------------------------------------
nuamb AS REAL DEFAULT 15.23E-6
# m^2/s; air kinetic viscosity at 294.36 K
kamb AS REAL DEFAULT 0.0259
# W/m.K; thermal conductivity of air  at 294.36 K
Pramb AS REAL DEFAULT 0.71
# -; Prandlt number of ambient air outside column
Alphamb AS REAL DEFAULT (15.57+(22.07-15.67)*(Tamb-250)/50)*(10^(-6))
#% m^2/s; thermal diffusivity of air:


# Mass Transfer and Diffusivity coefficients (Micropore Diffusion)
#-------------------------------------------------------------------------------
kb AS ARRAY(Components) OF REAL
# 1/s; mass transfer coefficient at micropore mouth
Dc_rc2 AS ARRAY(Components) OF REAL
# s^-1; reverse of diffusion time constant

# Temperature Dependant SIPS Isotherm Parameters
#-------------------------------------------------------------------------------
```

```
T0 AS REAL DEFAULT 283.15
#°K; reference temperature
b0 AS ARRAY(Components) OF REAL
# atm^-1; adsorption affinity constant at some reference temperature
Heat_RTg AS ARRAY(Components) OF REAL
# -; constant parameter of toth isotherm model
qm0 AS ARRAY(Components) OF REAL
# mol/kg; adsorption saturation capacity at some reference temperature
DeltaH AS ARRAY(Components) OF REAL
# J/mol; isosteric heat
X AS ARRAY(Components) OF REAL
# -; constant parameter of SIPS isotherm model
n0 AS ARRAY(Components) OF REAL
# -; adsorption exponents or number of active sites at some reference temperature
alfa AS ARRAY(Components) OF REAL
# -; constant parameter of SIPS isotherm model

b0_CH4 AS REAL DEFAULT 0.808900568215052
# atm^-1; adsorption affinity constant at some reference temperature
b0_CO2 AS REAL DEFAULT 1.44733512515504
# atm^-1; adsorption affinity constant at some reference temperature
b0_He AS REAL DEFAULT 0
# atm^-1; adsorption affinity constant at some reference temperature
Heat_RTg_CH4 AS REAL DEFAULT 5.03955811380626
# -; constant parameter of toth isotherm model
Heat_RTg_CO2 AS REAL DEFAULT 9.41333325056097
# -; constant parameter of toth isotherm model
Heat_RTg_He AS REAL DEFAULT 0.0000001
# -; constant parameter of toth isotherm model
n0_CH4 AS REAL DEFAULT 1.08594777550726
# -; adsorption exponents or number of active sites at some reference temperature
n0_CO2 AS REAL DEFAULT 1.4164472249844
# -; adsorption exponents or number of active sites at some reference temperature
n0_He AS REAL DEFAULT 0.0000001
# -; adsorption exponents or number of active sites at some reference temperature
alfa_methane AS REAL DEFAULT 0.322732007064096
# -; constant parameter of toth isotherm model
alfa_CarbonDioxide AS REAL DEFAULT 0.318706297307062
# -; constant parameter of toth isotherm model
alfa_Helium AS REAL DEFAULT 0.0000001
# -; constant parameter of toth isotherm model


# Molecular Diffusivity Parameters
#-------------------------------------------------------------------------
MWi AS ARRAY(Components) OF REAL
```

g/mol; molecular weight of component i
MWj AS ARRAY(Species) OF REAL
g/mol; molecular weight of species j
epsiloni AS ARRAY(Components) OF REAL
-,Lennard-Jones characteristic energy parameter of component i
epsilonj AS ARRAY(Species) OF REAL
-,Lennard-Jones characteristic energy parameter of species j
sigmai AS ARRAY(Components) OF REAL
Å,Lennard-Jones characteristic length parameter of component i
sigmaj AS ARRAY(Species) OF REAL
Å,Lennard-Jones characteristic length parameter of species j
Y_in_j AS ARRAY(Species) OF REAL
-; feed mole fraction of species j in gas mixture

DISTRIBUTION_DOMAIN

Axial AS [0 : H]
Axial_BFDM AS [0 : H]
Axial_FFDM AS [0 : H]

VARIABLE

cgendnorm AS ARRAY(Components) OF Dimensionless2
-; Normalized gas phase concentration at the outlet of the column
cg AS DISTRIBUTION (Components,Axial_BFDM) OF GasConcentration
mol/m^3; concentration of component i in the gas phase
Ctotal AS DISTRIBUTION (Axial) OF GasConcentration
mol/m^3; total concentration in the gas phase
q AS DISTRIBUTION(Components,Axial) OF SolidConcentration
mol/kg; adsorption capacity of component i in micropores
qm AS DISTRIBUTION (Components,Axial) OF SolidConcentration
mol/kg; adsorption saturation capacity
n AS DISTRIBUTION (Components,Axial) OF Dimensionless2
-; adsorption exponents or number of active sites
rhog AS DISTRIBUTION (Axial) OF Density
kg/m^3; density of gas mixture
vs, v_interstitial AS DISTRIBUTION(Axial_BFDM) OF Velocity
m/s; superficial and interstitial gas velocity
Cpg_CH4, Cpg_CO2, Cpg_He, Cpg, Cvg_CH4, Cvg_CO2,Cvg_He,Cvg AS
DISTRIBUTION (Axial) OF HeatCapacity
J/mol.K; molar heat capacity at constant pressure and constant volume for component i and gas mixture
mug, Mu_CH4, Mu_CO2, Mu_He AS DISTRIBUTION (Axial) OF DynamicViscosity
kg/m.s = N.s/m2 = Pa.s ; dynamic viscosity of component i and gas mixture

Re AS DISTRIBUTION (Axial) OF Dimensionless2#notype_gtzero
-; Reynolds number
Sc, Sh AS DISTRIBUTION (Components,Axial) OF Dimensionless2
-; schmidt and sherwood number
Dpore,Dk,Dz AS DISTRIBUTION (Components,Axial) OF Diffusivity
m^2/s; effective pore diffusivity, knudesn diffusivity, axial dispersion coefficient
hi, ho, hw AS DISTRIBUTION (Axial) OF HeatTransferCoeff
W/m^2.K; heat transfer coefficient between fluid and adsorbent,between fluid and column wall and outside column
kL,kg,Lambda_CH4,Lambda_CO2,Lambda_He AS DISTRIBUTION (Axial) OF ThermalConductivity
J/s.m.k = W/m.k; effective axial heat dispersion, thermal conductivity of gas mixture and component i
b AS DISTRIBUTION (Components,Axial) OF Molar_Volume
m^3/mol; Langmuir constant
P AS DISTRIBUTION (Axial_ffdm) OF Pressure
atm; pressure
kf AS DISTRIBUTION (Components,Axial) OF MassTransferCoeff
m/s; film mass transfer coefficient from fluid to particle surface
qe AS DISTRIBUTION (Components,Axial) OF SolidConcentration
mol/kg; adsorbed amount in equilibrium with the macropore gas
#qe AS DISTRIBUTION (Components,Axial) OF SolidConcentration
mol/kg; adsorbed amount in equilibrium with the macropore gas
Tg, Tw AS DISTRIBUTION (Axial_BFDM) OF Temperature
K; gas temperature, temperature of column wall
Ts AS DISTRIBUTION (Axial) OF Temperature
K; solid temperature
Pr, Nui, Nuw, Nuo AS DISTRIBUTION (Axial) OF Dimensionless2
-; prandlt number, nusselt between fluid and adsorbent,between fluid and column wall and outside column
Rao AS DISTRIBUTION (Axial) OF Dimensionless2
-; Rayleight number outside column
Fc_CH4, Fc_CO2,Fc_He AS Dimensionless2
-; factor acoounting molecular shapes and polarities of dilute gases of component i
Tstar_visc_CH4, Tstar_visc_CO2, Tstar_visc_He AS DISTRIBUTION(Axial) of Dimensionless2
-; parameter used in gas viscosity calculation of component i
Omega_visc_CH4, Omega_visc_CO2,Omega_visc_He AS DISTRIBUTION(Axial) of Dimensionless2
-; viscosity collision integral of component i
phi_12, phi_21, phi_13, phi_23, phi_31, phi_32 AS DISTRIBUTION(Axial) of Dimensionless2
-; parameter used in gas mixture viscosity calculation of component i and species j
Betaa_CH4, Betaa_CO2,Betaa_He AS Dimensionless2
-; empirical correlation used in gas thermal conductivity calculation of component i
alfa_CH4, alfa_CO2,alfa_He AS DISTRIBUTION(Axial) of Dimensionless2

-; parameter used in gas thermal conductivity calculation of component i
Z_CH4, Z_CO2,Z_He AS DISTRIBUTION(Axial) of Dimensionless2
-; number of collisions required to interchange a quantum of rotational energy with translational energy of component i
Psi_CH4, Psi_CO2,Psi_He AS DISTRIBUTION(Axial) of Dimensionless2
-; empirical correlation used in gas thermal conductivity calculation of component i
MW_Final AS Array(Species,Components) OF Molecular_Weight
g/mol; parameter used in molecular diffusivity calculation of component i and species j
Tstar AS Distribution(Species,Components,Axial) OF NoType
-; parameter used in molecular diffusivity calculation of component i and species j
Omega AS Distribution(Species,Components,Axial) OF NoType
-; collision integral for diffusion of component i and species j
Sigmaa AS Array(Species,Components) OF Collision_Diameter
Å; collision diameter of component i and species j
D_molecular AS Distribution(Species,Components,Axial) OF Diffusivity
m^2/s; molecular diffusivity of component i and species j
Dm_comp_in_mix AS Distribution(Components,Axial) OF Diffusivity
m^2/s; molecular diffusivity of component i and gas mixture
Qvol AS DISTRIBUTION(Axial) OF VolumetricFlowrate
m^3/s; volumetric flow rate
A_erg, B_erg AS Dimensionless2
-; Constant for Ergun equation (momentum balance)
MW_avg AS DISTRIBUTION(Axial) OF Molecular_Weight
g/mol; molecular weight of gas mixture
MW_avg_prime AS DISTRIBUTION(Axial) OF Molecular_Weight_Prime
kg/mol; molecular weight of gas mixture
Y AS DISTRIBUTION(Components,Axial_BFDM) OF MoleFraction
-; mole fraction of component i
#Y_j AS DISTRIBUTION(Species,Axial) OF MoleFraction
-; mole fraction of species j
K_LDF AS DISTRIBUTION (Components,Axial) OF LumpedMassTransferCoeff
1/s; Overall LDF film mass transfer coefficient from fluid to particle

Y_out_CO2 AS MoleFraction
Y_out_CH4 AS MoleFraction

SELECTOR
cal_mode AS (initialize, calculate) DEFAULT calculate

BOUNDARY

Boundary Conditions for Gas-Phase Component Mass Balance
#---
FOR i in Components DO

PARTIAL(cg(i,0),Axial_BFDM) = (-vs(0) * (cginlet(i) - cg(i,0)))/ Dz(i,0)/eb ;

```
PARTIAL(cg(i,H),Axial_BFDM) = 0 ;

END


# Boundary Conditions for Gas-Phase Energy Balance
#-------------------------------------------------------------------------

PARTIAL(Tg(0),Axial_BFDM) = (rhog(0)*Cpg(0)*vs(0)*(Tg(0) - Tfeed))/kL(0)/eb;
PARTIAL(Tg(H),Axial_BFDM) = 0 ;

# Boundary Conditions for Energy Balance of Column Wall
#-------------------------------------------------------------------------

Tw(0) = (Tfeed+Tamb)/2 ;
PARTIAL(Tw(H),Axial_BFDM) = 0 ;


# Boundary Conditions for Momentum balance
#-------------------------------------------------------------------------

P(H) = Pfeed ;

# Velocity Boundary Conditions for the Overall Mass Balance
#-------------------------------------------------------------------------
vs(0) = Qin / Area  ;
PARTIAL(Ctotal(H)*vs(H), Axial_BFDM) = 0 ;
```

EQUATION

```
# Molecular Weight
#-------------------------------------------------------------------------

# Gas Mixture
#-------------------------------------------------------------------------

FOR z := 0 TO H DO
  CASE cal_mode OF
    WHEN initialize:
      MW_avg(z) = ((MW('CH4') * Y_in('CH4')) + (MW('CO2') * Y_in('CO2')) + (MW('He')
* Y_in('He'))) ;
      # g/mol;
```

```
    WHEN calculate:
      MW_avg(z) = ((MW('CH4') * Y('CH4',z)) + (MW('CO2') * Y('CO2',z)) + (MW('He') *
Y('He',z))) ;
      # g/mol;

  END

   MW_avg_prime(z) = MW_avg(z)*1E-3 ;
   # kg/mol;

END

# Thermophysical Properties of the Fluid
#---------------------------------------------------------------------------

# Viscosity
#---------------------------------------------------------------------------

# Pure Component Gas
#---------------------------------------------------------------------------


 Fc_CH4 = 1 -(0.2756*W_c('CH4')) ;
 Fc_CO2 = 1 -(0.2756*W_c('CO2')) ;
 Fc_He = 1 -(0.2756*W_c('He')) ;

 FOR z := 0 TO H DO
  CASE cal_mode OF
    WHEN initialize:
       Tstar_visc_CH4(z) = 1.2593 *(Tfeed/T_c('CH4')) ;
       Tstar_visc_CO2(z) = 1.2593 *(Tfeed/T_c('CO2')) ;
       Tstar_visc_He(z) = 1.2593 *(Tfeed/T_c('He')) ;
       Mu_CH4(z) = ((40.785*Fc_CH4*(MW('CH4')*Tfeed)^0.5)/((V_c('CH4'))^0.66666667
* Omega_visc_CH4(z)))*(10^(-7)) ;
       Mu_CO2(z) = ((40.785*Fc_CO2*(MW('CO2')*Tfeed)^0.5)/((V_c('CO2'))^0.66666667
* Omega_visc_CO2(z)))*(10^(-7)) ;
       Mu_He(z) = ((40.785*Fc_He*(MW('He')*Tfeed)^0.5)/((V_c('He'))^0.66666667 *
Omega_visc_He(z)))*(10^(-7)) ;

    WHEN calculate:
       Tstar_visc_CH4(z) = 1.2593 *(Tg(z)/T_c('CH4')) ;
       Tstar_visc_CO2(z) = 1.2593 *(Tg(z)/T_c('CO2')) ;
       Tstar_visc_He(z) = 1.2593 *(Tg(z)/T_c('He')) ;
       Mu_CH4(z) = ((40.785*Fc_CH4*(MW('CH4')*Tg(z))^0.5)/((V_c('CH4'))^0.66666667
* Omega_visc_CH4(z)))*(10^(-7)) ;
```

```
      Mu_CO2(z) = ((40.785*Fc_CO2*(MW('CO2')*Tg(z))^0.5)/((V_c('CO2'))^0.66666667
* Omega_visc_CO2(z)))*(10^(-7)) ;
      Mu_He(z) = ((40.785*Fc_He*(MW('He')*Tg(z))^0.5)/((V_c('He'))^0.66666667 *
Omega_visc_He(z)))*(10^(-7)) ;
  END
 Omega_visc_CH4(z) = (1.16145/(Tstar_visc_CH4(z))^0.14874)+ (0.52487*(EXP((-
0.7732)*Tstar_visc_CH4(z))))+ (2.16178*(EXP((-2.43787)*Tstar_visc_CH4(z)))) ;
 Omega_visc_CO2(z) = (1.16145/(Tstar_visc_CO2(z))^0.14874)+ (0.52487*(EXP((-
0.7732)*Tstar_visc_CO2(z))))+ (2.16178*(EXP((-2.43787)*Tstar_visc_CO2(z)))) ;
 Omega_visc_He(z) = (1.16145/(Tstar_visc_He(z))^0.14874)+ (0.52487*(EXP((-
0.7732)*Tstar_visc_He(z))))+ (2.16178*(EXP((-2.43787)*Tstar_visc_He(z)))) ;
 END



# Gas Mixture
#-------------------------------------------------------------------------------

FOR z := 0 TO H DO

 phi_12(z) = (1 + (Mu_CH4(z)/Mu_CO2(z))^0.5 * (MW('CO2')/MW('CH4'))^0.25)^2/(8 * (1
+ (MW('CH4')/MW('CO2'))))^0.5 ;
 phi_21(z) = (Mu_CO2(z)/Mu_CH4(z)) * (MW('CH4')/MW('CO2')) * phi_12(z) ;
 phi_13(z) = (1 + (Mu_CH4(z)/Mu_He(z))^0.5 * (MW('He')/MW('CH4'))^0.25)^2/(8 * (1 +
(MW('CH4')/MW('He'))))^0.5 ;
 phi_31(z) = (Mu_He(z)/Mu_CH4(z)) * (MW('CH4')/MW('He')) * phi_13(z) ;
 phi_23(z) = (1 + (Mu_CO2(z)/Mu_He(z))^0.5 * (MW('He')/MW('CO2'))^0.25)^2/(8 * (1 +
(MW('CO2')/MW('He'))))^0.5 ;
 phi_32(z) = (Mu_He(z)/Mu_CO2(z)) * (MW('CO2')/MW('He')) * phi_23(z) ;


  CASE cal_mode OF
    WHEN initialize:
      mug(z) = ((Y_in('CH4')*Mu_CH4(z))/(Y_in('CH4') + (Y_in('CO2')*phi_12(z)) +
(Y_in('He')*phi_13(z))))
            + ((Y_in('CO2')*Mu_CO2(z))/(Y_in('CO2') + (Y_in('CH4')*phi_21(z)) +
(Y_in('He')*phi_23(z))))
            + ((Y_in('He')*Mu_He(z))/(Y_in('He') + (Y_in('CH4')*phi_31(z)) +
(Y_in('CO2')*phi_32(z)))) ;


    WHEN calculate:
      mug(z) = ((Y('CH4',z)*Mu_CH4(z))/(Y('CH4',z) + (Y('CO2',z)*phi_12(z)) +
(Y('He',z)*phi_13(z))))
            + ((Y('CO2',z)*Mu_CO2(z))/(Y('CO2',z) + (Y('CH4',z)*phi_21(z)) +
(Y('He',z)*phi_23(z))))
```

```
            + ((Y('He',z)*Mu_He(z))/(Y('He',z) + (Y('CH4',z)*phi_31(z)) +
(Y('CO2',z)*phi_32(z))) ;

  END

END

# Density
#-------------------------------------------------------------------------

# Gas Mixture
#-------------------------------------------------------------------------

FOR z := 0 TO H DO

  CASE cal_mode OF
    WHEN initialize:
      rhog(z) = ((Pfeed * ((MW_prime('CH4') * Y_in('CH4')) + (MW_prime('CO2') *
Y_in('CO2')) + (MW_prime('He') * Y_in('He'))))/(R_Latm * Tfeed))   ;

    WHEN calculate:
      rhog(z) = ((P(z) * ((MW_prime('CH4') * Y('CH4',z)) + (MW_prime('CO2') *
Y('CO2',z)) + (MW_prime('He') * Y('He',z))))/(R_Latm * Tg(z)))   ;

  END

END

# Heat Capacity at Contant Pressure
#-------------------------------------------------------------------------

# Pure Component Gas
#-------------------------------------------------------------------------

FOR z := 0 TO H DO

  CASE cal_mode OF
    WHEN initialize:
      Cpg_CH4(z) = ((4.568 +((-8.975*10^(-3))*Tfeed)+((3.631*10^(-5))*(Tfeed)^(2))+((-
3.407*10^(-8))*(Tfeed)^(3))+((1.091*10^(-11))*(Tfeed)^(4)))* R)/MW_prime('CH4') ;
      Cpg_CO2(z) = ((3.259 +((1.356*10^(-3))*Tfeed)+((1.502*10^(-5))*(Tfeed)^(2))+((-
2.374*10^(-8))*(Tfeed)^(3))+((1.056*10^(-11))*(Tfeed)^(4)))* R)/MW_prime('CO2') ;
      Cpg_He(z) = ((20.78603 +((4.850638*10^(-10))*(10^(-3))*Tfeed)+((-1.582916*10^(-
10))*(10^(-3))*(Tfeed)^(2))+((1.525102*10^(-11))*(10^(-
3))*(Tfeed)^(3))+(((3.196347*10^(-11)))/((Tfeed)^(2))*10^(-3))))/(MW_prime('He')) ;
```

```
      Cpg(z) = (Y_in('CH4') * Cpg_CH4(z)) + (Y_in('CO2') * Cpg_CO2(z)) + (Y_in('He') *
Cpg_He(z));
    WHEN calculate:
      Cpg_CH4(z) = ((4.568 +((-8.975*10^(-3))*Tg(z))+((3.631*10^(-5))*(Tg(z))^(2))+((-
3.407*10^(-8))*(Tg(z))^(3))+((1.091*10^(-11))*(Tg(z))^(4)))* R)/MW_prime('CH4') ;
      Cpg_CO2(z) = ((3.259 +((1.356*10^(-3))*Tg(z))+((1.502*10^(-5))*(Tg(z))^(2))+((-
2.374*10^(-8))*(Tg(z))^(3))+((1.056*10^(-11))*(Tg(z))^(4)))* R)/MW_prime('CO2') ;
      Cpg_He(z) = ((20.78603 +((4.850638*10^(-10))*(10^(-3))*Tg(z))+((-1.582916*10^(-
10))*(10^(-3))*(Tg(z))^(2))+((1.525102*10^(-11))*(10^(-
3))*(Tg(z))^(3))+(((3.196347*10^(-11)))/((Tg(z))^(2))*10^(-3))))/(MW_prime('He')) ;

      Cpg(z) = (Y('CH4',z) * Cpg_CH4(z)) + (Y('CO2',z) * Cpg_CO2(z)) + (Y('He',z) *
Cpg_He(z)) ;
  END

END


# Heat Capacity at Contant Volume
#-------------------------------------------------------------------------------

# Pure Component Gas
#-------------------------------------------------------------------------------

FOR z := 0 TO H DO

 Cvg_CH4(z) = Cpg_CH4(z) - (R/MW_prime('CH4')) ;
 Cvg_CO2(z) = Cpg_CO2(z) - (R/MW_prime('CO2')) ;
 Cvg_He(z) = Cpg_He(z) - (R/MW_prime('He')) ;

END

# Gas Mixture
#-------------------------------------------------------------------------------


FOR z := 0 TO H DO

  CASE cal_mode OF
    WHEN initialize:
      Cvg(z) = (Y_in('CH4') * Cvg_CH4(z)) + (Y_in('CO2') * Cvg_CO2(z)) + (Y_in('He') *
Cvg_He(z)) ;
    WHEN calculate:
      Cvg(z) = (Y('CH4',z) * Cvg_CH4(z)) + (Y('CO2',z) * Cvg_CO2(z)) + (Y('He',z) *
Cvg_He(z)) ;
  END
```

```
END


# Thermal Conductivity
#-------------------------------------------------------------------------------

# Pure Component Gas
#-------------------------------------------------------------------------------

Betaa_CH4 = 0.7862 - (0.7109*W_c('CH4')) + (1.3168*(W_c('CH4'))^2) ;
Betaa_CO2 = 0.7862 - (0.7109*W_c('CO2')) + (1.3168*(W_c('CO2'))^2) ;
Betaa_He = 0.7862 - (0.7109*W_c('He')) + (1.3168*(W_c('He'))^2) ;

FOR z := 0 TO H DO

alfa_CH4(z) = ((Cvg_CH4(z)*MW_prime('CH4'))/R) - 1.5 ;
alfa_CO2(z) = ((Cvg_CO2(z)*MW_prime('CO2'))/R) - 1.5 ;
#alfa_He(z) = ((Cvg_He(z)*MW_prime('He'))/R) - 1.5 ;
#alfa_He(z) = ((Cvg_He(z)*MW_prime('He'))/R) - 1.5 ;

alfa_He(z) = alfa_CO2(z);#((Cvg_He(z)*MW_prime('He'))/R) - 1.5 ;

  CASE cal_mode OF
    WHEN initialize:
      Z_CH4(z) = 2 + (10.5*(Tfeed/T_c('CH4'))^2) ;
      Z_CO2(z) = 2 + (10.5*(Tfeed/T_c('CO2'))^2) ;
      Z_He(z) = 2 + (10.5*(Tfeed/T_c('He'))^2) ;
    WHEN calculate:
      Z_CH4(z) = 2 + (10.5*(Tg(z)/T_c('CH4'))^2) ;
      Z_CO2(z) = 2 + (10.5*(Tg(z)/T_c('CO2'))^2) ;
      Z_He(z) = 2 + (10.5*(Tg(z)/T_c('He'))^2) ;

  END

Psi_CH4(z) = 1 + alfa_CH4(z)*(((0.215 + 0.28288*alfa_CH4(z)) - (1.061*Betaa_CH4) +
(0.26665*Z_CH4(z)))/(0.6366 + (Betaa_CH4*Z_CH4(z)) +
(1.061*Betaa_CH4*alfa_CH4(z)))) ;
Psi_CO2(z) = 1 + alfa_CO2(z)*(((0.215 + 0.28288*alfa_CO2(z)) - (1.061*Betaa_CO2) +
(0.26665*Z_CO2(z)))/(0.6366 + (Betaa_CO2*Z_CO2(z)) +
(1.061*Betaa_CO2*alfa_CO2(z)))) ;
Psi_He(z) = 1 + alfa_He(z)*(((0.215 + 0.28288*alfa_He(z)) - (1.061*Betaa_He) +
(0.26665*Z_He(z)))/(0.6366 + (Betaa_He*Z_He(z)) + (1.061*Betaa_He*alfa_He(z)))) ;
Lambda_CH4(z) =
(3.75*Cvg_CH4(z)*MW_prime('CH4')*Psi_CH4(z)*(Mu_CH4(z)))/(((Cvg_CH4(z)*MW_pr
ime('CH4'))/R)*MW_prime('CH4')) ;
```

```
Lambda_CO2(z) =
(3.75*Cvg_CO2(z)*MW_prime('CO2')*Psi_CO2(z)*(Mu_CO2(z)))/(((Cvg_CO2(z)*MW_pr
ime('CO2'))/R)*MW_prime('CO2')) ;
Lambda_He(z) =
(3.75*Cvg_He(z)*MW_prime('He')*Psi_He(z)*(Mu_He(z)))/(((Cvg_He(z)*MW_prime('He'
))/R)*MW_prime('He')) ;

END

# Gas Mixture
#---------------------------------------------------------------------------

FOR z := 0 TO H DO

  CASE cal_mode OF
   WHEN initialize:
     kg(z) = ((Y_in('CH4')*Lambda_CH4(z))/(Y_in('CH4') + (Y_in('CO2')*phi_12(z)) +
(Y_in('He')*phi_13(z))))
            + ((Y_in('CO2')*Lambda_CO2(z))/(Y_in('CO2') + (Y_in('CH4')*phi_21(z)) +
(Y_in('He')*phi_23(z))))
            + ((Y_in('He')*Lambda_He(z))/(Y_in('He') + (Y_in('CH4')*phi_31(z)) +
(Y_in('CO2')*phi_32(z)))) ;

   WHEN calculate:
     kg(z) = ((Y('CH4',z)*Lambda_CH4(z))/(Y('CH4',z) + (Y('CO2',z)*phi_12(z)) +
(Y('He',z)*phi_13(z))))
            + ((Y('CO2',z)*Lambda_CO2(z))/(Y('CO2',z) + (Y('CH4',z)*phi_21(z)) +
(Y('He',z)*phi_23(z))))
            + ((Y('He',z)*Lambda_He(z))/(Y('He',z) + (Y('CH4',z)*phi_31(z)) +
(Y('CO2',z)*phi_32(z)))) ;

  END
END


# Diffusivity Relations
#---------------------------------------------------------------------------

# Molecular Diffusivity
#---------------------------------------------------------------------------

FOR j in Species DO
FOR i in Components DO

MW_Final(j,i) = ((1/MWi(i))+(1/MWj(j))) ;
```

```
END
END

FOR j in Species DO
FOR i in Components DO
FOR z := 0 TO H DO

  CASE cal_mode OF
    WHEN initialize:
      Tstar(j,i,z) = Tfeed/(epsiloni(i) * epsilonj(j))^0.5 ;
    WHEN calculate:
      Tstar(j,i,z) = Tg(z)/(epsiloni(i) * epsilonj(j))^0.5 ;
  END

END
END
END

FOR j in Species DO
FOR i in Components DO
FOR z := 0 TO H DO

Omega(j,i,z) = (1.06036/(Tstar(j,i,z))^0.15610) + ( 0.19300/EXP(0.47635*Tstar(j,i,z))) +
(1.03587/EXP(1.52996*Tstar(j,i,z))) + (1.76474/EXP(3.89411*Tstar(j,i,z))) ;


END
END
END

FOR j in Species DO
FOR i in Components DO

sigmaa(j,i) = 0.5 * (sigmai(i) + sigmaj(j)) ;

END
END

FOR j in Species DO
FOR i in Components DO
FOR z := 0 TO H DO

  CASE cal_mode OF
    WHEN initialize:
      D_molecular(j,i,z) = ((0.0018583)*(((Tfeed)^3)*MW_Final(j,i))^0.5 /
(Pfeed*((sigmaa(j,i))^2)*Omega(j,i,z)))/10000 ;
```

```
    WHEN calculate:
      D_molecular(j,i,z) = ((0.0018583)*(((Tg(z))^3)*MW_Final(j,i))^0.5 /
(P(z)*((sigmaa(j,i))^2)*Omega(j,i,z)))/10000 ;
  END

END
END
END


FOR i in Components DO
FOR z := 0 TO H DO

  CASE cal_mode OF
    WHEN initialize:
      Dm_comp_in_mix(i,z) = (1 - Y_in(i)) / ((SIGMA(Y_in()/D_molecular(,i,z)))-
(Y_in(i)/D_molecular(i,i,z))) ;
    WHEN calculate:
      Dm_comp_in_mix(i,z) = (1 - Y(i,z)) / ((SIGMA(Y(,z)/D_molecular(,i,z)))-
(Y(i,z)/D_molecular(i,i,z))) ;
  END
#
#
END
END

# Knudsen Diffusivity
#-------------------------------------------------------------------------

FOR i in Components DO
FOR z := 0 TO H DO

  CASE cal_mode OF
    WHEN initialize:
      Dk(i,z) = (9700 * rpore_avg * (Tfeed/MW(i))^0.5)/10000 ;
    WHEN calculate:
      Dk(i,z) = (9700 * rpore_avg * (Tg(z)/MW(i))^0.5)/10000 ;
  END

END
END

# Effective Macropore Diffusivity
#-------------------------------------------------------------------------

FOR i in Components DO
```

```
FOR z := 0 TO H DO

Dpore(i,z) = ((ep * Dk(i,z) * Dm_comp_in_mix(i,z)) / (tortuosityfactor * (Dk(i,z) +
Dm_comp_in_mix(i,z)))) ;

END
END


# Mass Transfer Relations
#-------------------------------------------------------------------------------

FOR z := 0 TO H DO

#Re(z) =  rhog(z)*vs(z)*dp/(mug(z)) ;
Re(z) =  rhog(z)*MAX(1E-5,vs(z))*dp/(mug(z)) ;
# -; Reynolds number
END

FOR i in Components DO
FOR z := 0 TO H DO


Sc(i,z) =    (mug(z))/(rhog(z)*Dm_comp_in_mix(i,z));
# -; Schimdt number
Dz(i,z) =   (Dm_comp_in_mix(i,z)/eb)*(20 + 0.5*Re(z)*Sc(i,z)) ;
# m^2/s; axial dispersion coefficient
Sh(i,z) =    2 + 1.1*(ABS(Sc(i,z)+1E-5)^(1/3))*(ABS(Re(z)+1E-5)^0.6);
# -; Sherwood number
kf(i,z) =    Sh(i,z)*Dm_comp_in_mix(i,z)/dp;
# m/s; film mass transfer coefficient from fluid to particle surface

END
END



# Heat Transfer Relations (Inside Column)
#-------------------------------------------------------------------------------

FOR z := 0 TO H DO

Pr(z) =   (Cpg(z) * mug(z))/ kg(z) ;
# -; Prandlt number
#Nui(z) =   2 + 1.1*(Pr(z)^(1/3))*(Re(z)^0.6);
Nui(z) =   2 + 1.1*(ABS(Pr(z)+1E-5)^(1/3))*(ABS(Re(z)+1E-5)^0.6);
```

```
# -; Nusselt number between fluid and adsorbent
hi(z)  =   kg(z)*Nui(z)/dp;
# W/m^2.K; convective film heat transfer coeffient between fluid and adsorbent
Nuw(z) =   12.5 + 0.048*Re(z);
# -; Nusselt number inside column between fluid and column wall
hw(z)  =   kg(z)*Nuw(z)/di;
# W/m^2.K; internal convective heat transfer coeffient between fluid and column wall
kL(z) =    kg(z)*(7 + (0.5*Pr(z)*Re(z))) ;
# J/s.m.k; effective axial heat dispersion inside column
END

# Heat Transfer Relations (Outside Column)
#-------------------------------------------------------------------------

FOR z := 0 TO H DO

Rao(z)= ABS((Tw(z) - Tamb)*g*(do_^3)/Tamb/nuamb/Alphamb) ;
# -; Rayleight number outside column
Nuo(z)= 0.68 + (0.67*(ABS(Rao(z)+1E-5)^(1/4)))/(1 + (0.492/Pramb)^(9/16))^(4/9) ;
# -; Nusselt number outside column
ho(z) = kamb*Nuo(z)/do_ ;
# W/m^2.K; heat transfer coefficient outside column

END


#Multicomponent Temperature Dependent SIPS Isotherm
#-------------------------------------------------------------------------

FOR i in Components DO
FOR z := 0 TO H DO
b(i,z) = (b0(i)*EXP(Heat_RTg(i)*((T0/Tg(z))-1))) ; #atm^-1
qm(i,z) = (qm0(i)*EXP(X(i)*(1-(Tg(z)/T0))))  ;      #mol/kg
n(i,z) = (n0(i)+(alfa(i)*(1-(T0/Tg(z))))) ;        #dimensionless
END
END


FOR i in Components - "He" DO
FOR z := 0 TO H DO
CASE cal_mode OF
    WHEN initialize:
      qe(i,z) =
(qm(i,z)*(b(i,z)*((cginlet(i)*R_Latm*Tfeed)))^(1/n(i,z)))/(1+((b0_CH4*EXP(Heat_RTg_CH
4*((T0/Tfeed)-1)))*(cginlet('CH4')*R_Latm*Tfeed))^(1/(n0_CH4+(alfa_methane*(1-
(T0/Tfeed)))))+ ((b0_CO2*EXP(Heat_RTg_CO2*((T0/Tfeed)-
```

```
1)))*(cginlet('CO2')*R_Latm*Tfeed))^(1/(n0_CO2+(alfa_CarbonDioxide*(1-(T0/Tfeed)))))+
((b0_He*EXP(Heat_RTg_He*((T0/Tfeed)-
1)))*(cginlet('He')*R_Latm*Tfeed))^(1/(n0_He+(alfa_Helium*(1-(T0/Tfeed))))) ;
    WHEN calculate:
        qe(i,z) =
(qm(i,z)*(b(i,z)*((cg(i,z)*R_Latm*Tg(z))))^(1/n(i,z)))/(1+((b0_CH4*EXP(Heat_RTg_CH4*
((T0/Tg(z))-1)))*(cg('CH4',z)*R_Latm*Tg(z)))^(1/(n0_CH4+(alfa_methane*(1-
(T0/Tg(z))))))+ ((b0_CO2*EXP(Heat_RTg_CO2*((T0/Tg(z))-
1)))*(cg('CO2',z)*R_Latm*Tg(z)))^(1/(n0_CO2+(alfa_CarbonDioxide*(1-(T0/Tg(z)))))+
((b0_He*EXP(Heat_RTg_He*((T0/Tg(z))-
1)))*(cg('He',z)*R_Latm*Tg(z)))^(1/(n0_He+(alfa_Helium*(1-(T0/Tg(z))))))) ;

  END

END
END


qe("He",) = 0 ;




#% Mass Balances
#-------------------------------------------------------------------------------

# Gas-Phase Component Mass Balance
#-------------------------------------------------------------------------------

FOR i in Components DO
FOR z := 0|+ TO H|- DO



$cg(i,z) = Dz(i,z)*PARTIAL(cg(i,z),Axial_BFDM,Axial_BFDM)
       # -
((1/eb)*((vs(z)*PARTIAL(cg(i,z),Axial_BFDM))+(cg(i,z)*PARTIAL(vs(z),Axial_BFDM))))
          - ((1/eb)*(PARTIAL(vs(z)*cg(i,z),Axial_BFDM)))
          - (((1-eb)/eb)*rhop*($q(i,z))) ;
END
END

# Mass transfer rate to the particle for each component
#-------------------------------------------------------------------------------
```

```
FOR i in Components DO
FOR z := 0 TO H DO

$q(i,z) = K_LDF(i,z)*(qe(i,z)-q(i,z));

END
END


FOR i in Components DO
FOR z := 0 TO H DO
K_LDF(i,z) = 1/(((Rp/3*kf(i,z))*((qe(i,0)*((1-eb)/eb)*rhop)/cg(i,0))) +
(((Rp^2)/15*ep*Dpore(i,z))* ((qe(i,0)*((1-eb)/eb)*rhop)/cg(i,0))) + ((1/15)*(1/(Dc_rc2(i))))+
(1/kb(i))) ;

END
END



#Energy Balances
#---------------------------------------------------------------------------

# Gas-Phase Energy Balance
#---------------------------------------------------------------------------

FOR z := 0|+ TO H|- DO


$Tg(z) = kL(z)*PARTIAL(Tg(z),Axial_BFDM,Axial_BFDM)/rhog(z)/Cpg(z)/eb
        #- ((1/eb)*((vs(z)*PARTIAL(Tg(z),Axial_BFDM))+
(Tg(z)*PARTIAL(vs(z),Axial_BFDM))))
        - ((1/eb)*(PARTIAL(vs(z)*Tg(z),Axial_BFDM)))
        - 2*hw(z)*(Tg(z) - Tw(z))/eb/ri/rhog(z)/Cpg(z)
        - ((1-eb)/eb)*hi(z)*(3/rp)*(Tg(z)-Ts(z))/rhog(z)/Cpg(z) ;

END

# Solid Phase Energy Balance
#---------------------------------------------------------------------------

FOR z := 0 TO H DO

$Ts(z) = ((hi(z)*(3/Rp)*(Tg(z) - Ts(z))) - (rhop*SIGMA(DeltaH()*($q(,z)))))/rhop/Cpp ;

END
```

```
# Energy Balance for Column Wall
#-------------------------------------------------------------------------

FOR z := 0|+ TO H|- DO

$Tw(z) = kw*PARTIAL(Tw(z),Axial_BFDM,Axial_BFDM)/(rhow*Cpw)
        + 2*ri*hi(z)/((ro^2 - ri^2)*rhow*Cpw)*(Tg(z) - Tw(z))
        - 2*ro*ho(z)/((ro^2 - ri^2)*rhow*Cpw)*(Tw(z) - Tamb) ;

END

# Momentum Balance
#-------------------------------------------------------------------------

A_erg = 150 ;#* (1+2*dp/(3*di*(1-eb)))^2 ;
B_erg = 1.75 ;#* (1+2*dp/(3*di*(1-eb))) ;

FOR z := 0 TO H|- DO


-PARTIAL(P(z), Axial_FFDM)*101325 = (A_erg * (mug(z)) * (1 - eb)^2 * vs(z) /(eb^3 *
dp^2)
                + B_erg * (1-eb) / ((dp) * (eb)^3) * vs(z) * ABS(vs(z)) * rhog(z)) ;

END




# Normalized gas phase concentration at the outlet of the column
#-------------------------------------------------------------------------

FOR i in Components DO

cgendnorm(i) = cg(i,H)/SIGMA(cg(,H)) ;

END

# Total Concentration in the Gas Phase
#-------------------------------------------------------------------------

FOR z := 0 TO H DO

Ctotal(z) = (P(z)/(R_Latm*Tg(z))) ;
```

```
END


# Overall Mass Balance
#-------------------------------------------------------------------------------

FOR z := 0|+ TO H|- DO
Ctotal(z) = SIGMA(cg(,z));

END


# Volumetric Flow Rate
#-------------------------------------------------------------------------------
FOR z := 0 TO H DO

v_interstitial(z) = vs(z)/eb ;
Qvol(z) = Area * v_interstitial(z) * eb ;

END


# Mole Fraction of component i
#-------------------------------------------------------------------------------

FOR i in Components - Components.last DO
FOR z := 0 TO H DO

  Y(i,z) = cg(i,z)/Ctotal(z) ;

 END
END

FOR z := 0 TO H DO

  SIGMA(Y(,z)) = 1 ;

 END

Y_out_CO2 = Y('CO2',H) ;
Y_out_CH4 = Y('CH4',H) ;

INITIALISATION_PROCEDURE init
START
  cal_mode := initialize ;
END
```

```
NEXT
  JUMP_TO
    cal_mode := calculate ;
  END
END
```